Supercritical Carbon Dioxide Power Cycles for Waste Heat Recovery Applications

A Thesis Submitted for the Degree of
Doctor of Philosophy

By
Matteo Marchionni

Department of Mechanical, Aerospace and Civil Engineering
College of Engineering, Design and Physical Sciences
Brunel University London

June, 2021

Abstract

The growing energy demand and the increasingly stringent regulations on pollutant and greenhouse gas emissions are driving academia and industry to seek new approaches to increase the overall energy efficiency of existing industrial facilities. Among them, the recovery and utilisation of industrial waste heat is currently considered as one of the most effective approaches to reduce the energy demand of industrial processes as they are characterised by thermal energy losses, through high temperature exhausts above 300°C, that account for nearly 11.4% of primary energy consumption.

For these high temperature waste heat sources, the use of conventional heat to power conversion systems based on bottoming thermodynamic cycles is limited by technological and economic constraints. Most of the state-of-the-art working fluids are indeed not able to perform safely and efficiently at high temperatures. Supercritical Carbon Dioxide (sCO_2) power systems allow to overcome these limitations because of the chemical stability of CO_2 at high temperatures. Furthermore, the favourable CO_2 thermo-physical properties in the supercritical state, including high density, allow to achieve superior performance and lower footprint and cost compared to Organic Rankine Cycles and other more conventional technologies.

With the aim of giving a broad overview of the potential of sCO_2 power cycles in high temperature waste heat recovery (WHR) applications, this research firstly investigates the theoretical capabilities of several Joule-Brayton cycle configurations. The analysis involves performance indicators and economic metrics, which are calculated using cost correlations and budgetary quotations to estimate the investment costs of equipment. This aspect represents one of the main novel contributions of the research.

Among the investigated layouts, the simple regenerative cycle showed the highest competitiveness for industrial uptake of the sCO_2 technology at small-scales (<0.5 MW_e) in high-grade waste heat to power applications. For this reason, such cycle layout has been adopted as reference for the design and construction of a 50 kW_e state-of-the-art experimental facility. The facility comprises an 830 kW process air heater able of providing an exhaust mass flow rate of 1.0 kg/s at 70 mbarg and maximum temperature of 800°C, and a water dry cooler of 500 kW heat rejection capacity as heat sink. The sCO_2 heat to power conversion block utilises a single-shaft Compressor-Generator-Turbine unit and three types of heat exchanger technology. The main design features of the test facility as well as operation and safety considerations are discussed.

This research activity allowed to retrieve accurate geometrical and performance data by component manufacturers which have been used to develop a detailed numerical model of the facility with the objective of investigating the steady-state and transient performance of the sCO_2 system. Operating maps of the unit have been obtained which can form the baseline for the setting up of optimisation and control strategies. The dynamic analysis showed that the system is able to quickly adapt to transient heat load profiles, proving the flexible nature of the sCO_2 unit investigated. Start-up and shut-down strategies able to achieve a safer build-up and decline of pressures and temperatures in the circuit, thus eliminating the risk of flow shocks and excessive mechanical stresses, have also been identified.

A further novel contribution is assessment of the advantages of having the turbine and compressor driven independently as opposed to being mounted on the same shaft that dictates operation at the same speed. The results show only a small benefit at design conditions, but a power increase of 27% at 10% increase in heat source temperature, highlighting the advantage of independent drive at off design conditions.

The adoption of an inventory control strategy to regulate the sCO_2 system during transient operations showed that the imposed variation in the CO_2 mass circulating in the loop allows to achieve a 30% variation in the turbine inlet temperature with lower penalties on system performance compared to turbomachinery speed control.

List of Publications

Published Journal Papers

- Marchionni, M., Bianchi, G., Tassou, SA. (2018). "Techno-economic Assessment of Joule-Brayton Cycle Architectures for Heat to Power Conversion from High-grade Heat Sources Using CO_2 in the Supercritical State." *Energy 148*: 1140-1152.

- Marchionni, M., Bianchi, G., Karvountzis-Kontakiotis, A., Pesyridis, A., Tassou, SA. (2018). "An Appraisal of Proportional Integral Control Strategies for Small Scale Waste Heat to Power Conversion Units Based on Organic Rankine Cycles." *Energy 163*: 1062-1076.

- Marchionni, M., Chai, L., Bianchi, G., Tassou, SA. (2019) "Numerical Modelling and Transient Analysis of a Printed Circuit Heat Exchanger Used as Recuperator for Supercritical CO_2 Heat to Power Conversion Systems." *Applied Thermal Engineering 161*: 114190.

- Bianchi, G., Marchionni, M., Kennedy, S., Miller, J., Tassou, SA. (2019). "One-Dimensional Modelling of a Trilateral Flash Cycle System with Two-Phase Twin-Screw Expanders for Industrial Low-Grade Heat to Power Conversion." *Designs* 3(3): 41.

- Bianchi, G., Marchionni M., Miller J., Tassou, SA. (2020). "Modelling and Off-design Performance Optimisation of a Trilateral Flash Cycle System Using Two-phase Twin-screw Expanders with Variable Built-in Volume Ratio." *Applied Thermal Engineering 179,* 115671.

- Marchionni, M., Bianchi, G., Tassou, SA. (2020). "Review of Supercritical Carbon Dioxide (sCO_2) Technologies for High-grade Waste Heat to Power Conversion." *SN Applied Sciences* 2(4): 1-13.

- Marchionni, M., Bianchi, G., & Tassou., SA. (2021). "Transient Analysis and Control of a Heat to Power Conversion Unit Based on a Simple Regenerative Supercritical CO_2 Joule-Brayton Cycle." *Applied Thermal Engineering 183:* 116214.

Conference Proceedings

- Marchionni, M., Bianchi, G., Tsamos, K. M., Tassou, SA. (2017). "Techno-economic Comparison of Different Cycle Architectures for High Temperature Waste Heat to Power Conversion Systems Using CO_2 in Supercritical Phase." *Energy Procedia 123*: 305-312.

- Marchionni, M., Bianchi, G., Karvountzis-Kontakiotis, A., Pesyridis, A., Tassou, SA. (2017). "Dynamic Modelling and Optimization of an ORC Unit Equipped with Plate Heat Exchangers and Turbomachines." *Energy Procedia 129*: 224-231.

- Marchionni, M., Bianchi, G., Tassou, SA., Zaher, O., Miller, J. (2019). "Numerical Investigations of a Trilateral Flash Cycle Under System Off-design Operating Conditions." *Energy Procedia 161*: 464-471.

- Marchionni, M., Chai, L., Bianchi, G., Tassou, SA. (2019). "Numerical Modelling and Performance Maps of a Printed Circuit Heat Exchanger for Use as Recuperator in Supercritical CO_2 Power Cycles." *Energy Procedia 161* (2019): 472-479.

- Bianchi, G., Sayad Saravi, S., Loeb, R., Tsamos, K. M., Marchionni, M., Leroux, A., Tassou, SA. (2019). "Design of a High Temperature Heat to Power Conversion Facility for Testing Supercritical CO_2 Equipment and Packaged Power Units." *Energy Procedia 161*: 421-428.

- Marchionni M, Bianchi G, Tassou SA. "Modelling and Performance Analysis of a Supercritical CO_2 System for High Temperature Industrial Heat to Power Conversion at Off-design Conditions." 3rd European Conference on Supercritical CO_2.

- Marchionni M, Bianchi G, Usman M, Pesyridis A, Tassou SA. "Numerical Investigation of a Simple Regenerative Heat to Power System with Coupled or Independent Turbomachinery Drives." 4th European Conference on Supercritical CO_2.

- Marchionni M, Bianchi G, Tassou S. A. "Dynamics of SCO_2 Heat to Power Units Equipped with Dual Tank Inventory Control System." 6th International Seminar on ORC Power Systems.

Awards

- Honorable Mention at the 2019 ABTA Doctoral Researcher Awards, prize sponsored by the Academic British and Turkish Association. 11th May 2019 University College of London (UCL)

- 1st prize in the TRA VISIONS 2020 Young Researcher Competition for the most innovative idea in airborne transportation mode, 29th September 2020. Idea title: "A novel concept for a zero-emission aircraft turbofan engine using CO_2 in supercritical phase as working fluid".
https://www.travisions.eu/TRAVisions/young_researcher_results_2020

List of Contents

List of Figures

List of Tables

xv

Acknowledgements

Nomenclature and Glossary

Symbols:

α_p	Thermal diffusivity	[m^2/s]
β	Pressure ratio	[-]
ξ	Pressure loss coefficient	[-]
η	Efficiency	[-]
κ	Isothermal compressibility	[kg/m^3]
ρ	Density	[Pa]
σ	Surface tension	[m^2/s]
υ	Dynamic viscosity	[-]
ζ	Heat transfer coefficient	[W/(m^{2}K)]
dx	Displacement	[m]
f	Fanning friction factor	[-]
e	Total specific energy	[kJ/kg]
h	Specific enthalpy	[kJ/kg]
m	Mass	[kg]
$\dot{m}$	Mass flow rate	[kg/s]
p	Pressure	[bar]
s	Entropy	[kJ/(kgK)]
t	Time	[s]
v	Specific volume	[m^3/kg]
u	Velocity	[m/s]
A	Area	[m^2]
C	Investment cost	[$]
C_1	Pressure drop calibration coefficient	[-]
C_d	Discharge coefficient	[-]
C_p	Isobaric thermal capacity	[kJ/K]
C_v	Isochoric thermal capacity	[kJ/K]
CF	Cash flow	[$]
D	Diameter	[m]
$\dot{E}$	Exergy flow	[kW]
H	Specific enthalpy	[kJ/kg]
I	Irreversibility	[kW]
L	Length	[m]
Nu	Nusselt number	[-]
Pr	Prandtl number	[-]
Q	Heat load	[kJ]
R	Radius	[m]

e	electrical
ex	exergy
hot	hot source
i	inlet
$inst$	installation
is	isentropic
m	mechanical
o	outlet
rev	revenues
tot	total
wl	wall
wf	working fluid
xp	expenses
C	compressor
HX	heat exchangers
T	turbine
0	Total/dead state
∞	boundaries
0	Total/dead state
∞	boundaries

Acronyms:

CBV	Compressor By-pass Valve
CGT	Compressor-Generator-Turbine
HX	Primary heat exchanger
IRR	Internal Rate of Return
LCOE	Levelized Cost Of Electricity
LMTD	Logarithmic Mean Temperature Difference
ORC	Organic Rankine Cycle
PBP	Pay Back Period
PCHE	Printed Circuit Heat Exchanger
PH	Pre-Heating
PHE	Plate Heat Exchanger
PHPC	Pre-Heating with Pre-Compression
PHSE	Pre-Heating with Split Expansion
PI	Proportional-Integral

Ra	Surface roughness	[µm]	PP	Pinch Point
Re	Reynolds number	[-]	RC	Re-Compression
T	Temperature	[°C/K]	RCRH	Re-Compression Re-Heating
V	Volume	[m³]	RH	Re-Heating
$\dot{W}$	Mechanical/ Electrical Power	[kW/kWₑ]	SC	Specific Cost
			sCO₂	Supercritical carbon dioxide
			SHSE	Split-Heating with Split Expansion
			SR	Simple Regenerated
subscripts:			SS 316L	Stainless steel 316L
			TIT	Turbine Inlet Temperature
₆	bubble		TBV	Turbine By-pass Valve
₍ₛ	cold side		WHR	Waste Heat Recovery
₍ₒₘₚᵣ	compression		cs	Cold side
₍ᵤₘ	cumulative		hs	Hot side

1. Introduction

Currently the power generation sector is experiencing a steep rise in the use of renewable sources, which currently in Europe represents 80% of new installed capacity and showed the highest rate of growth among all energy sources. Their deployment is not just confined to the energy sector, but also to mobility, heating and cooling worldwide [1].

As a consequence, the investment and maintenance costs of renewable technologies decreased substantially in recent years, representing 70% reduction in photovoltaic (PV) panels, 25% reduction in wind turbo-generators and 40% in batteries. This consistent cost reduction has also been driven by China and India due to their role as both large manufacturers and consumers.

Despite the positive achievements, driven also by the more stringent regulations in terms of greenhouse gas (GHG) emissions promoted by governments and international institutions (i.e. the Kyoto and Montreal protocols or the Paris Agreement [2]), fossil fuels still play an important role in world power supply.

With reference to the global energy demand in 2019, coal, natural gas and oil still provide 38%, 23% and 4% of energy for electricity production respectively, while renewables provide 25%. The role of fossil sources is also accentuated by the estimated growth in the energy demand that cannot be balanced just with the use of renewables, especially if the rising demand by developing countries is considered [1].

An effective way to further reduce the fossil dependency, may be represented by a joint use of renewable sources together with the increase of the overall energy efficiency of existing power generation, buildings and industrial facilities.

Improvements in energy efficiency are considered one of the key priorities to reduce the impact of fossil fuel sources on the industrial system and economy [1]. The World Energy Outlook 2018 reports that, in advanced economies, new sources of electricity demand growth such as digitalization and electrification of heat and mobility have been outpaced by savings from energy efficiency. Energy efficiency initiatives and projects since 2000 have saved almost 1800 TWh in 2017, which is the equivalent of around 20% of the overall current electricity use [3].

Among the developed economies, the European Union (EU) has been at the forefront of energy efficiency and demand reduction. To date, greenhouse gas emissions have been reduced by 22.9% compared to 1990 levels while a key target for 2030 is at least a 40% reduction with respect to the same reference year [4]. Ambitious are also the UK targets, which aim to reduce emissions by at least 68% by 2030, compared to 1990 levels [5].

Therefore, many industrial and academic research activities are focused on helping to achieve these objectives. Among the several approaches, the recovery and utilisation of the heat lost during the processes represents the most effective solution for the enhancement of energy efficiency in industry, power generation and the mobility sector. It has been indeed estimated that 63% of the global energy consumption is due to energy lost during combustion and heat transfer processes [6]. This amount of wasted thermal energy includes the heat rejected to the environment under the form of radiation, effluents and exhausts.

The recovery and utilisation potential of waste heat also depends on the characteristics of the waste heat source. According to the processes involved, the waste heat can be supplied at low (<100°C), medium (100°C – 300°C) or high temperature levels (>300°C) [7].

A further distinction can be done according to the availability of the waste source, which can be continuous or discontinuous; on the composition of the heat carrier, which can pose corrosion problems; on the intensity of the heat supply, high or low mass flow rates in the case of exhaust or effluents; or on the ease and economic feasibility of its recovery and utilisation.

Besides these aspects, which can be addressed by adopting different technologies, the Waste Heat Recovery (WHR) sector has a huge economic potential and represents one of the main drivers for the reduction of energy consumptions and greenhouse gases emissions in the short and medium term in the European Union.

1.1 Waste Heat Recovery Potential in Europe

The European Union with its 28 member states (EU-28) until December 2020, is responsible for 16.1% of the world's final energy consumptions, 111.1 PWh in 2016, and for 11.2% of the world's final CO_2 emissions, 32.3 $GtCO_2$ in 2016 [8]. In particular, the overall final European energy consumption can be divided into four main sectors: industrial, transport, residential and general utilities, as showed in Figure 1.a and following the approach detailed in [8]. The industrial sector accounts for 25.9% of the final energy consumptions (Figure 1.a) and for 47.7% of the final CO_2 emissions [4].

For the industrial energy consumption, Figure 1.b highlights that only 52% is actually spent for energy services (i.e. motion, heating, cooling, and electricity) while the remaining can be considered to be energy loss. The 20% of this amount is lost through friction and irreversibility which is very difficult to recover, while almost 29% is rejected to the environment by exhausts and effluents, accounting for 918 TWh, which represents 7.4% of the European final energy consumption [7]. However, this is a theoretical figure and does not account for the physical and technical constraints of its recovery and utilisation.

As previously mentioned, one of the main limitations is the temperature at which waste heat sources are available. Figure 1.c distinguishes the theoretical industrial energy waste available under the form of effluents/exhausts by temperature level (High Temperature, HT, Medium Temperature, MT, or Low Temperature, LT). The theoretical work that can be extracted from a generic heat source which can be assumed to be at ambient temperature of (15°C), can be computed by multiplying the theoretical heat available by the Carnot efficiency. Then, from the data of Figure 1.c it is possible to compute the theoretical Carnot waste heat potential shown in Figure 1.d. This is 279 TWh, and represents 2.3% of the European final energy consumption.

Analysing the theoretical Carnot potential shown in Figure 1.d allows to observe that even though the low temperature sources constitute the larger share of the industrial waste heat recovery potential (51%), when the physical constraints arising for the recovery of those sources are considered, their contribution drops down to 23%, with the high temperature exhausts and effluents being the most feasible waste heat source for energy recovery (55%). Thus, the Carnot potential provides a more precise indication on whether waste heat can be used for technical work or would be more suitable for direct heat recovery for heating purposes.
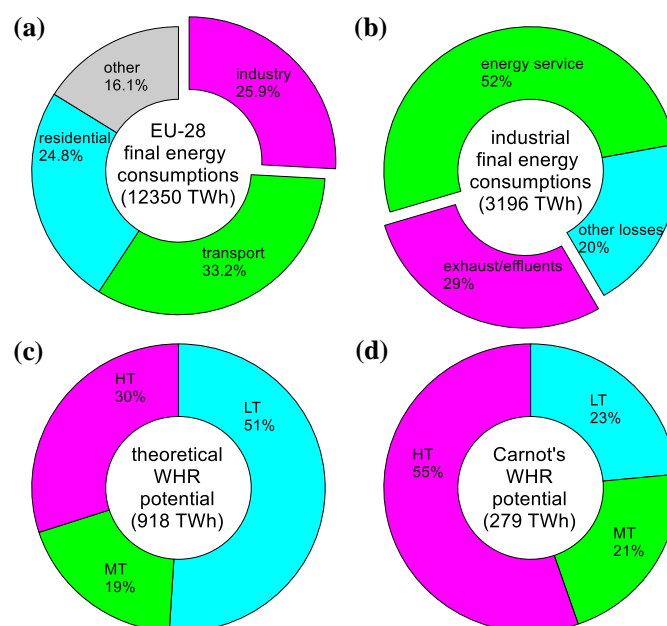
Figure 1 – Theoretical and Carnot waste heat recovery potentials in the EU28 industrial sector: overall EU28 energy consumption (a), overall industrial consumption (b), theoretical waste heat recovery potential per temperature level (c) and Carnot WHR potential (d) [7].

Figure 2 shows the distribution of the Carnot waste heat potential in the EU-28. It can be seen that Germany offers over 20% of the overall potential, followed by Italy, France and the United

Kingdom. The greatest share of this waste heat is produced by the most energy intensive industrial sectors, as shown in Table 1. Since the driving factor of the Carnot potential is the exergy content of the waste heat stream, i.e. the temperature level at which the heat is rejected to the environment, the industries characterised by high temperature processes are the ones with the highest Carnot potential.
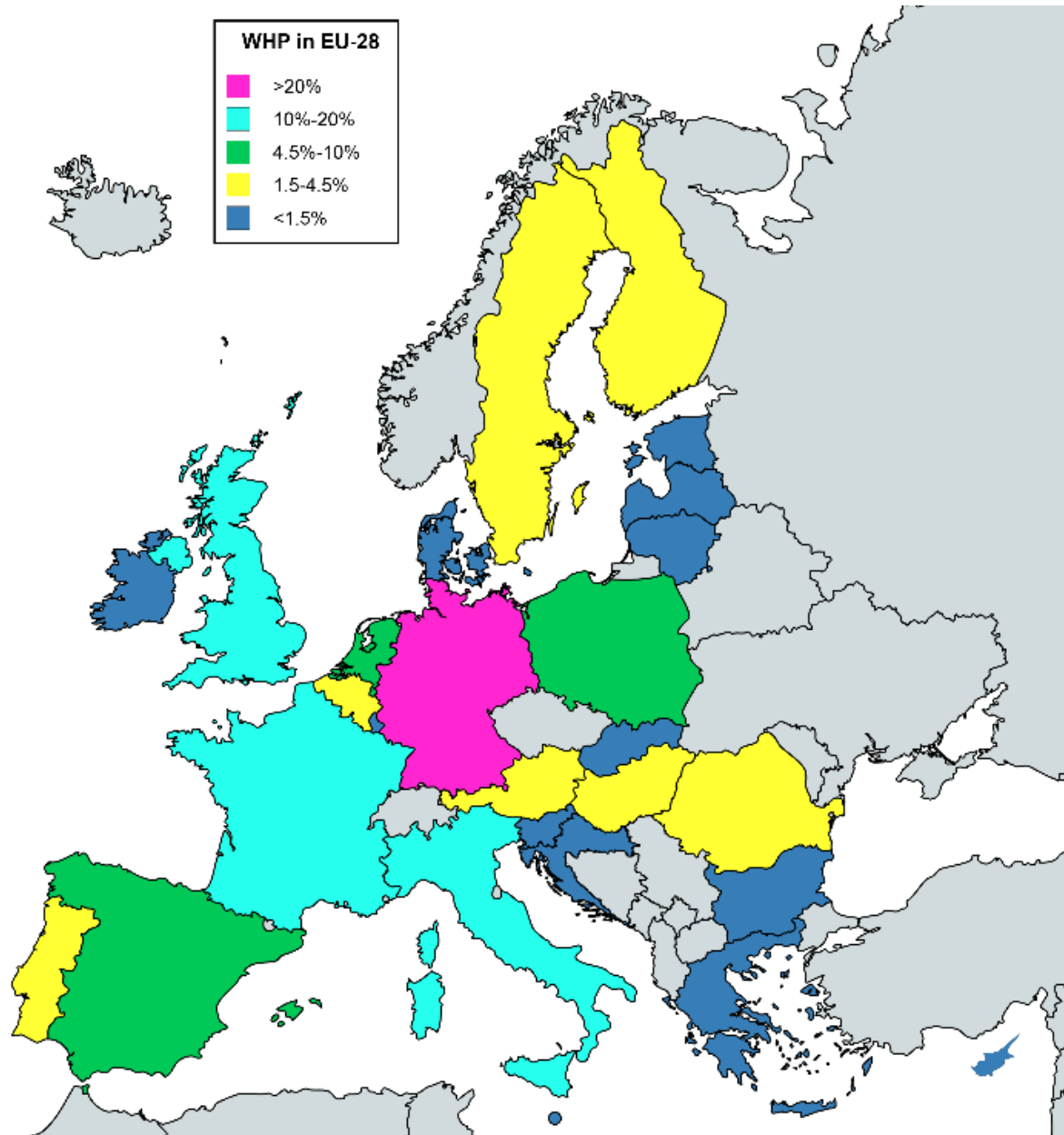
Figure 2 – Waste heat potential distribution among the 28-member states of the European Union (EU-28) [7]

For example, even though the theoretical potential of the food and tobacco sectors is 35% of the total primary energy consumption of the sector, the Carnot potential is only 6% because of the relatively low temperature of the waste heat. On the other hand, the Iron and Steel industry whose manufacturing processes involve energy dissipations at high temperatures has

a Carnot potential of 9.1%, more than one third of the theoretical value. Other industrial sectors characterised by high waste heat recovery potential are the ones related to non-metallic minerals, such as glass and cement industries as well as the Oil & Gas.

Exploiting these unused waste energy sources could lead not only to energy savings and lower emissions but also contribute to reinforce the EU's industrial position in a sector that already leads [9].

Table 1 – European Theoretical and Carnot waste heat potential by industrial sector [7]

Type of Industry	Theoretical potential	Carnot potential
Iron and Steel	25%	9.1%
Non-Ferrous Metals	26%	2.4%
Chemical and Petrochemical	25%	5.7%
Non-Metallic Minerals	22%	7.4%
Mining and Quarrying	36%	0.5%
Food and Tobacco	35%	5.9%
Textile and Leather	35%	0.9%
Paper, Pulp and Print	31%	4.5%
Transport Equipment	35%	1.3%
Machinery	35%	3.3%
Wood and Wood Products	30%	0.8%
Construction	37%	1.6%
Non-specified (Industry)	34%	3.3%

1.2. Waste Heat Recovery Technologies

In industrial waste heat recovery applications what usually drives the adoption of a particular technology is a combination of factors such as economy, profitability, and waste source temperature and availability. An additional factor influencing the quantity of heat that can be recovered is the Waste Heat Recovery (WHR) technology employed.

There are two main classes of WHR systems, the ones allowing the recovery of the waste heat to satisfy a heating or cooling demand, which can be referred to as heat recovery technologies, and the ones allowing the conversion of the waste heat to electric energy, which are usually referred to as heat to power conversion technologies.

The first class is usually characterised by a single or a group of devices that can recover heat from the waste source for direct use or storage for subsequent use. In these systems, the technical waste heat potential is very close to the Carnot potential due to the high efficiency of the devices. The heat to power technologies, on the other hand, are usually characterised by the use of additional components to perform the heat to power conversion. The complexity of these components as well as the physical and technical limitations arising from the

5

conversion of heat to mechanical and electrical power, cause a reduction in the technical potential to around 50% of the Carnot potential.

Despite the greater ease of implementation of heat recovery and its direct use in the plant for heating, in many occasions there is limited need for this heat within the plant. Conversion of heat to power where high temperature waste heat is available, is in many cases preferable due to the higher economic value of electricity and its potential to displace high emissions factor electricity from the grid.

Several heat to power conversion technologies are being studied for WHR applications. Thermionic and thermoelectric devices utilise the temperature gradient between the surface heated by the waste energy source and the environment for the conversion of thermal energy to electrical power [10,11]. Thermo-acoustic units, generate electrical power using heat-induced sound vibrations that drive piezoelectric transducers or acoustic turbines [12]. Despite the advantage of these technologies of having the capability to implement a direct heat to power conversion with a limited system complexity, at the current state-of-the-art several technical challenges limit their applicability and heat recovery potential [13].

A more established technology is the bottoming heat to power conversion system based on thermodynamic cycles. In these systems, a working fluid is used to convert, through a series of transformations realised by different components, the waste heat into mechanical power and then electricity. Depending on the temperature range at which the waste heat is available, several approaches can be adopted. For the low to medium temperature range (100oC-300oC), Organic Rankine Cycle (ORC) systems are proving to be a successful technological solution especially for large scale applications [14]. In the last decade, significant academic and industrial research has been also carried out to develop mid and small-scale ORC systems which are becoming commercially viable [14].

In the ORC technology, an organic working fluid, characterised by a greater molecular mass and vapour pressure than water, performs a Rankine or a Hirn cycle to recover and convert the thermal energy rejected by the topping facility [15]. The working fluid is compressed by a pump and it is vapourised and superheated (in case of a Hirn cycle) in the evaporator, where the heat recovery stage occurs. The refrigerant is then expanded in a turbine converting pressure and thermal energy into mechanical power and then through a generator to electricity. At the turbine outlet, the fluid is condensed in an additional heat exchanger, rejecting heat to the environment and its initial thermodynamic conditions are restored to allow the thermodynamic cycle to be repeated.

Despite the high technology readiness level of ORCs, their efficiency drops significantly at heat source temperatures below 100°C due to the low evaporation rate of refrigerant and low

power output. A possible alternative at these low temperatures is the Trilateral Flash Cycle (TFC), whose name comes from the triangular shape of the implemented thermodynamic cycle. Although TFC systems consist of the same components as ORCs, there is a major difference related to the state of the working fluid before the expansion process. In TFC units, there is a better matching of heat source and sink temperatures during heat addition to the cycle enabling the cooling of the heat source to a lower temperature, increasing the heat recovery potential. After the heating stage, the saturated liquid undergoes 'wet' expansion in the expander, increasing the power out per unit refrigerant flow compared to the ORC cycle [16].

For high temperature waste heat sources, however, both these technologies cannot be safely employed because of the lower chemical stability and high flammability of the working fluids used in the cycle. For high temperature waste heat sources, bottoming systems based on the Joule-Brayton cycle and adopting supercritical carbon dioxide (sCO_2) as working fluid are a promising alternative to harvest this substantial high temperature waste heat potential. CO_2 has a high chemical and thermal stability at temperatures up to 2000°C [17], which is much higher than the most demanding application temperature in the power generation field. In addition, the particular thermo-physical properties of the fluid allow to achieve high energy and exergy efficiencies that can lead to energy and economic energy savings [18]. The high density of CO_2 in the supercritical phase also enables the downsizing of the system components, which makes the technology a suitable alternative for the exploitation of widespread small to medium capacity waste heat recovery sources, typical of the industrial sector.

Despite the potential, few works are available in the literature on the topic. Research institutions and an increasing number of industries have been investigating the sCO_2 topic mostly for nuclear and concentrated solar power applications, whose requirements differ considerably from the waste heat recovery sector. Furthermore, very few studies have been conducted on sCO_2 system transient analysis and control, which are the main challenges the technology currently faces for industrial exploitation.

1.3. Aims and Objectives of the Research

The research work investigates the opportunity and feasibility of industrial waste heat to power conversion at high temperatures (>350°C) using the supercritical CO_2 heat to power cycle. The aim is to build on current knowledge on sCO_2 systems through cycle analysis to establish the advantages and disadvantages of different sCO_2 cycles for waste heat recovery applications, and investigate the characteristics of smaller capacity systems through modelling and design of a pilot test facility that can be used for experimental studies on system

performance and control. Currently there is limited research in the UK and rest of Europe on SCO_2 heat to power systems with most activity concentrated in the Japan, China, Korea and the USA. Limited research activity in Europe has mainly focused on cycle modelling and investigation of individual components at very small scale [19]. This thesis goes further than other studies in Europe through the development of a reasonable scale (50 kW_e power output) test facility for experimental investigations on sCO_2 heat to power systems and the investigation of key components and control of the overall system.

The thesis objectives are:

1. Review the state-of-the-art of the technology and provide a wide overview of the range of applicability of sCO_2 systems in waste heat recovery applications. This is done by comparing the operating range of sCO_2 systems with other more conventional technologies with a map-based approach;

2. Provide a theoretical but broad overview of the capabilities of sCO_2 systems in high temperature industrial waste heat recovery applications. This is done by comparing several sCO_2 cycle layouts in terms of technical performances as well as investigating the investment dynamics in this field. In order to do that, budgetary quotations from equipment manufacturers are used rather than data in the literature;

3. Address the need of bridging between fundamental energy research and industrial exploitation of the technology by presenting a state of the art 50 kW_e sCO_2 experimental facility able to allow the investigation of pilot flue gas/sCO_2, sCO_2/sCO_2 and sCO_2/water heat exchangers and plant dealing with high temperature waste heat recovery and conversion;

4. Develop a novel modelling approach able to balance complexity, computational effort, time and cost of numerical calculations in order to be suitable for optimization analyses and control purposes, which require an extensive number of simulations to be carried out;

5. Investigate the steady-state and transient behaviour of small-scale supercritical carbon dioxide (sCO_2) power system and provide a baseline for system optimisation and control. These are central aspects for the advancement of the technological readiness level of such systems from 3 (Experimental proof of concept) to 5 (Technology validated in relevant environment);

6. Assess optimal control strategies for the regulation of small scale sCO_2 power systems by identifying the most suitable process control variables and developing an appropriate control strategy for the 50 kW_e system.

1.4. Thesis Structure

Following the brief introduction, the thesis is structured as follows:

Chapter 2 presents a comprehensive literature review of the current state-of-the-art in sCO_2 heat to power conversion systems, highlighting the main benefits of the technology as well as the critical technical challenges to be addressed. The principal studies in the field of turbomachinery, system auxiliaries, heat exchanger technologies and materials are detailed. A brief overview of the possible applications of the sCO_2 power technology is also given.

Chapter 3 presents a techno-economic analysis of the main sCO_2 power cycle layouts. Firstly, the main cycle configurations in the literature are described as well as the underlying thermodynamic principles. Eight promising cycle architectures with particular reference to WHR applications are analysed in more detail. A sensitivity analysis is performed to assess the most representative variables for the sCO_2 power cycles.

Chapter 4 details the design and construction of a 50 kW_e sCO_2 plug-and-play test facility for industrial WHR applications. Details about the turbomachinery, heat exchanger technologies adopted, as well as the auxiliaries embedded in the unit have been provided and design challenges discussed. A control and remote monitoring system based on the IEC 61499 standard developed for the regulation of the facility is also presented.

The design and construction work outlined in this Chapter has been realised with the help of several members of the research team lead by Professor Savvas Tassou and many European and UK industrial partners. In particular, my main contribution was in the design of the measurement chain, control and monitoring system as well as hands-on help in the many day-to-day activities involved in the construction of the demonstrator.

Chapter 5 describes the development of a transient model of the sCO_2 system. The modelling methodology follows a novel approach which allows to balance complexity, time and cost of numerical calculations and for these reasons is very suitable for optimisation analyses and control purposes. The accuracy relies on the performance and geometrical data of each component, which have been provided by the component manufacturers.

In Chapter 6 the developed numerical model has been used to assess the steady-state performance of the system at design and off-design conditions. The results obtained from the simulations represent an operating map of the unit which can be used as baseline for the development of control strategies for the sCO_2 system. Transient analyses have also been

carried out to assess the dynamic response of the unit to time varying profiles of the flue gas operating parameters. Different time scales have been considered to investigate the time evolution of the main cycle parameters and to identify lags in response with respect to fluctuations of the heat source. The analysis aims to assess and prove the flexible features of the sCO_2 power system investigated.

In Chapter 7 a sensitivity analysis is carried out to identify the most suitable strategy for the control of the system. Control strategies to ensure safe operating conditions for the key components of the system are also presented and discussed.

Chapter 8 presents the Conclusions and recommendations for further research.

2. Literature Review

2.1 Introduction

Supercritical carbon dioxide (sCO_2) Brayton power cycle is a heat to power conversion technology which attracted recently a strong interest because of the special properties the CO_2 shows after the critical transition. The working principle of the technology is the recovery of the heat by the working fluid, CO_2, and the consequent conversion in electrical power. To do so, the working fluid undergoes through a series of transformations which are repeated continuously and together form a thermodynamic cycle. The name comes from the cyclic nature of such process, since after a finite number of transformations the initial thermodynamic conditions of the working fluid are restored. The most common thermodynamic cycle performed by sCO_2 systems is usually the Joule-Brayton one and its variants.

The Joule-Brayton cycle, or Brayton cycle, is mainly composed by four thermodynamic transformations of the working fluid, highlighted in Figure 3 in the pressure-volume (p-v) diagram (Figure 3.a), and in the Temperature-entropy (T-s) one (Figure 3.b). An adiabatic compression (line 1-2) is performed to pressurize the working fluid and then to increase the effectiveness of the heat transfer between the hot source and the working fluid. This heat transfer process (line 2-3), which occurs at constant pressure and increases the enthalpy content of the working fluid, represents the heat recovery stage. The fluid enthalpy content is converted into mechanical power and thus electricity by means of an adiabatic expansion (line 3-4).

Finally, an isobaric heat rejection (line 4-1) is performed to restore the initial cycle conditions. Eventually, a part of this residual thermal energy at the end of the expansion (point 4) can be used to heat up the fluid flow downstream the compression (point 3) and thus decreasing the primary thermal energy input provided by the heat source. This transformation is named regeneration, or recuperation, and allows to increase the overall cycle efficiency since the same power is extracted by the working fluid but with a reduced amount of thermal energy adsorbed from the heat source.

In conventional energy conversion systems based on the Brayton cycle, which usually use air as working fluid, the recuperation is rarely adopted, unless high efficiencies are required. A recuperated cycle needs additional components, which in turn increase system complexity and investment costs. However, when sCO_2 is used as working fluid, the recuperation must be considered because of the peculiar cycle characteristics.

Given the low pressure ratio typical of sCO_2 power cycles and the slow divergence of the CO_2 isobaric lines, high inlet turbine temperatures are required to have a positive net power output, with a consequent high enthalpy content of the fluid at the end of the expansion process, which if rejected to the environment will constitute a substantial energy loss.

For these reasons, to not excessively penalize the cycle efficiency, the sCO_2 simplest system configuration considers the recuperation and it is named simple regenerated Brayton cycle. Figure 4 details the various components required to perform the several thermodynamic transformations involved and above described. The adiabatic compression is realized by the compressor (C), while the regeneration of the CO_2 flow occurs in a heat exchanger, namely the recuperator, exploiting the high enthalpy content of the CO_2 at the end of the expansion. Afterwards, the fluid is further heated up in the heater, which allows the heat transfer from the primary energy source to the working fluid.
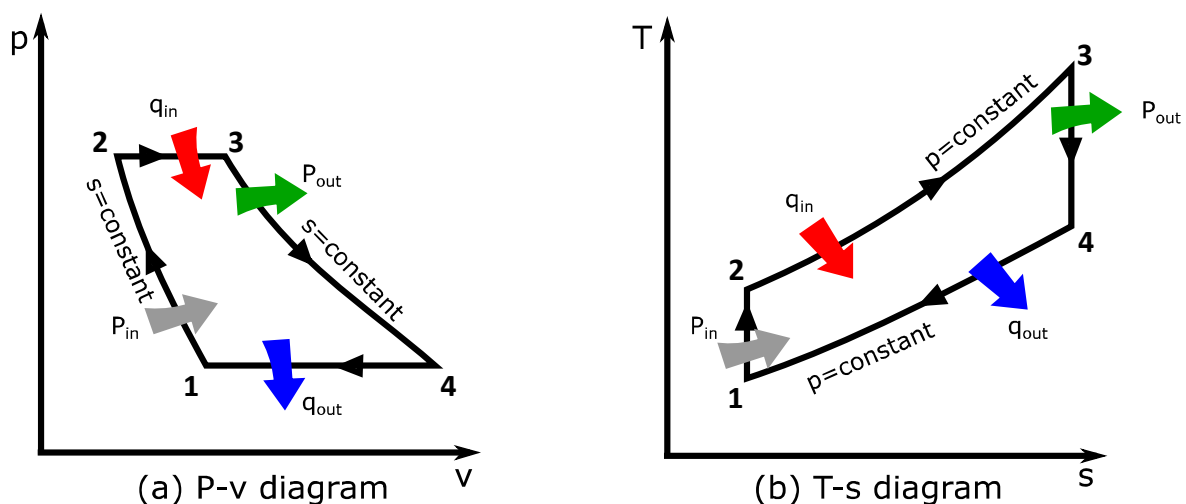
Figure 3 – Joule-Brayton cycle in the p-v diagram (a) and in the T-s diagram (b).

The CO_2 is then expanded in the turbine (T) and cooled down in the recuperator and after in a second heat exchanger, the gas cooler, where the isobaric heat rejection takes place. The difference between the mechanical power generated by the turbine and the one supplied to the compressor represents the system net power output and it is eventually converted in electricity by the generator (G).

The first reference in the literature on such systems can be dated back to 1948, when Sulzer Bros [20] patented a partial condensation sCO_2 cycle. Following the relevance of this work a lot of studies have been carried out since then. In 1967 Feher [21] proposed a regenerated sCO_2 Brayton cycle which was operating entirely above the critical pressure, with the cycle operating between the minimum and maximum temperature of 20°C and 700°C respectively. In the same period, Angelino [22–24] performed a comprehensive analysis of sCO_2 condensation cycles, where the minimum pressure and temperature have been considered

lower than the critical ones. In these works, he recognized the main relevant advantages deriving by the use of CO_2 as working fluid, as for instance the reduced compression work near the critical point and the high fluid density, allowing the downsizing of turbomachines and heat exchangers. The additional advantage of a high thermal stability has also been highlighted, with the observation of a low fluid degradation rate at 1500°C and in range of pressure between 2 and 40 MPa.

(a)   (b)
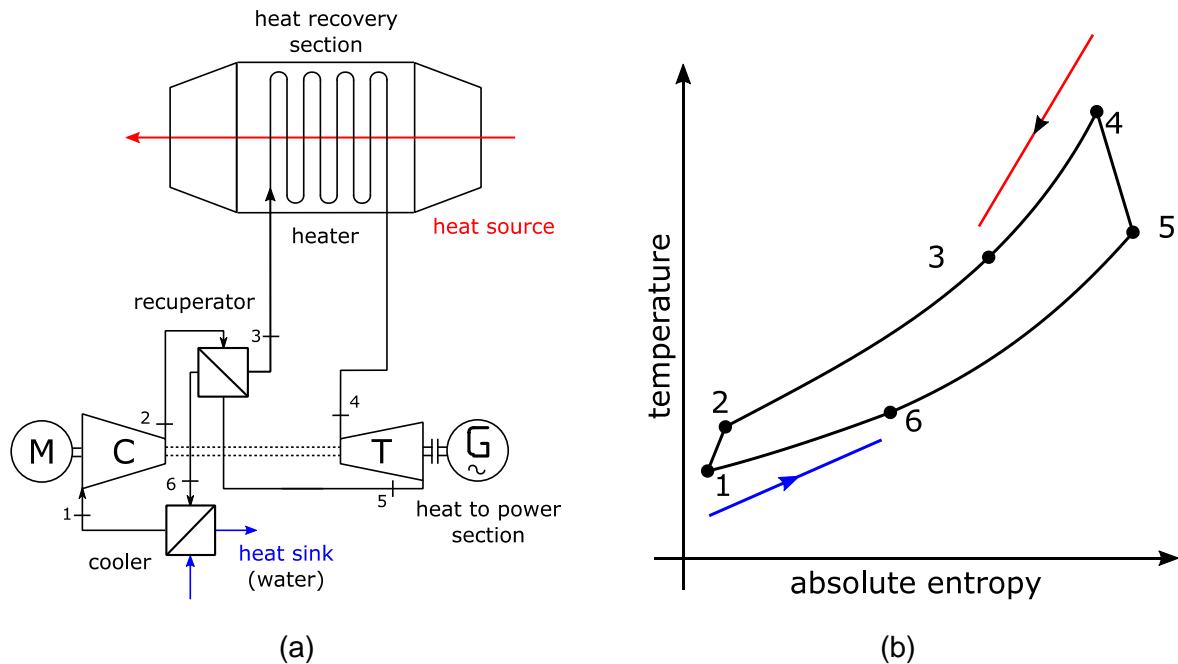
Figure 4 – Simple regenerated sCO_2 Brayton Cycle: layout (a) and T-s diagram (b)

In 1968 J. P. Van Dievoet [25] proposed a coupled sodium – CO_2 fast breeder reactor concept, pointing out the simplification two heat transfer loop instead than three thanks to the good chemical compatibility between CO_2 and sodium. The reaction products deriving by the reaction of sodium and CO_2, sodium carbonate and free carbon, are indeed not readily corrosive. In 1970 Strub and Frieder [26] investigated instead, the capabilities of a recompression sCO_2 Brayton indirect cycle using helium as intermediate heat transfer fluid between the nuclear reactor and the sCO_2 power cycle, in order to exploit the better cooling capabilities of Helium and its higher chemical inertness.

In 1976 General Electric [27] performed the Energy Conversion Alternatives Study comparing different advanced energy conversion systems for utility applications using coal and coal derived fuels as heat sources. The study compared 10 different energy conversion systems. In this comparison the thermal efficiency of the sCO_2 cycle was found to be 48%, assuming a maximum pressure and temperature of respectively 26.5 MPa and 732°C as well as a liquid CO_2 pump in place of the compressor (implying therefore the condensation of the working fluid in the gas cooler).

A renewed interest came from the work of Dostal [28], which investigated the technical and economic feasibility of the sCO_2 power technology for nuclear applications. Following the research of Dostal many research centers in the US started to investigate both theoretically and experimentally the sCO_2 power technology for nuclear and solar applications.

2.2 CO_2 Properties

Carbon dioxide (CO_2) is a molecule composed by two oxygen atoms bonded symmetrically to a carbon one. It is present in the atmosphere in very low concentrations (370 ppmv) but it plays a main role in nature. Natural sources of CO_2, i.e. volcanic activities, dominate the Earth's carbon cycle, insuring the presence and the reuse of carbon in all the Earth's geospheres. The production of CO_2 is also associated with the main natural processes as for example the fermentation of organic compounds as sugar or the oxidative metabolism (the process at the base of mitochondrial activity in the human breathing) [17].

The carbon dioxide is a colourless, thermal stable and not flammable gas, with a slightly irritating odour. Because of its role in nature, CO_2 is basically considered an environment friendly and not toxic gas. The only concerns related to the use of the carbon dioxide are due to its higher density respect to air. At high concentrations, the CO_2 can form extensive and transparent bubbles which could eventually cause asphyxia or hypoxia [17]. Furthermore, the increasing presence of this gas in the atmosphere due to the intensive use of fossil sources has risen concerns about the role the carbon dioxide as greenhouse gas. However, CO_2 has a unitary Global Warming Potential (GWP) and a null Ozone Depletion Potential (ODP), being therefore preferred to other conventional organic compounds used as refrigerants or generic working fluids.

Carbon dioxide is currently used in many industrial applications: such as the manufacture of inorganic carbonates and fertilizers (i.e. urea); the pharmaceutical sector (to provide an inert atmosphere in several processes); the food and beverage industry, (for chilling purposes or carbonation of beverages); the metal industry (used basically to protect the environment by dangerous fumes); and chemical solvent (for slightly polar and not polar compounds) [17]. Only in recent years, the advantageous physical and chemical properties of this fluid have driven the attention of researchers and industrial players to employ this compound as a working fluid for power generation. The benefits given using this fluid will be outlined in the following sections, together with a brief description of the CO_2 properties.

CO_2 Physical and Chemical Properties

The symmetric arrangement of the oxygen atoms in the CO_2 molecule and its geometrical planar structure affects the chemical properties of the compound as well as its thermo-physical

properties at a macroscopic level, which are summarized in Table 2. Because the carbon dioxide is a not-polar substance, at ambient temperature and pressure it presents in a gaseous state. In order to reach a liquid or solid phase, higher pressures and lower temperatures are required, as showed in the phase diagram reported in Figure 5.

Table 2 – CO_2 thermo-physical properties [17]

Molecular mass	44.01
Critical temperature	31.1°C
Critical pressure	73.9 bar
Density at critical point	467 kg/m^3
Viscosity at critical point	
Boiling point (at atmospheric pressure)	-78.5°C
Gas phase (at Standard Temperature and Pressure conditions)	
Density	1.98 kg/m^3
Specific thermal capacity at constant pressure (cp)	0.036 kJ/(kgK)
Cp/cv	1.308
Viscosity	13.7 µPa-s
Thermal conductivity	0.015 W/(mK)
Liquid phase	
Density (at -10°C and 19.9 bar)	1032 kg/m^3
Vapour pressure (at 25°C)	58.5 bar
Viscosity (at 25°C)	99.0 µPa-s

The continuous lines in the diagram represent the pressure and temperature coordinates at which two phases coexist. It can be observed the melting (solid and liquid) and saturation (liquid and gas) lines merge in a single point where both solid, liquid and gaseous phase of the compound are in equilibrium, namely the triple point, at -56.5°C and 5.1 bar. For lower pressure and temperatures only a solid to gas transition is observable, identified by the sublimation line. The saturation line is not infinite as the melting one, and it stops when the liquid to gas phase change occurs continuously, namely the critical point, at 31.1°C and 73.9 bar.

When carbon dioxide assumes pressures and temperature above the critical ones, it is referred as supercritical CO_2 and it is characterized by particular properties. In the supercritical region, the liquid and gas phase are not distinguishable anymore and the properties of the fluid become a mix of the two phases. However, nonetheless this smooth and continuous transition, it is possible to identify three zones: the liquid-like region, where the fluid properties resemble more the ones of a liquid, the gas-like region, where the fluid properties resemble

more the ones characteristic of the gas phase, and an area where the thermo-physical properties of the compound diverge to infinite, namely the Widom region. This distinction is showed in Figure 6.a.
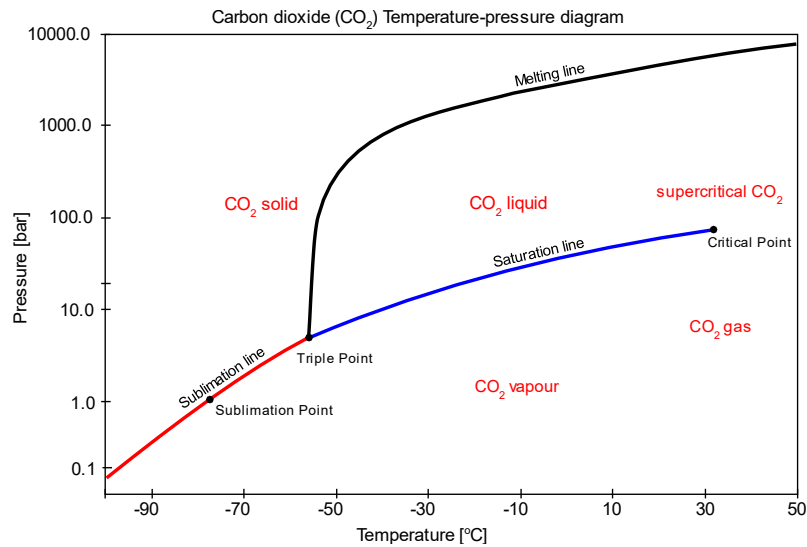
Figure 5 – CO_2 phase diagram (P-T diagram) [17].

Among the main thermo-physical properties of the CO_2 diverging in the Widom region, of main interest are the isochoric and isobaric thermal capacity, the density, the thermal diffusivity and the isothermal compressibility, which represents the measure of the density change in response to a change in pressure occurring at constant temperature (Equation (1)). It is also possible to identify the locus of points on the phase diagram at which these thermo-physical properties of the fluid reach their maxima, the so called Widom lines [29] which are showed in Figure 6.b and can be approximated using the Span and Wagner equation of state [30]. The divergence of some of the CO_2 thermo-physical properties as its thermal diffusivity and capacity is considered as the main factor to explain complex phenomena as the Piston effect [31–34], which has been intensively investigated for the potential breakthrough in thermo-acoustic applications [35,36].

$$\kappa_T = \frac{1}{\rho} \frac{\partial \rho}{\partial p}\bigg|_T \tag{1}$$

This property divergence near the critical point and the low temperature at which the critical transition occurs has attracted the interest of academic and industrial research for the use of the fluid in power generation application. As already outlined, the first advantage of the higher density in the supercritical state, is the downsizing of the main components conventionally used in power generation systems. Considering equal thermodynamic conditions, the density of the supercritical CO_2 is 2 and 3 times higher than the one of air and steam respectively, which are the most common working fluids in energy conversion systems. The supercritical

CO_2 is also denser than the typical organic fluids used in ORC and TFC applications, which are also less eco-friendly.
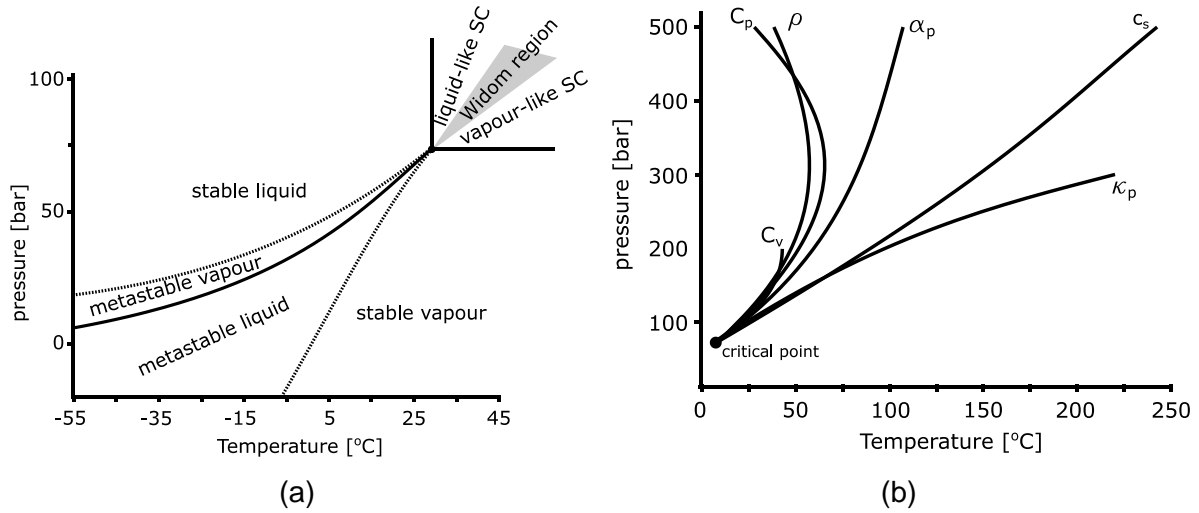
Figure 6 – Supercritical region division in the CO_2 phase diagram (a) and trends of the values assumed by the main CO_2 thermophysical properties in the Widom region (b).

A further benefit is represented by the high isothermal compressibility, which allows to strongly reduce the compression work required to pressurize the fluid with a consequent improvement of the system power output and cycle thermal efficiency. If a generic adiabatic compression is considered, the work required to bring the fluid from pressures p_1 to pressure p_2 is given by Equation (2), where v is the fluid specific volume. From this equation, it can be noticed then the lower the specific volume remains during the compression (so higher the fluid density) and the lower will be the work required for the pressurization. Then, if the CO_2 is compressed close to the critical point, where the fluid assumes a high density, the compression work can be substantially reduced.

$$w_{compr} = \int_{p_1}^{p_2} v\,dp \qquad (2)$$

To better understand this concept, reference can be done to Figure 7.a, which shows a p-v diagram of CO_2 with isothermal curves. It can be seen that if the temperature stays low and close to the critical one (31.1°C), the specific volume does not change considerably during the compression from 75 bar to 160 bar, and the work required is low (green area). Increasing the temperature and so operating far from the critical point the isothermal compressibility decreases and indeed the specific volume change to perform the same transformation increases. This leads to an augmented compression work (red area).
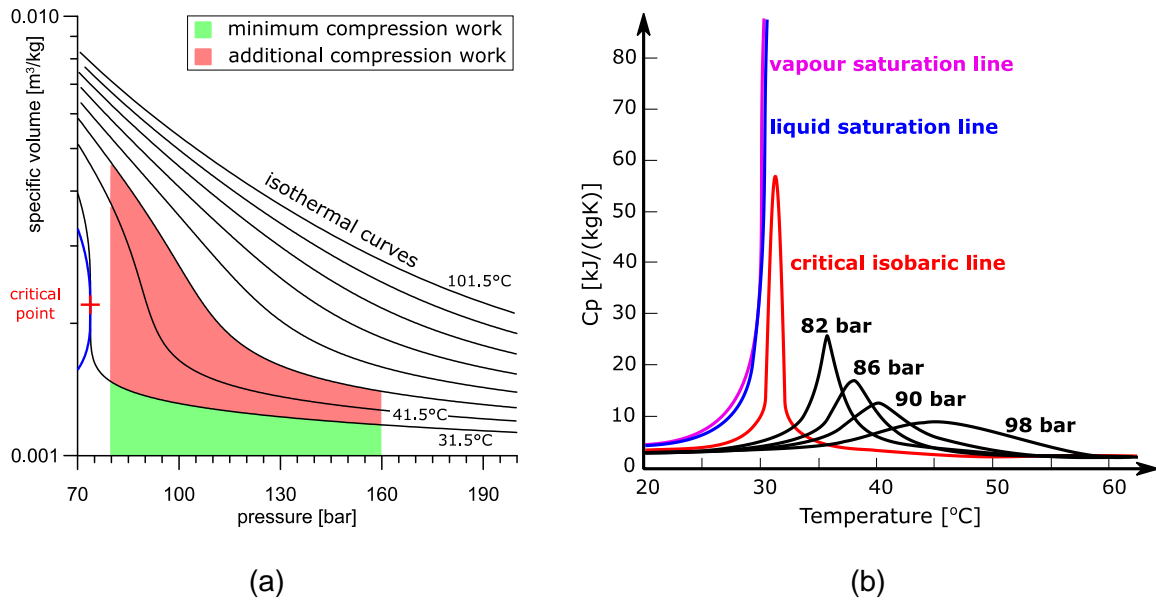
Figure 7 – P-v diagram of the CO_2 compression at different temperature levels (a) and specific heat of CO_2 as a function of pressure and temperature near the critical point.

On the other hand, the closer fluid is to the critical point the more its thermo-physical properties change with temperature and pressure. As an example, Figure 7.b reports the variation at different pressure levels of the specific heat of CO_2 as a function of temperature. This poses a challenge in terms of system regulation since accurate instrumentation is required to control the compressor inlet temperature and pressure.

The CO_2 critical point also limits the maximum pressure ratio achievable in the cycle, being the minimum pressure fixed by the critical transition (73.9 bar) and the maximum one by technological constraints (typically around 250-300 bar). As a result, typical cycle pressure ratios achievable are in the order of 4-5, which are extremely low if compared to the ones achieved in the state-of-the-art Rankine steam power units, in the order of 200 [37].

The low cycle pressure ratio achieved leads to elevated temperatures at the end of the expansion and then a high level of recuperation is needed to obtain reasonable performance [38]. Even though this fact guarantees high thermal efficiency, at the same time it limits the system net power output, and hence high temperatures at the turbine inlet are needed to generate electric power (especially considering the slow divergence of the CO_2 isobaric lines [24]).

Furthermore, the divergence of the isobaric thermal capacity close to the critical point leads to extensive heat duties in the heat exchangers required to cool down or heat up the fluid, and then innovative designs are needed [19]. Among the alternatives to overcome these limitations, research is being carried out in the field of CO_2 doping, which consists in blending carbon dioxide with smaller amounts of other compounds with the objective of lowering its critical pressure [39,40].

Supercritical CO_2 Mixtures

In recent years, many research activities have been carried out on CO_2-refrigerant mixtures, especially for refrigeration and ORC applications, to improve the eco-friendly characteristics of the conventional HFC and HFO fluids. Additionally, since the CO_2 is a strong flammability suppressor, it can be used to employ these fluids, usually flammable or thermally unstable, even for higher temperature applications (i.e. heat pumps or ORC systems). The main outcomes of these activities could be very useful also in sCO_2 power cycle applications.

A deeper understanding of the CO_2 miscibility with other fluids can enhance the advancement of this technology and improve the overall performance of sCO_2 heat to power conversion systems. For instance, the use of properly designed CO_2 mixtures could lead to a better matching of temperature profiles of the working fluid and the hot or cold source in the heat exchangers of the system, with a consequent improvement of exergy and thermal efficiency [19].

Additional advantages of CO_2 doping could be represented by the shifting of the CO_2 critical point. The lowering of the critical pressure could allow to increase the pressure ratio of the cycle and consequently the cycle net power output and thermal efficiency. On the contrary, increasing the fluid critical temperature could enhance the use of the sCO_2 power technology in Concentrated Solar Power plants [41]. Usually, these facilities are in fact located in dry areas, which typically face warmer environmental temperatures (up to 50°C) and limited availability of water sources. Therefore, cooling CO_2 down to the critical temperature of 31.1°C represents a relevant technical challenge that must be addressed in order to enable an optimal operation of sCO_2 power cycles in such applications.

Clifford [42] showed these effects proving that the critical temperature and pressure switches depend mainly on the amount and kind of substance mixed with the carbon dioxide. The grade of doping also affects other properties of the fluid (i.e. viscosity, density, thermal capacity, etc.) with potential advantages for the mixture dynamic stability. However, the mechanisms behind the phenomenon have not been properly addressed and further theoretical and experimental analyses are required.

Conboy *et al.* [43] showed that discrepancies between the theoretical estimations and experimental data for supercritical CO_2 mixtures exists. The authors tested a sCO_2/4%Ne and a sCO_2/SF_6 mixture with various mass percentage of SF_6. While the sCO_2/Neon mixture did not show a significant shift of the critical point, as instead predicted by equations, the critical temperature of sCO_2/SF_6, around 38°C following theoretical calculations (the average between the critical temperatures of the two compounds), was experimentally identified below the 27°C.

Further research has been carried out on the topic by Ayub *et al.* [44] which showed a methodology for calculating the thermophysical properties of CO_2 mixtures with equations of state experimentally calibrated with vapour-liquid equilibrium measurements. Despite the authors highlighted the thermodynamic benefits of adopting such mixtures on cycle performance, some crucial aspects have been identified in terms of mixtures thermal stability and compatibility with materials typically used for the system components' manufacturing.

2.3 Materials

In SCO_2 Brayton power systems performance strongly depend on the pressure ratio and the maximum temperature achieved in the cycle. Since the minimum cycle pressure is fixed by the CO_2 critical point (73.9 bar) and the highest temperature achieved in the cycle is the one at the turbine inlet, the parameters that most affect the system performance are thus the maximum cycle pressure and the Turbine Inlet Temperature (TIT). Higher maximum temperatures and pressures allow increase in the power output and thermal efficiency of the cycle but pose also concerns related to corrosion and erosion effects for the unit components. Hence, the development of suitable innovative materials that can stand to these harsh operating conditions represent a key aspect for the advancement of the sCO_2 power cycle technology readiness level [19].

Before the development of testing facilities for sCO_2 Brayton power units very few studies have been conducted on CO_2 corrosion properties. Among them, the most relevant have been carried out by Dunlevy [45] and Gibbs [46], Saari *et al.* [47], Anderson [48], Parks [49], Fleming *et al.* and Sridharan and Anderson [51]. Some experimental results have also been published by the Sandia National Laboratories [43] and in the framework of the SunShot initiative [52]. The results of these works can constitute a useful basis for a first stage selection of the materials of the sCO_2 Brayton unit components and to understand the main CO_2 corrosion mechanism. This is especially relevant for the turbine design, which is the most stressed component and in turn one more exposed to failure risks. Among the several forms of corrosion that can lead to catastrophic damages in Brayton cycle gas turbines, the main relevant corrosion mechanisms occurring when CO_2 is considered are high temperature oxidation, carburization and metal dusting [49].

High Temperature Oxidation
High temperature oxidation usually occurs when a metal is exposed to an oxidizing environment at high temperature levels, such that the oxidation driving force is merely thermodynamic and does not require any aqueous medium to take place. The formation of an oxide layer on the metal surface can lead to a substantial loss of material and a consequent

risk of component catastrophic failure. In general, since this corrosion mechanism occurs also in gas turbines, the technical know-how acquired in this field can be successfully applied also in sCO$_2$ power systems. Among the main adopted practices, there is the extensive use of high content chromium (Cr) and nickel (Ni) alloys because of their ability to form highly stable oxides even at elevated temperatures. In particular, the addition of nickel increases even more the corrosion resistance of the alloy, since combined with chromium form a duplex layer with high mechanical properties and stability.

Carburization

Unlike high temperature oxidation, carburization is a corrosion mechanism which usually does not occur in conventional energy conversion systems, because of the low carbon content of the adopted working fluids. In a carbon rich environment in fact, chromium carbides formation as Cr_3C_2, Cr_7C_3 and $Cr3C_6$ may occur due to the greater affinity of carbon with chromium than oxygen. Consequently, the alloy is depleted from the chromium which cannot be used to form the oxide layer required to prevent the alloy corrosion. Of course, this phenomenon is particularly significant in sCO$_2$ applications because of the high carbon content which the materials are exposed [53].

The carbon atoms produced by the carbon dioxide decomposition react then with the chromium elements contained in the alloy forming interstitial carbides along the grain boundaries of the alloy, reducing its toughness and creep resistance. To overcome these issues, usually nickel, vanadium and titanium are used as alloying elements. While Nickel slows down the carbon migration toward the alloy surface thanks to the poor solubility with carbon, Vanadium and Titanium rapidly react with the element to form interstitial carbides (V_2C and TiC) along the grain boundaries. For temperatures higher than 600°C, a higher content of titanium is preferred to Vanadium because of its stronger chemical affinity with carbon at those temperature levels [19].

Metal Dusting

Metal dusting is a widespread form of carburization that occurs when a material is exposed in carbon-rich environment. Usually, the oxide layer formed on the material surface can present some local defects or porosity. The carbon atoms exploit these imperfections to migrate toward the oxide/alloy interface forming chromia carbides and thus depleting the material from chromium. If this process occurs for a prolonged amount of time, with the deposition of carbon increasing, the extended carbide zone becomes supersaturated and the nucleation of graphite may become thermodynamically favourable. Once the nucleation is triggered, the graphite nuclei start to grow and break the oxide layer previously formed. At this point, the graphite amalgamated with oxides and alloy components start to extend outside the substrate and into

the alloy, forming what is called the "coke" corrosion product. This phenomenon can be very dangerous for a component since can reduce drastically its toughness, mechanical resistance and functionality.

Materials in Supercritical CO_2 Brayton Cycle

Among the material investigated for the sCO_2 power technology, stainless steels and nickel-chromium alloys showed to be the most suitable for high temperature components (i.e. turbine, primary heater and high temperature recuperator). While aluminum-based alloys have been considered and tested for components subjected to less harsh operating conditions (i.e. compressor and gas cooler).

At the Massachusetts Institute of Technology, Dunlevy et al. [45] measured the weight gain rates of the oxide layers formed on a wide range of samples of nickel-based alloys (IN-690, IN-693, IN-718, IN-725, IN-740, IN-740+) exposed to a pure CO_2 gaseous environment for different temperatures, pressures and durations (705°C and 20 MPa for 500 hours, 650°C and 12.5 MPa for 500 hours and 750°C and 12.5 MPa for 1000 hours). It has been found that the stainless steel SS316L formed a stable oxide layer in the first two cases, while showing an unstable behavior in the third operating condition (750°C and 12.5 MPa for a testing time of 1000 hours), with the weight gain rate of the oxide increasing with time (linear trend).

On the contrary, the nickel-based alloys showed much better performance of the 316L stainless steel, which makes them more suitable for components operating at higher temperature and pressures. In particular, the Inconel 718 (IN-718) showed a higher sensitivity to the operating pressure, while the Inconel 693 (IN-693) to the operating temperature. However, the Inconel 740 (IN-740) showed the highest corrosion resistance. Also the investigation carried out by Parks [49] proved the superior performance of nickel-based alloys at higher temperatures (700°C), while stainless steel 316L showing a good corrosion resistance only at temperatures below 550°C.

However, these tests only considered the weight gain rate of the oxide layer of the different samples, without paying enough attention to the oxide layer thickness and shape, of main relevance to avoid the exfoliation phenomenon typically occurring in pipes and heat exchangers operating at high temperatures. In this sense some work has been published recently by Kung *et al.* [54], Mahaffey *et al.* [55] and Sabau *et al.* [56], which have also considered how the presence of some impurities in the CO_2 flow, as water, oxygen and nitrogen oxides, may affect the corrosion resistance of the analyzed materials.

Another interesting study has been realized for the 10 MW Supercritical CO_2 Turbine Test project financed by the U.S Department Of Energy (DOE) in the framework of the SunShot

initiative [52]. A summary of this study and of the other investigations is detailed by component has been reported in Table 3.

Table 3 – Tested materials for sCO_2 power cycles applications at a pressure of 200 bar for a minimum duration time of 3000 hours (LT=Low Temperature, HT=High Temperature) [52]

Temperature	Component	Alloy	Type
T ≤ 250°C	Compressor, gas cooler	304ss, P91, T22 [52]	Low cost austenitic or ferritic alloys
T ≤ 400°C	LT Recuperator	347ss [52]; 310ss and 316ss [46]	Austenitic alloys recommended
T ≤ 550°C	HT Recuperator, LT Primary heater, LT turbine	347ss [52]; 310ss [48]; 316L [49].	Austenitic steels with a lower level of Ni, Cr and Co (316)
T ≤ 650°C	HT Turbine, HT Primary heater	Haynes 230 [46]; IN-617[48]; 800H [57].	Higher Ni/Cr alloys are recommended
T > 650°C	Very high temperature applications	Haynes 282 [52]; IN-713 [58]; IN-718 and IN-738 [47]; IN-690, IN-693, IN-725 and IN740 [45]; EP823 [59]	Little testing completed.

2.4 Turbomachines

As already mentioned, the high density of CO_2 allows to downsize turbines and compressors and thus to decrease the overall capital and operating expenditures of the system. However, the smaller pressure ratio achievable in the cycle (due to the high critical pressure of the fluid) and the higher volumetric flow rate across the machines (compared to conventional technologies as steam and gas turbines) pose design constraints in terms of revolution speed and size. Indeed, higher revolution speeds and lower impeller diameters are needed to achieve optimal isentropic efficiency [60–62]. This leads to additional technological challenges in terms of machine design, bearings, sealing, rotor dynamics and pressure containment [19].

For low power capacity systems, these challenges become even more critical and severe leakage problems may occur. At higher power scales, technical solutions available from other technologies as gas turbines or ultra-supercritical steam power plants are available. Figure 8 shows the selection of the different design choices for turbomachinery in terms of dimensions, type, revolution speed, bearings and seals should be made depending on their power scale following the findings available in [63].

The range considered by the authors is between 300 kW_e up to 300 MW_e. In this thesis, design choices which can be adopted for capacities below 100 kW_e (red line in Figure 8) have been considered thanks to the experience in constructing the sCO_2 facility at Brunel University London. It is possible to notice that below 8 MW_e, radial machines with single stages are

preferred, whereas multiple stages have been adopted for higher power. The adoption of axial machines becomes instead preferable for power capacities higher than 10 MW_e, with multiple stages when the power generation higher than 100 MW_e are considered. In general, the adoption of multiple stages allows to achieve higher efficiencies, but require longer shafts, which are more difficult to balance. Geared configuration help to overcome this problem, but cause additional power losses (of the order of 1-4% [64,65]).

Among the bearing technologies considered, for medium to high power sCO_2 turbomachines, fluid film bearings, hydrodynamic or hydrostatic, seems to be the most suitable candidate also because of their high load capability, optimal damping properties and long working life due to the reduced wear action between the shaft and the housing. Widely used in conventional turbomachinery applications, these components are a ready-to-market technology.

For smaller turbomachines, more unconventional technologies such as magnetic and gas foil bearings are considered, because of the technical challenges posed by the high revolution speeds achieved. The main advantage of magnetic bearings is the active control on the shaft, but they present limitations in terms of maximum temperature and revolution speed achievable.

Tested technologies		Early-stage technologies

TM Feature	Power (MW$_e$) 0.1 0.3 1.0 3.0 10 30 100 300
TM Speed/Size	75000RPM/5cm 30000RPM/14cm 10000RPM/40cm 3600RPM/1.2m
TM type	Single stage Radial Multi stage / Single stage Axial Multi stage
Bearings	Hybrid Gas Foil Magnetic / Gas foil Hydrodynamic oil / Magnetic Hydrostatic / Tilting Pad
Seals	Labirinth Float ring oil / Dry lift off
Freq/Alternator	Permanent magnet Wound, Synchronous / Gearbox, Synchronous
Shaft Configuration	Dual/Multiple Single shaft

Figure 8 – Turbomachinery size, speed and technological features as a function of the sCO_2 power capacity [63]

Gas foil bearings on the other hand can be very effective at high revolution speeds but at lower ones their damping properties drastically drop since the force acting between the shaft and

the casing depend on the motion of the working fluid itself. Innovative solutions are being investigated trying to conjugate the two concepts, such as in Hybrid Gas Foil Bearings [66 – 68] or Hybrid Gas Foil Magnetic bearings, whereas in the latter ones the passive stiffness and damping provided by a spring and a wire mesh is replaced by the active action of an electromagnetic field [69]. These innovative alternatives however are still in a development stage. Tilting pads bearing have also been used widely since offer a good trade-off between performance, limited cost and reliability.

As concerns for the sealing, which is critical especially for small turbomachines, where the leakage becomes a relevant issue, mainly two technologies have been adopted so far: labyrinth and dry lift off seals. The Sandia National Laboratory (SNL) has been among the first research institution to test and patent a labyrinth seal using an abradable material, Graphitar 3030, in order to reduce the clearance between the rotating part of the seal and the stator [38]. Despite the good performance showed, formation of dry ice during the expansion of the leaked gas repetitively occurred, which can lower the seal performance and operating life. This kind of technology is usually adopted for power size lower than 10 MW$_e$.

At higher power scales, Dry Gas Seals (DGS) are preferred, which have been proposed and studied in [70–72]. Despite the greater complexity, better performance can be achieved. The working principle is to exploit the high pressures generated by the hydrodynamic forces due to the thin gas film which develops between the rotating and the stationary ring of the seal. The reduction of the leakage flow between the high and the low pressure side is achieved in a contactless operation mode, increasing the higher operating life of the seal. Figure 9 shows a schematic representation of the technology and its working principle.

(a)   (b)
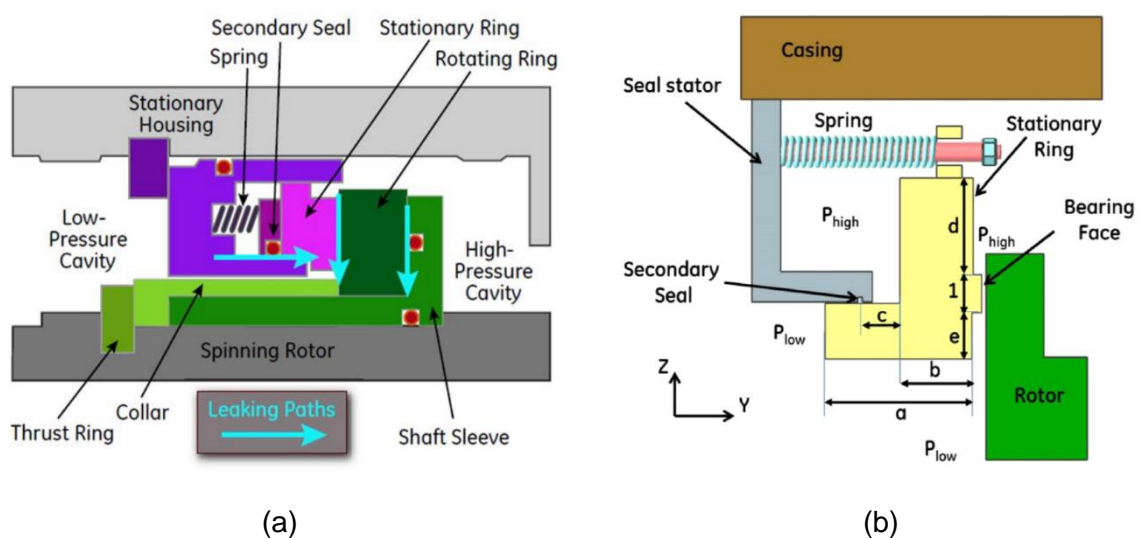
Figure 9 – Dry gas seal technology: (a) seal scheme, (b) detail of the bearing face generating the hydrodynamic forces [72]

Further technologies proposed in the literature are the float ring oil seals, widely used in the oil and gas industry which however have the great disadvantage of requiring a dedicated oil circuit and thermal management system [71]; the hole pattern damper seals, which use a series of cylindrical or hexagonal machined holes to introduce a dissipative effect in the machine and thus increase the damping [73,74]; or the swirl brake labyrinth seals, which use axial vanes to create counter rotating vortices to reduce the swirl motion of the working fluid and then reduce its destabilizing action [75].

From a generator perspective synchronous or a permanent magnet alternator can be selected depending on the revolution speed achieved by the turbomachines, which can be coupled to the shaft directly or by means of a gearbox (Figure 8). Depending also on the particular design of the sCO_2 power cycle, different machine configuration can be adopted to achieve the optimal trade-off between:

- balancing of the elevated axial thrust due to high pressures achieved in the cycle;
- matching the optimal revolution speed of the machine with the one of the generator;
- minimisation of bearings and seals to reduce dynamic instabilities for the rotor shaft and the overall complexity and maintenance costs of the assembly;
- enhancing the compactness of the assembly to minimise pressure containment challenges.

Figure 10 shows different possible turbomachines configurations proposed by Kalra *et al.* [72]. While these major challenges are common to both compressor and turbines, particular considerations must be made for the compressors, whose operation close to the CO_2 critical point poses several technical challenges. Among the main ones, the partial condensation of the working fluid can lead to a strong reduction of performance and operating life of the component itself. Close to the critical point, formation of CO_2 liquid droplets may occur at the impeller inlet, where high flow deflections are realised [76,77]. This can detrimentally affect the compressor aerodynamic performance by modifying the blade inlet attack angle [78,79], and may lead to the erosion of the compressor blades, elevated synchronous vibrations, modification of the damping and stiffness coefficient with consequent dynamic instability, and a higher risk of seal damage, due to liquid presence.

A further challenge derives from the management and control of the compressor. Since close to the critical point a slight change of pressure and temperature translates in a dramatic variation of the fluid thermo-physical properties (i.e. density, thermal conductivity or thermal capacity), very accurate sensors are needed to be able to regulate effectively the device and thus the overall system [80].

Investigations in this sense have been carried out by Hacks et al. in [81], which pose a strong accent in controlling the temperature and the density at the inlet of the machine to optimize the compressor performance. Further analysis and experimental studies are however required to understand the compressor behavior near the critical point, and during transient operations in order to design more suitable control strategies.

The real gas effects of CO_2 can instead be neglected in the design of sCO_2 turbines, because of the ideal gas behaviour of sCO_2 far from the critical point. Many research activities on this topic and on the fluid dynamic analysis of the flow in this kind of machines have been carried out in [82–88]. Not fully addressed technical challenges are mostly related to the containment of thermo-mechanical stresses due to the combined action of high temperatures and pressures [89], as well as dynamic modelling and control. Table 4 and Table 5 summarise the features of the first prototypes of turbines, compressors and Turbine-Alternator-Compressor (TAC) units designed by the different industrial and academic institutions worldwide.
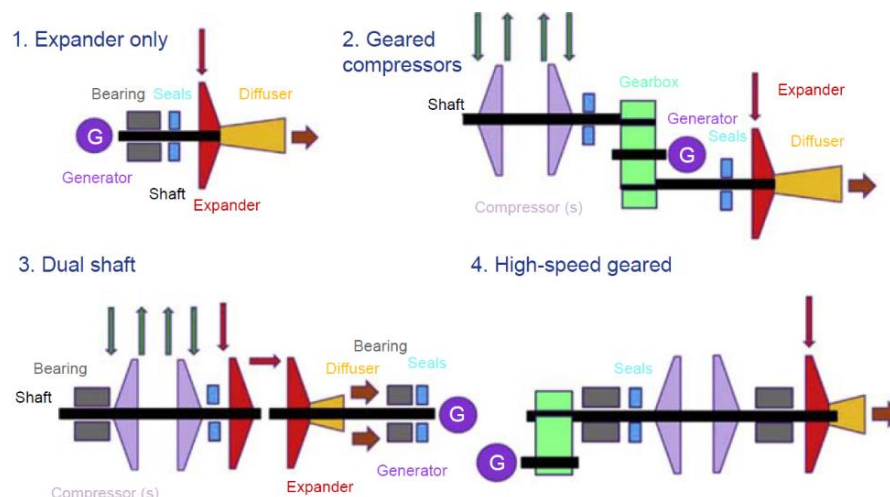
Figure 10 – Different turbomachine configurations [72]

Table 4 – Technical features of the first prototypes of sCO_2 turbines and compressors commissioned and operating in the different academic and industrial organisations involved in research on sCO_2 power cycles (n.a. stands for information not available)

Institution	Type	Rotational Speed	Diameter	Power	Design Point	Bearings type
		[RPM]	[mm]	[kW$_e$]	([°C]/[bar]/[kg/s])	
Turbines						
BMPC [90]	Radial	55000	45	100	282/141/2.1	Gas foil
SWRI/GE [91]	Axial	n.a.*	n.a.	1000	700/250/8.4	Tilting pad
Echogen [92]	Radial	30000	n.a.	8000	275/n.a./n.a.	Tilting pad
KIER [93]	Axial	45000	73	93	116/123/1.5	Tilting pad
KAIST [94]	Radial	80000	325	n.a.	435/125/5.0	n.a.
Compressors						
KAIST [94]	Radial	35000	272	100	33/78/6.4	n.a.

Table 5 – Technical features of the first prototypes of sCO$_2$ Turbine-Alternator-Compressor (TAC) units commissioned and operating in the different academic and industrial partners involved in the research on sCO$_2$ power cycles

Institution	Rotational Speed	Mass flow	Cmp inlet	Trb inlet	Net power	Bearing type	Lubrication
	[RPM]	[kg/s]	([°C]/[bar])	([°C]/[bar])	[kW$_e$]		
KIER [95]	70000	3.1	36/79	180/130	13	Gas foil	CO$_2$
BUL/ENO [96]	60000	2.1	35/75	435/127	50	Rolling	oil
SNL [38]	75000	3.5	33/77	487/105	150	Gas foil	CO$_2$
HeRo [97]	50000	0.6	33/74	185/117	4	Ball	Grease
TIOT [98]	69000	1.1	31/75	250/106	0.11	Gas foil	CO$_2$

2.5 Heat Exchangers

Heat transfer equipment for sCO$_2$ applications is fundamental to enhance the efficiency and the economic viability of this technology. While a simple regenerated sCO$_2$ system one would require only three heat exchangers, up to five devices would be needed for more complex and performant cycle architectures [99]. These devices also represent the largest components in the system and must withstand high temperatures and pressures.

Furthermore, to avoid the excessive erosion of the already limited cycle pressure ratio, sCO$_2$ heat exchangers must be designed to minimize the pressure drops, which is not trivial especially considering that a trade-off exists between the minimization of pressure drops, maximization of the heat duty and reduction of costs [100]. Reducing the pressure drops across heat exchangers leads to a reduction of their wet surface, which limits their effectiveness and heat transfer capabilities. Increasing the heat duty however, allows to increase cycle efficiency and power output, but requires also greater heat transfer area, thus increasing pressure drops and costs.

Additional design specifics must also be fulfilled depending on the type of heat exchanger considered. For the gas cooler, despite the lower operating pressure and temperatures, the heat duty requirements and the type of heat sink considered (air or water) can considerably affect the component design and optimization [101]. The recuperators are instead more challenging because of the higher pressures and temperatures involved. In this case also long-term creep and fatigue resistance are required because of the wide range of temperatures occurring across the different heat exchanger sections and the limited operation maintenance due to the extreme compactness of these devices [19]. Even more ambitious is the design of the primary heater, which not only is the component exposed to the highest temperature and pressure of the cycle, but depending on the nature of the heat source, it may

have to operate also in an extremely corrosive environment (i.e. nuclear or WHR applications). A further requirement could be the minimization of the pressure drops on both the working fluid and the heat source side, especially if exhausts are considered as heat source. Hence, considering all these aspects different technologies have been considered and investigated for sCO_2 heat exchangers.

Primary Heater Technologies

Due to the aforementioned design and operational requirements, when the heat source is in a gaseous form, shell and tube (S&T) heat exchangers are usually adopted a primary CO_2 heaters. The sCO_2 usually flows inside the tubes, while the heat source/sink flows along the shell. Plate baffles are embedded to enhance the heat transfer, but they also lead to increased pressure drops. The main drawbacks of this heat technology are the low compactness and the high heat transfer surface required to achieve an effectiveness at least higher of 0.85 for sCO_2 power cycle applications [19].

To increase the compactness of these heat exchangers and further enhance the heat transfer performance, the tube size can be reduced (tube diameter lower than 1 mm), obtaining a so-called micro-tube heat exchanger. The enhanced heat transfer coefficient obtainable thanks to the smaller tubes allows to avoid baffles and thus to decrease the pressure drops on the flue gas side, even if this leads to an increase of the pressure drops and a reduced flow velocity on the CO_2 side. Further advantages of micro-tube heat exchangers with respect to the conventional shell and tube ones are a greater scalability and modularity as well as a better resistance to harsh operating conditions; on the other hand, a drawback is represented by the higher manufacturing cost due to the special welding operations required to assemble the tubes in the headers [19]. Should the heat source be an effluent, Printed Circuit Heat Exchangers (PCHEs) also become a viable option.

Recuperator Technologies

Recuperators also operate in severe duties and harsh operating conditions. High effectiveness and heat transfer area are required together with contained pressure drops. The result are very compact heat exchangers that must accommodate high pressure differential, given the pressure difference between the heating and the cooling fluid. As a consequence, these devices must have the following technical features:

- Mechanical integrity;
- High creep and corrosion resistance, because of the high operating pressures and temperatures;
- Long term stable materials because of the limited maintenance due to the extreme compactness of the device;

- Micro-channels to meet the high effectiveness and the low pressure drops targets.

Besides these characteristics, the physical properties of the working fluid change deeply during the heat transfer, and often a pinch analysis is required to minimize the exergy losses in the heat exchanger at design and off-design conditions. A common practice to minimize this exergy loss is the split of the recuperation stage in a high and low temperature side. The high temperature recuperator is usually realized with expensive nickel-based alloys to face the high temperature of the working fluid, while the low temperature one can be realized with more conventional stainless-steel materials. This solution allows also to reduce the thermal gradient in one single heat exchanger and simplifies the maintenance operations.

PCHEs and Formed Plate Heat Exchangers (FPHEs) are always preferred for sCO_2 recuperators, thanks to their extremely high heat duty per unit volume, compactness, creep and fatigue resistance as well their capability to withstand high pressure and temperatures. The reduced material shrinkage due to the additive manufacturing techniques can make FPHE cheaper than PCHE [102]. On the other hand, PCHE can be operated at higher pressures (up to 1000 bar) compared to the 250 bar achievable by the FPHE technology [103].

To further reduce the cost of these components, industrial and academic organizations are investigating new technical solutions. Among the different ongoing alternatives, the most promising heat exchanger technologies are the Plate-Matrix and Wire-Mesh Heat Exchangers (PMHE and WMHE) [103,104], which guarantee even higher compactness, heat duty and lower costs due to a lower material use. Figure 11 shows a representation of such heat exchangers.

(a)   (b)
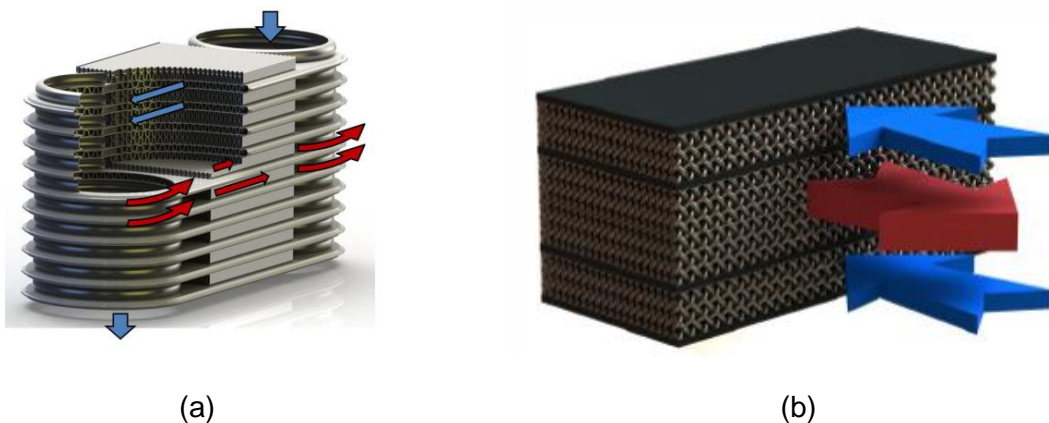
Figure 11 – Innovative compact heat exchangers technologies considered for sCO_2 recuperators: (a) Plate Matrix Heat Exchangers (PMHE) and (b) Wire Mesh Heat Exchangers (WMHE) [103]

The use of the PHE requires still additional technological development and could lead to a substantial decrease of the overall sCO_2 system costs. A brief overview of these different heat exchangers technologies is given in the following paragraphs.

Gas Coolers Technologies

The shell and tube technology can be adopted as gas coolers if air is used as cooling medium [19,38]. If a liquid coolant is considered, PCHE provide a compact yet pricey technological solution. At small power scales or when the footprint is not a major issue for the sCO_2 system, components available from the CO_2 refrigeration sector, such as Plate Heat Exchangers (PHE), can be used instead of PCHE with an extreme reduction of capital and operational costs [105]. Table 6 summarizes the heat exchanger technologies available for each of the heat exchanger typology in sCO_2 power cycles as well as the average cost per kW_t/K of the devices.

Table 6 – Cost per UA unit ($/($kW_t$/K)) of the different heat exchangers used in sCO_2 power cycles (gas cooler, recuperator and primary heater) grouped by technology (green colour when the heat source/sink is in gaseous state and light blue when it is in liquid form).

Heat exchangers	S&T	Micro-tube	PCHE	FPHE	PHE	PMHE	WMHE
Gas cooler	1700 [19]		>2500 [109]	2000 [19]	50 [109]		
Recuperator			>2500 [109]	>2000 [19]		FOAK* [110]	FOAK* [110]
Primary heater	>5000 [19]	>5000 [105]	>5000 [19]				

*FOAK stands for First Of A Kind component

2.6 Recent Test Rigs

To prove the concept of sCO_2 power cycles, different industrial and academic research institutes developed prototypes of sCO_2 heat to power conversion systems. Sandia National Laboratories (SNL) and the Knolls Atomic Power Laboratories (KAPL) were the first research centers to develop two integral sCO_2 power cycle test facilities for nuclear applications. Afterwards, many institutes started their own research activities, both in the United States (e.g. Argonne National Laboratories, ANL, South West Research Institute, SWRI, Bechtel Marine Propulsion Laboratories, BMPL) and in Asia, especially in Japan (Tokyo Institute of Technology, TIT) and South Korea (Korea Advanced Institute of Science and Technology, KAIST, and Korea Institute of Energy Research, KIER). In the latest years, European institutions also developed laboratory scale facilities. Table 7 summarizes the experimental test rigs currently commissioned and their main characteristics.

Table 7 – Integral sCO₂ heat to power conversion testing facilities

Institution	Cycle Layout	Net power	Turbomachinery	Heat source	Heat source capacity
		[kW$_e$]			[kW$_t$]
United States					
Echogen [92]	Pre-heating / Split expansion	8000	1 pump 2 turbines	Flue gas	33000
SNL [38]	Recompression	300	2 TAC	Electric	780
KAPL [106]	Simple regenerated	100	1 TAC 1 turbine	Electric	835
South Korea and Japan					
KAIST/ KAERI [94]	Simple regenerated	300	1 TAC 1 LP turbine 1 LP compressor	Electric	1300
KIER [107]	Simple regenerated	80	1 compressor 2 turbines	Flue gas	611
TIT/IAE [98]	Simple regenerated	10	1 TAC	Electric	160
European Union					
sCO₂ HeRo [81]	Simple regenerated	9	1 TAC	Steam/Electric	6/195
BUL [105]	Simple regenerated	50	1 TAC	Flue gas	700
CVR [108]	Simple regenerated	n.a.*	1 pump 1 exp. valve	Electric	110

n.a. stands for information not available

2.7 Supercritical CO₂ Power Applications

Supercritical CO₂ Brayton Power Cycle for Nuclear Power Generation

In recent years the need for nuclear power generation facilities to increase efficiency, reduce costs and increase the power plant safety led to the development of a new generation of reactors (IV Generation) [111]. Among them, the most promising candidate is the Sodium-cooled Fast neutron Reactor (SFR), which exploit the good physical properties of molten sodium to enhance the heat transfer from the core to the working fluid of the heat to power conversion cycle in a safer and more efficient way.

However, since the sodium is highly reactive with water, the coupling of the sodium primary loop with a conventional steam Rankine Cycle can lead to unsafe operating conditions. On the contrary, CO_2 has a lower affinity with sodium, at least at temperatures below 500°C [99].

This advantage, coupled with the smaller speed of sound in CO_2, which allows to limit the leaking gas flow rate in case of a major tube rupture, has driven the interest of researchers and industrial players towards sCO_2 Brayton power cycles for the nuclear power generation sector. Competing technologies are Brayton cycles using Nitrogen and Helium as working fluid, which have an even a lower affinity with sodium than CO_2 [112]. However, the wider range of applications of sCO_2 power cycles could establish a firm supply chain for a wide spectrum of energy industries, leading to a drastic reduction of the manufacturing costs of single components and to more competitive capital and operational expenditure costs.

Supercritical CO_2 Brayton Power Cycle for Fossil Fuel Applications

The sCO_2 power cycle can also be considered as a potential candidate to replace the conventional power generation system operating with fossil resources. Apart from the efficiency and cost savings benefits, sCO_2 power plants could present much more competitive costs for the integration for carbon capture and storage systems [113], especially when direct fired sCO_2 systems are considered.

In such units, the oxy-combustion of coal, methane or other fuels is used to provide the thermal energy to the CO_2 stream [114]. The excess of CO_2 produced in the combustion reactor can be extracted by the cycle after the compression stage and directly stored thanks to the high pressure of the fluid. However, the design of the combustor chamber represents a major technological challenge and the production of pure oxygen, which is very energy intensive process, can undermine the thermodynamic cycle efficiency. A promising solution addressing these issues is the Allam cycle [114], whose technical feasibility will be assessed by a 50 MW thermal pilot plant.

Additional benefits from using sCO_2 power cycles for fossil fuel applications are the higher efficiency at part load conditions and the fastest dynamics compared to steam Rankine power systems, conventionally used in the sector. These aspects, together with a much more reduced footprint and lower cooling water consumptions requirements (thanks to the single-phase heat rejection stage of the CO_2), make sCO_2 power systems a much more flexible energy conversion technology. Several power plant vendors and operators including Pratt Whitney & Rocketdyne (PWR, California, USA) and Electricite De France (EDF, Paris, France) are investigating sCO_2 cycle design for application to coal power plants [113,115].

Supercritical CO_2 Brayton Power Cycle for Concentrated Solar Power

SCO_2 power cycles are considered as the most promising solution to enhance the efficiency of Concentrated Solar Power (CSP) plants and to make the solar thermodynamic technology economically competitive with Photovoltaic systems [52]. The use of sCO_2 as working fluid would allow to improve the cycle efficiency and to decrease the capital expenditures of the

power block [116,117], thanks to higher temperatures achievable in the cycle and lower system complexity [118]. In particular, the lower complexity can be achieved thanks to the possibility of directly recovering the solar radiation without any intermediate heat transfer loop, as instead is used in conventional CSP systems using steam Rankine Cycle power conversion units which employ molten salts.

However, in order to implement such direct energy recovery, the high pressures of CO_2 pose technical challenges in the design of solar collectors, and further research is thus required [119]. Another important aspect is the design and control of the CO_2 cooling, given the lack of water sources in areas where CSP plants become economically viable. To overcome this issue several research activities are being carried out to develop CO_2 mixtures able to increase the critical temperature of the fluid in order to allow the adoption of dry cooling even in warmer climates.

Supercritical CO₂ Brayton Power Cycle for Geothermal Energy

Several research activities have been also carried out to assess the suitability of SCO_2 power systems in geothermal applications. The high pressure and high thermal capacity of CO_2 allow in fact to reach higher depth compared to more conventional technologies. As a result, a higher amount of heat could be recovered and thus elevated turbine inlet temperatures achieved, increasing the plant performance [120]. Figure 12 shows a comparison between the plant schemes of a conventional hydrothermal power plant and a sCO_2 based one, which has been proposed by Higgins *et al.* [121].
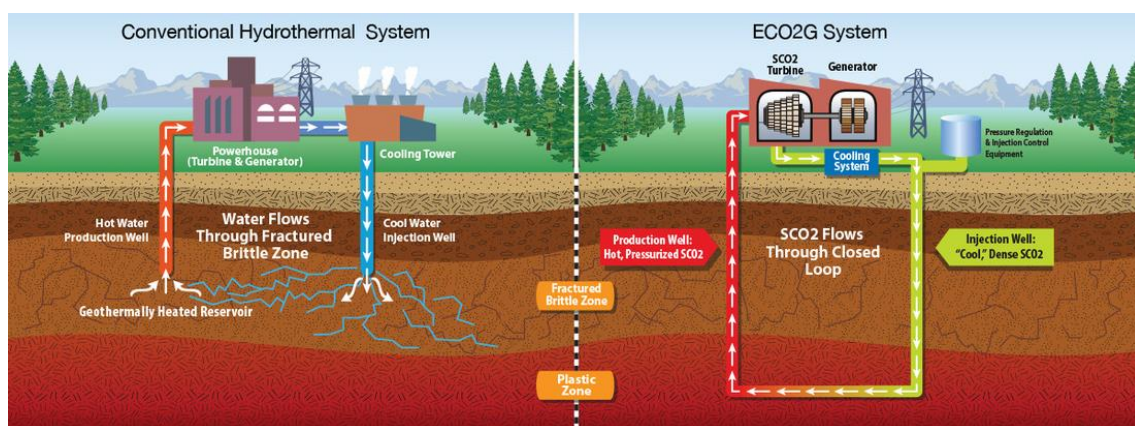
Figure 12 – Plant scheme comparison between conventional Hydrothermal (left-hand side) and ECO_2G sCO_2 geothermal (right-hand side) system [121]

Supercritical CO₂ Brayton Power Cycle for Waste Heat Recovery

Even among the technologies for the direct conversion of the waste heat into electric energy, which are usually referred as waste heat to power conversion technologies, sCO_2 power systems show a disruptive innovation potential. Indeed, sCO_2 systems could allow the

recovery and conversion of waste heat sources in a range of capacities and temperatures which currently cannot be exploited because of the lack of techno-economically feasible technologies.

Figure 13 displays the operating ranges of conventional and innovative heat to power conversion technologies as a function of the waste heat source temperature level and capacity, i.e. including type and mass flow rate of the waste exhaust or effluent. It is possible to notice the potential gap coverable by the sCO_2 power systems.

Thermoelectric (TE in Figure 11) , thermionic and thermoacoustic devices, which realise the conversion thanks to a temperature gradient between the surface heated by the waste energy source and the environment [9-11], are still not reliable for higher capacities and their use is often limited up to a maximum of tens of kW_t waste heat sources [122].

The use of ORC technology is limited in a range of temperatures of the waste heat source that goes from 100°C up to 400°C [123]. The upper limit is imposed by the flammability and low chemical stability of the organic fluids at high temperatures, while the lower one by their vapour pressure which, in turn, limits the efficiency and the output of ORC units at extremely low temperatures. Depending on the amount of the waste heat available, positive displacement machines (for waste source capacities from 10 kW_t up to 200 kW_t) or axial and centrifugal turbines (for power scales between 200 kW_e and 15 MW_e) can be selected [124] (Figure 13).

Steam Rankine cycles are usually preferred to ORC to exploit waste heat sources with higher thermal capacities (from 10 MW_t up to hundreds of MW_t) [125], because of the higher efficiency and the lower capital cost due to more standard components [125]. The operating range of this technology can be further extended to power scales lower than 10 MW using micro steam turbines (Figure 13) which are however characterised by lower performance than large machines due to high tip leakage losses [125].

The temperature range at which the Steam Rankine technology is usually employed goes from 250°C up to 700°C (Figure 13) [125,126]. The lower limit is given by the low vapour pressure of water, while the upper one from material and technological constraints. More advanced units, as the ultra-supercritical steam power systems, can also exploit heat sources beyond 620°C, but they require significant additional investment costs [125].

Waste heat source available at temperature levels lower than 100°C can be still exploited by adopting the Trilateral Flash Cycle (TFC) technology (Figure 13). To realise the conversion of thermal energy at such low temperature levels, these systems embed volumetric machines to perform a two-phase expansion of the working fluid, which is usually a refrigerant. The size of these machines, however, limits the maximum thermal capacity of the waste heat source

exploitable, which can go up to 5 MW [16,127]. For capacities lower than 1 MW, ORC systems are more competitive [127].

Hence, for waste heat source temperatures higher than 700°C, sCO_2 power cycles are the only option available (Figure 13). If lower capacities of the waste heat source are considered (lower than 1 MW), sCO_2 systems remain the only technically feasible alternative even for lower waste heat source temperatures (higher than 400°C as showed in Figure 5). This is due to the high chemical stability of CO_2, which allows to directly recover and convert heat at temperatures up to 850°C (Figure 13), limit posed by current material technologies [54].
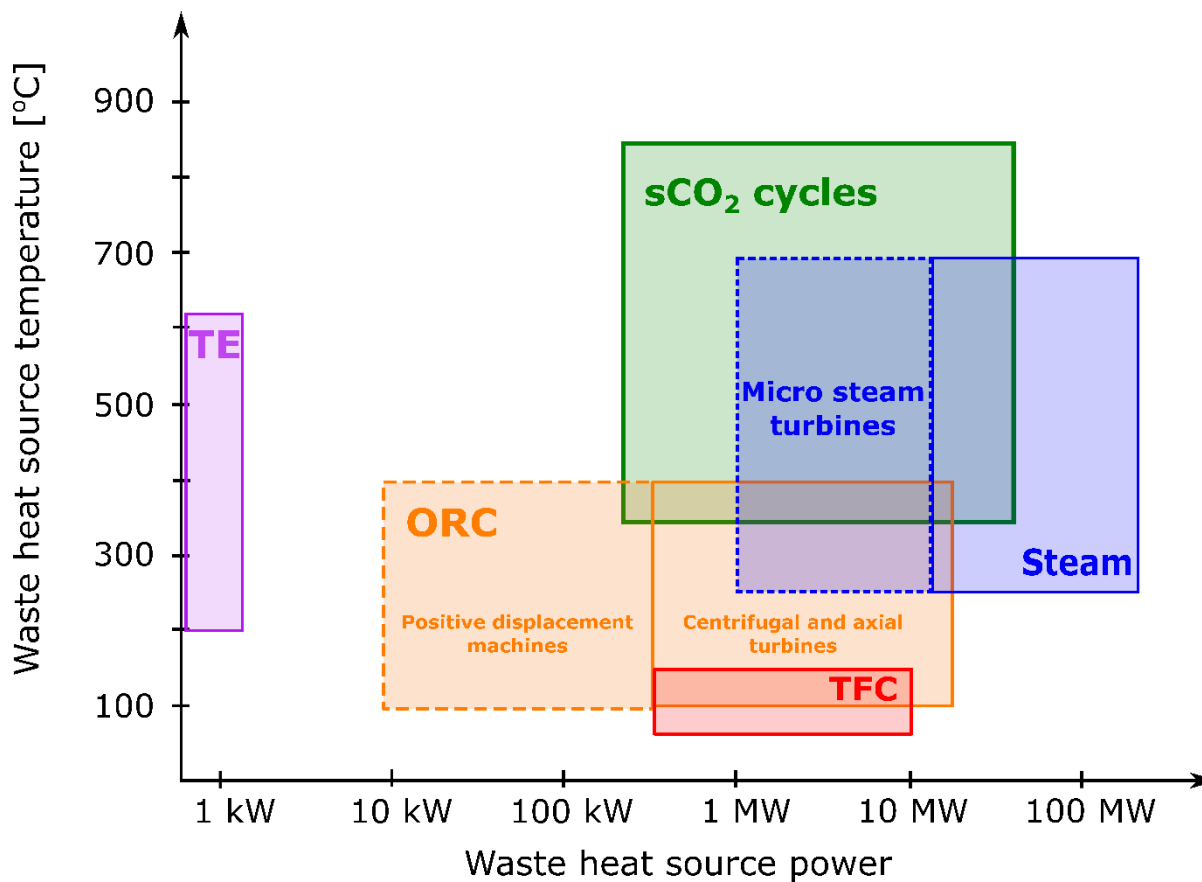
Figure 13 – Comparison of different operating range of heat to power conversion technologies based on bottoming thermodynamic cycles for WHR applications

The lower operational limit is instead set at 350°C considering a simple regenerated layout, which represents the most convenient option for WHR applications [128]. For such low-cost systems, characterized by a low cycle pressure ratio, the achievement of higher temperatures at the turbine inlet to obtain a positive net electric output is required [128]. From a power scale perspective, several technological challenges and the high investment costs set the lowest feasible unit capacity at 50 kW_e [105], which correspond to a waste source thermal power of 300 kW_t assuming a 20% system thermal efficiency [128]. Among the technical limitations, the

main ones arise from the reduced size of the turbomachines. Typical wheels diameters range from 30 mm to 50 mm, with consequent issues of leakage, high vibrations level and friction due to the elevated revolution speeds (over 60000 RPM) [61,105].

On the other side, it is possible to scale up sCO_2 systems until tens of MW (Figure 13), as it has been proved by the Echogen unit [52,92]. In this case, rather than on the turbomachinery side, which can benefit from the knowledge acquired in the gas turbine and steam power plants sectors, technological limitations arise on the scaling up of heat exchangers.

2.8 Summary

This chapter highlighted the potential of sCO_2 power cycles as heat to power conversion technology in several applications and especially for the Waste Heat Recovery (WHR) sector. Figure 13 shows in fact how the development of such systems could fill a gap in the efficient exploitation of high temperature waste heat sources available in the European Union, United Kingdom but in more general terms worldwide, since India, China and developing countries will need to decrease the environmental impact of their economies in the next decades.

In order to shorten the Time To Market of sCO_2 power cycles in this sector, it has been showed that several technical barriers in the development of main components (turbomachines and heat exchangers) and suitable materials must be addressed. In general, for WHR applications, these issues are even accentuated by the needs of reducing capital and operational expenditures and therefore the payback period of the technology. Furthermore, suitable heat exchangers able to guarantee an efficient waste heat recovery (usually available from flue gases) are not available.

This research aims then to tackle such challenges first by providing a comprehensive theoretical assessment for the identification of concepts able to improve the economic attractiveness of sCO_2 power cycles for WHR applications. Secondly, it tries to pose the foundation for the demonstration of the technology close to an industrial environment by providing detailed design and construction choices adopted for the development of a 50 kW_e sCO_2 testing facility. The facility allows to test advanced gas to CO_2 heat exchangers and then represents an important starting point for the technological improvement of such components.

Finally, the facility construction allowed to retrieve geometrical and performance data about components, which have been used to develop detailed numerical models able to provide researchers and engineers valuable insights on the dynamics of standalone components and the entire unit as well as improve the understanding of main concepts behind the working principle of the technology. A further important aspect will be the assessment and design of

suitable controls strategies able to optimise the system performance for different off-design operating conditions and during transient operations.

3. Thermo-economic Analysis

3.1 Introduction

It has been shown in the first chapter that for high temperature WHR applications the sCO_2 Brayton cycle presents numerous benefits with respect to conventional energy conversion systems, as for instance Rankine ones or gas turbines [17]. For these reasons, several theoretical analyses have been carried out to assess the actual performance of sCO_2 Brayton cycles in different applications, as nuclear [129], Concentrated Solar Power [130] or fossil fuel fired plants [131]. In these cases, however, the objective is the maximisation of the system overall efficiency since it is directly related to the primary energy source consumptions and thus to the plant variable costs. Then, the Capital Expenditures (CAPEX) and the plant complexity can be increased to reduce the Operating Expenditures (OPEX) of the facility. On the contrary, when WHR bottoming units are considered, the thermal energy input is provided by the waste heat source, which is "free" and thus does not account as a plant expense. Hence, the objective becomes the maximization of this waste energy recovery and thus of the system net power output rather than its efficiency.

In the literature, few works consider this aspect in the theoretical performance analysis and the economic convenience of the different solutions is usually discarded. Therefore, the chapter aims at filling this gap of knowledge and presents a holistic assessment of the theoretical capabilities of eight different sCO_2 cycle layouts for small-scale high-grade WHR applications. Unlike nuclear or solar power contexts, the nature of the heat source involves different goals and constraints such as reduced heat transfer coefficient, need to decrease pressure losses in the CO_2 heater and increased maintenance requirements to avoid excessive fouling when dirty exhausts are employed as heat source.

Firstly, an overview of the most common sCO_2 Brayton cycle variants, or layouts, proposed in the literature are detailed with particular emphasis on the ones specifically designed for WHR uses. Afterwards, eight layouts are analyzed and compared with reference to the same turbine inlet temperature and in terms of performances, exergy losses and several economic indicators, such as the Specific Cost per unit power (SC), the Internal Rate of Return (IRR), the Levelized Cost Of Electricity (LCOE) and the Payback Period (PBP).

Among these architectures, an innovative layout is presented and compared with the literature ones. The analysis further includes an estimation of the investment costs of heat exchangers and turbomachinery with reference to literature correlations, which were further validated through actual budgetary quotations obtained by the manufacturers during the design of a 50 kW_e sCO_2 power unit.

3.2 Supercritical CO₂ Power Cycle Layouts

The cycle architecture described in Chapter 2, namely the simple-regenerative layout, constitutes the simplest configuration for sCO₂ power cycles since it employs the lowest number of main components, i.e. 3 heat exchangers and 2 turbomachines. Additional devices can be embedded in the system and combined in order to create new cycle architectures with increased performance (i.e. higher efficiency and net power output). With this aim several variants of the basic layout have been proposed in the literature, and mainly designed for power generation applications (i.e. nuclear or concentrated solar power). Certain solutions have been taken from the extensive knowledge acquired in decades of conventional gas turbine technology development, while others have been specifically designed to take advantage of the thermo-physical properties of the carbon dioxide. A review of all these alternative schemes will be given in the following pages.

Reheating

It is well known from the thermodynamic theory that the work extractable from an expansion of a unitary mass flow of gas between two pressures p_1 and p_2 is directly related to the magnitude of this pressure difference and the specific volume assumed by the gas during the expansion process. This statement can be summarized by the mathematical expression reported in Equation (2). Where v is the gas specific volume, p_1 and p_2 the high and low pressure respectively at which expansion occurs, and w is the specific work extractable from the gas.

Considering that during the expansion the specific volume decreases, the work obtainable diminishes during the process. Then, if the average specific volume during the process is increased, a higher work output could be achieved. A possible alternative is the splitting of the expansion in two steps, considering an intermediate heating stage of the working fluid as showed in Figure 14. Hence, an additional heat exchanger (HX2) and an additional turbine (T2) are embedded in the system to realize the reheating of the fluid.

The first expansion in the first turbine is realized from pressure p_1 to an intermediate pressure p_i, while the second one is realized in the second turbine up to the pressure p_2 once the flow is heated up through the heat exchanger HX2 thanks to additional thermal energy or to a better utilization of the heat source available.

In general, the optimal value of the intermediate pressure p_i that maximises the expansion work when reheating is adopted (w_{reheat}, Equation (3)) can be calculated with the Equation (4). When multiple reheating stages are considered, Equation (5) can be used, where N is the

number of reheating stages adopted and $p_{i,k}$ is the optimal intermediate pressure at the *k-th* reheating stage.

$$w_{(no\ reheat)} = \int_{p_2}^{p_1} vdp < \int_{p_i}^{p_1} vdp + \int_{p_2}^{p_i} vdp = w_{reheat} \tag{3}$$

$$p_{intermediate,optimal} = \frac{p_1}{\sqrt{p_1/p_2}} \tag{4}$$

$$p_{i,k} = \frac{p_{i,k-1}}{\sqrt[N]{p_1/p_2}} \tag{5}$$

Multiple authors investigated the performance change of sCO_2 power cycles considering also a reheating stage. Halimi and Suh [132] analyzed the performance increase given by the introduction of reheating in a recompressed sCO_2 power cycle for nuclear power applications. The results showed that introducing the reheating can allow to increase the cycle thermal efficiency from 42.4% up to 43.1%. The same analysis has been carried out by Padilla *et al.* [133] referring to a sCO_2 heat to power conversion system for CSP applications. The reheating configuration allowed to increase both the thermal and exergy efficiency of the cycle of 1%. In general, the reheating layout can improve slightly the cycle thermal efficiency, but the increment of investment cost against the small performance increase available confine this variant only for power generation applications.

Intercooling

The concept detailed in the previous section for the improvement of the expansion efficiency through the reheating applies also for compression. In this case however, the theoretical principle is to maintain a reduced gas specific volume during the process. To do so, the compression can be divided in two or multiple steps with intermediate cooling stages. The outcome is a reduced compression power required and thus a higher net power output and cycle thermal efficiency.

As drawback, the system complexity increases, since for each intercooling stage an additional compressor and heat exchanger is required. Figure 15 shows the system layout and the T-s diagram of the intercooled Brayton cycle. The additional compressor (C2) and gas cooler (GC2) required for the adoption of a single intercooling step are also shown.

In the literature several studies have been carried out to assess the eventual benefits of the intercooling variant for sCO_2 power cycles. Mondal *et al.* [134] presented a sCO_2 Brayton cycle with multi-stage intercooled compression considering as waste heat source a flue gas stream at 350°C. The number of compression stages together with the key parameters of the cycle have been optimized in order to achieve the best cycle thermal and exergy efficiency.
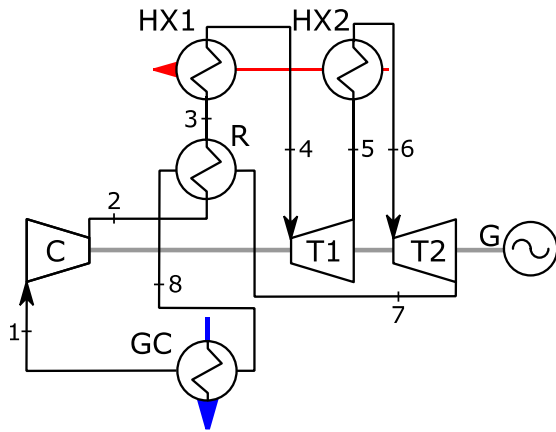
(a) Cycle layout
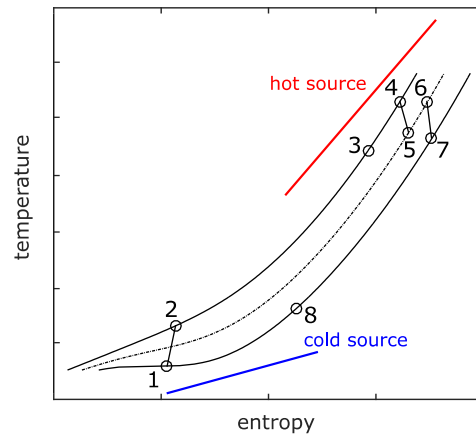
(b) T-s diagram

Figure 14 – Reheating configuration
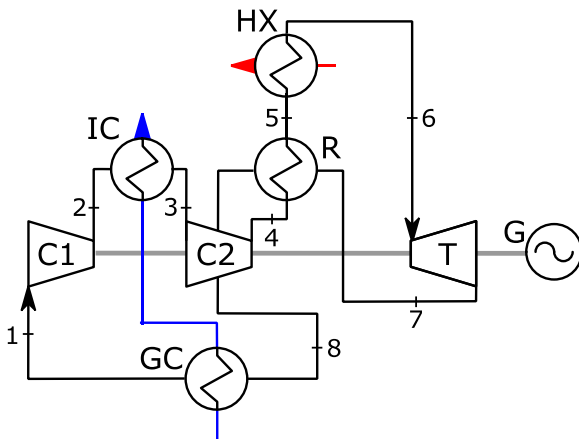
(a) Cycle layout
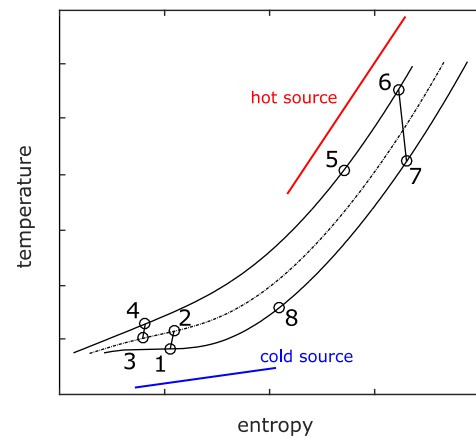
(b) T-s diagram

Figure 15 – Intercooling configuration

Combined Reheating and Intercooling

The theoretical principle behind the reheating and the intercooling is to use split compression and expansion to get closer to an isothermal process, which allows to maximisation of the work term in Equation (2). In theory, splitting the adiabatic compression or expansion in an infinite number of stages, an isothermal process as the one showed in the T-s diagram of Figure 16 could be obtained.

The Brayton cycle then becomes what is named an Ericsson cycle, composed by two isobaric heat transfer processes and an isothermal compression and expansion. The Ericsson cycle has the highest theoretical efficiency achievable in a heat to power conversion process, being equal to the Carnot one. Its efficiency in last instance depends only from the ratio between the two temperatures of the heat source and sink respectively ($T_{H,avg}$ and $T_{C,avg}$ in Figure 16).
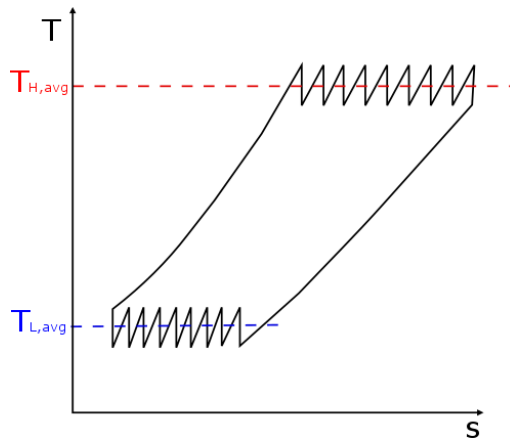
Figure 16 – Ericsson cycle obtained by multiple intercooling and reheating stages

In real applications however, usually the maximum number of intercooling or reheating stages is limited by the plant increasing complexity and investment cost, which make the solutions showed in Figure 16 impractical to realize. In typical air-based Brayton cycles applications, no more than three reheating and intercooling stages are usually adopted. When sCO_2 systems are considered, Moisseytsev *et al.* [99] found that for power plants in the power scale of hundreds of MW_e, the small increase of performance does not justify the resulting increased plant complexity and no more than two reheating or intercooling stages should be adopted.

Recompression

The previous described layouts have been typically used in conventional Brayton power cycle applications, which use air as working fluid. When sCO_2 is used however, different technological limitations arise due to the particular properties the compound assumes close to the critical point (see Chapter 1) and to its considerable thermal capacity. For these reasons, specific cycle layouts have been designed and proposed.

Among them, the recompression layout has been widely studied in the literature. The concept of this architecture is to split the compression of the CO_2 in two stages to decrease the amount of heat rejected by the working fluid into the environment. Because close the critical point the thermal capacity of the CO_2 increases exponentially, high mass flow rates of cooling fluid are needed to adsorb this great amount of heat rejected by the working fluid. Then, the adoption of the recompression allows also to obtain a better matching of the temperature profiles in the gas cooler, with a consequent reduction of exergy loss.

The CO_2 stream split occurs upstream the gas cooler, as showed in Figure 17. The main flow is cooled in the gas cooler (GC) and eventually compressed by the main compressor (MC), while the remaining one is directly compressed in a second device, named the recompressor (RC), and joins the main flow at the outlet of the high-pressure side of the low temperature recuperator (LTR). The adoption of two recuperators, the low and the high temperature one

(LTR and HTR respectively), allows also a better temperature profile matching in these heat exchangers and a further reduction of exergy losses.
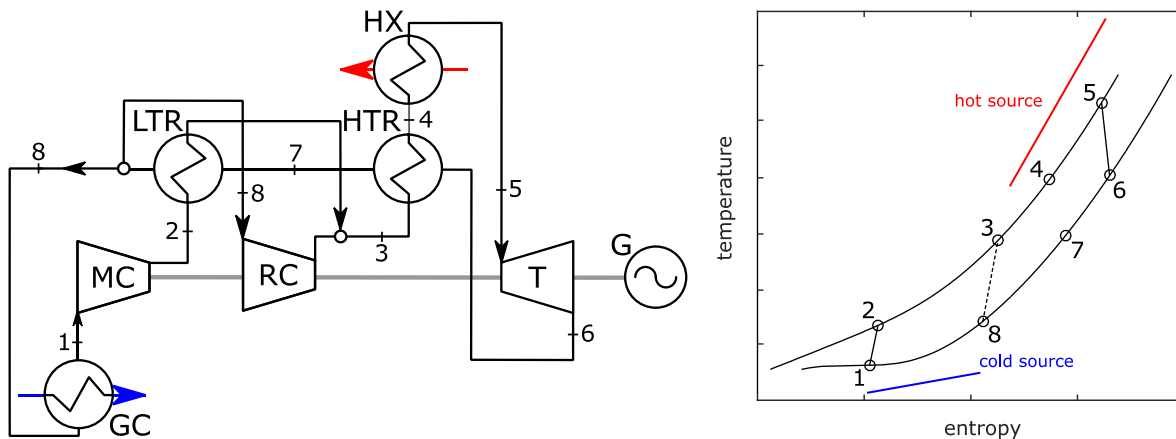
(a) Cycle layout   (b) T-s diagram

Figure 17 – Recompression configuration

Despite the recompression improves the thermal efficiency of the cycle, it also limits the maximum heat recoverable from a given heat source, and thus the power output extractable. This aspect makes the cycle architecture preferable for power generation applications rather than WHR ones, as confirmed by the analysis of Wright *et al.* [xx1].

In this work the authors presented an optimisation of a recompressed layout considering an exhaust stream of 100 kg/s as primary energy source. The recompression layout despite guaranteeing the highest value of thermal efficiency, does not provide benefits in terms of net power output, which is much more relevant for energy recovery systems.

To further enhance the capabilities of the layout Song *et al.* [135] Mohammad *et al.* [136] considered the recompression layout coupled with a further bottoming heat to power conversion unit, an ORC system and a Kalina cycle respectively. In both cases the layout proposed achieved a higher efficiency, even if few considerations on the economic feasibility of the proposed layouts have been reported.

Preheating

The high thermal capacity of the CO_2 can lead also to substantial exergy loss also in the primary heater, if the primary heat source presents a low thermal capacity, as for instance flue gases or air. In this case, a pinch point can occur with a consequent reduction of the thermal energy utilization of the heat source, which can represent a relevant drawback in WHR applications. To overcome this limitation, another configuration proposed for sCO_2 power systems is the preheating one. As showed in Figure 18 the layout considers the spit of the

sCO$_2$ flow downstream the compressor (C1) to heat the two streams in parallel in two heat exchangers.

(a) Cycle layout   (b) T-s diagram
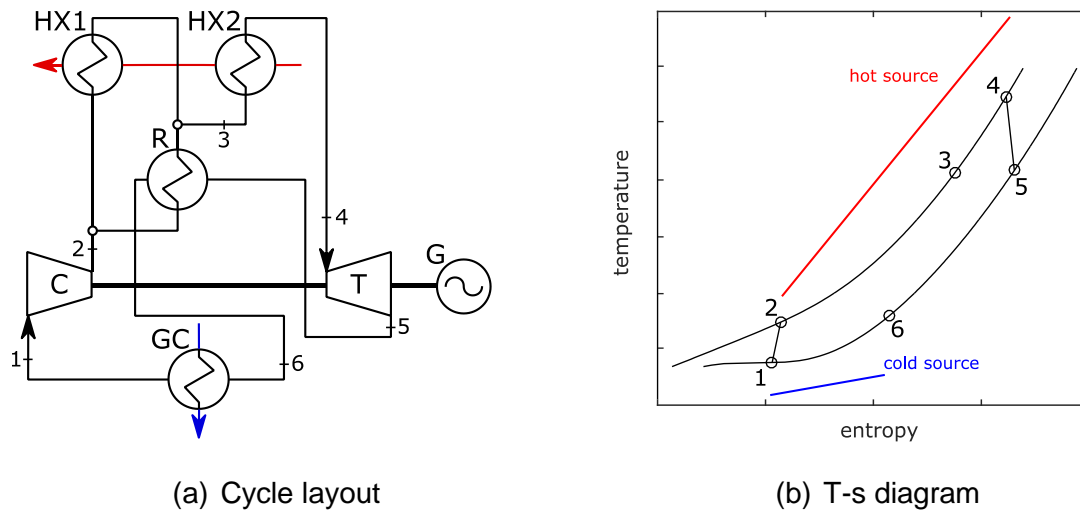
Figure 18 – Preheating configuration

The main flow is heated up in the recuperator (R1), while the remaining one is heated in the secondary heater (HX2). Afterwards, the two contributions merge downstream these two components, are heated up in the primary heater (HX1) and finally expand up to the lowest cycle pressure. Then the hot source flows at its highest temperature at the primary heater inlet and after the first heat transfer to the working fluid, is used in the secondary heater and finally discarded into the environment.

The preheating configuration has been analyzed by Wright *et al.* [137], which compared the layout to other sCO$_2$ cycle variants as bottoming power unit for a gas turbine power plant. The results showed that the preheating cycle can provide the highest net power output and thermal utilisation of the waste heat source with also a competitive investment cost per kW$_e$. The techno-economic study considered high capacity sCO$_2$ systems, with a power scale ranging from 5 up to 10 MW$_e$.

Precompression

Another cycle architecture specifically proposed for sCO$_2$ systems is the precompression layout. This alternative allows to increase the pressure ratio of the cycle by embedding an additional compressor before the gas cooler. This compressor allows to slightly pressurize the fluid before it enters in the gas cooler, allowing a higher pressure ratio across the turbine and still to avoid the condensation of the fluid in the latter heat exchanger. The schematic layout is showed in Figure 19 together with the cycle representation in the T-s diagram and it has been proposed by Kulhanek and Dostal [138].

After the expansion in the turbine (T1), the fluid is cooled down in the recuperator (R1), compressed until the critical pressure in the precompressor (PC) and finally cooled down in the gas cooler (GC). In this configuration the important parameters to consider in the cycle design stage are the minimal cycle pressure and the temperature at which the pre-compression occurs. The choice of these two parameters is of paramount importance to assess the cycle convenience from a purely thermodynamic perspective.

(a) Cycle layout   (b) T-s diagram
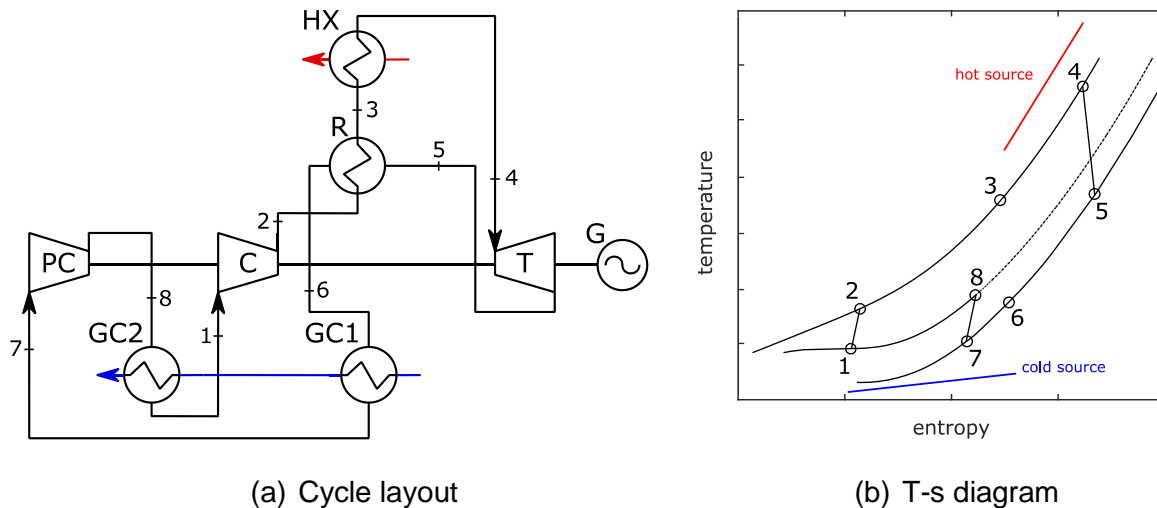
Figure 19 – Precompression configuration

Apart from a performance point of view, these parameters also affect the economic feasibility of the cycle, since are strictly related to the number of extra-components required. For instance, if the temperature at which the precompression occurs is lower than the one at the main compressor (MC) outlet, two gas coolers are needed. On the contrary, if it is higher, only an additional compressor is required.

More Complex Layouts

Other more complex layouts have been proposed in the literature to further increase the performance of sCO$_2$ power cycles. Kulhanek and Dostal [138] proposed a partial cooling Brayton cycle for nuclear power applications. The layout combines the features of the precompression and the recompression cycles. The results showed that the partial cooling allowed to achieve the highest thermal efficiency, almost 43%, for cycle pressure ratios higher than 2.8 and at the maximum cycle temperature of 650°C.

An improved version of the partial cooling layout, named by the authors partial cooling with improved regeneration, also allowed to achieve high performance. However, the high number of heat exchangers required by this architecture and the considerable system complexity poses concerns for its economic feasibility.

A further configuration has been reported in Figure 20. In this alternative, the flow is split downstream the compressor, the main flow is heated up in the heater (HX) and after is expanded in the turbine (T1). After the expansion, the residual heat is used to increase the temperature of the secondary flow in the high temperature recuperator (HTR), which is consequently expanded in the second turbine (T2). The two contributions finally merge upstream the low temperature recuperator (LTR). The layout aims to increase the thermal energy utilization of the waste heat source and to reduce the exergy losses in the several heat exchangers. The configuration, which present an increased complexity will be referred in this work as Split-Heating Split-Expansion (SHSE) layout.

Kimzey [139] proposed also one cycle configuration with split expansion and split heating showed in Figure 21. The architecture is similar to the preheating one for what concerns the heating stage of the sCO_2. In this case however, the flow heated in the secondary heater (HX2) is directly expanded in one turbine (T2) and eventually merges upstream the low temperature recuperator (LTR).
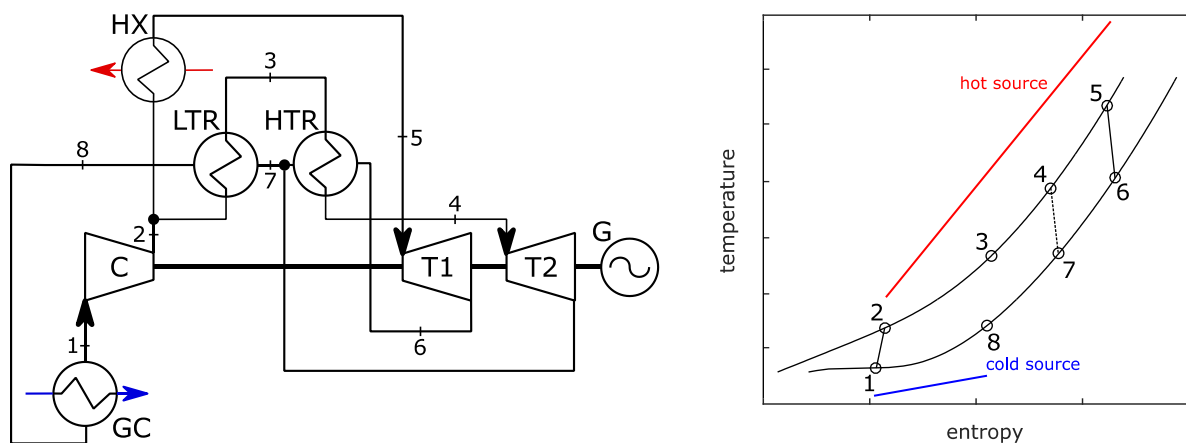
(a) Cycle layout   (b) T-s diagram

Figure 20 – Split-Heating Split-Expansion (SHSE) configuration [139]

The main flow on the contrary is heated up first in the low and high temperature recuperator (LTR and HTR respectively) and after in the primary heater (HX1) thanks to the residual thermal energy of the waste heat source. Then, it is finally expanded in the turbine T1 and cooled until the cycle initial conditions are restored. The layout requires thus two primary heaters with an additional turbine and recuperator.

Both the layouts aim to increase the thermal energy utilization of the waste heat source and to reduce the exergy losses in the several heat exchangers. However, the drawbacks of the introduced increased complexity have not been considered in the analysis.

Even more complex layouts have been considered and analysed by Ahn et al. [140]. The results showed that high complex configurations did not provide a net power output greater

than the reference Rankine cycle even if re-heating and pre-compression positively affected the performance of the sCO₂ bottoming unit. Nevertheless, the power scale of the system analysed was higher than 100 MW$_e$, a range in which steam power plants can achieve very high efficiency thanks to their mature Technological Readiness Level (TRL).
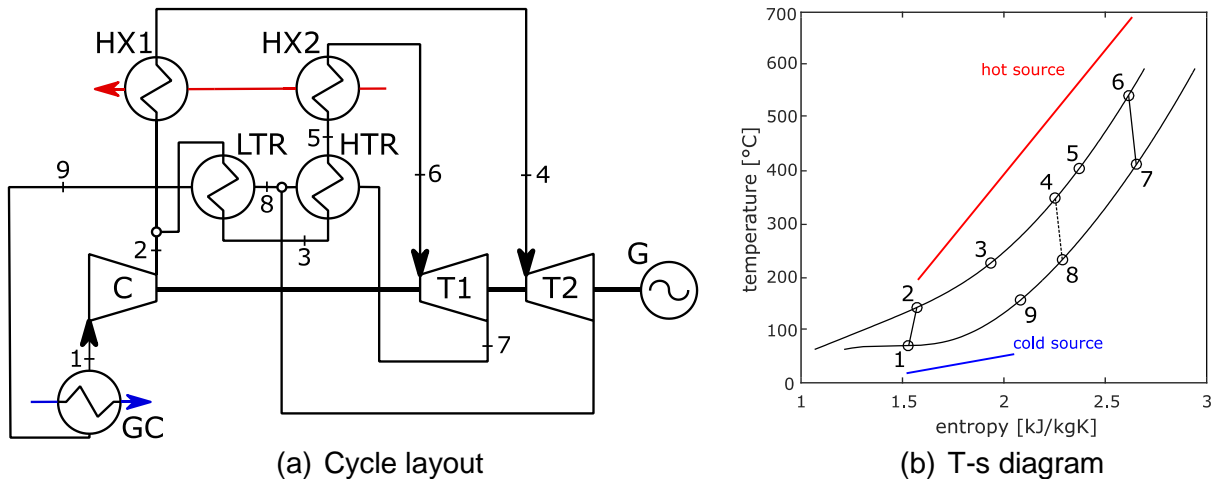
(a) Cycle layout   (b) T-s diagram

Figure 21 – Configuration proposed by Kimzey [139]

The power scale of sCO₂ systems analysed so far in literature is not suitable for high temperature stationary WHR applications which could provide power outputs in the order of tens or hundreds of kilowatts due to the widespread nature of the waste heat sources. Nonetheless, these streams have a remarkable impact on overall consumptions reduction since they are responsible of a global energy waste of 4.79 PWh/ year [7].

Suitable systems to tackle the aforementioned opportunities should be small-scale plug and play sCO₂ power units whose technical and economic viabilities have not been addressed yet. Hence, this chapter aims to provide a comprehensive techno-economic analysis of sCO₂ cycle layouts for WHR uses with the final objective to assess the optimal architecture for the application. The investigation considers small capacity heat to power conversion systems (from tens to hundreds of kW$_e$) from both a component performance and economic perspective. Among the analysed configurations, a novel layout is proposed.

3.3 Selected Configurations

All the architectures selected for the study are reported in Figure 22 and Figure 23, together with the corresponding T-s diagrams. Among them, a novel layout which considers the combination of the preheating and the precompression feature is proposed and studied. Other layouts have been retrieved by the literature. In particular, Figure 22 refers to the most conventional layouts for sCO₂ power cycle applications, namely the Simple Regenerated (SR-Figure 22.a), the Reheating (RH-Figure 22.b), the Recompression (RC-Figure 22.c) and the Recompression Reheating (RCRH-Figure 22.d). As stated in section 2, these configurations

have been typically developed for concentrated solar power and nuclear applications. On the contrary, Figure 23 displays the ones conceived for WHR purposes.
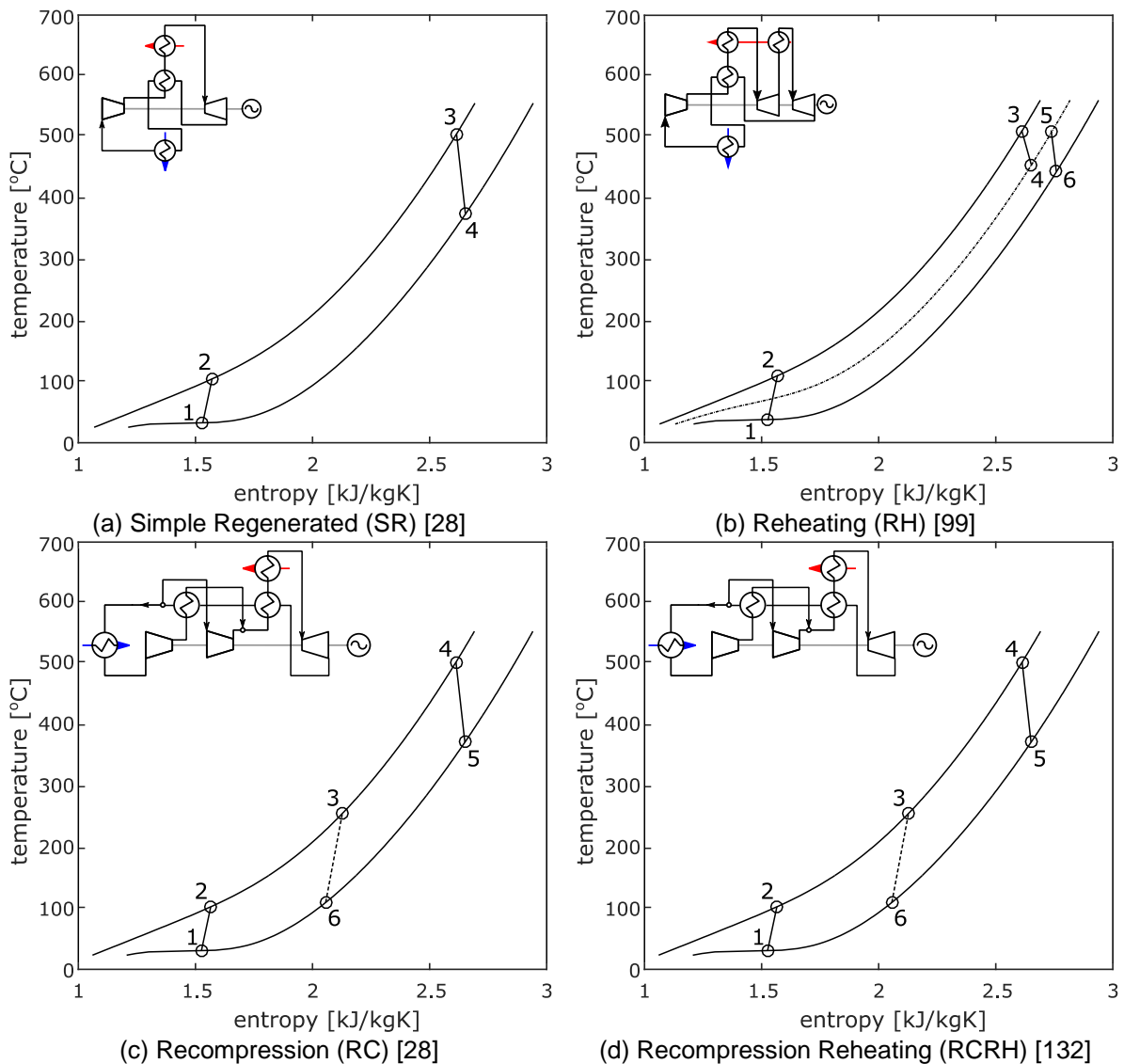
Figure 22 – sCO$_2$ cycle architectures proposed for nuclear and solar power applications

The distinctive feature of these architectures is the maximization of the waste heat utilization of the hot source and, in turn, of the electrical net power output produced. Among them, the least complex cycle scheme is the Preheating one (PH – Figure 23.a), while the Preheating with Split Expansion (PHSE – Figure 23.b) and the Split-Heating with Split Expansion (SHSE – Figure 23.c), which are the layout patented by Echogen and the one proposed by Kimzey [139] respectively, are characterised by a higher complexity. Finally, a less complex novel layout is proposed by the Author, namely the Preheating with Precompression (PHPC), in Figure 23.d. A summary of the equipment involved in each layout considered in this thesis is given in Table 8.

(a) Pre-Heating (PH) [137]

(b) Pre-Heating Split-Expansion (PHSE) [139]

(c) Split-Heating Split-Expansion (SHSE) [139]

(d) Preheating Precompression (PHPC) (new)
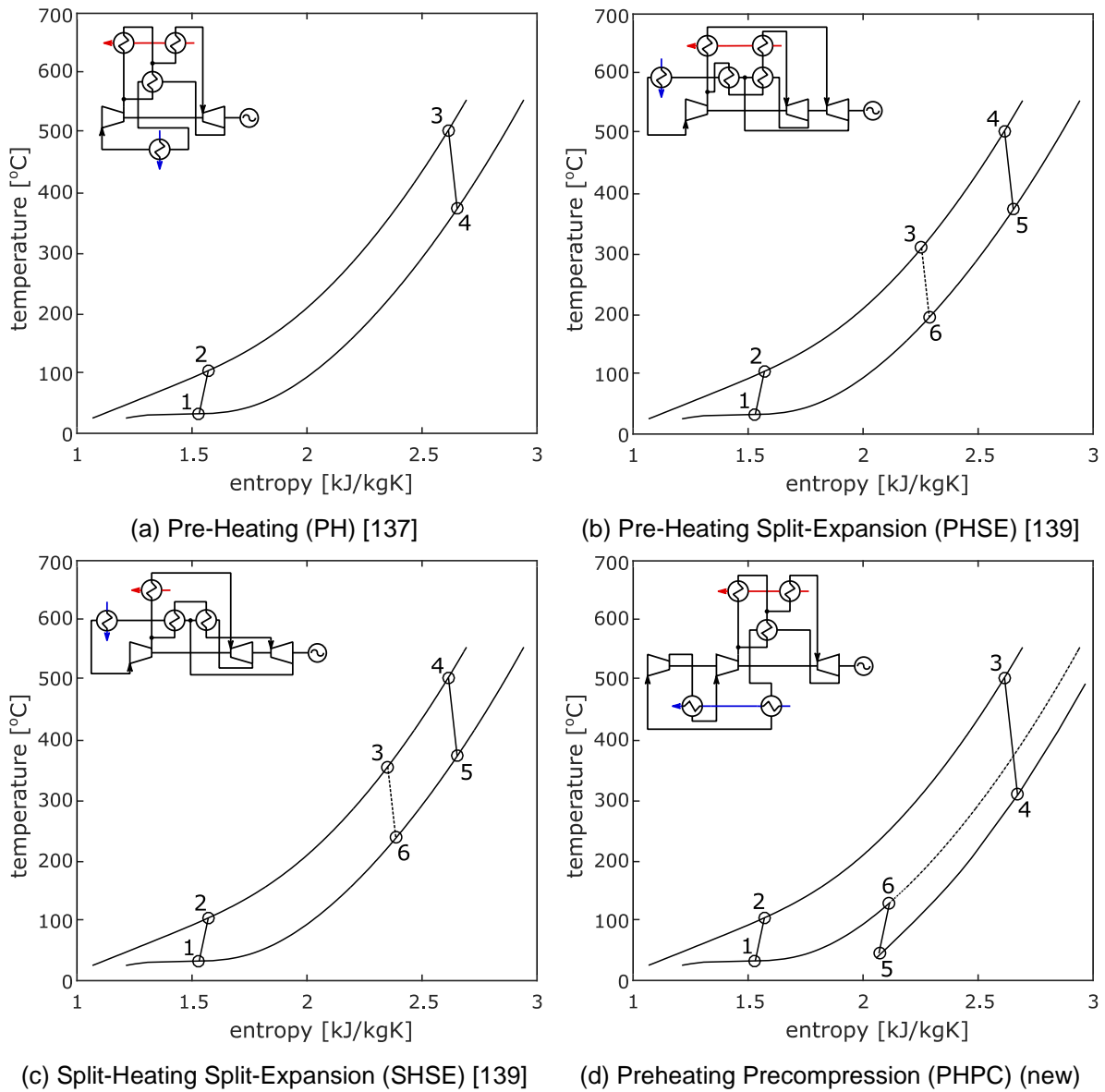
Figure 23 – sCO₂ cycle architectures for waste heat to power conversion

Table 8 – Equipment summary for the cycle layouts displayed in Figure 22 and Figure 23

	SR	RH	RC	RCRH	PH	PHSE	SHSE	PHPC
Compressors (NC)	1	1	2	2	1	1	1	2
Turbines (NT)	1	2	1	2	1	2	2	1
Heaters	1	2	1	2	2	2	1	2
Recuperators	1	1	2	2	1	2	2	1
Coolers	1	1	1	1	1	1	1	2
Total heat exchangers (NHX)	3	4	4	5	4	5	4	5
Total turbomachines	2	3	3	4	2	3	3	3
Total no. of components	5	7	7	9	6	8	7	8

3.4 Methodology

All these different cycle configurations were investigated from both thermodynamic and economic perspectives. In particular, 1st and 2nd laws steady state analyses were carried out using the software CycleTempo™ [141] coupled with the NIST thermophysical property database [142]. To set up the sensitivity analysis, which allowed to identify the operating parameter that mostly affects the sCO2 cycle performance, and to perform parametric studies at different operating ranges, the two software were further linked with a MATLAB® script. Finally, the economic assessment was performed with reference to literature correlations as well as budgetary quotations that have been requested during the design of a small-scale simple regenerated sCO2 test rig at Brunel University London.

Energy Analysis

The governing equations for cycle analysis are the steady state mass and energy balances. In particular, for each component of the system, heat exchanger or split/joint location Equations (6-8) respectively apply:

$$\dot{m}_i = \dot{m}_o \tag{6}$$

$$\dot{m}_{hs}(h_i - h_o)_{hs} = \dot{m}_{cs}(h_o - h_i)_{cs} \tag{7}$$

$$\sum_{j=1}^{IN} \dot{m}_{i,j} h_{i,j} = \sum_{j=1}^{OUT} \dot{m}_{o,j} h_{o,j} \tag{8}$$

where IN and OUT are respectively the total number of flows merging and splitting from the j-th node considered.

As concerns the turbomachines, isentropic efficiency, inlet temperature and pressures at the inlet and outlet of the machine are the input data. Hence, enthalpy at the turbine and compressor outlets are computed through Equations (9) and (10) respectively, while for the temperature at the machine outlets Equation (11) applies.

$$h_{T,o} = h(p_o, s_i) \eta_{T,is} \tag{9}$$

$$h_{C,o} = h(p_o, s_i) / \eta_{C,is} \tag{10}$$

$$T_o = T(p_o, h_o) \tag{11}$$

Electrical power produced by the turbines or required by the compressors are calculated using Equations (12) and (13). The parameters η_m and η_e, whose values are reported in Table 9, refer to the mechanical and electrical efficiencies.

$$\dot{W}_T = \dot{m}_T (h_{T,i} - h_{T,o}) \eta_m \eta_e \tag{12}$$

$$\dot{W}_C = \dot{m}_C (h_{C,o} - h_{C,i}) / (\eta_m \eta_e) \tag{13}$$

Net power output and overall efficiency of the cycle are eventually calculated as per Equations (14) and (15):

$$\dot{W}_{net} = \sum_{j=1}^{NT} \dot{W}_{T,j} - \sum_{j=1}^{NC} \dot{W}_{C,j} \tag{14}$$

$$\eta_{tot} = \frac{\dot{W}_{net}}{m_{hot} (h_{hot,i} - h_{hot,o})} \tag{15}$$

where NT and NC are respectively the number of turbines and compressors installed in each layout, as shown in Table 8.

Exergy Analysis

Assuming that the dead state is defined at ambient conditions (1 bar, 25°C), inlet and outlet exergy flows for each sCO₂ stream in each component are calculated as per Equations (16) and (17):

$$\dot{E}_i = \dot{m}_i (h_i - T_0 s_i) \tag{16}$$

$$\dot{E}_o = \dot{m}_o (h_o - T_0 s_o) \tag{17}$$

The exergy irreversibility for heat exchangers $\dot{I}_{HX}$ for heat exchangers can be evaluated through Equation (18), while Equation (19) applies for the one of compressors and Equation (20) for turbines ($\dot{I}_C$ and $\dot{I}_T$ respectively).

$$\dot{I}_{HX} = \dot{E}_{cs,i} + \dot{E}_{hs,i} - \dot{E}_{cs,o} - \dot{E}_{hs,o} \tag{18}$$

$$\dot{I}_C = \dot{E}_{C,i} + \dot{W}_C - \dot{E}_{C,o} \tag{19}$$

$$\dot{I}_T = \dot{E}_{T,i} - \dot{W}_T - \dot{E}_{T,o} \tag{20}$$

Therefore, the overall exergy efficiency of each thermodynamic cycle can be calculated through Equation (21):

$$\eta_{ex,i} = 1 - \frac{\sum_{j=1}^{NC} \dot{I}_{C,j} + \sum_{j=1}^{NT} \dot{I}_{T,j} + \sum_{j=1}^{NHX} \dot{I}_{HX,j} + \dot{E}_{hot,o}}{\dot{E}_{hot,i}} \tag{21}$$

where the $\dot{E}_{hot,o}$ is the exergy flow of the exhaust gases downstream the primary heater (Equation (18)).

Economic Indicators

In order to assess economic aspects of the different layouts analyzed, several economic indicators have been considered, namely the Specific Cost (SC), the Levelized Cost Of Electricity (LCOE), the Internal Rate of Return (IRR) and the Payback Period (PBP).

The SC is a simple indicator representing the unitary cost of a plant per electrical kilowatt (kW$_e$) installed and can give a qualitative idea to compare similar systems.

$$SC = \frac{C_{tot}}{\dot{W}_{net}} \tag{22}$$

In Equation (22), the numerator is the investment cost of the sCO$_2$ system that not only accounts for the cost of the equipment but also for the ancillaries as well as the installation costs (Equation (23)).

$$C_{tot} = \left(\sum_{j=1}^{NHX} C_{HX,j} + \sum_{j=1}^{NT} C_{T,j} + \sum_{j=1}^{NC} C_{C,j} \right) C_{inst} \tag{23}$$

The investment cost of the heat exchangers was calculated using the data available in [19]. These correlations refer to a specific cost per heat transfer capacity (UA-value), which in turn depends on the heat exchanger duty and the Logarithmic Mean Temperature Difference (LMTD), as shown in Equation (24). Therefore, this approach allows an estimation of the costs without going into a detailed exchanger modelling. Nevertheless, the costs calculated with Equation (19) are in well agreement with budgetary quotations requested to multiple manufacturers of sCO$_2$ heat exchangers. Values for the λ coefficient, which depends on the type of heat exchanger considered and its technology (heater, recuperator or cooler), are reported in Table 12.

$$C_{HX,j} = \lambda (UA)_j = \frac{\lambda Q_j}{LMTD_j} \tag{24}$$

Costs for turbine and compressor can be calculated according to Equations (25) and (26). These correlations relate the investment cost to operating parameters of the machines, such as mass flow rates, pressure ratio, isentropic efficiency and turbine inlet temperature expressed in Celsius degrees [143].

$$C_T = 479.34 \dot{m}_T \left(\frac{1}{0.93 - \eta_T} \right) \ln(\beta_T) \left(1 + \exp(0.036 T_{T,i} - 54.4) \right) \tag{25}$$

$$C_C = 71.10 \dot{m}_C \left(\frac{1}{0.92 - \eta_C} \right) \beta_C \ln(\beta_C) \tag{26}$$

The plant installation costs were taken into account through a multiplier of the investment cost equal to 30%. This coefficient is slightly overestimated to also include the cost for the auxiliaries (i.e. refrigeration compressors for drainage removal, motorized valves, electrical connections etc.).

Unlike SC, the LCOE is instead a more general metric that allows to assess the profitability of an investment in a generic power plant. In fact, the LCOE estimates the average cost of the electricity that will be produced by the facility. This parameter can be calculated according to Equation (27) as the ratio of the Present Value of the plant Expenses (PVE) and the plant productivity over its total operating time, which in turn depends from the net electrical power, the lifetime and the utilization factor. These parameters are all reported in Table 12.

$$LCOE = \frac{PVE}{8760 \, u \, NY \, \dot{W}_{net}} \tag{27}$$

The PVE, whose formulation is reported in Equation (28), involves the cash flows calculation of the plant expenses through Equation (29). In this study, operation and maintenance costs per kW$_e$ of power installed are taken into account through the parameter OM while the escalation rate of this cost over the years is considered through the coefficient er. These informations are reported in Table 12 together with the discount rate r.

$$PVE = C_{tot} + \sum_{k=1}^{NY} \frac{CF_{xp,k}}{(1+r)^k} \tag{28}$$

$$CF_{xp,k} = \dot{W}_{net} (OM (1+er)^k) \tag{29}$$

The IRR is a financial metric indicating the final value of the investment interest rate to get a Net Present Value (NPV) equal to zero with reference to the plant lifetime as interval period. According to this definition, the IRR was calculated as per Equation (30). In this case, the cash flows of the plant revenues must be also considered; the reference formulation is reported in Equation (31) where C_e is the cost of electricity, whose value is presented in Table 12 and decreased over the plant lifetime through the coefficient dr.

$$-C_{tot} + \sum_{k=1}^{NY} \frac{CF_{rev,k} - CF_{xp,k}}{(1+IRR)^k} = 0 \tag{30}$$

$$CF_{rev,k} = \dot{W}_{net} (8760 \, u \, C_e (1-dr)^k) \tag{31}$$

Finally, the PBP represents the time required to recover the initial investment for each plant layout. Because of the degradation of the productivity and the increase of the maintenance costs, the revenues are uneven during the system operating lifetime, so the cumulative cash flows for all the layouts are computed for each year of the operating lifetime. Then, the approximated PBP is the year (Y_A) when this cumulative cash flow (CF_{cum,Y_A}) becomes positive. However, to get a more accurate figure, the Equation (32) is used, where CF_{rev,Y_A} and CF_{xp,Y_A} indicate the revenues and the expenses for that specific period.

$$PBP = Y_A - \frac{CF_{cum,Y_A}}{CF_{rev,Y_A} - CF_{xp,Y_A}} \qquad (32)$$

Solution Routine

A general flow chart of the calculation procedure is shown in Figure 24 and applies to all the architectures investigated. Each cycle layout is preliminary built in the Cycle Tempo™ environment by assembling a series of standardized components considered as black boxes and characterized by their distinctive features: turbines and compressors by the isentropic efficiencies, pressure ratio, and inlet temperature; heat exchangers by the pinch point.

Based on the number of mass and energy equations that can be written for a given cycle layout, a system of linear equations is built and solved iteratively. The coefficient matrix of the system contains also the enthalpies computed in the previous iterations while the vector of unknowns is populated with the mass flow rates in each pipe of the physical system, whose number is equal to the one of the components. The vector of constants eventually contains thermal or electrical powers provided as inputs. During the iterative procedure, enthalpy calculation occurs through a Dynamic-link library (DLL) to the NIST database. Once the mass convergence criterion is satisfied, energy and exergy performance parameters are calculated.

The difference in the resolution of simple or complex cycle layouts lies in the size of the matrixes but not in their structure. An additional element of complexity can be due to specifying pressure and heat losses in pipes or heat exchangers since this would make the coefficient matrix denser. For these reasons, in the analysis heat exchangers were considered as insulated (negligible heat losses towards the environment) and pressure and heat losses in pipes were discarded as well to simplify the calculations and make the comparison independent from the pipe layout required by the different cycle architectures.

Fluid property variation inside the heat exchangers is instead taken into account during the creation of temperature-enthalpy diagrams for each device in order to check that the crossing

of the temperature profiles is prevented. In order to do that, a discretization based on the share of thermal power exchanged is carried out and allows to trace the heat transfer curves.

To automate the calculations for parametric and optimization studies, Cycle Tempo™ has herein run in batch mode through a script developed in the Matlab® environment which also included the economic correlations of paragraph 3.3. A further advantage of this approach is the possibility to use the Matlab® Optimization toolbox. This feature is particularly handy in the design of a specific cycle for a given application. With regards to the goal of the current study, however, a comparison between optimized configurations would have been inconsistent since the cycle parameters would have differed from a layout to another one. Hence, the optimization feature was not employed.
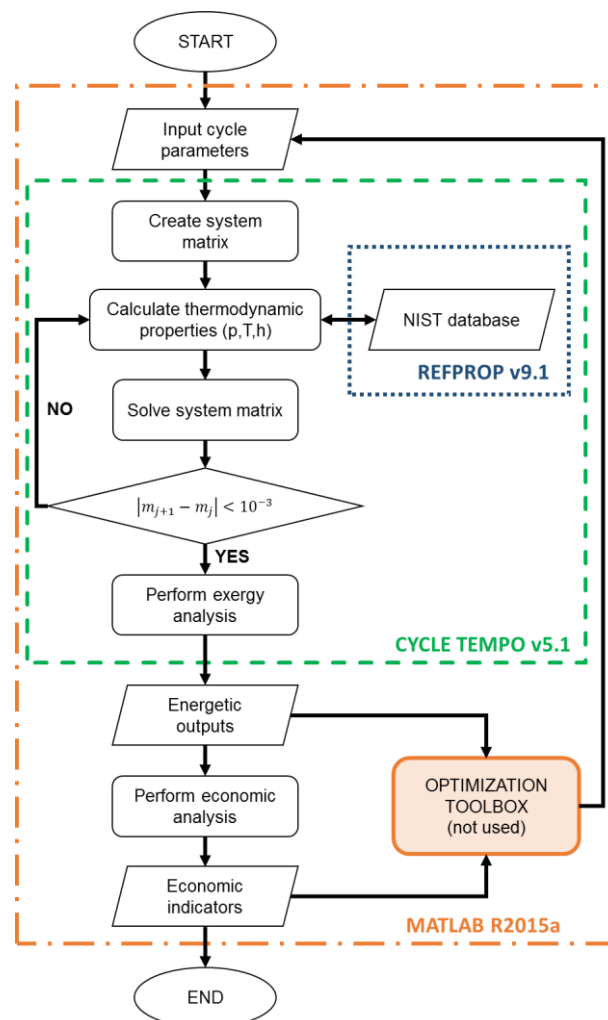
Figure 24 – Flow chart of the solution routine

3.5 Sensitivity Analysis

In general terms, the sCO$_2$ power cycle performance are affected by several thermodynamic parameters such as: pressure ratio, operating conditions at the compressor inlet, turbine inlet

temperature, pressure losses inside the system, turbomachinery efficiency, hot source inlet temperature and mass flow rate, and pinch point in the heat exchangers. Therefore, a comprehensive techno-economic comparison between different plant layouts should accurately consider the different design conditions and operating modes.

However, such a comparison would not only imply high computational and post-processing efforts but could also be inconsistent. Consequently, a sensitivity analysis was carried out beforehand to understand the thermodynamic parameter that mostly affected the plant performance, such that the different operating regimes in the techno-economic analysis could be expressed in terms of this variable.

To perform this preliminary analysis, several simulations have been carried out using as reference layout the simple regenerated one. The influence of the cycle operating parameters has been compared in terms of net electrical power output due to the relevance of this quantity in waste heat recovery applications. The dependent variables investigated are temperature (TIC) and pressure (PIC) at the compressor inlet, the turbine inlet temperature (TIT), the pinch point of the heat exchangers (PP_{HX}) and the maximum cycle pressure (POC).

On the other hand, the inlet and outlet conditions of the hot and the cold sources have been kept constant together with their respective mass flow rates. Similarly, the isentropic efficiencies of the turbomachines were assumed as constant and equal to the values measured at Sandia National Laboratories during the testing campaign on the 300 kW_e recompressed sCO_2 power cycle test rig unit [53,116]. In particular, the compressor efficiency was taken from [38], in which a compressor having the same power size of the one considered in the current study was tested at different operation conditions.

The experimental campaign showed that, in the whole range of pressure and temperatures considered in our analysis, an efficiency of 0.7 was always achievable acting on the compressor speed. For the turbine efficiency, a sCO_2 turbine was tested for a pressure ratio of 1.24, a mass flow rate of 1.74 kg/s, and an inlet temperature of 391°C and reached an efficiency of 0.846 [116]. Since in our case we took in account a pressure ratio of 2.63 and a slightly higher range of mass flow rates, the assumed efficiency of 0.85 can be considered a conservative choice. Such value of pressure ratio resulted from the reference value for the minimum and maximum cycle pressure adopted.

In fact, turbine isentropic efficiency generally increases with pressure ratio, inlet temperature and mass flow rate of the working fluid. Finally, the values considered for mechanical and electrical efficiencies come from design considerations that the supplier of the electrical generator for the sCO_2 system under construction at Brunel University shared with the Authors. Table 9 summarizes the constant parameters considered in the sensitivity analysis

while Table 10 reports the variation of the independent variables with respect to a reference case, which is an intermediate point within the operating range considered in this work that is suitable for sCO_2 applications and generates a power output of 100 kW_e.

Table 9 – Constant parameters in the sensitivity analysis

Hot/Cold sources	Inlet Temperature [°C]	Outlet Temperature [°C]	Mass flow rate [kg/s]
Hot source – flue gas	650	350	1
Cold source – water	15	45	not fixed
Turbomachines	Compressor		Turbine
Isentropic efficiency	0.70 [38]		0.85 [116]
Mechanical efficiency (η_m)		0.95	
Electrical efficiency (η_e)		0.91	

Table 10 – Ranges of variation for the independent variables of the sensitivity analysis

	min	ref	max
PIC [bar]	74	76	80
TIC [°C]	32	35	38
POC [bar]	150	200	250
TIT [°C]	350	450	550
PP_{HX} [°C]	10	15	20

In Figure 25, the results of the analysis are reported. The variation of the net power output produced by the SR configuration is displayed, both in relative and absolute terms, as a function of the several input parameters. For each set of simulation, one variable has been decreased or increased while the others were maintained constant and equal to the values in the reference case. Among all these variables, the ones that least affect the plant power output are the minimum and the maximum pressures of the cycle, and the pinch point in the heat exchangers.

In fact, considering a change of the compressor inlet pressure from 74 bar to 80 bar, the net power output increases only from 96 kW_e to 101 kW_e. The same small variations can be observed for the compressor outlet pressure and for the heat exchangers' pinch points; in fact, the net power output changes from 93 kW_e to 100 kW_e when the maximum pressure is set respectively from 150 bar to 220 bar, and from 101 kW_e to 95 kW_e when the pinch points are set respectively from 10°C to 20°C.More pronounced is instead the effect of the compressor inlet temperature, since the net power output of the system decreases from 104 kW_e to 93 kW_e due to a greater compressor input power when TIC increases from 32°C to 38°C. This analysis also shows that the worsening of the overall system performance when the

compression of the working fluid occurs far from the critical point is primarily due to the temperature rather than a pressure increase, in agreement with the literature.

Nonetheless, the most influencing parameter for the sCO_2 performance is undoubtedly the turbine inlet temperature (TIT). In fact, when this variable increases from 350°C to 550°C, the plant power output variation is maximized, going from 74 kW_e to 115 kW_e. For this reason, the turbine inlet temperature has been chosen as dependent variable for the techno-economic cycle comparison reported in Section 5.
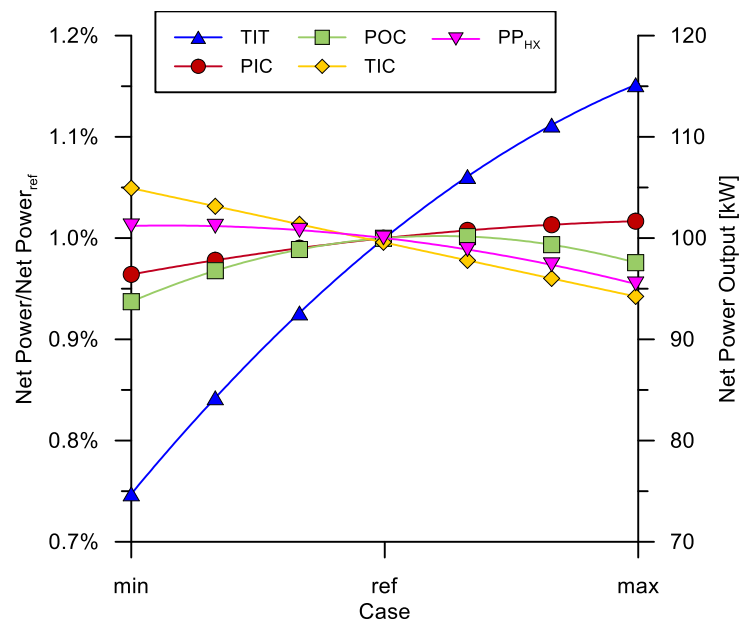
Figure 25 – Sensitivity analysis on the net power output and with reference to the SR layout (layout showed in Figure 22)

3.6 Techno-economic Comparison

Due to the diversity that characterizes the sCO_2 cycle layouts considered in Section 2, to perform a consistent performance comparison, a given number of assumptions had to be made. First of all, the analysis is carried out with reference to 1.0 kg/s of flue gas at 650°C, such that the all the results could be easily scaled for any high temperature heat source, provided that the gas composition leads to the same specific heat at constant pressure (1.1 kJ/kgK). As concerns the final temperature of the hot source after the heat recovery, two main approaches are pursued: the cycle layouts similar to the SR one (i.e. RC, RH and RCRH), in which the sCO_2 flow is not split in two branches, considered an outlet gas temperature of 350°C, as it was assumed in the sensitivity analysis reported in Section 3.5. On the other hand, for the cycle schemes more oriented to WHR applications such as the PH, PHPC, SHSE and PHSE ones, the outlet gas temperature has been set equal to 150°C, which is the

conventional threshold to prevent low temperature corrosion issues. Therefore, this second category of layouts is characterized by high recovery potential compared to the first set of cycle schemes. In fact, without a flow split, an outlet temperature of 150°C cannot be achieved in the first family of cycle architectures since the temperature profiles of flue gas and CO_2 in the heater would intersect. Conversely, splitting the sCO_2 stream allows a suitable matching with the temperature glide of the heat source and, in turn, to maximize the heat utilization.

On the other hand, those simulation parameters that apply only to a subset of cycle architectures have been optimized for each simulation in order to achieve the maximum net power output and thus compare only optimal layouts. Example of such variables are the split ratio for the RC layout or the pre-compressor inlet pressure for the PHPC configuration. Finally, the efficiencies assumed for the turbomachines are reported in Table 9, while Table 11 summarizes the values of the parameters kept constant throughout the study. Among them, it is assumed that the cold source is a water stream whose mass flow rates varies such that an inlet temperature at the cooler of 15°C and an outlet temperature of 45°C are always maintained.

Table 11 – Assumptions in the thermodynamic comparison (N/A= not applicable, OPT=optimized)

	SR	RH	RC	RCRH	PH	PHSE	SHSE	PHPC
Exhaust inlet temperature [°C]					650			
Exhaust outlet temperature [°C]			350				150	
Exhaust mass flow rate [kg/s]					1			
Water inlet temperature [°C]					15			
Water outlet temperature [°C]					45			
Water mass flow rate [kg/s]				Not fixed				
Compressor inlet pressure [bar]					74			
Compressor outlet pressure [bar]					200			
Split ratio	N/A	N/A	OPT	OPT	OPT	OPT	OPT	OPT
Pre-compressor inlet pressure [bar]	N/A	N/A	N/A	N/A	N/A	N/A	N/A	60

Thermodynamic Analysis

Figure 26 shows the net power output (Figure 26.a) and the overall energy efficiency (Figure 26.b) in each layout at turbine inlet temperatures from 250°C to 600°C. However, not all the configurations analyzed can operate in the range considered since, at high TIT, some schemes might present an intersection of the temperature profiles of the flue gases and the CO_2 in the heater. These cases have not physical meaning and they have been therefore omitted from the results. For instance, the maximum TIT displayed for the PHPC architecture is equal to 475°C, since it is the highest value achievable by the architecture.

Considering then only the meaningful cases, both the figures show the positive effect that an increase of the TIT has on the cycle performance. Among the more conventional sCO_2 layouts,

Figure 26.a shows that the ones which generate a higher power output are the RH and the RCRH ones, thanks to the split expansion feature. Indeed, when the TIT goes from 250°C to 400°C these two configurations generate from 59 kW_e to 95 kW_e and from 49 kW_e to 98 kW_e of electric power respectively, against the one produced by the SR and the RC configurations that in the same range of temperature goes from 51 kW_e to 89 kW_e and from 38 kW_e to 90 kW_e respectively.

Beyond 400°C, in RH and RCRH layouts, the split of the heat load in two separate heaters limits the achievable TIT. This fact, on one hand allows to enhance the cycle efficiency (Figure 26.b) but on the other one it constraints the power output (Figure 26.a). Therefore, in absolute terms, the SR and the RC layouts eventually show higher performance since they allow to produce 115 kW_e and 113 kW_e of electric power at TIT of 550°C and 500°C respectively.
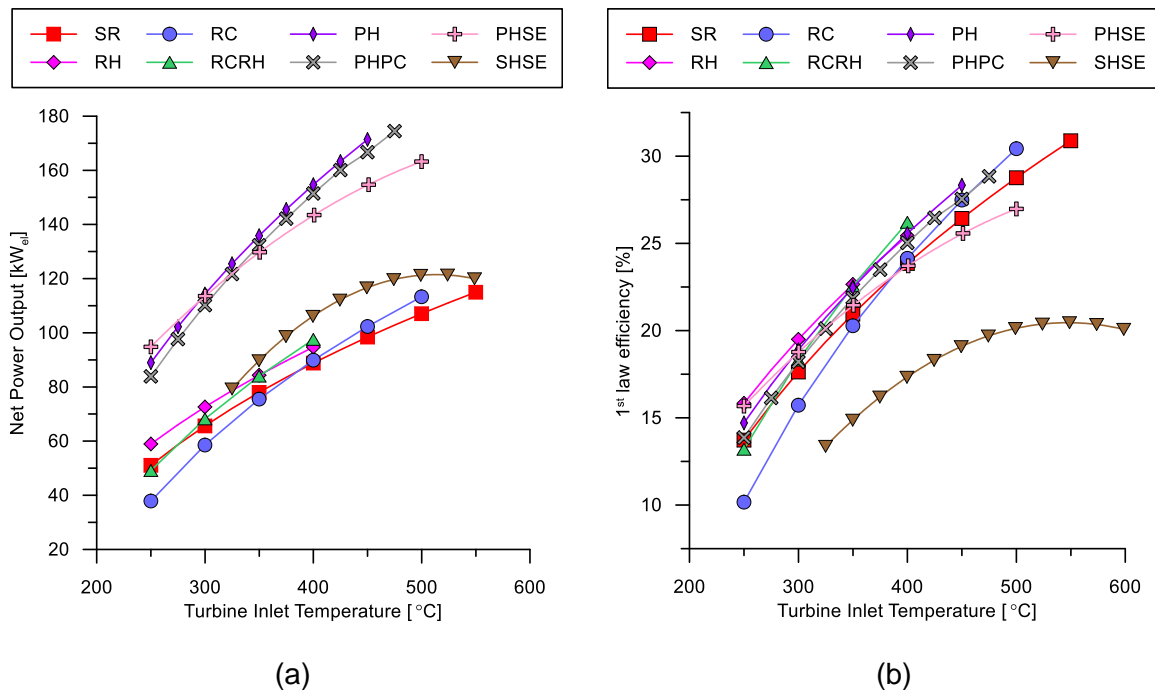
Figure 26 – Comparison between the net power output (a) and the 1st law (energy) efficiency (b) of the several configurations under analysis

The layouts conceived for WHR applications can harvest a greater amount of thermal power from the heat source. To balance this higher thermal load, a greater amount of CO_2 is required in these systems. This results in power outputs higher than those that characterize the configurations previously mentioned but, on the other hand, also in lower overall efficiency since the relative increase of thermal power recovery (that appears in the denominator of Equation (15)) is greater than the relative increment in electrical power output. The SHSE layout, at 500°C and 550°C, is able to generate up to 119 kW_e and 121 kW_e of electric power, more than the one produced by the SR and RC configurations at the same TITs. A much higher net power output can be generated by the PHSE, PHPC and PH architectures that,

with a maximum cycle temperature of 450°C, are able to produce up to 153 kW$_e$, 167 kW$_e$ and 171 kW$_e$ respectively. In absolute terms however, the layout which shows the higher power output is the PHPC one which, thanks to the addition of a pre-compressor, allows to increase the expansion ratio across the turbine and thus to generate up to 174 kW$_e$ with a TIT of 475°C against the 171 kW$_e$ of the PH configuration at a TIT of 450°C

Regarding the exergy efficiency, it is possible to see from Figure 27 that all the layouts show, on average, similar performance. For low TIT, the RH configuration shows higher efficiencies, going from 15.8% up to 19.9% when the TIT goes from 250°C to 350°C. At a TIT of 400°C the RCRH performs better, with an efficiency equal to 26.2%. At a TIT equal to 450°C, the PH layout achieves a higher efficiency, namely 28.3%. The highest performances are however shown by the RC and the SR architectures, which present efficiency values of 30.9% and 30.4% at a TIT of 500 and 550°C respectively.

Lower efficiencies are achieved by the SHSE configuration (20.4% at a TIT of 600°C), since the sCO$_2$ flow, which is heated from the low and high temperature recuperators, expands at lower TIT. The lower net power output additionally affects the exergy efficiency of this layout, which in fact is the lowest among its similar architectures. The SHSE scheme presents indeed a maximum exergy efficiency of 29.3% against the 38.9%, 40.5% and the 41.2% of PHSE, PH and PHPC architectures (Figure 27).
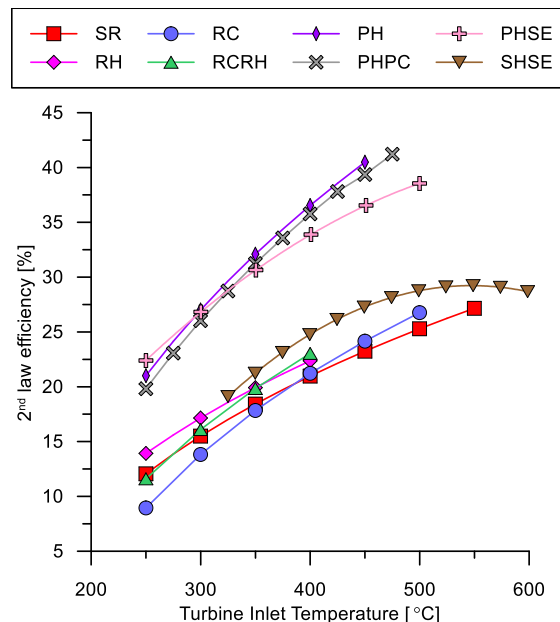
Figure 27 – 2nd law (exergy) efficiency comparison

Worst exergy efficiencies are those achieved by the conventional sCO$_2$ cycle schemes since the outlet temperature of the heat source downstream the heat recovery process is still very high (350°C). In fact, it is possible to notice that the SR and RC layouts show a maximum exergy efficiency respectively equal to 27.2% and 26.7% (for a TIT of 550°C and 500°C), while

for the RH and the RCRH schemes, which are not able to reach that temperature, the maximum exergy efficiency achievable for a TIT of 400°C is respectively equal to 22.4% and 26.2%.

Investment Cost Analysis

In each thermodynamic simulation, several financial metrics have been computed accordingly to formulations presented in the paragraph 3.3. Components cost data and additional parameters herein assumed are listed in Table 12. It is worth to notice that the specific cost for heat exchangers depends on the type and the technology, namely fin tube heater, printed circuit recuperator and plate heat exchangers as gas coolers. Although previous studies considered either printed circuit or shell and tube gas coolers, thanks to the increasing role of natural refrigerants in the refrigeration sector, plate heat exchangers are nowadays available also for CO_2 applications at low temperatures (<250°C) but high pressure. Therefore, in the current analysis, the plate heat exchanger technology, which has a specific cost two orders of magnitude lower than the printed circuit one, was considered.

Figure 28 shows the Specific Cost for kW_e installed (SC) and the Levelized Cost Of Electricity (LCOE) for the eight layouts as a function of the TIT. The results obtained for both the indicators present the same tendency, since both can be seen the ration between total investment cost and power production capacity. In each layout, SC and LCOE show a parabolic trend with a minimum cost for a turbine inlet temperature in a range between 325°C and 425°C. The only exceptions are represented by the SHSE and the PHSE configurations, which present the minimum cost point shifted towards 500°C.

Table 12 – Assumptions in the economic comparison

Components	
λ Heater [$/UA]	5000
λ Recuperator [$/UA]	2500
λ Gas cooler [$/UA]	36
Plant	
O&M operations (*OM*) [$/kW$_e$]	30
O&M escalation rate (*er*) [%]	3
Plant degradation rate (*dr*) [%]	1
Electricity market price (*C$_e$*) [$/kWh]	0.06
Plant lifetime (*NY*) [years]	20
Plant utilization factor (*u*) [%]	85
Discount rate (*r*) [%]	5
Plant installation cost (*C$_{inst}$*)	1.3

These minima are mainly due since the cost of the units is driven by the heat exchangers' one. In fact, while the costs for turbomachines, auxiliaries and installation are, on average, constant between the range of power sizes analyzed in this work, the heat exchangers ones experience a remarkable variation due to their heat transfer area, which in turn depends on the Logarithmic Mean Temperature Difference (LMTD). Therefore, at low TIT, the size of the heat exchangers, and thus the costs, is reduced since the LMTD is large.

However, the power generated by the unit is low and in turn the SC and LCOE become relevant. At higher TIT, the heat exchangers cost increases, but not excessively since the LMTD is still large, and so does the power produced by the plant, causing then a decrease of the SC and LCOE. Increasing even more the TIT, although it allows to have a higher net power output, it also leads to a reduction of the LMTD in the heat exchangers and especially in the heater, with a consequential increase of the heat transfer area, the heat exchangers' cost and thus the cost indicators.

A further interesting result is that the SR configuration, which has the lowest complexity and number of components, also presents the lowest minimum SC and LCOE, which are equal respectively to 770 $/kW$_e$ and 0.0083 $/kWh for a TIT of 425°C. Even the architecture more oriented to WHR applications present higher SC and LCOE. Indeed, the PHSE and the PH configurations show a minimum SC, respectively at a TIT of 500°C and 325°C, equal to 1577 $/kW$_e$ and 1516 $/kW$_e$, and a minimum LCOE equal to 0.0137 $/kWh and 0.0130 $/kWh; while the SHSE and PHPC show lower minimum specific costs, 981 $/kW$_e$ and 948 $/kW$_e$, and LCOE, 0.0095 $/kWh and 0.0097 $/kWh, which however are still higher than the ones related to the SR architecture.

Among the conventional and more complex layouts, the RH scheme presents the minimum SC and LCOE, equal to 1123 $/kW$_e$ and 0.0106 $/kWh (at a TIT of 350°C), which are also competitive with respect to the ones of the WHR plant schemes. Eventually, the RC and the RCRH architecture show much higher minimum costs, as 1775 $/kW$_e$ and 2247 $/kW$_e$ for the SC and 0.0150 $/kWh and 0.0182 $/kWh for the LCOE, respectively at a TIT of 400°C and 350°C.

The same considerations outlined above also hold for the payback period (Figure 29.a), which shows the same trend lines of the two metrics before analyzed. In particular, it is possible to notice that the SR configuration presents a payback period of 1.86 years for a TIT of 425°C, which is the lowest among all the layouts and it could be also attractive from a market perspective. Also, the PHPC, the RH and the SHSE layouts present low payback periods, at a TIT of 325°C, 350°C and 500°C, equal respectively to 2.38, 2.73 and 2.30 years, which are still interesting for heat to power conversion systems oriented to WHR industrial applications.

One of the main reasons for these promising outcomes is due to having considered a plate heat exchanger as gas cooler; indeed, this allows to drop the investment cost of nearly 20%.

(a)   (b)
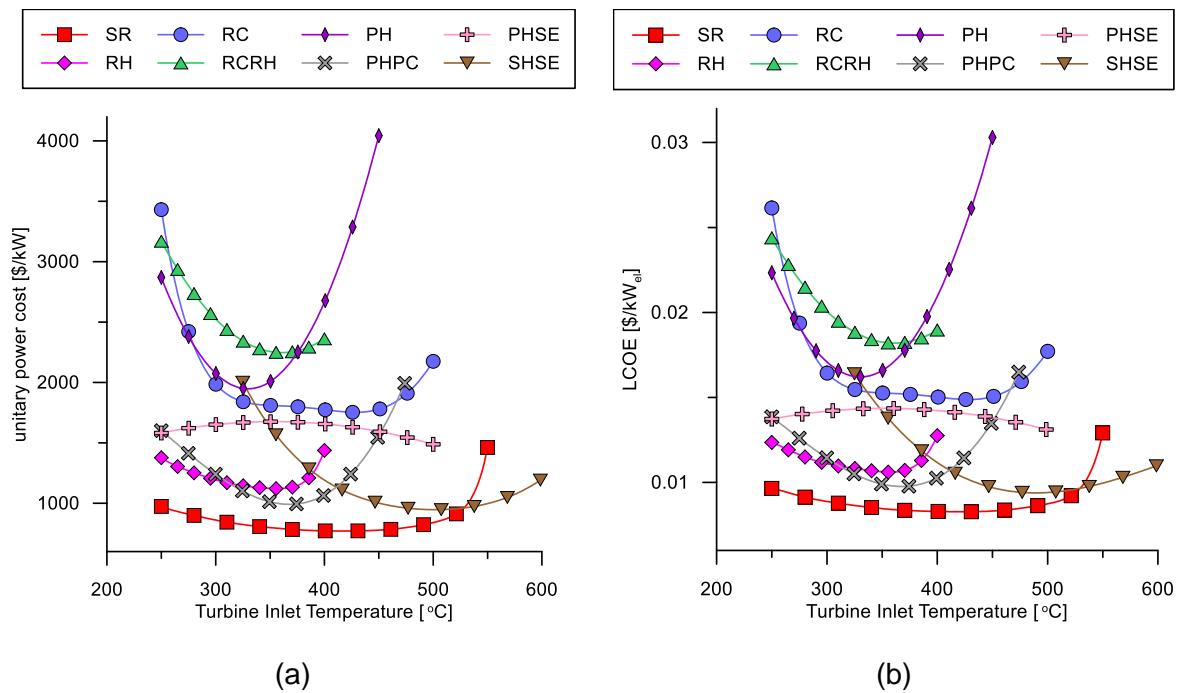
Figure 28 – Comparison between the unitary power cost (a) and the Levelized Cost Of Electricity (LCOE) (b) of the several configurations under analysis

(a)   (b)
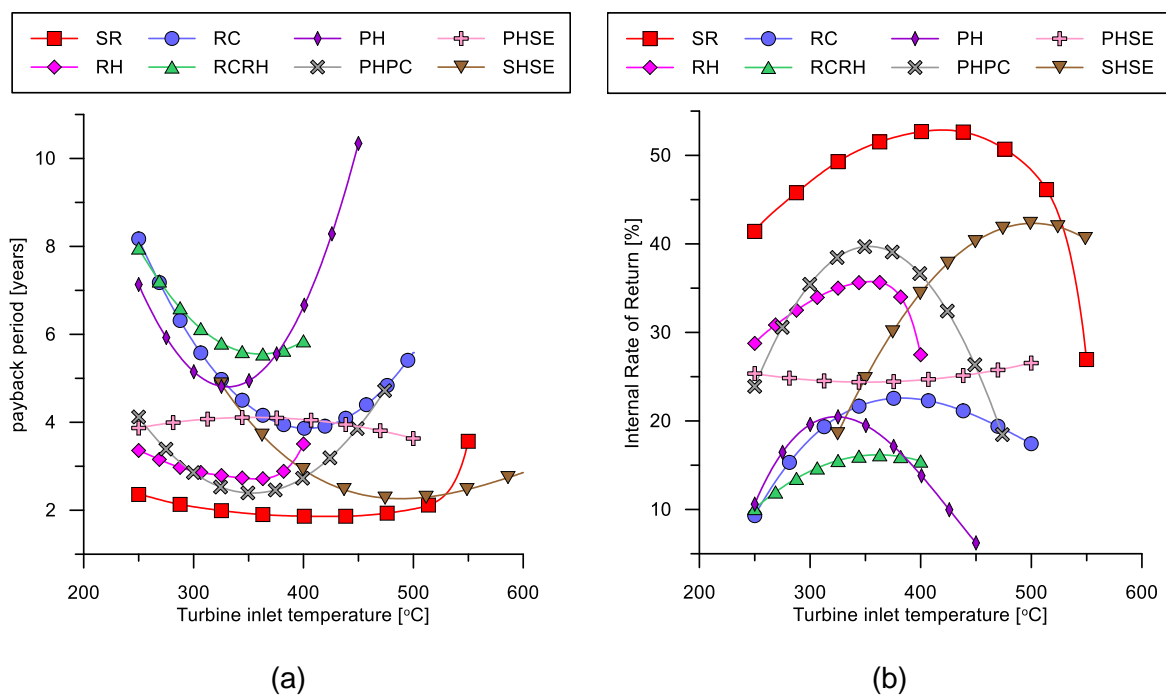
Figure 29 – Comparison between the payback period (a) and the internal rate of return (b) of the several configurations under analysis

Figure 29.b instead, shows the IRR again as a function of the TIT for all the eight different sCO_2 layouts. Also, in this case the SR configuration shows the best IRR, equal to 53% for a TIT of 425°C, while lower rates characterize the PHPC, RH and SHSE layouts, which show respectively a maximum IRR of 41%, 36% and 43% with a TIT of 325°C, 350°C and 500°C.

On the other hand, the PH configuration presents the worst rate, equal to 6% for a TIT of 450°C. It is worth to notice that the results related to these two indicators, contrarily to the LCOE and SC parameters, are strongly affected by the electricity price chosen during the analysis (0.06 $/kWh), and the incentives and taxation rate assumed (which have been neglected in this work).

3.7 Summary

The techno-economic analysis considered eight different sCO_2 power cycle configurations. In particular, four layouts originally developed for concentrated solar power and nuclear applications, the Simple Regenerated (SR), Reheating (RH), Recompression (RC) and Recompression Reheating (RCRH), have been compared to architectures more oriented to waste heat recovery and conversion uses, such as the Split-Heating Split-Expansion (SHSE), Pre-heating (PH), Pre-Heating Split-Expansion (PHSE) and Pre-Heating Pre-Compression (PHPC). The net power output, the thermal and exergy efficiencies, and several investment cost parameters have been investigated at different plant operating conditions using cost correlations, and other published data and assumptions with reference to small to medium scale systems.

The results showed that the turbine inlet temperature is the most influencing parameter on cycle net power output and overall energy and exergy efficiencies. The second most important parameter was identified to be the compressor inlet temperature, which must be very close to the critical point of the CO_2 working fluid. Among the layouts specifically designed for WHR applications, the novel PHPC architecture achieved the highest net power output, 170 kW$_e$ for a turbine inlet temperature of 500°C.

Despite the waste heat recovery architectures have been found to be able to generate a much higher net power output in comparison to the more conventional layouts, the investment cost analysis revealed that the SR plant scheme, which is characterized by the lowest complexity, provides the highest economic effectiveness with a specific cost of 770 $/kW$_e$ and payback period of 1.86 years. This is largely due to the higher contribution of the high temperature heat exchanger(s) to the overall cost of the system, which increases proportionally to the exhaust gas temperature.

Because of the SR layout reduced cost figures, which are of paramount importance in WHR applications, this configuration has been selected for the design of a 50 kW$_e$ sCO$_2$ power cycle facility constructed at Brunel University London that will be presented in the next chapter.

4. Heat to Power Experimental Facility Design

4.1 Introduction

It has been shown in Chapter 2 that among the several sCO_2 layouts investigated, for waste heat recovery applications, the most cost-effective configuration is represented by the simple regenerated one, because of its lower complexity and superior economic figures. However, the technical feasibility of such systems has been so far assessed mostly at theoretical level and mostly at a MW scale.

Therefore, to advance the technological readiness level (TRL) of low capacity sCO_2 systems and demonstrate their technical feasibility, in this chapter the development of a High Temperature sCO_2 Heat To power Conversion facility (HT2C) is presented. The nominal power output of the unit is 50 kW_e and a flue gas stream is employed to simulate a typical waste heat source.

The gas/sCO_2 heat transfer represents one of the main novel aspects of the facility since all the laboratory prototypes developed worldwide embed as heating sources electric heaters directly immersed in the working fluid or using diathermal oil as intermediate heat transfer mid. Other important highlights are the design challenges faced during the development stage of such packaged, plug and play sCO_2 heat to power conversion unit, the description of a state-of-the-art facility for high-temperature equipment testing at pilot scale and the description of a centralized remote monitoring and control system of different assemblies of the facility based on the IEC 61499 standard.

4.2 High Temperature Heat to Power Conversion Facility (HT2C)

The facility has been developed at the Institute of Energy Futures in the framework of the European Union's Horizon 2020 research and innovation program I-Therm [144]. The heat source of the HT2C is an 830kW_t gas fired process air heater, which allows to simulate typical operating conditions of industrial exhausts. The sCO_2 system, composed by a series of components which allow the working fluid (sCO_2) to perform a series of thermodynamic transformations typical of a Joule-Brayton cycle, recovers this thermal energy converting it into electrical power.

The system is a closed loop, whereas the CO_2 is confined at high pressure and, during operation, experiences temperature changes. From the recovered heat, only part of the energy is used to generate electricity while the remaining share is rejected into the environment thanks to a 500 kW_t dry cooler system, which represents the heat sink of the facility.

The key components of HT2C are three heat exchangers (gas cooler, recuperator and heater), one compressor, one turbine and one electrical generator. There are also two by-pass globe motorized valves for the regulation of the compressor and the turbine, and thus in last instance of the system operating point. At design conditions the valves are fully closed. Figure 30 shows a scheme of the sCO_2 system with the related T-s diagram.

Thermodynamic Design

The CO_2 system operates at two different pressure levels (p_{min}, p_{max}). From point 1, CO_2 is compressed from p_{min} to p_{max} using the compressor. At p_{max}, the working fluid is heated first in the recuperator (2-3 = CO_2/CO_2 heat exchanger) and then in the heater (3-4) $CO_2/flue$ gas heat exchanger) where the actual heat recovery takes place. A turbine located at the heater outlet (point 4) converts the CO_2 enthalpy in mechanical power which in part drives the compressor and the remaining one is eventually converted into electricity through the generator.

Figure 30 – sCO_2 unit scheme and T-s diagram

From the turbine outlet (5), the CO_2 is brought back to p_{min} and cooled down to ambient temperature through the recuperator (5-6) and the gas cooler (6-1 $CO_2/water$ heat exchanger). Downstream of the gas cooler, a tank has been considered for storage and control purposes. As such, this component will not alter pressure and temperature of the working fluid during stationary operation.

The thermodynamic design of the sCO_2 unit has been performed through a steady state model set up in Engineering Equation Solver (EES). The model accounts for heat and pressure losses along the pipes that connect the components of the supercritical system. Heat exchanger effectiveness as well as turbine and compressor efficiencies (isentropic, mechanical and electrical) are additional constant input parameters of the model. The

recuperation rate, intended as the ratio between the real and ideal enthalpy, of the regenerative heat exchanger has also been varied to optimise the cycle performance [145].

Thermo-physical properties of carbon dioxide have been calculated using the fluid library of EES while constant values have been considered for specific heats at constant pressure of hot (exhaust gas) and cold (water) sources. Using the input data, isentropic relationships and energy balances across the heat exchangers, the model calculates pressure and temperature values in all the key points in the cycle, before and after each component.

Table 13 summarises the design and maximum operating conditions of the different points of the cycle displayed in Figure 30. Table 14 lists the key components of the HT2C while Table 13 details the performance of the cycle obtained in the thermodynamic analysis as well as the mass flow rate of the working fluid and the dimensions of the turbomachines, also an output of the model.

Table 13 – Maximum operating and design pressure and temperatures at the different points displayed in Figure 30 and cycle performance parameters.

Thermodynamic points	Max/Design op. pressure [bar]	Max/Design op. temperature [°C]
1	75.0/90.0	35.0
2	127.5/140.0	72.9
3	127.5/140.0	284.9
4	127.5/140.0	400.0
5	75.0/90.0	344.3
6	75.0/90.0	81.6
Performance parameters		
Net power output	[kW$_e$]	50.0
Thermal efficiency	[%]	20.0
Exergy efficiency	[%]	33.1
Mass flow rate	[kg/s]	2.06

Table 14 – Key components and type of the HT2C (with reference to Figure 30)

Points in Figure 30	Equipment name in Figure 30	Type
1-2	Compressor	Radial turbomachinery
2-3 and 5-6	Recuperator	Printed circuit heat exchanger
3-4	Heater	Micro-tube heat exchanger
4-5	Turbine	Radial turbomachinery
6-1	Gas cooler	Plate heat exchanger
6-1	Tank	Vessel

Facility Overview

The facility is located in the Centre of Sustainable Energy in Food chains (CSEF) laboratories of Brunel University London. The facility is outdoor. Figure 31.a shows a full view of the area, which includes the heat source (Process Air Heater plus the CO_2/flue gas heat exchanger) and the heat sink located in the top floor (Figure 31.a).
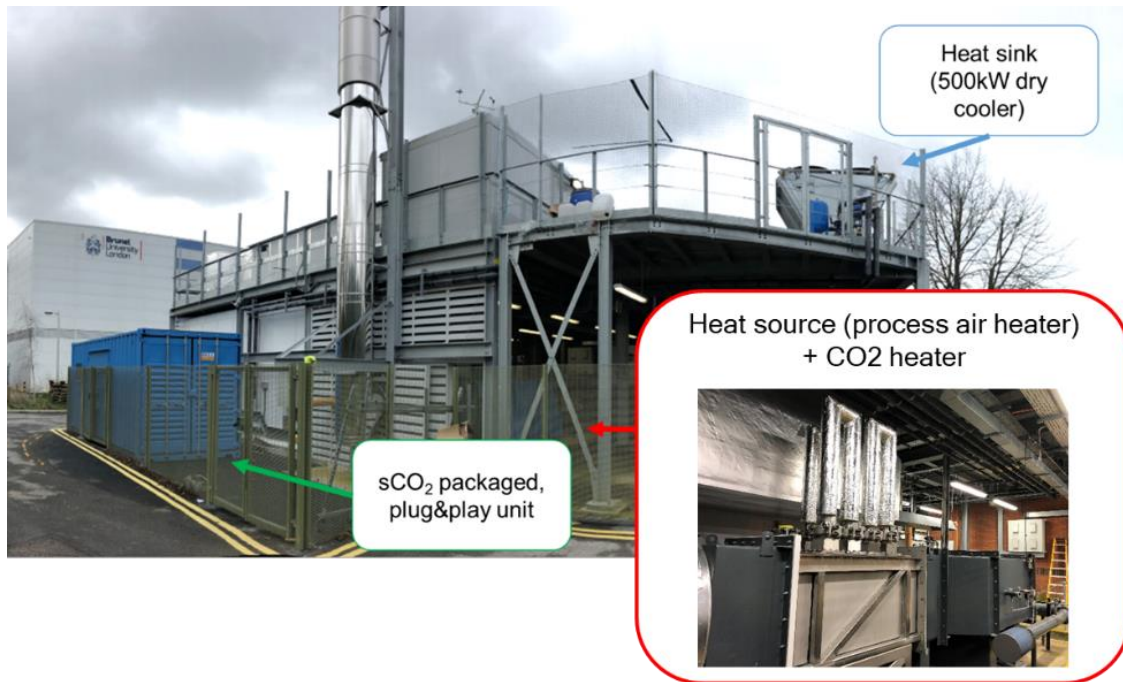
(a)
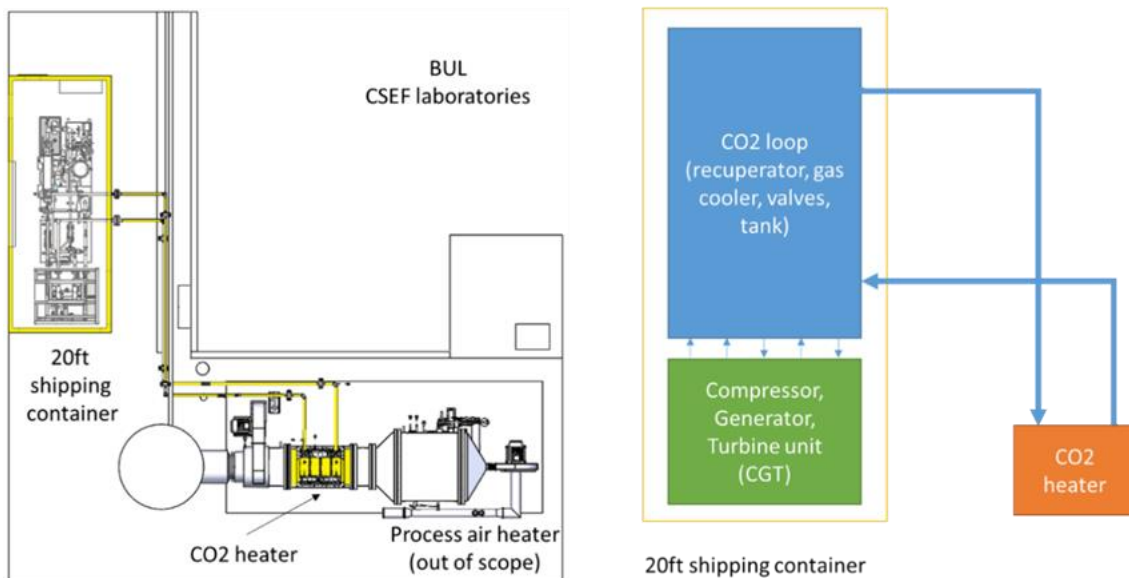
(b)

Figure 31 – Overview of the sCO_2 test facility at Brunel University London (a) and plant scheme and sub-systems (b)

Figure 31b proposes a top view of the facility. Except for the CO_2 heater which is located along the flue gas line of the process air heater, the CO_2 system is fully enclosed in a 20ft shipping container, the blue one showed in Figure 31.a. Inside the container, there are two main subsystems: the CGT unit and the sCO_2 loop. Two 10-meter-long pipes connect the sCO_2 loop in the blue container with the heater.

The CGT unit embeds in addition to the generator, turbine and compressor, some cooling and lubrication ancillaries. On the other hand, the sCO_2 loop gathers the other heat exchangers and ancillaries. The three subsystems are connected together through suitable piping and flanged joints. Figure 32 reports an inner view of the container (Figure 32.a) and displays the main sensors and components through a CAD scheme (Figure 32.b). The facility is operated from a remote location inside the CSEF laboratories using a centralized control and monitoring system developed by SYNESYS.
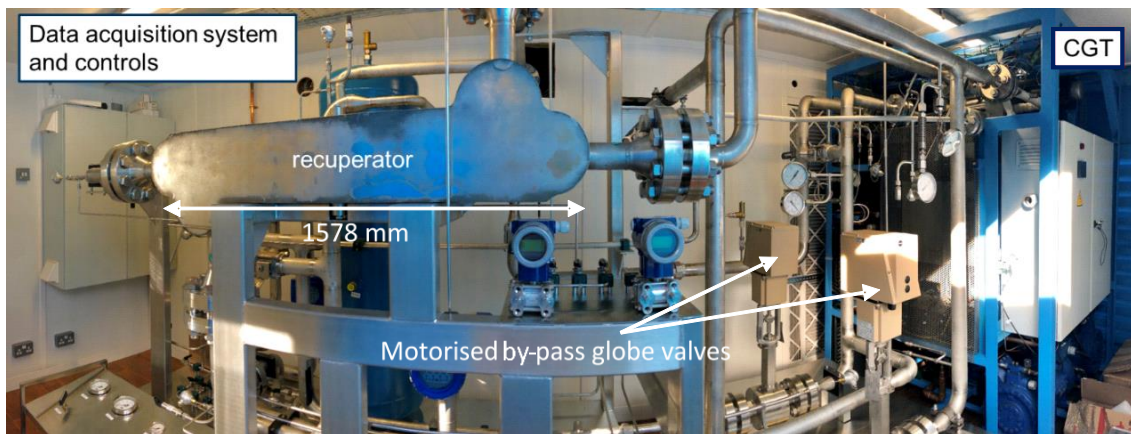
(a)
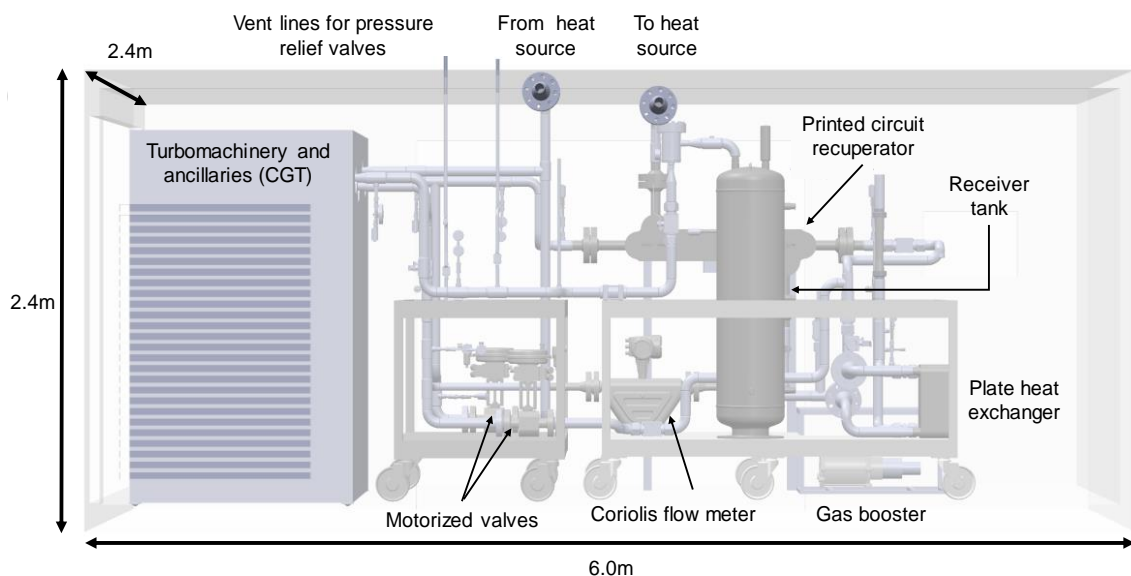
(b)

Figure 32 – sCO_2 container inner view (a) and CAD scheme (b)

4.3 HT2C Facility Assemblies

There are four main sub-system composing the H2TC facility, a Process Air Heater (PAH), which provides the thermal power to the sCO_2 trough a stream of flue gases at high temperature; a Dry-Cooler, a water/air heat rejection system acting as the sink for the sCO_2 gas cooler; a CGT (Compressor-Generator-Turbine) unit, composed by the compressor, turbine, generator and their ancillaries; and the sCO_2 loop, which is the assembly of pipes, valves, sensors and equipment which connects the key components of the system.

Heat Source (Process Air Heater)

The high flexibility of operation is the key feature of the heat source and the whole facility. Inlet conditions to the high temperature test section are controlled with a proprietary system that relies on primary fan speed and flow rate of flue gas as control signals while temperature downstream the process air heater and airflow rate are used as control feedback.

A schematic P&ID of the Process Air Heater, manufactured by Babcock Wanson, is displayed in Figure 33.a. The continuous lines represent the passages for the natural gas and the air while the dashed line represent the control feedbacks used to regulate the main and cooling fan and the gas supply. In particular, the signal from the air flow meter is used to close the control loop of the air mass flow rate (controlled by varying the speed of the main fan), the temperature signal from the thermocouple located at the end of the flame (TH2) is used to close the control loop of the gas supply (which is regulated through the change of the opening position of a ball valve).

Downstream the high temperature recovery section (represented by the CO_2/flue gas heat exchanger), a cooling fan is considered to lower the flue gas temperature through dilution with ambient air and to provide additional pressure rise for the low temperature heat recovery section, which however will not be used in this work.

The temperature signal (TH4) is used to regulate the cooling fan speed and therefore the flow rate of the dilution air. As it is possible to notice from Figure 33, feedback signals of flow (F), temperature (T), pressure (p) and speed (s) are indicated with different colours. The control system to achieve these targets is proprietary. However, all the variables from/to the heater PLC can be accessed through a TCP/IP Ethernet connection.

The high temperature test section has a maximum length of 2000 mm while the cross-section is 500x500 mm with 200mm alkaline earth silicate wool insulation. Figure 33.b and Figure 33.c show a detailed image of the Process Air Heater (PAH) before the installation of the CO_2/flue gas primary heater and provides the geometrical details of the heat exchangers that could be tested in the facility.
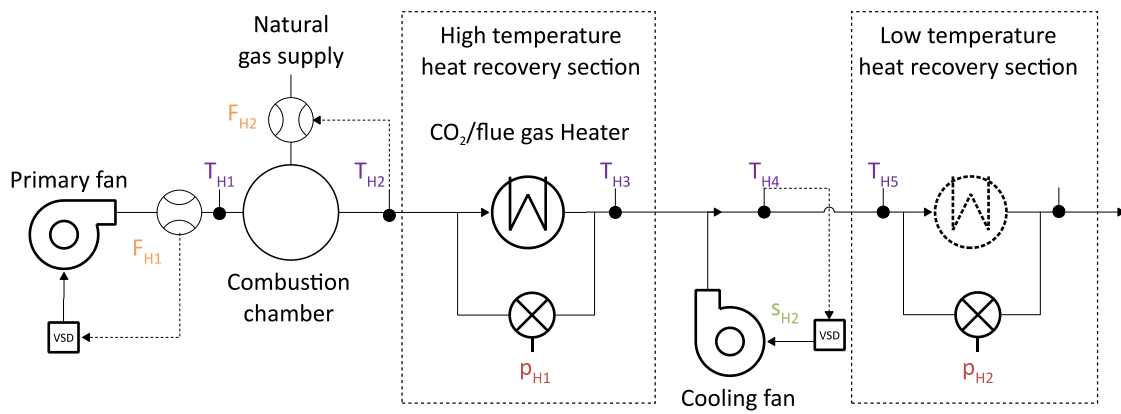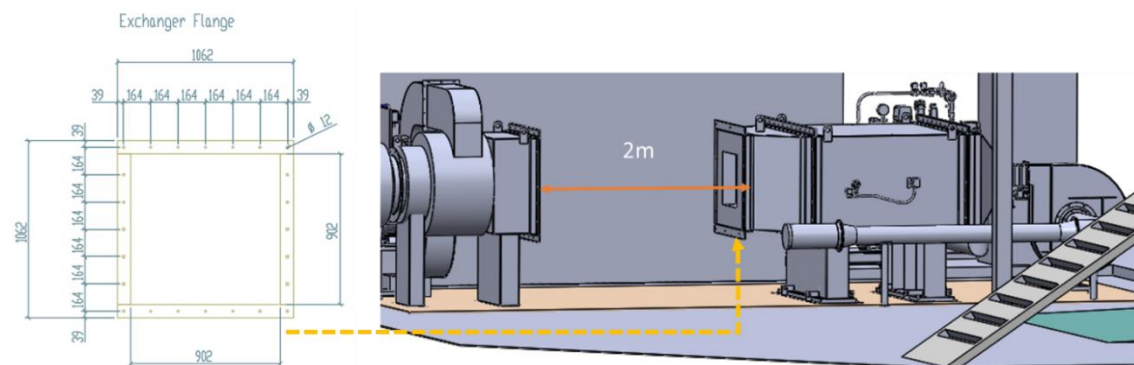
Figure 33 – Process and Instrumentation Diagram (P&ID) of the Process Air Heater (PAH) (a) image of the PAH before the installation of the sCO₂ primary heater (b) and geometrical details of the heat exchangers that could be tested (c).

The heat sink is responsible of rejecting the thermal energy from the heat recovery or heat to power conversion systems that the facility employs. With regards to the sCO₂ heat to power conversion system, a major goal of the cooling loop is also the control of the operating

conditions at the compressor inlet. This secondary loop needs also to be used to heat up the low pressure part of the sCO$_2$ circuit during the startup phase of the facility.

The heat sink is responsible of rejecting the thermal energy from the heat recovery or heat to power conversion systems that the facility employs. With regards to the sCO2 heat to power conversion system, a major goal of the cooling loop is also the control of the operating conditions at the compressor inlet. This secondary loop needs also to be used to heat up the low pressure part of the sCO2 circuit during the startup phase of the facility.

Table 15 summarizes the overall specifics of the heat source.

Heat Sink (Dry Cooler)

The heat sink is responsible of rejecting the thermal energy from the heat recovery or heat to power conversion systems that the facility employs. With regards to the sCO$_2$ heat to power conversion system, a major goal of the cooling loop is also the control of the operating conditions at the compressor inlet. This secondary loop needs also to be used to heat up the low pressure part of the sCO$_2$ circuit during the startup phase of the facility.

Table 15 – Process Air Heater (PAH) specifics

Nominal thermal power	830 kW$_t$
Max air mass flow rate	3600 kg/h
Max working temperature	780°C
Max working temperature (lock out)	800°C
Out Exhaust temperature (cooled)	300°C
Max pressure drop for HT section heat exchanger	70 mbar
Max pressure drop for LT section (future) heat exchanger	10 mbar
Fuel	Natural Gas (G20)
Gas input peak design	83.5 Nm³/h
Gas pressure available	180-200 barg

The P&ID of the system is shown in Figure 34.a. The dry cooler, manufactured by Transtherm, employs variable speed drives for the fans, which allow to change the cooling load provided at the gas cooler. The cooling of the CO$_2$ occurs by means of an intermediate heat transfer loop which connects the dry cooler to the gas cooler. The working fluid used in such intermediate heat transfer loop is a mixture of water/glycol, but the facility allows also to test alternative fluids if needed.

The intermediate heat transfer loop is provided with a variable speed pump which allows to change the mass flow rate of water/glycol flowing to the sCO$_2$ gas cooler and therefore to test the behavior of the gas cooler heat exchanger at different operating conditions, giving an additional degree of freedom to the system.

Degrees of freedom are flow rate and temperature of the water/glycol mixture at the outlet of the dry cooler. Control signals are fans and pump speeds through the variable speed drives. The control system to achieve these targets is proprietary. However, also in this case all the variables from/to the cooler PLC will be accessed through an Ethernet interface with Modbus protocol Figure 34.b shows an image of the Dry-cooler while Table 16 summarizes its specifics.

(a)   (b)
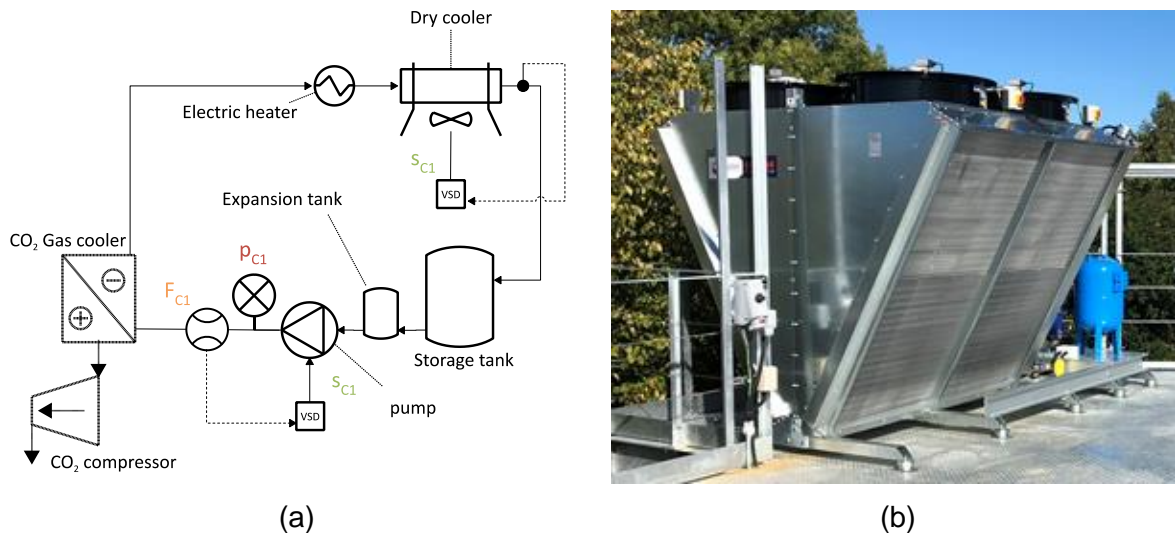
Figure 34 – Process and Instrumentation Diagram of the heat sink (a) and image of the dry cooler (b)

Table 16 – Heat sink characteristics

Total cooling duty	500 kW$_t$
Water on temperature	60°C
Mono-Ethylene glycol	25%
Total airflow at standard conditions	35.7 kg/s
Total fin and tube surface area	850 m^2
Maximum fluid temperature	100°C
Pump motor power	4 kW$_e$
Pump maximum pressure	5.09 bar

Compressor-Generator-Turbine (CGT) Assembly

The CGT assembly, manufactured and designed by Enogia™, is rather complex due to the CO_2 and ancillary loops required for lubrication, drainage and cooling [61]. Different ancillary circuits are indeed required for a safe operation of the compressor, turbine and the generator. The oil line provides the lubrication for the roll bearings, the water circuit allows the cooling of

the devices and the CO_2 draining line allows to extract the leaked CO_2 into the generator cavity, preventing windage losses and eventual generator malfunctioning.

For the CO_2 draining, two piston compressors with plate intercoolers have been considered to inject the drainage, after oil separation, back to the main loop. The selection of a dual-stage intercooled compression has been adopted to limit the drainage recovery temperature at a value suitable for refrigeration compressors (<120°C) and to reduce parasitic electric

Figure 35 shows the operating principle of the only Compressor – Generator - Turbine (CGT) unit. The device employs a one shaft technology linking the rotational speed of the 3 different rotating components: the compressor and the turbine (respectively compressing and expanding the CO_2 fluid in its supercritical state), and the generator (that converts the mechanical motion into electricity). The red arrows represent the streams of CO_2 (inlet and outlet of the compressor and turbine as well as the drainage line) while the blue line represents the water-glycol mixture which is responsible of cooling down the generator coils during the unit operation.

For these reasons, the unit is the core of the sCO_2 heat to power conversion system, especially for its reduced dimensions and elevated revolution speed. Its design involved diverse expertise and it is reported in more detail in [61,146]. The results of the aerodynamic design are summarized in Table 17. Figure 36 shows also the CGT assembly (compressor-generator and turbine plus ancillaries, Figure 36.a), the CGT CE marking plate (Figure 36.b) and the unshrouded compressor and turbine impellers (Figure 36.c), which have been machined from material block and milled to desired shapes derived from the aerodynamic design.
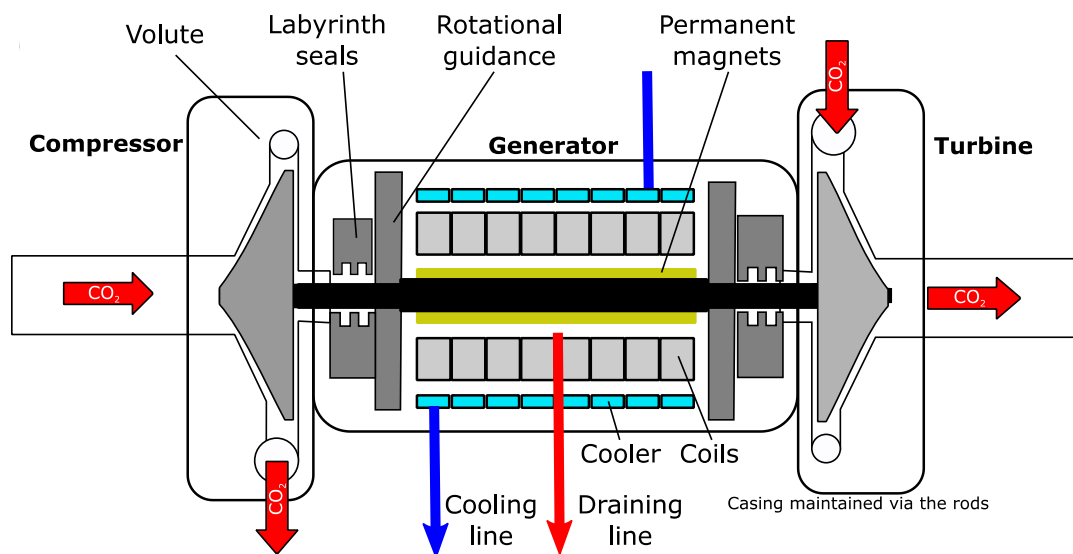
Figure 35 – CGT device schematic operating principle

Table 17 – Compressor and turbine aerodynamic design

		Compressor	Turbine
Rotor	Diameter	55 mm	72 mm
	No. of blades	7	14
Nozzle	No. of blades	11	17
Isentropic efficiency (total-static)		76%	70%
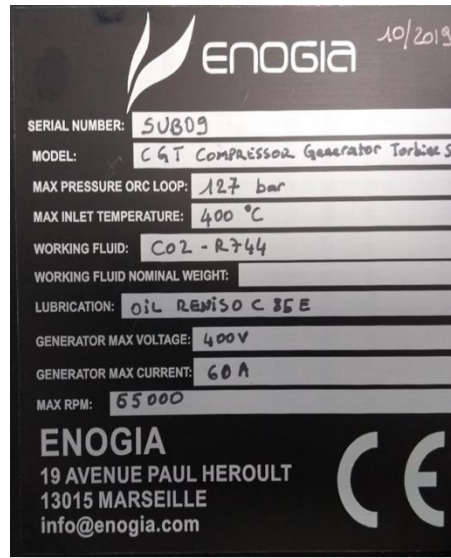
(a)   (b)   (c)

Figure 36 – CGT assembly (a), CE marking plate (b) and images of the unshrouded compressor and turbine impellers (c)

Supercritical CO$_2$ Loop

The sCO$_2$ loop is represented by all the pipes and devices that connect the previous three assemblies and allow the heat transfer between the working fluid and the heat sink and the heat source. Among the main components there are three heat exchangers, a compressor, a turbine, an electrical generator and other auxiliary devices as the gas booster, the tank and the globe valves. The high temperature heat exchanger named "primary heater" enhances the actual heat recovery, while the low temperature one, named "gas cooler" is connected to the heat sink. The intermediate heat exchanger, named recuperator allows the heat transfer from the low to the high-pressure regions of the sCO$_2$ system. The heater is based on a novel micro-tube technology while the recuperator is a Printed Circuit Heat Exchanger (PCHE); the gas cooler, on the other hand, is a plate heat exchanger for refrigeration applications. Figure 37 summarizes the thermodynamic operating conditions of the heat exchangers.

Except for the CO$_2$ heater, all the components have been enclosed in a 20ft standard shipping container. Pipework is in SS316 while flanged connections are of ring joint type (RTJ). This arrangement fulfills the needs of a packaged solution which is required for a high-TRL plug-

and-play compliancy of the developed unit. The connections required are indeed inlet and outlet pipes for heat source and sink, a compressed air supply and electrical connections to the grid. An additional requirement is the compliancy to the Pressure Equipment Directive (PED) (2014/68/EU). Figure 38 shows the CAD representation of the sCO$_2$ loop, the part of the system enclosed in the container is the one on the left-hand side.
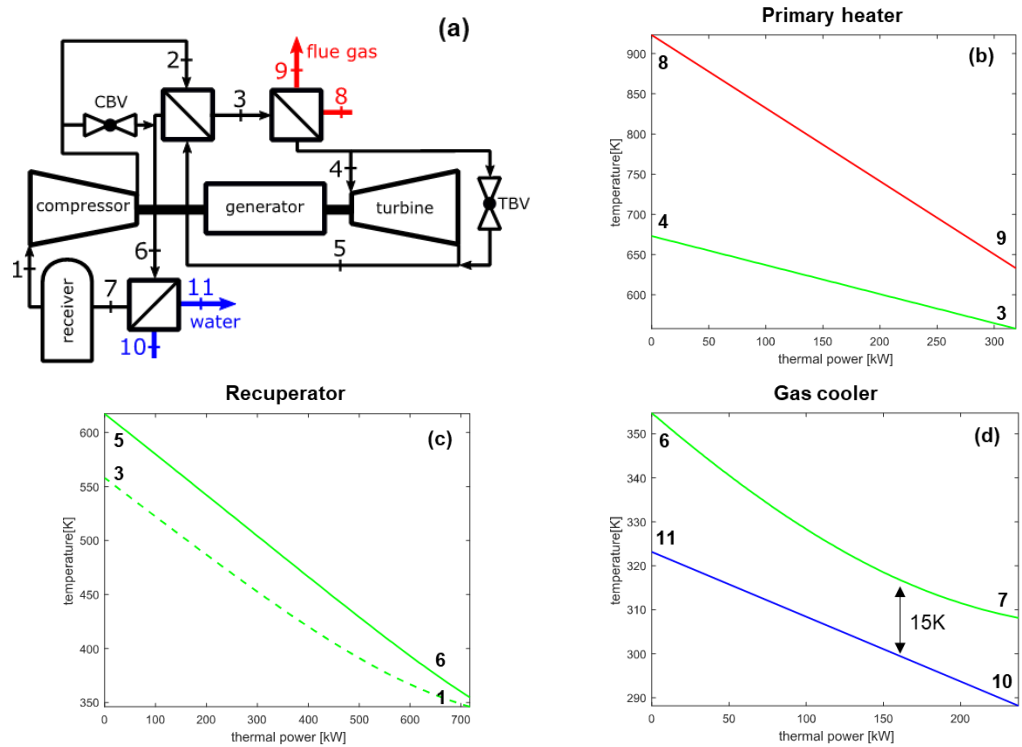
Figure 37 – Design specifics of the Brunel's HT2C facility: sCO$_2$ system layout (a) and Temperature vs. heat load diagrams of primary micro-tube heater (b), printed circuit recuperator (c) and plate gas cooler heat exchangers (d)
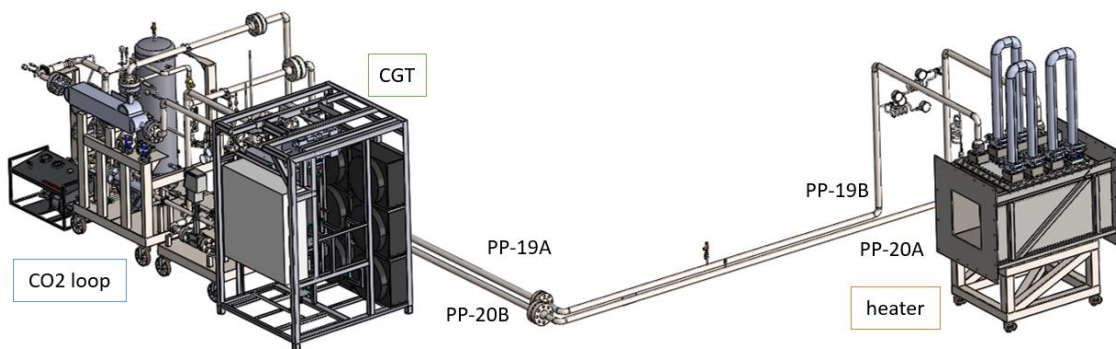
Figure 38 – CAD representation of the sCO$_2$ loop (including the CGT assembly)

Primary Heater

The primary heater is a micro-tube heat exchanger designed and manufactured by Reaction Engines Ltd (UK). The heater is a shell-and-tube heat exchanger in crossflow configuration.

While the flue gases flow in the shell side, the CO_2 flows in the micro-tubes, which are staggered and grouped in four different modules. Each module has more than 1200 micro-tubes. The particular arrangement of the tubes allows to enhance the heat transfer between the CO_2 and the flue gases and at the same time reducing the pressure drops on the flue gas side. A detail view of the heat exchanger is reported in Figure 39.a and additional details on are summarized in Table 18 and in Figure 39.b.

| (a) | (b) |

Figure 39 – View of the primary heater installed in the PAH (a) and CE marking plate (b)

Recuperator

The recuperator of the facility is a 630 kW_t Printed Circuit Heat Exchanger (PCHE) and it has been manufactured by Heatric-Meggitt (UK). Its overall dimensions are 190x1010x184 mm (width x height x length). The heat exchanger employs a series of zigzag shaped semi-circular channels that enhance the heat transfer between the high temperature and low pressure CO_2 stream coming from the outlet of the turbine to the cold one, flowing from the outlet of the compressor. Further details on the device are detailed in Table 19.

Gas Cooler

The gas cooler is a plate heat exchanger (PHE) supplied by SWEP. This kind of technology has been considered because of the substantial lower costs respect to a PCHE. For low capacity systems PHEs represent a valid solution because of their reduced dimensions and investment costs. For high capacity systems, the use of PHEs would be impractical because of the greater dimensions of the gas cooler required. For such cases, PCHE and shell and tube heat exchangers are preferred. Further details of the device are reported Table 20.

Table 18 – Primary heater features

Flow parameters		
Nominal heat duty	kW_t	388.3
Nominal UA value	kW/K	20.3
Flue gas pressure drop	kPa	11
CO_2 pressure drop	kPa	64
Geometrical features		
Tube wall thickness	mm	0.1
Tubes in transverse direction	#	125
Tubes in longitudinal direction	#	10
Tubes in a module	#	1250
Number of modules	#	4
Module width	mm	500.0
Module depth	mm	35.4

Table 19 – PCHE recuperator specifics

Flow parameters		
Nominal heat duty	kW_t	630.0
Nominal UA value	kW/K	20.3
Pressure drop (hs)	kPa	128
Pressure drop (cs)	kPa	120
Geometrical features		
Wetted perimeter	mm	5.14
Hydraulic diameter	mm	1.22
Cross-sectional area	mm^2	1.57
Length	mm	1012.00
Heat transfer area	m^2	12.00
channels per row	#	54
Number of rows	#	42
Type		Zig-zag
Material		SS 316L

Table 20 – PHE gas cooler (CO_2/water) specifics

Flow parameters		
Nominal heat duty	kW_t	237.5
Nominal UA value	kW/K	16.8
Dry weight	kg	52.4
Pressure drops (water)	kPa	8.7
Pressure drops (sCO_2)	kPa	89.1
Geometrical features		
Length	mm	186.00
Width	mm	203.00
Height	mm	425.00
Heat transfer area	m^2	6.21
Channels per pass (water)	#	42
Channels per pass (sCO_2)	#	41
Plates	#	84
Plate material		SS 316L

Gas Booster

The gas booster supplier is Maximator (Germany). The purpose of the gas booster is to act as a circulating device during the start-up of the sCO_2 system, i.e. when the CO_2 needs to transition from liquid to supercritical state. This alternative represents a cheaper option than a CO_2 pump. The operating mass flow rate of the gas booster is roughly the 10% of the one processed by the sCO_2 system at design conditions. Its specifics are summarised in Table 21 and the device is shown in Figure 40.

Table 21 – Gas booster specifics

		Air side	CO_2 side
Maximum inlet pressure	[bar]	10	80
Minimum inlet pressure	[bar]	1	7
Pressure ratio		1:15	
Maximum operating pressure	[bar]	300	
Particles admitted	#	100 (1.0 to 5.0 µm) / 6000 (0.5 to 1.0 µm)	
Oil content		Oil-free	
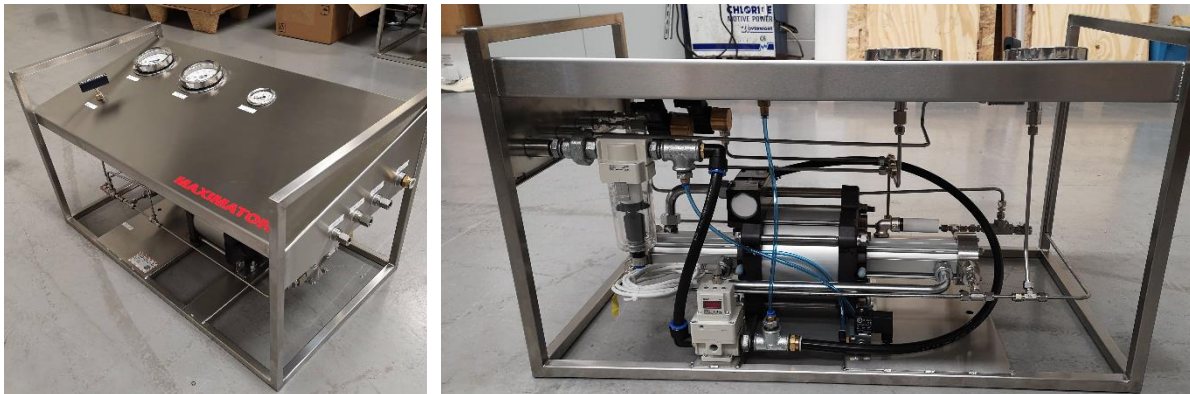
Figure 40 – Upper and lateral view of the gas booster

Globe Valves and Receiver

Two motorised globe valves have been foreseen to bypass compressor and turbine during particular large transient operations or for the system regulation. Figure 41 shows dimensions and picture of the devices while Table 22 summarises their specifics. A receiver has also been placed between the gas cooler and the compressor with the function of adsorbing the thermal expansion of the fluid during the system operation. The overall volume of the tank is 0.165 m^3 and it can be isolated from the rest of the system by means of two ball valves (and thus used for the working fluid storage). A condensing unit and a tape heater are embedded in the receiver to provide additional heating or cooling to the CO_2 during the system startup or shutdown.
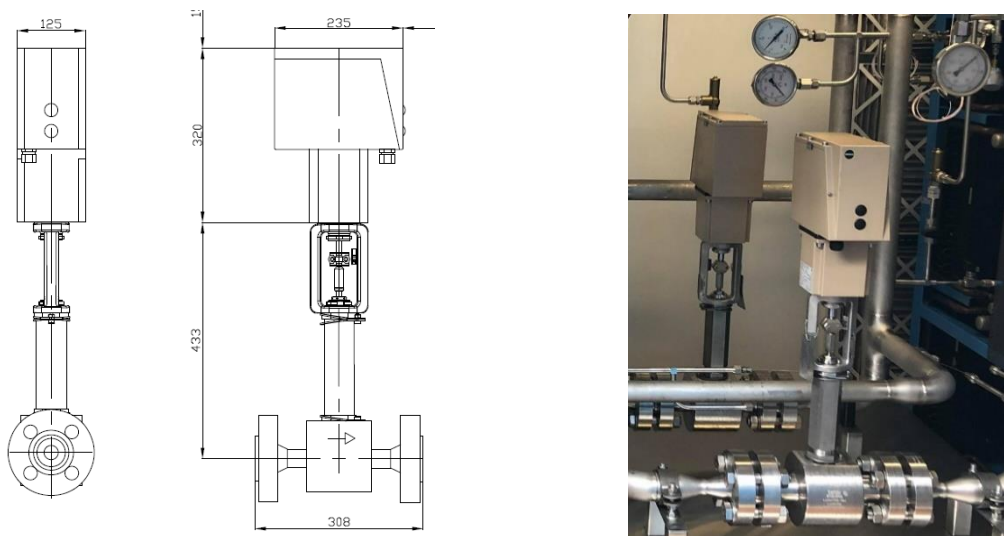
Figure 41 – CAD and picture of the motorised globe valves

Table 22 – Globe valve features

Valve body	Kvs / Cv	4.0 / 5.0
	Valve diameter	25.4 mm
	Flow direction	FTO
	Plug seal	Metal (Leakage class IV)
	Plug type	Parabolic
Actuator	Type of actuator	Electrohydraulic
	Maximum Force	4300 N
	Transit time	0.25 mm/s
	Power supply	24 V / 50 Hz
	Transmitter resistance	1000 Ohm

Pipes, Receiver and Equipment Insulation

The sub-systems described in Section 2 are connected through flanged joints and a series of pipes whose material is SS316L A312, which is suitable to operate with CO_2 since high temperature corrosion issues takes place beyond the maximum allowable working temperature of the system (400°C instead of 550°C).

The piping of the sCO_2 system has been designed and assessed according to the code ASME B31.1 – power piping. As concerns the process pipes, 2" nominal bore has been considered to also minimise the distributed pressure losses. Depending on the operating conditions of the pipe (high/low pressure, temperature), different thicknesses have been employed to optimise the costs.

Besides the process pipes, ancillary ½" pipes of the same material have been used to connect the gas booster and the pressure relief valves while ¼" for pressure signals to the differential

pressure transducers. With regards to flanged joints, ANSI flanges of Ring Joint Type (RTJ) have been used everywhere except for the connections to the micro-tube heater where Techlok flanges have been employed.

Welded joints have been outsourced to specialists (Orbital fabrications Ltd) with approved qualifications in terms of welding procedures and qualifications of the operators. The whole loop has been strength-tested at the pipe fabricator using oxygen free nitrogen up to 107 and 170 bar for the high and low pressure sides of the loop.

Two 10-meter-long pipes connect the heat recovery section with the rest of the loop (Figure 38). Despite the absence of pulsating flow, the combination of high pressure and temperature load required an assessment of their flexibility during operation. As such, a finite element analysis study has been outsourced (Pickering Engineering Design Ltd) and reviewed by the notified body (Lloyd's Register UK) in charge of the design appraisal for the compliance with the Pressure Equipment Directive (PED) 2014/68/EU. The FEA analysis has been carried out taking into account the effect of pipe lagging.

The results of the analysis have been summarized in Appendix A. Based on the recommendations of the pipe flexibility study, the pipes connecting the recuperator outlet to the heater inlet had to be replaced with a higher schedule one (160 instead of 80). The pipe supports had to be replaced as well with some bespoke fixings allowing a correct deformation of the pipes during operation. The layout of the pipe fixings is also reported in Appendix A, together with the results of the pipe flexibility assessment.

To minimize the heat losses in the system, the pipes and the components have been fully insulated. The insulation jackets have been manufactured by Contraflex and are made of an inner layer of carbon fiber material covered by an outer layer of plastic material to minimise wear over time. Further specifications about the insulation jackets are available in Appendix A.

4.4 Instrumentation, Control and Operation of the Facility

The sCO_2 facility is equipped with high-end instrumentation to ensure scientific-grade measurements during the testing. The different assemblies of the facility can be controlled remotely thanks to the centralized control system designed by Synesis. This supervisory controller is based on the IEC 61499 standard [147] and allows the other PLC controllers of the several assemblies of the facility to communicate via Modbus protocol.

Figure 42 shows a schematic view of the interaction between the different Programmable Logic Controllers (PLCs) embedded in the several sub-systems composing the demonstrator. While the data from the sCO_2 loop are directly read through current signals, the ones collected

by the several sensors of the heat source (Process Air Heater), the heat sink (Dry cooler) and the CGT assembly are sent from their PLCs to the centralized control platform through a Modbus protocol.

The data acquired by the controller are stored in a dedicated computer and are transmitted to an online monitoring platform, Einstein, which has been designed by the E4-Experts GmbH (EXP). This online platform allows to evaluate the performance of the system in real time and in a real industrial case could be used to make decisions on the operation of the system (start-up, shutdown or partial loads) accordingly also to external factors as the status of the topping industrial process or the actual cost of the electricity.
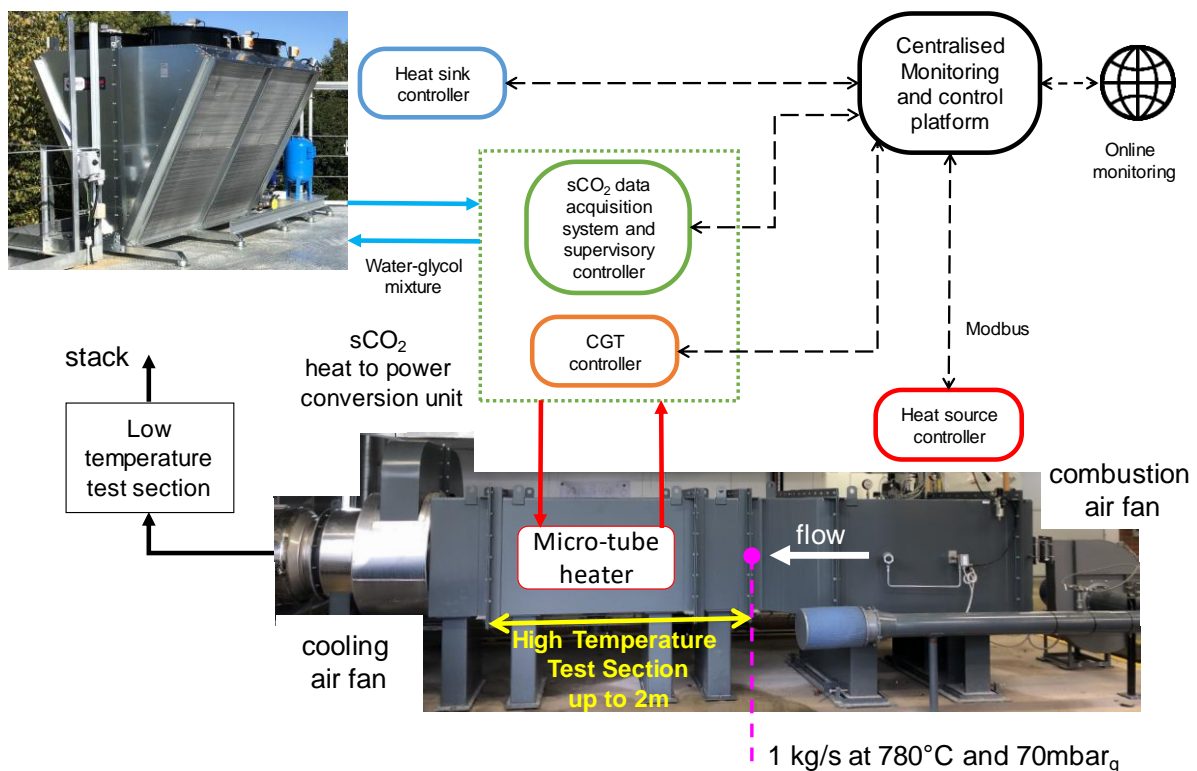
Figure 42 – Overview of the control system of the facility

To enable the storage, elaboration and visualization of data of the facility online, a server has been installed at the CSEF laboratories of Brunel University London. The data storage has been set up by Synesis through a SQL database. A VPN-based remote connectivity has been set up by Brunel University London to comply to the university cyber security regulations. The data workflow is summarised in Figure 43.

All data are displayed on a Graphical User Interface (GUI) designed in collaboration with Synesis, which is structured as follows. All the main data regarding the different sub-systems of the demonstrator are grouped in one single GUI showed in Figure 44. From this interface it is possible to command remotely the several actuators considered in the sCO_2 loop and the

CGT as for instance the motorized globe valves, the tape heater and the condensing unit or the revolution speed of the turbomachines.

More detailed information can be accessed on each assembly GUI, which can be opened by the main one by clicking on the related icons showed in Figure 44. In particular, the "HEAT EXCHANGER" opens the Process Air Heater GUI, the "TURBOMACHINERY" the one of the CGT assembly, while the "Dry Cooler" opens the heat sink interface. Different led have been considered to identify the real-time status of the several actuators and safety instrumentation embedded in the facility.
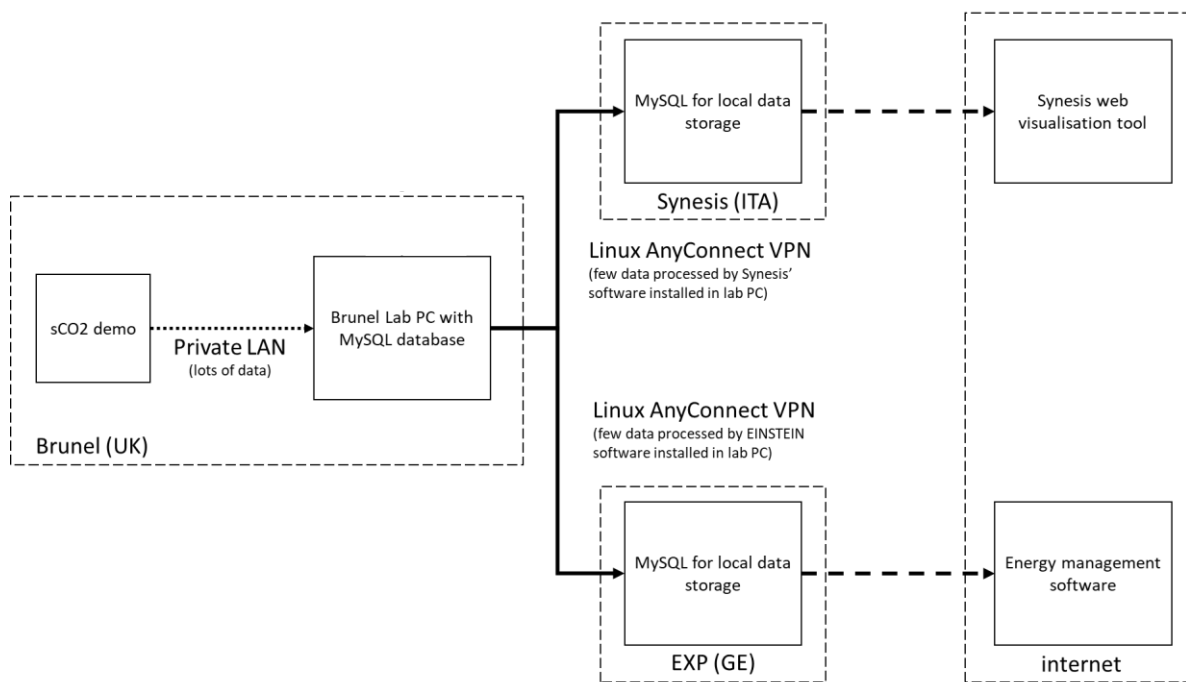
Figure 43 – Data infrastructure

The blue and red rectangular boxes in Figure 44 represent the pressures and temperatures of the system respectively in the main parts of the system and allow to rapidly understand the thermodynamic conditions of the working fluid in the min parts of the cycle.

The green, yellow and pink boxes display instead the revolution speed of the rotating machines, the power output/consumptions and the mass flow rate of the different fluids used in the demonstrator respectively. The trend of the variable displayed by each box can be observed by dedicated and customizable graphic tools.

Sensors and Instrumentation

Figure 45 shows a simplified P&ID of the sCO$_2$ facility. As it is possible to notice, to assess the hydraulic performance of the heat exchangers as well as to properly test the behaviour of the turbomachines, high-accuracy piezo resistive pressure transducers have been adopted in

different locations of the circuit. Differential pressure transducers have been considered to measure the pressure drops along the heat exchangers.
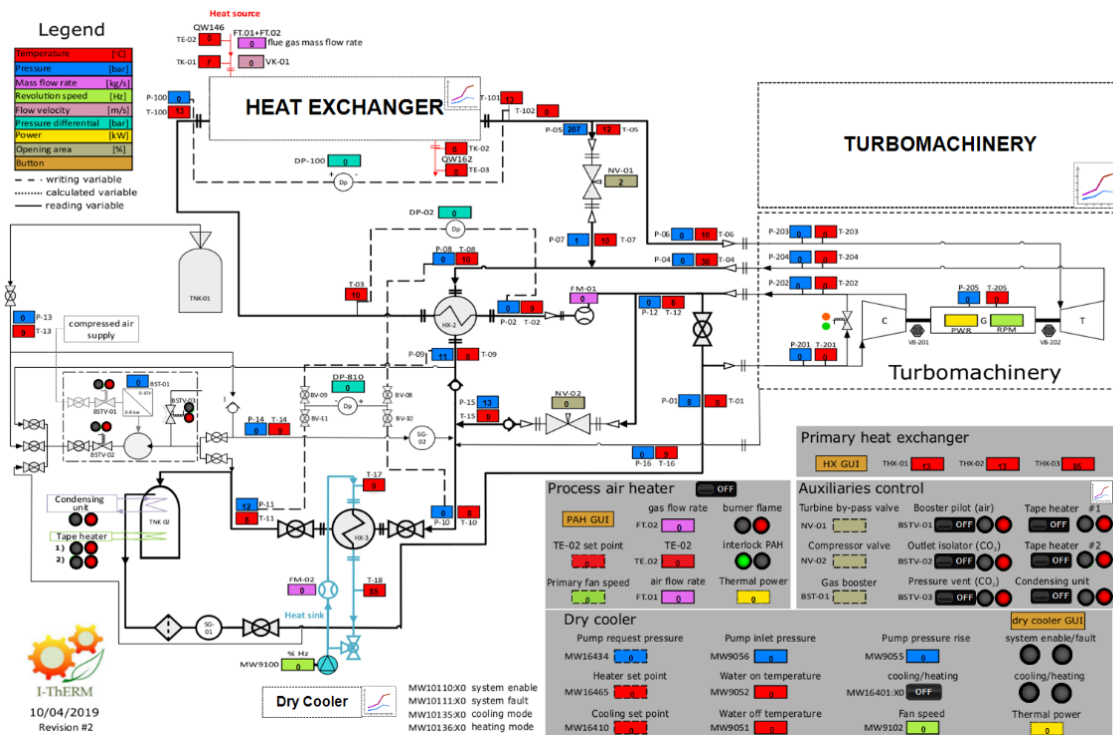
Figure 44 – Graphical User Interface (GUI) of the sCO$_2$ demonstrator

As concerns the temperature transducers, 3-wire resistance temperature detectors (RTDs) type PT100 are considered throughout the CO$_2$ loop except the measurement locations across the compressor where 4-wire RTDs have been selected, to obtain more accurate measurements when the fluid thermophysical properties change more steeply as a function of the fluid temperature. Flue gas temperatures are measured, on the contrary, with K-type thermocouples. A Coriolis gas flow meter is installed downstream of the compressor. The instrument can give in addition to mass flow rate signal, also a measurement of the fluid temperature and density, which is an important variable for the compressor regulation. Table 23 summarizes the transducers embedded in the sCO$_2$ loop as well as their main characteristics as measurement range, type, transmission signal, power supply and accuracy. The sCO$_2$ loop is also equipped with actuators to control the fluid during the different operating conditions of the demonstrator.

In particular, for the gas booster, three valves are used to vent the CO$_2$ from the device (Gas booster-CO$_2$ vent), to open/close the gas booster CO$_2$ line (Gas booster-CO$_2$ outlet) and to open/close the air supply which drives the CO$_2$ pressurization (Gas booster-air inlet). An inverter (Gas booster-main) is used to regulate the air pressure and therefore the CO$_2$ volumetric flow rate and outlet pressure supplied by the device.
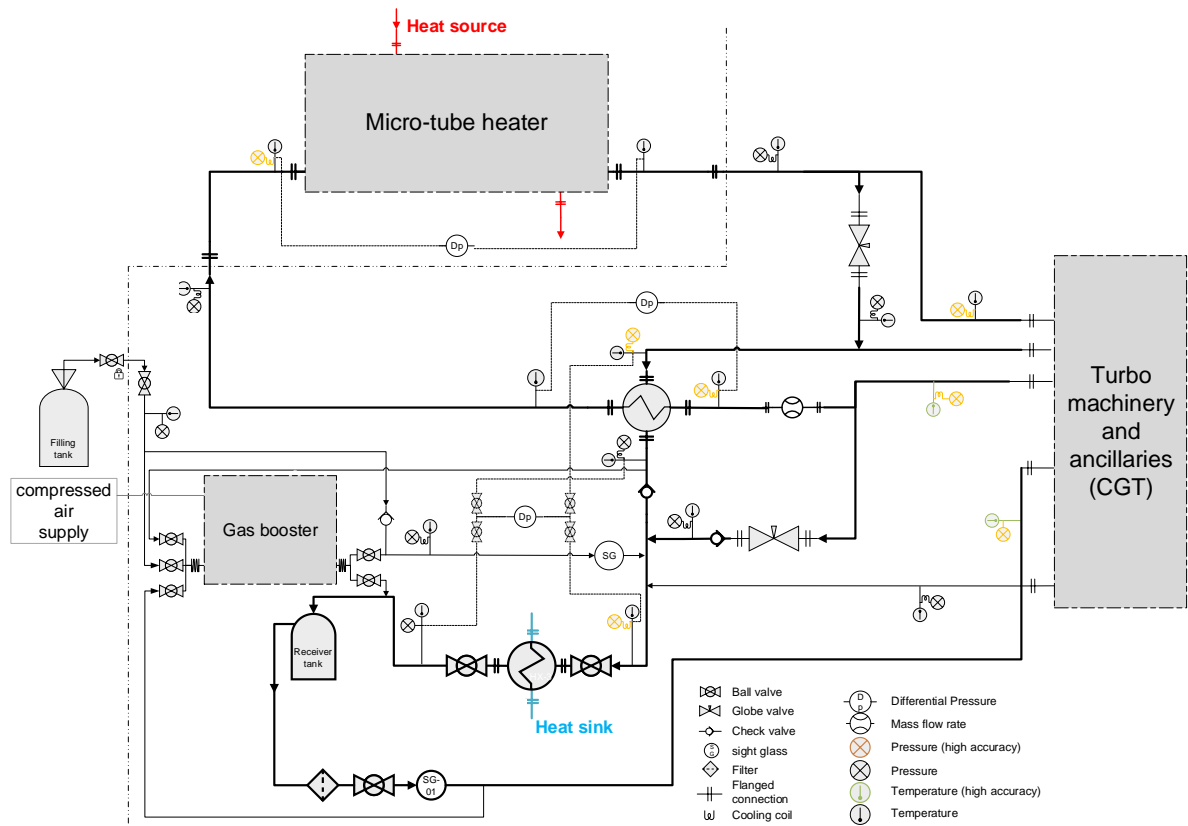
Figure 45 – Simplified Process and Instrumentation Diagram (P&ID) of the facility

Table 23 – Summary of instrumentation in the sCO_2 loop

Sensors	#	wires	Input signal	Power supply	Range	Accuracy
HT RTD (500mm)	9	3	RTD	N/A	-75°C+600°C	0.06°C
LT RTD (250mm)	10	3	RTD	N/A	-75°C+250°C	0.06°C
Prec RTD (250mm)	2	4	RTD	N/A	-50°C+250°C	0.03°C
Gauge pressure	4	2	4-20 mA	9-30 VDC	0-207 barg	0.25% FS
Gauge pressure	5	2	4-20 mA	9-30 VDC	0-138 barg	0.25% FS
pressure	3	2	4-20 mA	9-30 VDC	0-100 barg	0.10% FS
pressure	4	2	4-20 mA	9-30 VDC	0-175 barg	0.10% FS
Differential pressure	3	2	4-20 mA	12-42 VDC	2.5 bar	N/A
Coriolis flow meter	2	2	4-20 mA	no	0-7.9 kg/s	±0.35% RD
Water flow meter	1	2	4-20 mA	no	250 L/min	±0.5% RD
Pitot tube - velocity	1	2	4-20 mA	no	0-100 m/s	±1% RD
Pitot tube - temp	1	2	4-20 mA	no	0-1000°C	±0.15% RD
Thermocouple K	3	2	4-20 mA	9-30 VDC	0-1000°C	±1.5°C

A condensing unit and different silicon mat heaters are used to respectively cool down and heat up the CO_2 during the system startup and shutdown stages. As already mentioned, two actuators regulate the position of the compressor and turbine by-pass valve. Table 24 summarizes the actuators in the sCO_2 loop and their main features.

Table 24 – Summary of controls

Variable description	Type	Unit	Sensor type	Signal
Compressor out by-pass	Integer	%	Globe valve	4-20 mA
Turbine by-pass	Integer	%	Globe valve	4-20 mA
Condensing unit	Boolean	on/off	Switch	switch
Tape heater	Boolean	on/off	Switch	switch
Gas booster - main	Integer	barg	inverter	0-10 V
Gas booster – air inlet	Boolean	on/off	Solenoid v	24 VDC
Gas booster – CO_2 outlet	Boolean	on/off	Solenoid v	24 VDC
Gas booster – CO_2 vent	Boolean	on/off	Solenoid v	24 VDC

Table 25 – Estimated measurement uncertainty at design conditions

Uncertainty	Power	Efficiency
Compressor	2.66%	3.32%
Turbine	0.43%	0.47%
Heater	0.36%	
Recuperator (cold/hot side)	0.36%/0.35%	
Cooler	0.61%	

System Charging, Startup and Shutdown Sequence

To charge the system, CO_2 gas and liquid cylinders at a pressure of 50 bar have been used. The procedure firstly considers two vacuum pumps to remove the air from the circuit. Afterwards, the gas cylinders are used to inject the CO_2 in gaseous phase in the loop through a pressure regulator which sets the pressure at 10 bar, in order to avoid the dry ice formation.

Once the pressure of 10 bar is achieved in the loop, the gas cylinders are replaced with the liquid ones. As the fluid is continued to be injected in the circuit, the pressure of the loop rises until it equalises the one in the liquid cylinder. Usually this equilibrium pressure is 35 bar, even if slight changes can occur depending on the environmental conditions. To additionally charge the system, the condensing unit embedded in the receiver is switched on to lower the pressure of the CO_2 inside the loop. At the same time, the gas booster can be used to further drop the pressure at the circuit charging point allowing to ease the CO_2 filling.

Once the system is completely charged, the startup procedure considers the heating of the fluid up to a safe temperature of 35°C, to ensure that the supercritical phase is achieved in each part of the loop and there are not CO_2 liquid droplets before starting the compressor. To

do so, the water flowing in the gas cooler is heated up to 45°C thanks to the electric heaters embedded in the dry cooler and the water mass flow rate is set to 1.6 kg/s. At the same time the gas booster is switched on to let the CO_2 circulate through the heat exchanger. Either the Process Air Heater (PAH) is started, setting the flue gas inlet temperature at 150°C to avoid excessive thermal shocks for the heater modules.

The mass flow rate of CO_2 provided by the gas booster during this stage can achieve a value between 5% and 10% of the nominal mass flow rate. Because of this reduced flow rate available at this stage, the heating process can require a substantial amount of time.

For a faster startup, additional electric heaters have been placed upon the receiver and in the more remote parts of the circuit, and their switching can be commanded separately by dedicated relays. In addition to these heaters, a heat pump system is being installed and it will operate in parallel with the condensing unit, allowing thus to further speed up the heating of the CO_2 inside the receiver when required.

Once the temperature of 35°C is achieved in all the parts of the system. The CGT is started to the minimum speed of 7000 RPM. This allows to increase the magnitude of mass flow rate of working fluid flowing through the circuit and thus a quicker heating up of the working fluid. Once the CGT achieves the nominal speed of 60000 RPM through a maximum acceleration rate of 100 RPM per second, the PAH inlet temperature is increased in steps of 5°C per minute up to the nominal temperature of 650°C. During this process, the heaters in the dry cooler are turned off and the cooling of the CO_2 is ensured by the operation of the dry cooler fans.

From nominal operating conditions, the shutdown procedure considers in this order: the decrease of the flue gas inlet temperature down to 150°C with a cooling rate of 5°C per minute, the shutdown of the PAH, the deceleration of the CGT revolution speed from the nominal value of 60000 RPM down to 7000 RPM and its consequent shutdown, and, as last, the shutdown of the dry cooler, to ensure that during the previous operations residual thermal energy of the CO_2 is dissipated.

4.5 Summary

This Chapter has presented the design and layout of a state of the art high-temperature facility suitable for testing heat recovery and heat to power conversion equipment at pilot scale. The facility comprises a 830kW$_t$ gas fired process air heater and a 500 kW$_t$ water dry cooler as heat sources and sink respectively. There are two test sections for heat exchangers testing at low and high temperatures and a centralized control and monitoring system based on Modbus protocol to supervise the whole facility.

The facility serves to provide heat gain and rejection to a 50kW$_e$ supercritical CO_2 unit based on a simple recuperated Joule-Brayton cycle. The core of the sCO$_2$ unit is a compressor-generator-turbine unit (CGT) composed of a single shaft turbomachinery. The experimental rig is packaged in a 20ft container and has been CE marked according to the Pressure Equipment Directive (PED) (2014/68/EU).

High accuracy instrumentation based on RTD temperature transducers, Coriolis flow meter and piezoresistive pressure transducers have been used to ensure a reduced uncertainty in the calculation of main importance quantities as for instance thermal and electrical power provided and generated respectively to and from the demonstrator.

However, still challenging remains the measurement of thermophysical properties of the fluid in some critical parts of the system, as for instance for the compressor isentropic efficiency, where a preliminary uncertainty analysis showed a maximum uncertainty of 2.3% mostly due to the inlet pressure measurement. The facility presented has been considered as reference for the development of a one-dimensional computational fluid dynamic (CFD) model which will be presented in the next chapter.

5. Numerical Model of the Supercritical CO$_2$ System

5.1 Introduction

A numerical model of the facility described in Chapter 4 has been developed to support the design activities carried out during the system construction. This allowed, after the model validation, also to test new ideas for the system optimization and control during several operating conditions without the same commitment of resources and time that such trials would require if done experimentally. For these objectives, more detailed models respect to the thermodynamic ones presented in Chapter 3 are required, given the several simplifying assumptions introduced.

On the contrary, Computational Fluid Dynamics (CFD) techniques are more suitable and wide adopted in the engineering practice, because of their accuracy in predicting complex fluid dynamic phenomena. Currently, the results produced by models developed with such methodologies are reliable in certain cases even as the experimental testing (i.e. the direct solution of the Navier-Stokes equations (DNS) for turbulent flows).

However, despite the huge progresses in numerical methodologies, exponential growth in computing power and dramatic cost reduction for computing hardware, still the use of these approaches for energy systems poses a trade-off to balance complexity, time and cost of the calculations. For instance, higher order models, as three dimensional (3-D) Computational Fluid Dynamics (CFD) ones, are very accurate but still require substantial investments in computational resources with sometimes limited additional outcomes than more simplified approaches.

When energy conversion systems are considered, indeed lower order models can be successfully employed to provide useful insights of the unit behaviour with a reduced simulation time. Furthermore, their low complexity allows to perform an extensive number of simulations for optimization studies or for control studies. For these reasons, in this thesis a one-dimensional (1-D) CFD model for the 50 kW$_e$ simple regenerated sCO$_2$ Brayton has been developed. The model has been implemented in GT-SUITE^{TM}, a commercial software platform capable of performing 1-D CFD analyses.

Firstly, the theoretical principles behind the one-dimensional approach adopted are detailed and afterwards, a more detailed description of the methodology is presented with reference to the system modelled. The approach proposed, despite being extensively employed in the automotive simulation field, it has not been applied so far in the literature to stationary heat to power conversion systems. The approach is highly replicable, and it can be applied also to other energy conversion systems.

5.2 Modelling Methodology

GT-SUITE[TM] is based on a one-dimensional formulation of Navier-Stokes equations and on a staggered grid spatial discretization. According to this approach and with reference to Figure 46, each system is discretized into a series of capacities such that manifolds are represented by single volumes while pipes are divided into one or more volumes. These volumes are eventually connected by boundaries. The scalar variables (pressure, temperature, density, internal energy, enthalpy, etc.) are assumed to be uniform in each volume. On the other hand, vector variables (mass flux, velocity, mass fraction fluxes, etc.) are calculated for each boundary.
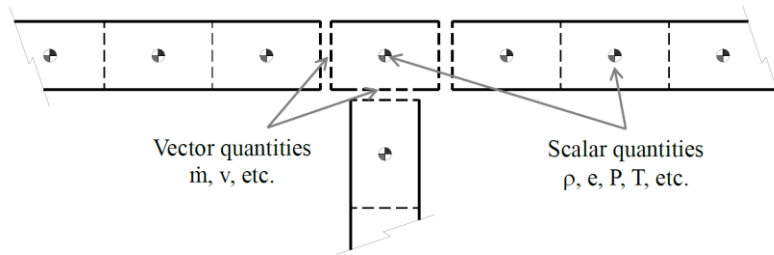
Figure 46 – One-dimensional staggered grid formulation (courtesy of Gamma Technologies) [148].

The continuity equation (33) in a given capacity takes into account the algebraic sum of all the inflow and outflow contributions from the neighboring capacities that occur through the boundaries that characterize the reference element [148].

$$\frac{dm}{dt} = \sum_{i=1}^{B} \dot{m}_i \qquad (33)$$

The momentum equation (34) neglects body forces and takes into account the algebraic sum of momentums through the boundaries, pressure forces and dissipations due to friction and pressure drops [148]. In pipes, the latter two terms are respectively related to distributed (i.e. due to surface finish) or concentrated (i.e. due to bends) pressure losses.

$$\frac{d\dot{m}}{dt} = \frac{1}{dx}\left(\sum_{i=1}^{B}(\dot{m}_i u_i) + dpA - 4f\frac{\rho u|u|}{2}\frac{dxA}{D} - K\left(\frac{1}{2}\rho u|u|\right)A \right) \qquad (34)$$

The energy equation (35) states the conservation of total internal energy, i.e. the sum of internal energy and kinetic energy [148]. This formulation applies when using the explicit solver, as in the case of standalone machines; on the other hand, in the solution of circuits, implicit solver is used and the energy equation becomes an enthalpy balance. Neglecting variations of potential energy, for a given capacity the rate of change of total internal energy

depends on the volume capacity variations, on the enthalpy fluxes and on heat transfer phenomena. The first term on the right-hand side of equation (35) relates to the cell volume, thus it is of paramount importance in positive displacement machines.

$$\frac{d\left(me\right)}{dt} = -p\frac{dV}{dt} + \sum_{i=1}^{B}\left(\dot{m}_i\left(e_i + \frac{p_i}{\rho_i}\right)\right) - \zeta A\left(T_{fluid} - T_{wall}\right) \tag{35}$$

When the conservation equations are solved through an explicit method, a 5th order Runge-Kutta integration scheme is usually employed. With this approach, primary solution variables are mass flow rate, density, and internal energy. In particular, to calculate mass and energy in a given volume at the following time step (that needs to satisfy the Courant condition for numerical stability), continuity and energy equations are firstly used and involve the reference volume and its neighbors. With the volume and mass known, the density is calculated yielding density and energy.

Numerical issues that can be typically found in models which use the discretization approach are solved by the software with several damping and relaxation factors which can be also modified by the user. These coefficients are set to smooth these numerical errors arising in the solution of the mass, momentum and energy balance equations in the iterative calculation. The drawback of this approach is the higher computational time required to perform the simulations.

Using a dynamic-link library (DLL) of the NIST REFPROP database [142] embedded in the software package, the solver iterates on pressure and temperature until they satisfy the density and energy already calculated for this time step.

5.3 System Description

Figure 47 shows the model scheme developed in GT-SUITE^{TM}. As it is possible to notice from the figure, the heat recovery takes place through the micro-tube heat exchanger (primary heat exchanger in Figure 47) having flue gases on the hot side and the working fluid of the system, CO_2 in the supercritical state, on the cold side.

After being pressurized in a single-stage radial compressor, the working fluid is heated up in the printed circuit recuperator and its temperature is further increased by the heat recovery process. Afterwards, it is expanded in a turbine, where the useful energy conversion process takes place. After the expansion, the working fluid is cooled down in the recuperator and then in the gas cooler, which uses water as heat sink.

A receiver is eventually positioned between the gas cooler and the compressor such that thermal expansion during start-up or large transients can be absorbed. As showed in Figure

47, the turbine and the compressor are in a single-shaft configuration, which means that a part of the power generated by the expansion is used to drive the compressor, while the excess is converted in electricity by the generator fitted on the shaft.
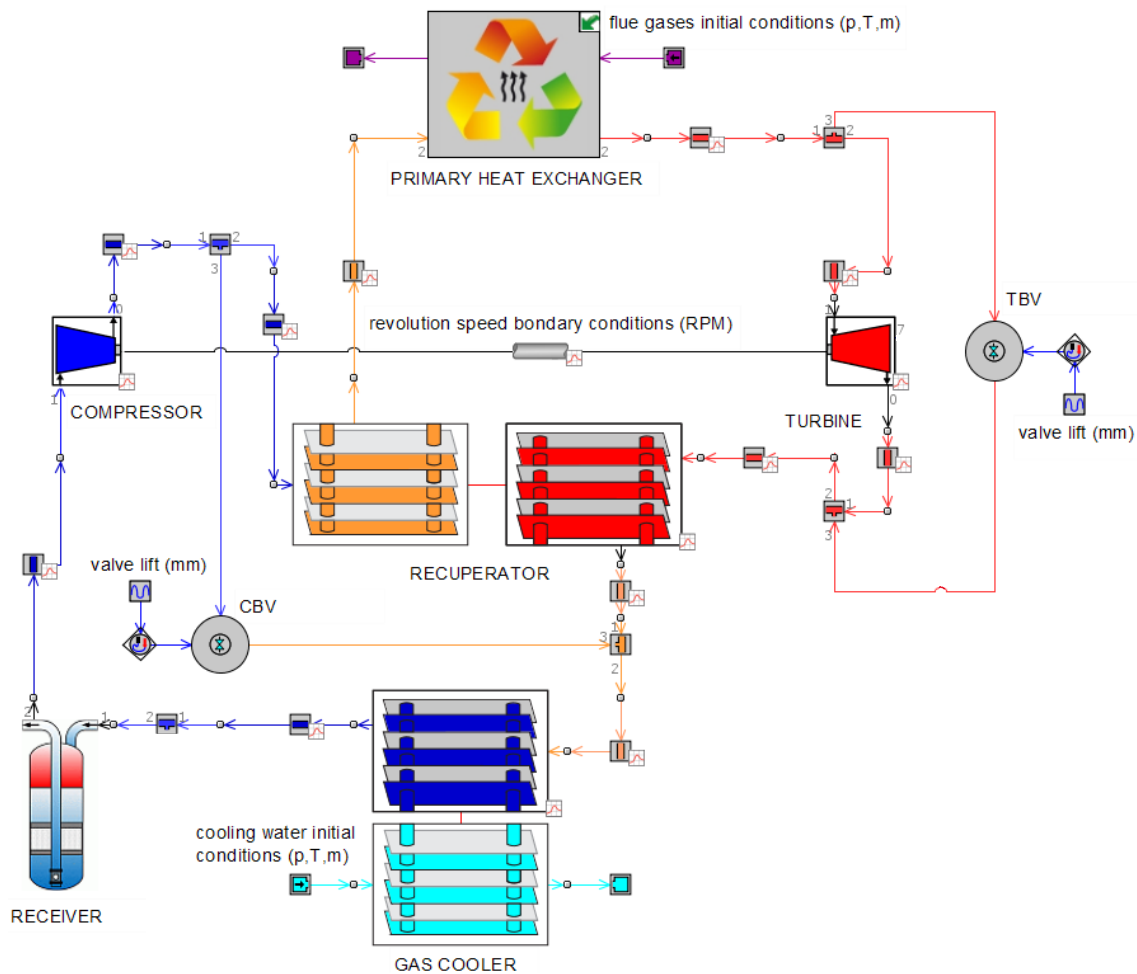
Figure 47 – sCO$_2$ system model developed in GT-SUITE^{TM}.

Two motorised compressor and turbine by-pass globe valves (CBV and TBV respectively, Figure 47) have been foreseen to control the system at nominal, startup, shutdown and emergency operations. The first one is located between the compressor outlet and gas cooler inlet; the second one is installed between the turbine inlet and outlet (Figure 47). Finally, connections between these devices are made through piping sub-models. The full modelling methodology adopted for each of these components is detailed in the next sections. Some boundary and initial conditions are needed to solve the set of equations describing the one-dimensional representation of the unit model. For the specific case, the revolution speed of the compressor-generator-turbine set as well as inlet temperatures and flow rates of hot and cold sources are required (as highlighted by lowercase captions in Figure 47).

5.4 Heat Exchangers

Heat exchangers are a fundamental part of energy conversion systems since they usually contain the largest amount of working fluid volume circulating in the unit, affecting the thermal inertia of the system and in turn its promptness and performance. It is then important to catch these aspects when modelling such devices. One dimensional models allow to do it with a reasonable computational effort.

In general, according to their geometrical features, the hot and cold sides of the heat exchangers are approximated as 1-D channels with an equivalent length and cross-sectional area. Both sides are therefore interconnected through convective connections to a thermal mass, which accounts for the thermal inertia of the heat exchanger and considers its real material properties.

To account of the thermo-fluid property change, the channels and the thermal masses are discretized along the flow direction in a certain number of sub-volumes. Consequently, following the previously detailed 'staggered grid approach' [148], the 1-D Navier-Stokes equations are numerically solved to calculate the mass flow rates, pressures and total enthalpies of the hot and cold flows at the boundaries of the channels' sub-volumes. The other thermodynamic scalar quantities are computed through a dynamic-link library of the NIST Refprop database [142] and assumed constant in the whole sub-volume domain.

In order to solve the energy equation, the computation of the local heat transfer coefficients between the heat exchanger walls and the cold and hot channels respectively is required. Local heat transfer coefficients between the heat exchanger walls and the cold and hot channels respectively is required. For both the refrigerant and the non-refrigerant side, data provided by the manufacturers or from more complex models (as for instance 3-D CFD ones) are employed to calculate the best fitting coefficients of the Nusselt-Reynolds (Nu-Re) correlations for the equivalent 1D networks [148].

Both the performance data provided by the manufacturer and the ones retrieved by more complex models are related to several operating conditions of the heat exchangers. Different mass flow rates of the two working fluids processed are considered, to span a wider range of Reynolds number and improve the accuracy of the model predictions also in off-design. The pressure drops across the heat exchanger are computed using a modified version of the Colebrook relationship reported in Equation (36).

In this expression, f is the Fanning factor calculated using the explicit approximation of the Colebrook equation proposed by Serghides [149], which is valid for the turbulent regime ($Re_D>2100$), the quantities A and B, which can be calculated using Equation (37) and (38),

account for the roughness of the heat exchanger channels Ra, and C_1 is the calibration coefficient used to resemble the performance data provided by the heat exchanger supplier.

$$f = C_1 \left(\frac{1}{4} \left(4.781 - \frac{(A - 4.781)^2}{B - 2A + 4.781} \right)^{-2} \right)$$ (36)

$$A = -2.0 \log_{10} \left(\frac{Ra/D}{3.7} + \frac{12}{\mathrm{Re}_D} \right)$$ (37)

$$B = -2.0 \log_{10} \left(\frac{Ra/D}{3.7} + \frac{2.51A}{\mathrm{Re}_D} \right)$$ (38)

Nevertheless, this general modelling methodology is common for the all the three heat exchangers considered in the sCO_2 unit, the gas cooler, the recuperator and the primary heater, some aspects differ from case to case and it will be described in more detail in the following paragraphs.

Primary Heater

The primary heat exchanger employs a micro-tube technology to enhance the air-sCO_2 heat transfer. As for a shell and tube heat exchanger, the high pressure sCO_2 flows in the micro-tubes while the flue gas in cross flow in the shell side.

As it is possible to notice by its 1-D schematic representation showed in Figure 46.a, the heat exchanger is divided in four modules composed by a certain number of micro-tubes of 2 mm of outer diameter. Figure 48.a shows also a cross-sectional view of the modules, which displays the typical arrangement of the micro-tubes.

The tube spacing (Figure 48.b) in the transverse direction (X_p) and in the longitudinal one (X_n), 4 mm and 3 mm respectively, are specifically designed to enhance heat transfer without increasing excessively the pressure drops on the flue gas side. Table 18 summarizes the detailed geometrical features of the heat exchanger.

Figure 48.c shows on the contrary the model of the heat exchanger developed in GT-SUITE™. Each module is represented by a pre-defined template which considers as input the geometrical features of the module as tube diameter, thickness, wetted perimeter, cross sectional area and number of parallel tubes. Because of the 1D modelling approach adopted, the tube staggered configuration cannot be reproduced in the model. To take in account of its effect on the pressure drops and heat transfer, multiplying coefficients have been used to resemble the performance data provided by the manufacturer.

97

CO2 OUT

CO2 IN

500 mm

FLUE GAS IN

FLUE GAS OUT

A······A

HX MODULE 1

HX MODULE 2

HX MODULE 3

HX MODULE 4

1500 mm

(a)

X_p

D

X_n

Cross-section A-A

(b)

CO2 outlet
(p,T)

CO2 inlet
(m,p,T)

Flue gas inlet
(m,p,T)

Flue gas outlet
(p,T)

1st MODULE   2nd MODULE   3rd MODULE   4th MODULE
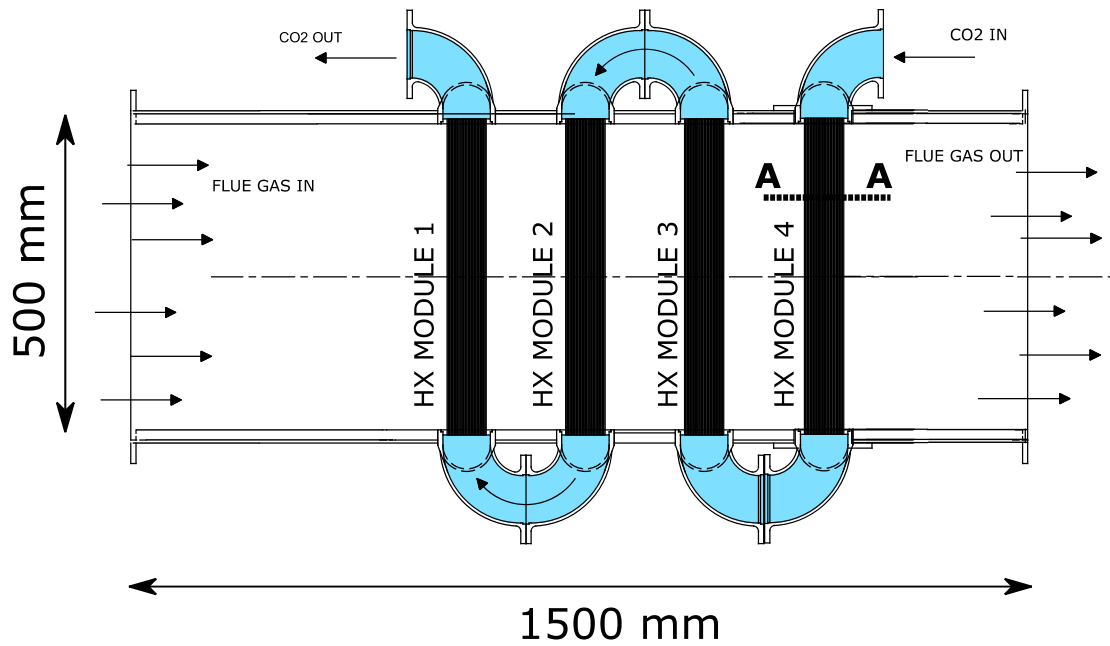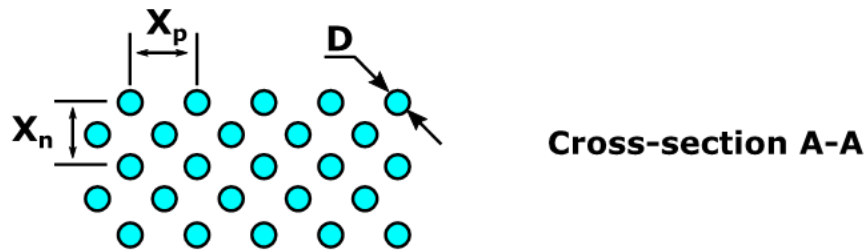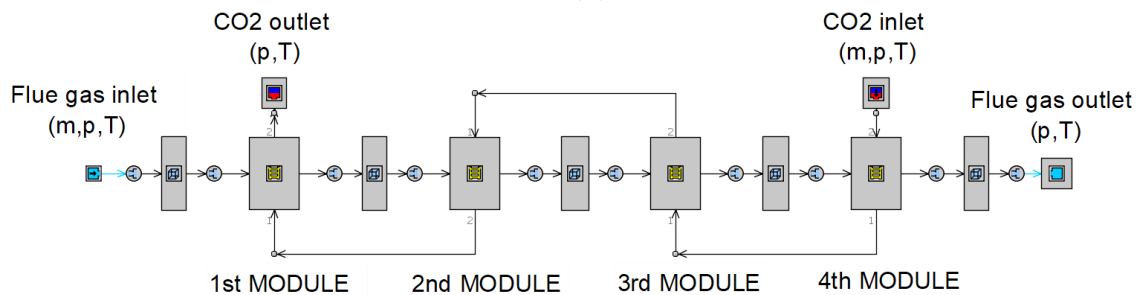
(c)

Figure 48 – Schematic 1-D representation of the Primary heater and cross-section of each module (a) and related model in GT-SUITE^{TM} (b)

To set these coefficients a calibration procedure for different Reynolds number has been carried out. The results are reported in Table 26 which compares the Re-Nu curve interpolation of the different data provided by the manufacturer against the ones obtained by using the Gnieliski [150] and Dittus-Boelter [151] heat transfer correlations.

The boundary conditions of the model are, for the flue gas side, the inlet pressure, temperature and mass flow rate as well as their composition; for the sCO_2 side, inlet pressure, temperature and mass flow rate are specified. The pressure and temperature of both the sCO_2 and the flue gas are set in the model in case of backflow conditions. Table 27 reports the flow parameters

of the heat exchanger at the design point and the model settings, including the number of sub-volumes in which each module is discretized and the time constant of the heater (identified as the ratio between its metallic thermal capacity over its conductance, UA).

Table 26 – Heat exchanger calibration data (cal) and comparison with model interpolation (Int), Gnieliski (Gn) and Dittus-Boelter (DB) correlations

		Re=20000		Re=25000		Re=30000	
		Nu	Err%	Nu	Err%	Nu	Err%
Heater	Cal	73.0	N/A	92.2	N/A	106.8	N/A
	Int	73.4	1.3	92.5	0.3	107.2	0.4
	Gn	75.7	2.7	90.9	1.4	101.9	4.8
	DB	80.1	8.7	96.5	4.4	108.6	1.6

Table 27 – Primary heater nominal operating conditions and model settings

sCO_2 side		
Inlet pressure	MPa	12.75
Inlet temperature	°C	272
Outlet temperature	°C	450
Mass flow rate	kg/s	2.1
Flue gas side		
Inlet pressure	MPa	0.103
Inlet temperature	°C	650
Outlet temperature	°C	300
Mass flow rate	kg/s	1
Model settings		
Number of sub-volumes (per module)	#	25
Time constant	s	1.55

Recuperator

The recuperator of the sCO_2 system is a 630 kW_t Printed Circuit Heat Exchanger (PCHE). The PCHE comprises 42 stainless steel 316L metal plates, chemically etched to 54 semi-circular channels per plate which are bonded together through a process thermal diffusion. The hot and cold side channels are stacked alternatively on top of each other, and nozzles divide the fluid stream in the several channels.

These channels are equally spaced and with identical geometrical features. As such, the model of this heat exchanger can be substantially simplified by considering a series of elementary heat transfer units composed of a pair of channels surrounded by solid substrates and periodic boundary conditions. A calibration procedure can thus be used afterwards to eventually take in account of geometrical features that cannot be considered by a 1D modelling approach. Table 19 summarizes the geometrical features of the PCHE channels as well as the heat exchanger material.

In order to assess the scientific soundness, i.e. potential and limitations, of the modelling methodology for such heat exchanger, a benchmark against results from higher order models (3-D RANS CFD) is presented. In particular, the comparison between 1-D and 3-D CFD results is carried out with reference to an elementary heat transfer unit of a PCHE recuperator.

Afterwards, a regression analysis has been used to minimize the error between the data provided by the manufacturer and the predictions given by the chosen heat transfer and pressure drop correlations.

3-D Approach

The symmetry axis of the elementary PCHE unit is located in the middle of the semi-circular channel cross-section. With reference to Figure 49.a, the computational domain is composed of half hot channel (depicted in red), half cold channel (depicted in blue), and surrounding stainless steel substrate (depicted in grey). The periodic boundary conditions, which refer to the heat transfer rates between the channels, are set on the top and bottom surfaces of the elementary heat transfer unit.

The Reynolds number was found to be higher than 10,000 in both the cold and hot sides of the heat exchanger, confirming turbulent flow, which was modelled using the standard k-ε approach with standard wall factions. The buoyancy and entrance effects were also considered. The thickness of the first near-wall mesh was selected to ensure the dimensionless distance from the wall y^+ in the range between 15 and 50.

To account for the variation of the thermophysical properties of the CO_2 due to variations in temperature and pressure, the NIST Refprop database was coupled with the ANSYS™ FLUENT 17.0 CFD solver through a Dynamic-Link Library (DLL) [142]. The SIMPLEC algorithm [152] was used to implement the coupling between pressure and velocity, while the second order upwind scheme was applied to discretize the convection terms. A grid independence study was carried out using different mesh sizes listed in

Table 28. The computational grid selected for the model, shown in Figure 49.b, comprised of 1.8 million cells.

(a)   (b)
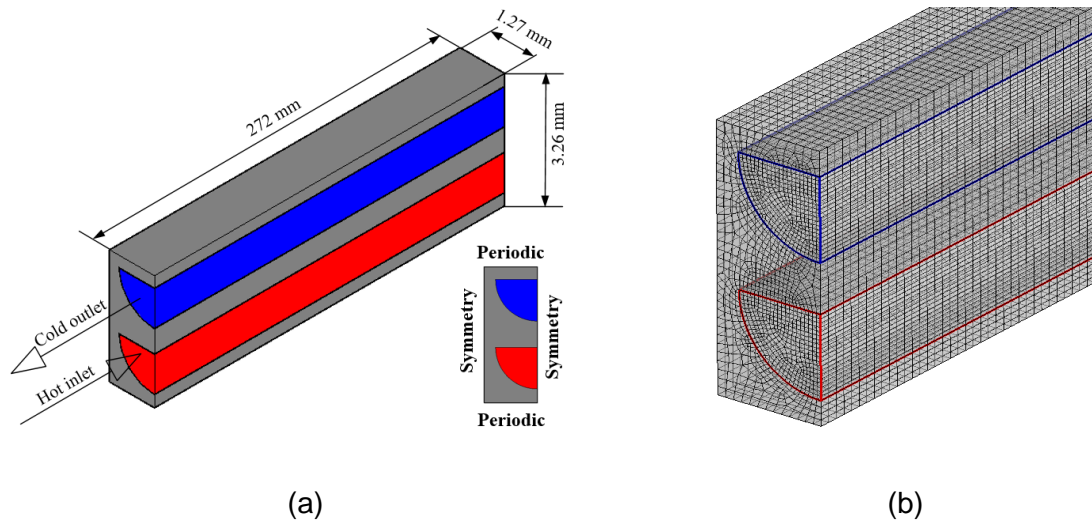
Figure 49 – Elementary heat transfer unit of a PCHE (a) and computational grid (b)

Table 28 – Grid sensitivity study of the 3-D model

Number of cells	cs dp [kPa]	hs dp [kPa]	cs htc [W/(m²·K)]	hs htc [W/(m²·K)]
352658	3.946	8.177	2065.3	2091.1
704898	3.837	8.276	2032.1	2078.1
1843953	3.763	8.342	1997.6	2052.6
3686753	3.749	8.355	1982.8	2037.5

1-D Approach

The 1-D model of the elementary heat transfer unit developed in GT-SUITE™ is shown in Figure 50. The semi-circular flow channels of the PCHE were considered as circular channels of an equivalent hydraulic diameter. In particular, the hot and cold channels (red and blue colours respectively) have been discretized along the flow direction in a fixed number of sub-volumes (80 per channel), as shown in Figure 50.

Each flow channel block is connected through a convective connection (grey circle denoted by the letter "h" in Figure 50) to a discretized metallic mass, which represents the metal portion of the elementary PCHE unit delimited by the two sub-volumes of the channels (the grey square with a red point in the centre, Figure 50). This metallic mass represents the discretized thermal inertia of the heat exchanger, which is calculated from the geometrical features and the material properties of the metallic substrate (i.e. the thermal conductivity and the density) specified as inputs. The discretized thermal masses, shown in Figure 50 with grey boxes, are all interrelated by means of conductive connections to take into account the conductive heat transfer between them.
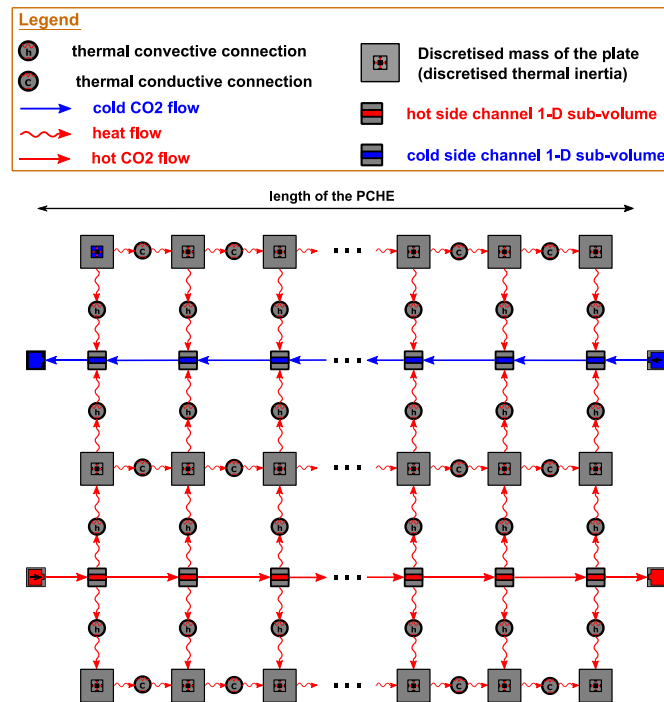
Figure 50 – 1-D model of the PCHE elementary heat transfer unit

Table 29 – Boundary conditions used for the models comparison

Boundary conditions	Cold side	Hot side
Mass flux [kg/m^2]	509.3	
Inlet temperature [°C]	100	400
Outlet pressure [bar]	150	75

Further inputs to the model are the mass flux of the working fluid (which is equal for both the cold and the hot side of the heat exchanger), and the inlet temperatures and pressures of the hot and the cold sCO$_2$ flows (Table 29). Either for the 1-D case, a grid independence study has been carried out and it is summarized in Table 30. The discretisation length used for the simulations is 3.4mm.

Table 30 – Grid sensitivity study for the 1-D model (cs=cold side, hs=hot side, htc=heat transfer coefficient, dp= pressure drop, DL= Discretisation Length)

DL [mm]	cs dp [kPa]	hs dp [kPa]	cs htc [W/(m^2·K)]	hs htc [W/(m^2·K)]
13.6	4.024	8.931	2238.7	2174.6
6.8	4.093	8.799	2254.9	2163.0
3.4	4.110	8.761	2257.4	2161.5
1.7	4.114	8.746	2258.6	2161.0

To make the comparison consistent, both 1-D and 3-D simulations have been performed assuming the same boundary conditions reported in Table 29 for fluid mass flux, temperature and pressure. The full CFD 3-D simulation case required 24 hours to run, whilst a test run for the 1-D simulation only required 5 seconds. This fact confirms why 1-D modelling approaches are suitable for transient simulations and complex optimization studies of multi-component systems. The higher computational time needed by the 3-D approach is not only due to the larger computational domain but also to the DLL interface with the Refprop database.

Due to the high computational time and cost of the 3-D simulations, this benchmarking study considered a channel length for the PCHE of only 272 mm. This choice led to a very large approach temperature in the results, which is an operating condition not representative of an actual regenerative process. However, this did not influence the results comparison of the two modelling approaches.

Figure 51.a shows the comparison of the temperature profiles for the two sCO_2 flows in the PCHE as a function of the channel length. The temperatures along the channel obtained by the 1-D simulation match well that from the 3-D simulations, with a maximum relative error of 5% for the hot side and 8% for the cold side of the heat exchanger.

The cumulative pressure drops along the channel length computed by the two models are shown in Figure 51.b. Because the channels are in counter-flow, in Figure 51.b the channel length of 272 mm represents the outlet of the hot side channel and the inlet of the cold side one. While the channel length of 0 mm represents the outlet of the cold side channel and the inlet of the hot side one. For this reason, the cold and hot side cumulative pressure drops are both 0 at a channel length of 272 mm and 0 mm respectively (Figure 51.b).

The highest difference between the comparison of the results of the two simulations is shown at the outlet of the channels (0 mm for the cold side and 272 mm for the hot one), where the pressure drops predicted by the 1-D model are 4.0 kPa and 8.9 kPa for the cold and hot side respectively. For the 3-D model, cold and hot side pressure drops are 3.8 kPa and 8.3 kPa respectively.

The differences are mainly due to the empirical correlations used in the 1-D simulation for the friction factor were based on circular tubes (since the modelling approach approximates the semi-circular channel cross-section with an equivalent circular one), while the 3-D simulations consider semi-circular channels. These conclusions agree with the findings in [153]; this study indeed shows that, for the same hydraulic diameter, friction factor in semi-circular channels is about 4.5% smaller than the one in circular tubes.

The estimation of the local heat transfer coefficients with the two models is presented in Figure 52. With reference to the middle cross-section (136 mm from the channel entry cross-section), the local heat transfer coefficient of the cold side was determined to be 1.90 kW/(m^{2}K) with the 3-D model and 2.16 kW/(m^{2}K) with the 1-D model.

For the hot side, the value of the local heat transfer coefficient was predicted at 2.04 kW/(m^{2}K) with the 3-D model and 1.98 kW/(m^{2}K) with the 1-D model. The difference in the predictions of the local heat transfer coefficients with the two models is due to the correlation for circular tubes for the channels used in the 1-D case, which can contribute to an error in the calculation of the Nusselt number of up to 9% [153], and the different calculation procedure for the local heat transfer coefficient by the two models.

In fact, the 3-D model computes the heat transfer coefficient from the geometrical properties of the channel and the velocity and thermal field for each cross section. The 1-D model does not account for the effect of the temperature difference between the channel wall and the one of the bulk fluid and large differences between the two temperatures can give rise to increased errors in the prediction [154]. The 1-D model, unlike the 3-D one, also does not account for the entry effects to the heat exchanger and this, as can be seen in Figure 52, can lead to further differences in the predictions.

(a)   (b)
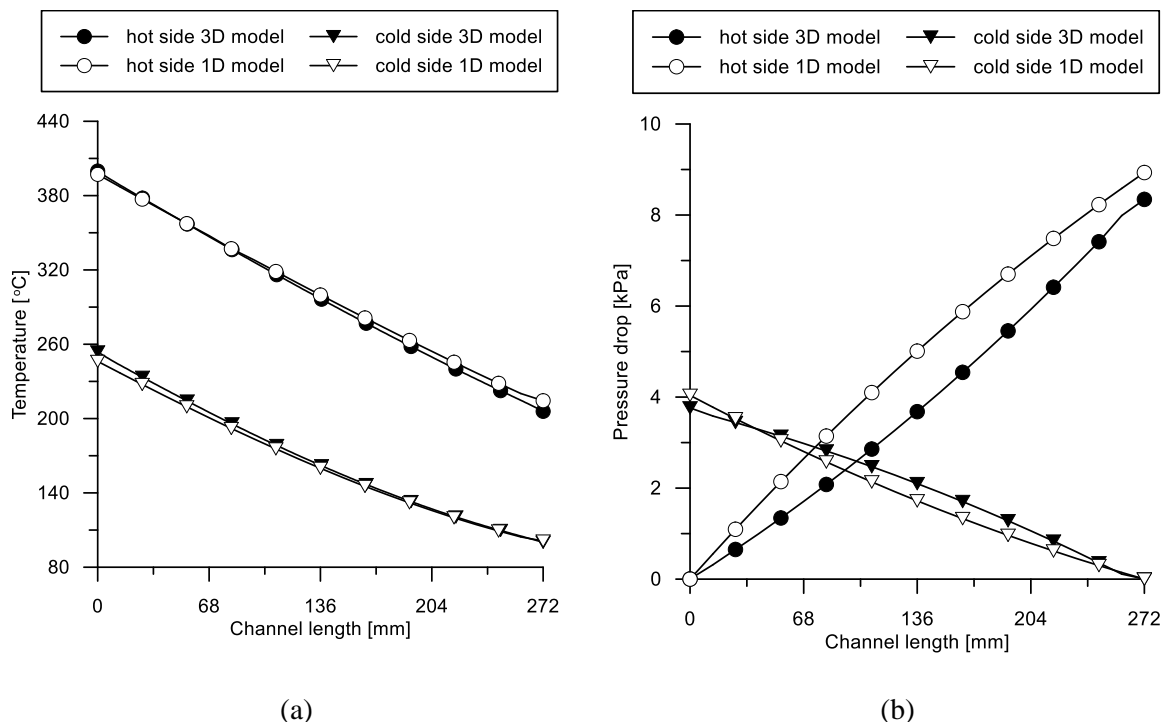
Figure 51 – Comparison of temperatures (a) and cumulative pressure drops (b) along the PCHE channel resulting from 1-D and 3-D simulations

Despite the different local heat transfer coefficients calculated by the two models, the predictions of the global performance of the heat exchanger is very close. For the same inputs, the computed outlet temperature of the hot side of the heat exchanger is 213.4°C and 205.8°C for the 1-D and 3-D models respectively and for the hot side 246.2°C and 253.9°C respectively, a difference of only 4% and 3%.

The percentage deviation of the overall heat transfer coefficient was found to be 2%, and a value of 7% and 5% were found for the pressure drops across the hot and cold sides respectively. These prediction differences are quite small, and much smaller than experimental uncertainties [154], and thus it can be concluded that the 1-D model can be used with confidence for fast simulation of the overall performance of the heat exchanger.
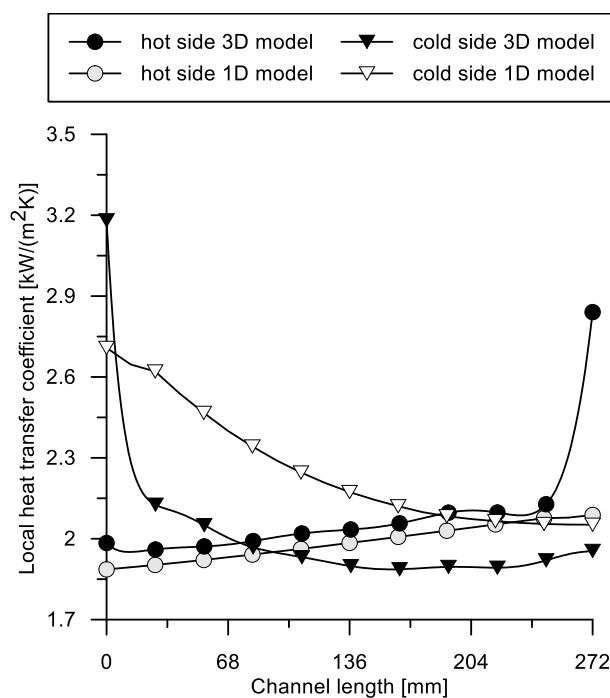
Figure 52 – Comparison of local convective heat transfer coefficient along the PCHE channel from 1-D and 3-D simulations

Full Scale PCHE Model Development and Calibration

After the validation of the methodology a regression analysis has been used to minimize the error between the data provided by the manufacturer and the predictions given by the chosen heat transfer and pressure drop correlations. Heat transfer and friction multiplier coefficients have been adjusted to also account for the additional pressure drops and the higher heat transfer rates for the zig-zag shape of the channels, whose effects cannot be reproduced by considering just a one-dimensional modelling approach. Values for C_1 in Equation (36) after calibration was greater than one, namely 1.1. This magnitude is in agreement with the theory since rough walls lead to greater pressure drops.

The calibration data provided by the manufacturer relate to five different working points of the PCHE which are not referred to particular operating conditions of the heat exchanger or the sCO_2 system (Table 31). Nonetheless, they have been chosen to appreciate the variability of the heat transfer performance. This approach justifies the selection of mass flow rate and temperature as exploratory variables rather than pressures. Mass flow rate has a direct impact on the Reynolds number while temperature variations reflect their greater influence on changes in the thermophysical properties of the working fluid compared to pressure variations.

Table 31, which refers to the calibration procedure of the PCHE, shows that the predictions of the model are in agreement with the manufacturer's data. The results of the pressure drop calculations show the highest error to be 5.7% on the cold CO_2 flow for the 4th off-design case (working fluid mass flow rate of 2.62 kg/s, at 125% of the design value).

Table 31 – Off-design operating conditions of the full scale PCHE (cold side (cs) and hot side (hs))

	Design		Off-design #1		Off-design #2		Off-design #3		Off-design #4	
	1-D	OEM	1-D	OEM	1-D	OEM	1-D	OEM	1-D	OEM
mass flow rate [kg/s]	2.06		1.57		2.09		2.09		2.62	
cs inlet temperature [°C]	72.9		72.9		87.5		62.0		72.9	
cs inlet pressure [bar]	75		75		75		75		75	
hs inlet pressure [bar]	125		125		125		125		125	
hs inlet temperature [°C]	344.3		344.3		344.3		344.3		344.3	
hs pressure drop [kPa]	131	130	80	79	146	145	123	122	205	202
hs outlet temperature [°C]	81.4	80.5	79.5	78.6	99.4	99.7	67.7	66.6	83.6	82.7
cs pressure drop [kPa]	119	120	73	74	138	139	104	106	183	184
cs outlet temperature [°C]	283.0	284.9	285.4	287.2	293.2	294.5	267.7	269.3	280.1	282.3
heat load [kW$_t$]	629	631	484	485	588	586	682	684	789	793

Average errors are 1.1% and 2.2% for the hot and cold sides respectively. Also, the outlet temperatures and the heat loads computed, present negligible deviations compared to the manufacturer's data. The average errors for the cold and hot side outlet temperatures are 2.2% and 1.2% respectively, and the error for the overall heat transfer across the heat exchanger is only 1.2%. Table 32 resumes the nominal operating conditions of the PCHE as well as the number of sub-volumes in which the heat exchanger is discretized and the time constant of

the recuperator (identified as the ratio between its metallic thermal capacity over its conductance, UA, see Table 19).

Gas Cooler

The gas cooler employs a more conventional technology, Plate Heat Exchangers (PHEs), compared to the recuperator and the primary heater, given the less harsh operating conditions (lower pressure and temperature). Because the widespread use of these heat exchangers in low capacity waste heat recovery systems (i.e. ORC or TFC units) [155], for the refrigeration sector [156] and in general for a wide range of stationary and mobile heat transfer applications [13], a pre-defined template has been used to model the device.

In particular, a simulation tool provided the manufacturer has been used to retrieve several operating points of the plate heat exchangers [157]. These operating points have been obtained by varying several model inputs, such as the refrigerant mass flow rate; the inlet temperature of the refrigerant; and the inlet and outlet temperatures of the cold and hot sources.

The output data were instead the temperatures and the quality of the CO_2 at the outlet of the heat exchanger; the cooling water mass flow rate required; and the pressure losses on both sides. These quantities have been eventually entered into the plate heat exchanger template of GT-SUITE^{TM} to calculate the best fitting coefficients of Nusselt-Reynolds (Nu-Re) correlations for both the refrigerant and the non-refrigerant side. These correlations are eventually used to compute the heat transfer coefficients along the equivalent one-dimensional passages with whom the heat exchanger channels are approximated [148].

The heat exchanger channels, whose geometry is specified by the user, are discretized in a finite number of sub volumes (reported in Table 33) following the staggered grid approach detailed in the section 5.2. To set the channel geometry, the main geometrical features of the PHE must be inserted in the template as input as well as the material used to manufacture the heat exchanger plates. Table 33 summarize the geometrical features of the PHE selected as well as the main flow parameters of the heat exchanger and the main model settings.

Since the CO_2 is cooled down in this heat exchanger close to critical conditions, if the PHE is operated in off-design (meaning that the cooling load provided is higher than the one required by the CO_2 stream eventually processed), the condensation of the fluid may occur. To predict the phase change, the formation of vapor bubbles or liquid droplets is addressed by evaluating the fluid density in each sub volume, while the extension of the two-phase area is computed following the vapor Rayleigh-Plesset formulation [158], reported in Equation (39).

$$p_b - p_\infty = R\frac{d^2R}{dt^2} + \frac{3}{2}\left(\frac{dR}{dt}\right)^2 + \frac{4\upsilon}{R} + \frac{2\sigma}{\rho R} \tag{39}$$

Where p_b and p_∞ are the bubble and fluid pressure respectively, ρ is the fluid density, R is the radius of the bubble, υ is the fluid viscosity and σ is the surface tension. If the phase change occurs, the Gnieliski correlation has been used to predict the heat transfer [148].

Table 32 – Recuperator nominal operating conditions and model settings

sCO$_2$ cold side		
Inlet pressure	bar	127.5
Inlet temperature	°C	72.9
Outlet temperature	°C	284.9
Mass flow rate	kg/s	2.1
sCO$_2$ hot side		
Inlet pressure	bar	75.0
Inlet temperature	°C	344.3
Outlet temperature	°C	81.4
Mass flow rate	kg/s	2.1
Model settings		
Number of sub-volumes	#	50
Time constant	s	7.25

Table 33 – PHE gas cooler nominal operating conditions and model settings

sCO$_2$ side		
Inlet pressure	bar	75.0
Inlet temperature	°C	80.0
Outlet temperature	°C	35
Mass flow rate	kg/s	2.1
Cooling water side		
Inlet pressure	MPa	3.0
Inlet temperature	°C	15.0
Outlet temperature	°C	50.9
Mass flow rate	kg/s	1.6
Model settings		
Number of sub-volumes	#	50
Time constant	s	2.38

$$\overline{Nu_L} = C_2\left(\frac{(f/2)(\mathrm{Re}-1000)\,\mathrm{Pr}}{1+12.7(\mathrm{Pr}^{2/3}-1)\sqrt{f/2}}\right) \tag{40}$$

Table 34 – Heat exchanger calibration data (cal) and comparison with model interpolation (Int), Gnieliski (Gn) and Dittus-Boelter (DB) correlations

		Re=20000		Re=25000		Re=30000	
		Nu	Err%	Nu	Err%	Nu	Err%
Gas cooler	Cal	371.5	N/A	464.0	N/A	560.1	N/A
	Int	373.4	0.5	454.6	2.1	554.5	1.0
	Gn	376.5	1.3	445.4	4.2	544.7	2.8
	DB	369.1	0.6	437.0	6.2	533.2	5.0

The correlation is reported in Equation (40), where f is the Fanning Factor, Pr is the Prandtl number and C_2 the calibration coefficient. While Table 34 shows the calibration the results of the regression analysis performed on the data retrieved by the manufacturer online tool, the operating points considered refer to cases where no phase change occurs in the heat exchanger.

5.5 Integration of Turbomachinery Maps

In the sCO_2 system model of Figure 47, the sub-models related to the compressor and turbine are modelled following a lumped approach, because of their faster dynamics compared to the ones of heat exchangers. Therefore, performance maps have been used. The maps result from a 3D RANS CFD simulation methodology, details on the methodology can be found in [146,159]. A summary of this approach has also been reported in Appendix A.

The models have been used to run a set of simulations, whose results have been employed to generate the turbine and compressor performance maps in GT-SUITE™, which require, to ensure an accurate interpolation of the operating curves, at least five operating points for each revolution speed considered (at least a minimum number of five different revolution speeds is required for the map generation [148]). Beyond the speed range of the simulated working points, a linear extrapolation method is used to predict the performance of the turbomachines.

Figure 53 shows the turbine maps in the reduced dimensional format typically adopted in turbomachinery [160]: the operating curves (Figure 53.a) and the isentropic efficiency (Figure 53.b) of the machines are reported as a function of the pressure ratio, the reduced mass flow rate and the reduced revolution speed. The reduced quantities (as mass flow rate and revolution speed) are adopted to make the maps independent from the reference conditions used to calculate the maps itself.

The approach is equivalent to use non-dimensional quantities assuming that the gas properties (ratio of specific heat and gas constant) and the flow area would be constant along the whole maps operating range. In case of sCO_2 power cycles the assumption holds for the turbine, but not for the compressor (because of the highly variable gas properties of CO_2 close to the critical point). In the compressor case then, an approximation method described in the following paragraphs has been used to take in account of this aspect.

Because the turbine operates in a region where it is reasonable to assume an ideal gas behaviour for the CO_2, a unique reference state (temperature and pressure) for the normalisation of the reduced quantities has been chosen, and it is equal to 650K and 145 bar. In this part of thesis Kelvin are used instead of degrees Celsius because in the literature about turbomachines reduced quantities are conventionally expressed with this measurement unit.

As shown by the turbine operating curves reported in Figure 53.a, the maximum mass flow rate that the machine can deliver before choking occurs at 3.4 kg/s. From the isentropic efficiency map shown in Figure 53.b instead, it is possible to notice that the optimal operating range for the designed turbine occurs at high revolution speeds (over 80000 RPM) and for a pressure ratio between 1.7 and 2.3.
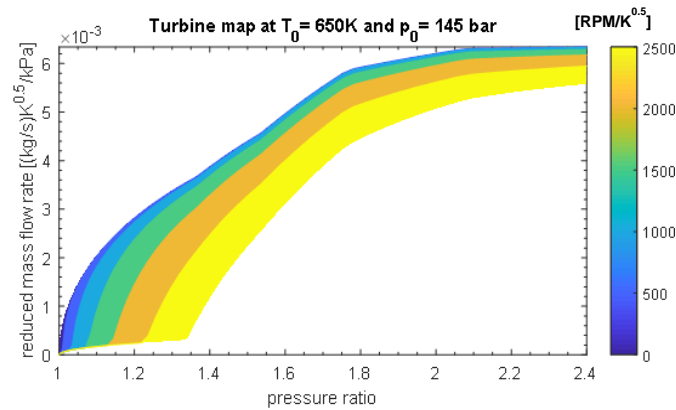
(a)
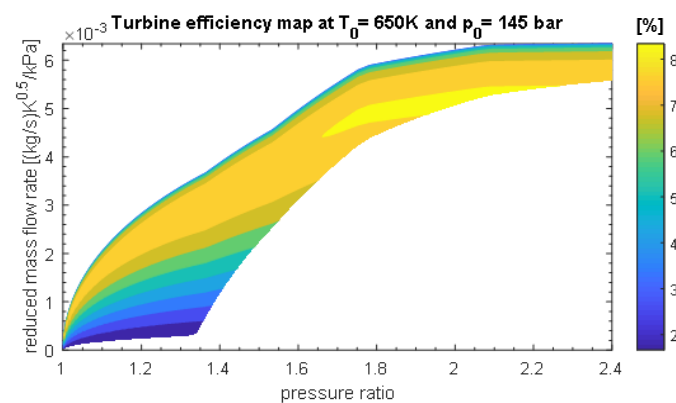
(b)

Figure 53 – Turbine operating map (a) and efficiency map (b) generated for a reference temperature and pressure of 650K and 145 bar respectively (revolution speed expressed in reduced RPM [RPM/$K^{0.5}$] and efficiency in percentage units [%]).

As already mentioned, the assumption of ideal gas behaviour is not valid for the compressor, which instead operates close to the critical point. In this region, the real gas properties of the fluid must be considered and the use of reduced quantities via normalization can lead to errors in the compressor performance predictions [18]. To overcome this issue, the model considers multiple compressor maps at four reference states that span the whole CO_2 critical region (308.15K at 70, 75, 80 and 85 bar). Each of these maps has been generated by maintaining constant the inlet conditions of the working fluid (pressure and temperature) and changing the outlet static pressure at different revolution speeds. At least five pressure ratios for each revolution speed are required to ensure an accurate interpolation of the operating curves.

Beyond the speed range available from the calibration data, a linear extrapolation method is used to predict the performance of the turbomachines. Figure 54 shows the compressor performance maps, operating curves (Figure 54.a) and total-to-static isentropic efficiency (Figure 54.b) for the reference state at 75 bar and 308.15K. The small distortion located near the surge line at high revolution speeds is due to the supercritical CO_2 thermophysical properties, which affect the pressure changes inside the compressor at different speeds.

To overcome this issue, the model considers multiple compressor maps at four reference states that span the whole CO_2 critical region (308.15K at 70, 75, 80 and 85 bar). Each of these maps has been generated by maintaining constant the inlet conditions of the working fluid (pressure and temperature) and changing the outlet static pressure at different revolution speeds. At least five pressure ratios for each revolution speed are required to ensure an accurate interpolation of the operating curves.
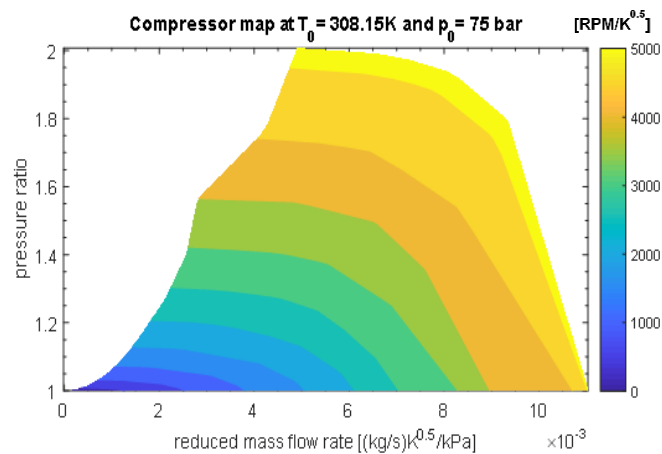
(a)
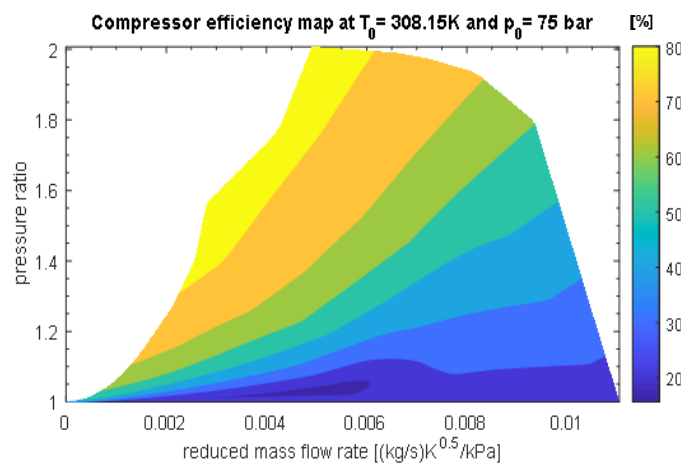
(b)

Figure 54 – Compressor operating map (a) and efficiency map (b) generated for a reference temperature and pressure of 308.15K and 75 bar respectively (revolution speed expressed in reduced RPM [RPM/$K^{0.5}$] and efficiency in percentage units [%])

Beyond the speed range available from the calibration data, a linear extrapolation method is used to predict the performance of the turbomachines. Figure 54 shows the compressor performance maps, operating curves (Figure 54.a) and total-to-static isentropic efficiency (Figure 54.b) for the reference state at 75 bar and 308.15K. The small distortion located near the surge line at high revolution speeds is due to the supercritical CO_2 thermophysical properties, which affect the pressure changes inside the compressor at different speeds.

The design point for the compressor used in the current study approaches the critical point. This condition has positive effect on the choke line. In fact, its slope suggests that an operation of the compressor close to the critical point would be beneficial in terms of choke margin compared to the one typical of conventional machines using ideal gases. This is in line with the findings in [93]. In particular, for a pressure ratio of 2, the compressor can process a minimum mass flow rate of 2.1 kg/s before choking.

For lower pressure ratios, for instance 1.3, the minimum mass flow rate of working fluid processable is 1.1 kg/s, which shows the advantage of using sCO_2 as working fluid in terms of operational flexibility (Figure 54.a). The compressor optimal operating region is located close to the choke line, as shown in Figure 54.b, where the isentropic efficiency assumes a value of 0.8 in a range of revolution speeds and pressure ratios of 50000 -90000 RPM and 1.3-2.0 respectively.

5.6 Valves, Piping and Auxiliaries

The valves are modelled as orifices. The valve template is in the form of a look-up table which requires the flow coefficient as a function of the pressure difference across the device. The globe valves have been designed to follow equal percentage characteristic curve, which has been provided by the manufacturer. A series of forward and reverse discharge coefficients have been inserted as a function of the lift position of the valve actuator.

These discharge coefficients are used by the software to calculate the effective flow area at the throat, while the pressure ratio across the valves is used to compute the velocity at the throat and, consequently, the mass flow rate through the valve. Equation (41) correlates the valve discharge coefficient to ratio between the lift L and the valve diameter D.

$$C_d = 0.0112e^{0.196\frac{L}{D}} \qquad (41)$$

Straight pipes and bends are instead treated with the 1D modelling approach described at the beginning of Section 3. In the current study, pipes are considered smooth and insulated, thus friction and thermal losses are neglected. This is assumption is fair since the actual pipes in the Brunel's sCO_2 facility have an oversized diameter (2") to reduce pressure losses and are

insulated through a ceramic wool layer wrapped between a silica wash treated glass cloth as inner layer and a grey PTFE coated glass cloth as outer layer.

The receiver has been modelled as a capacity with fixed volume. In the current case, the tank has been placed downstream of the gas cooler to absorb the thermal expansion of the fluid in the circuit, decoupling the high-pressure side from the low pressure one (Figure 2). Its size has been chosen equal to 0.165 m^3 and accounts for almost the 50% of the overall system capacity.

The inertia of the shaft and of the generator is also taken into account. However, the full model of the electrical generator has been neglected. This implies that the power quantities are purely thermal. Parasitic losses of the system ancillaries (water cooling pump and fans, oil pump for turbomachinery lubrication, CO_2 drainage compressors) have been also discarded.

5.7 Summary

In this chapter the model of a low capacity sCO_2 heat to power conversion unit designed for medium to high thermal grade WHR applications has been detailed. To model each component, performance data provided by manufacturers or obtained from more complex CFD models have been used. In particular, the operating maps of the radial compressor and turbine have been generated and presented. To account for the significant variation of CO_2 properties in the critical region, four sets of maps were generated between 70 and 85 bar and a linear interpolation based on the upstream compressor conditions was set up.

The approach adopted allows to perform complex optimization and transient analyses with a reduced computational effort and with an acceptable accuracy, also when the system is operated in off-design conditions. As a drawback, the simplifying assumptions introduced, don't allow to catch detailed phenomena occurring in the system which must be investigated with more complex and dedicated models.

6. System Analysis and Optimisation

After the modelling stage, the steady-state and transient behaviour of the sCO_2 unit has been assessed. The steady state analysis aimed to mainly investigate the performance of the system at design and off-design, meaning at different conditions of the heat source and the heat sink. To do so, several operating conditions of the sCO_2 system have been simulated in GT-SUITE^{TM} by varying the inlet conditions of the heat source (flue gas) and the heat sink (water-glycol mixture), inlet temperatures and respective mass flow rates. During the whole set of simulations, the revolution speed of the turbomachines has been maintained constant and equal to the design point, whose value is showed in Table 35.

The results of the analysis have been presented with reference to the heat exchangers and to overall system. For the heat exchangers, several performance indicators as for instance effectiveness, thermal duty, pressure drops and heat transfer coefficients have been calculated varying the components operating conditions. This analysis allows to generate not only performance maps of the components employed in the sCO_2 facility built at Brunel University, useful for optimization and control purposes, but also to give more general insights which are not dependent upon the system considered.

Regarding the system overall performance on the contrary, the net power output and thermal efficiency as well as the main cycle parameters, as for instance the compressor and turbine inlet pressure and temperature [128], have been obtained as a direct function of the heat source and heat sink inlet conditions. The obtained results form a sort of performance map of the heat exchangers and the system, which can be used as an optimisation tool at different operating conditions or for control purposes.

The adoption of independent drive configuration for the turbine has also been considered in order to understand the benefits and limitations deriving from such layout. The same performance indicators have been plotted against the variation of the heat load conditions, mass flow rate and temperature, for the baseline (coupled drive) and the new (independent drive) solution.

Finally, the dynamic response of the system has been assessed. Time varying heat load profiles have been investigated and the CO_2 temperature and pressure at the turbine and compressor inlet have been taken as representative variables, given their highlighted relevance. The system behaviour during startup and shutdown has also been investigated.

Table 35 – Operating conditions of the sCO$_2$ unit at the design point

Supercritical CO$_2$		Design	Model I/O
Mass flow rate	[kg/s]	2.1	Output
Highest pressure	[bar]	128	Output
Lowest pressure	[bar]	75	Output
Heat source: flue gas			
Mass flow rate	[kg/s]	1.0	Input
Inlet temperature	[°C]	650	Input
Inlet pressure	[bar]	1	Input
Cold source: Water			
Mass flow rate	[kg/s]	1.6	Input
Inlet temperature	[°C]	15	Input
Inlet pressure	[bar]	3	Input
Compressor			
Revolution speed	[RPM]	86000	Input
Isentropic efficiency	[%]	75	Output
Inlet temperature	[°C]	35	Output
Turbine			
Revolution speed	[RPM]	86000	Input
Isentropic efficiency	[%]	80	Output
Inlet temperature	[°C]	450	Output
sCO$_2$ unit			
Mechanical net power output	[kW]	50	Output
Overall efficiency	[%]	20	Output

6.1 Steady-state Analysis

Heat Exchangers Off-design Performance Maps

The three heat exchangers embedded in the sCO$_2$ facility have been investigated performing a series of steady-state simulation considering different operating conditions of the devices. For the heater and the gas cooler, the varying of such operating conditions have been related to the variation of the heat sink/source inlet conditions, such as inlet temperature and mass flow rate. For the working fluid on the contrary, three different mass flow rates have been considered and the thermodynamic inlet conditions, such as pressure and temperature, maintained constant.

For the PCHE recuperator instead, the impact on changes in the operating pressure and temperature of the working fluid has been instead showed.

Heater

Figure 55 shows how the inlet conditions of the heat source (i.e. flue gas) affect the performance of the heater. The simulations have been carried by assuming the inlet thermodynamic conditions of the CO_2, such as pressure and temperature, unchanged and equal to 128 bar and 240°C respectively. Three values of working fluid mass flow rates have been considered and are equal to 1.57 kg/s (Figure 55.a-d), 2.09 kg/s (Figure 55.e-h) and 2.62 kg/s (Figure 55.i-n). Since the heater is composed by four separated modules, the heat load and the pressure drops have been calculated as a sum of the individual contributions of each module while the overall heat transfer coefficient and the effectiveness result from an average of them.

In particular, the heat load, or namely thermal power, transferred by the heat exchanger at the different operating conditions is showed in Figure 55.a,Figure 55.e and Figure 55.i. An increasing mass flow rate of working fluid leads to an increase of the heat rates, as for a heat source inlet temperature and mass flow rate of 850°C and 1.4 kg/s a thermal power of 700 kW_t, 800 kW_t and 900 kW_t is recovered for a CO_2 mass flow rate of 1.57 kg/s (Figure 55.a), 2.09 kg/s (Figure 55.e) and 2.62 kg/s (Figure 55.i) respectively.

The overall heat transfer coefficient and the effectiveness of the heat exchanger resemble the same trend correlation, showing higher values for higher mass flow rate of working fluid processed. The mass flow rate is indeed related to the velocity of the fluid flowing through the component which in turn affects its thermo-hydraulic performance. The increase is quite pronounced, since when the CO_2 mass flow rate is varied from 1.57 kg/s to 2.62 kg/s, the overall heat transfer coefficient and the effectiveness of the heat exchanger change from the maximum value of 0.27 $kW/(m^2K)$ and 65% (Figure 55.b and Figure 55.c) to the maximum values of 0.34 $kW/(m^2K)$ and 85% (Figure 55.l and Figure 55.m) respectively.

Different trends are showed instead if the inlet conditions of the heat source are considered. The heat transfer coefficient presents an increasing trend with the heat load supplied by the waste heat source. Assuming in fact a mass flow rate of working fluid of 2.09 kg/s, the overall heat transfer coefficient increases following either an increase of the inlet temperature or of the mass flow rate of the waste heat source (Figure 55.f). This because higher heat loads lead to higher temperature of the working fluid and consequently lower densities. To balance the density decrease, the flow velocity must grow, leading to higher local convective and thus overall heat transfer coefficients.

On the contrary, the effectiveness of the heater decreases for higher mass flow rates of waste heat source beside despite being unsensitive to changes in its inlet temperature, as showed in Figure 55.g. Assuming a CO_2 mass flow rate of 2.09 kg/s and a waste heat source inlet temperature of 650°C, the effectiveness of the heater increases from the value of 55% to 75% for a heat source mass flow rate decrease from 1.0 kg/s to 0.6 kg/s.

This trend can be explained by considering that a decrease of the mass flow rate of the waste heat source, which is the fluid with the lower thermal capacity, leads to a drop in both the thermal power exchanged and in the one potentially transferrable if an infinite heat exchanger was adopted. The magnitude of the decrease is higher in the latter term, which stands at the denominator of the effectiveness, resulting in an increase of such variable.

The pressure drops of the working fluid in the heat exchanger show instead the same trend of the overall heat transfer coefficient. Indeed, as showed in Figure 55.d, Figure 55.h and Figure 55.n, the pressure drops increase following an increase in the mass flow rate of the working fluid and in the inlet temperature or mass flow rate of the waste heat source. The results show also that the pressure drops are contained, with a maximum value of 0.54 bar for a mass flow rate of working fluid processed of 2.62 kg/s and a heat source inlet temperature and mass flow rate of 850°C and 1.4 kg/s respectively (Figure 55.n). This is an important aspect since the reduction of the pressure losses in a simple regenerative sCO_2 Brayton cycle is important to avoid an excessive erosion of the already reduce pressure ratio available across the turbine.

In general, low values of overall heat transfer coefficients are achieved, as it can be noticed in Figure 55.b Figure 55.f and Figure 55.l, and it is mainly due to the fact that in the heater a gas/sCO_2 heat transfer takes place, which limits the local heat transfer coefficient especially on the flue gas/heat exchanger wall side and therefore the overall heat transfer coefficient.

A further aspect is that, from a system design perspective, a trade off exists in selecting the maximum heat load exploitable by the unit. Higher thermal loads increase from one side the overall heat transfer coefficient achievable, but also reduce the heat exchanger effectiveness, meaning a need for higher heat transfer surfaces and material costs. They also lead to an increase of the pressure drops across the device, causing an erosion of the pressure ratio across the turbine and therefore a slight decrease in the system net power output. The results however show a possible alternative to reduce the trade-off, which could be increasing the heat load provided to the unit by only increasing the inlet temperature of the waste heat source. This could limit the impact on the heat exchanger effectiveness increasing at the same time the overall heat transfer coefficient, with a reduced increase in the pressure drop across the device. However, this solution whenever possible would require an intermediate heat transfer loop, with a consequent negative impact on the capital expenditures.
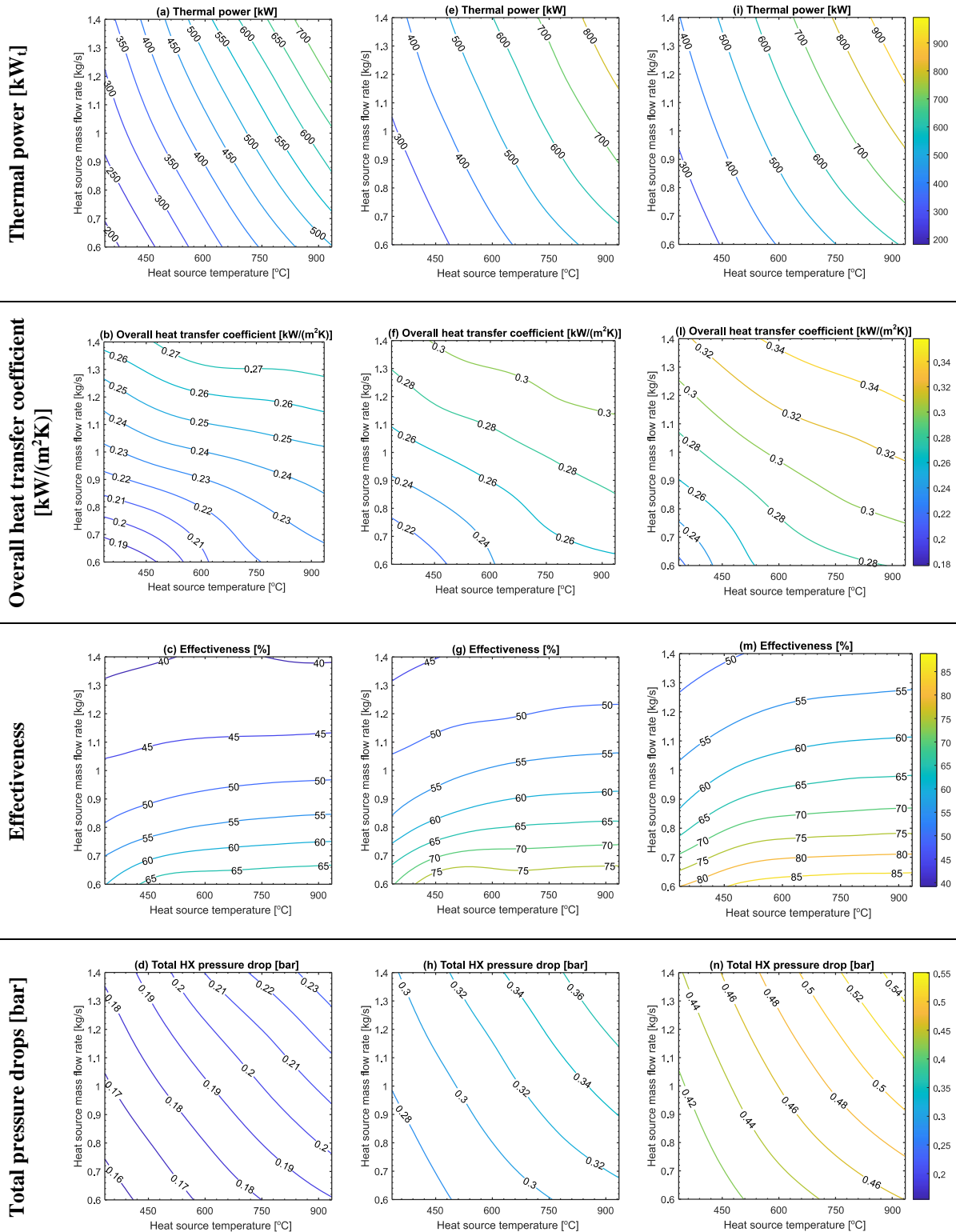
Figure 55 – Off-design performance maps of the Heater (HX) obtained varying the heat source mass flow rate and inlet temperature for different values of sCO$_2$ mass flow rates: 1.57 kg/s (a-d), 2.09 kg/s (e-h) and 2.62 kg/s (i-n)

In the PCHE recuperator analysis, all the maps assume as independent variables the maximum temperature and pressure achieved by the working fluid in the cycle. From these maximum values of pressures and temperatures, the inlet conditions of both streams of CO_2 (pressures and temperatures) flowing through the heat exchanger (at the cold and the hot side respectively) can be uniquely calculated and are assumed as inputs of the simulations. The inlet pressure of the CO_2 at the hot side inlet is assumed equal to the minimum cycle pressure, equal to 75 bar. The CO_2 inlet pressure of the cold side is the one at the outlet of the compressor and therefore the maximum one achieved in the cycle.

The inlet temperatures at the cold and the hot side are calculated from the turbomachinery operations, which are defined from their isentropic efficiency (80% for the compressor and 75% for the turbine), the fixed compressor inlet temperature (35°C, which is the minimum one in the cycle) and the fixed turbine inlet temperature (which is the maximum one achieved in the cycle). The calculations of the CO_2 thermodynamic conditions at the compressor outlet give the inlet temperature of the CO_2 at the cold side inlet of the PCHE. The one related to the turbine outlet give the temperature of the CO_2 at the inlet of the PCHE hot side and is therefore directly related to the independent variable considered, the maximum temperature achieved in the cycle.

Figure 56 shows the results of the analysis for a CO_2 mass flow rate of 1.57kg/s (Figure 56.a–d), 2.09kg/s (Figure 56.e-h) and 2.62kg/s (Figure 56.i-n). As for Figure 55, also in this case the thermal power exchanged, the overall heat transfer coefficient and the effectiveness of the PCHE are presented. Regarding the pressure drop however, having two CO_2 streams flowing through the heat exchanger, the total pressure drops occurring in the component has been reported, i.e. the sum of pressure drops on the hot and cold sides.

Either in this case the thermal power transferred by the device increases following an increase of the working fluid mass flow rate processed as well as an increase of the maximum pressure and temperature achieved in the cycle (Figure 56.a, Figure 56.e and Figure 56.i). In particular, the heat load variation appears to be more sensitive to changes in the maximum temperature and the mass flow rate, given their major influence on the thermophysical and thermo-hydraulic properties of the fluid. As mentioned in the previous section, an increase of both variables leads to an increase of the flow velocity with a consequent increase of the thermal power transferrable.

With reference to a maximum temperature at the hot side inlet of 450°C and a maximum inlet pressure at the cold side of the recuperator of 125 bar, in the three reference mass flow rates of 1.57 kg/s, 2.09 kg/s and 2.62 kg/s, the thermal power exchanged (Figure 56.a, Figure 56.e and Figure 56.i) is equal to 505 kW_t, 680 kW_t and 810 kW_t respectively. A similar increase can be seen if a maximum inlet pressure at the cold side of 125 bar and a CO_2 mass flow rate of 2.09 kg/s are assumed, and the maximum temperature at the hot side inlet is changed from 300°C to 650°C. In such case the thermal power exchanged varies from 500 kW_t to 800 kW_t (Figure 56.e).

This increase in heat transfer rate is due to the greater overall heat transfer coefficient that, according to Figure 56.b, Figure 56.f and Figure 56.j, assumes values of 1.55 kW/(m^{2}K), 1.70 kW/(m^{2}K), 1.85 kW/(m^{2}K). As mentioned at the beginning of this paragraph, this trend depends on the high flow velocity.

On the other hand, as the mass flow rate increases, the total pressure drops in the heat exchanger also increase. In particular, as it can be noticed from Figure 56.d, Figure 56.h and Figure 56.n, at a maximum temperature and pressure of 350°C and 125 bar, the total pressure drops at 1.57 kg/s, 2.09 kg/s and 2.62 kg/s assume an increasing value of 1.6 bar, 2.6 bar and 4.0 bar respectively. Hence, a variation in the operating mass flow rate has two-fold effects on the heat exchanger performance, enhancing the heat transfer but also increasing the overall pressure drop across the heat exchanger. Negligible effects can be noticed on the heat exchanger effectiveness, since the mass flow rate term appears both at the numerator and denominator of the effectiveness expression.

More pronounced is the effect on the effectiveness of the maximum temperature variation. Assuming, in fact, a mass flow rate of 2.09 kg/s and a maximum pressure of 120 bar, the effectiveness of the PCHE varies from 74% at a maximum temperature of 250°C to 84% for a temperature of 500°C (Figure 56.g). The maximum pressure has on the contrary a detrimental effect on such indicator, since for the same reference case at a temperature of 350°C, a 50% variation on the CO_2 maximum pressure leads to a 5% decrease in the effectiveness of the PCHE.

Such decrease is due to the reduced heat rates achieved at higher CO_2 maximum pressure, given the negative impact of the latter variable on the overall heat transfer coefficients (Figure 56.b, Figure 56.f and Figure 56.k). Indeed the pressure affects the density of the CO_2 and, consequently, the flow velocity on the cold side of the heat exchanger. Higher pressure leads to higher densities and therefore to lower flow velocities. The nonlinear relationship between flow velocity and pressure drops eventually leads to a decrease in total pressure drop shown in Figure 56.h.
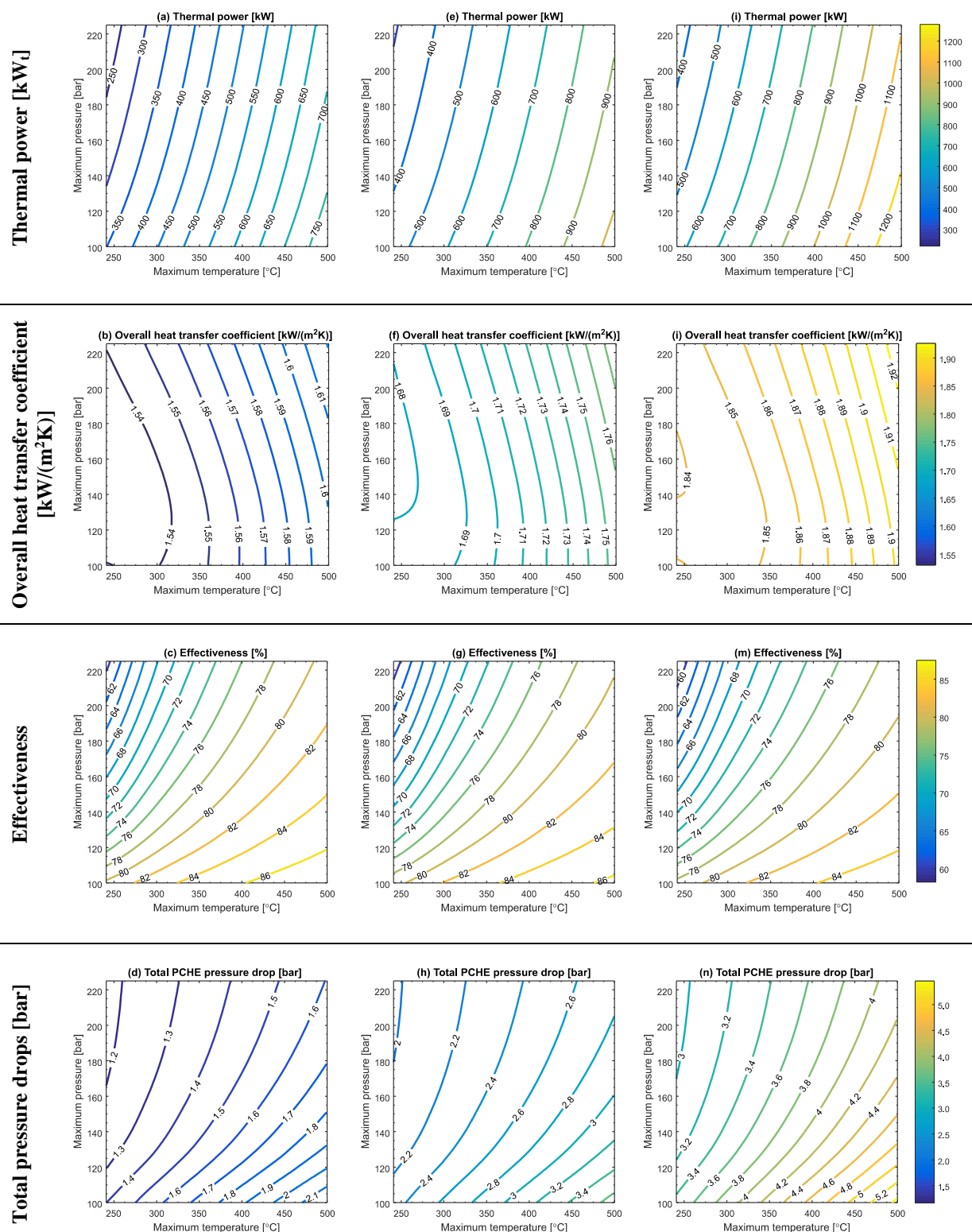
Figure 56 – Off-design performance maps of the PCHE recuperator obtained varying the maximum temperature and pressure of the cycle for different values of sCO$_2$ mass flow rates: 1.57 kg/s (a-d), 2.09 kg/s (e-h) and 2.62 kg/s (i-n)

The results from the above analysis should be taken into consideration in the selection of the recuperator for sCO_2 power systems. Amongst the main challenges in enhancing the efficiency of sCO_2 systems, are the high thermal duties heat exchangers have to operate at, and pressure drops along the cycle. High pressure drops in the components, limit the maximum expansion ratio across the turbine, which in turn influences the net power output.

Similarly, the off-design study shows that for the recuperator, interrelationships between maximum cycle pressure and temperatures and CO_2 mass flow rate have to be addressed during the selection of the cycle operating parameters. Even though a high maximum cycle temperature is always beneficial in terms of turbine efficiency and net power output, it also increases the pressure drop in the PCHE therefore reducing the available expansion ratio across the turbine.

Similarly, increasing the maximum cycle pressure leads to a higher cycle pressure ratio and to a reduction of the pressure drops (Figure 56.d, Figure 56.h and Figure 56.n) in the recuperator. At the same time this decreases the recuperator effectiveness and thus requires a larger device to accommodate the same thermal duty, i.e. higher capital expenditures due to the need to oversizing the heat exchanger to cope with these operating conditions.

Gas Cooler

Figure 57 shows the results of the analysis carried out on the Plate Heat Exchanger (PHE) gas cooler of the sCO_2 system. As for the heater, also in this case the independent variables of the analysis are the inlet temperature and mass flow rate of the cooling source (a water-glycol mixture). For the CO_2 side, the inlet temperature and pressure have been set as input and equal to 100°C and 75 bar respectively, while three values of mass flow rates have been considered. Either in this case the heat rate transferred to the heat sink, named cooling load, increases for higher mass flow rates of CO_2 (Figure 57.a, Figure 57.e and Figure 57.i).

This is largely due to the higher heat transfer coefficient achieved, as it is possible to notice in the in Figure 57.b and Figure 57.i, where for a temperature and mass flow rate of the cold source equal to 10°C and 2.5 kg/s, the overall heat transfer coefficient goes from 3.3 kW/(m²K) to 3.9 kW/(m²K) for an increase in the CO_2 mass flow rate from 1.57 kg/s to 2.62 kg/s.

Higher overall heat transfer coefficients are also achieved with higher cooling rates, available with lower cold source inlet temperatures or higher mass flow rates. In fact, higher cooling rates mean an ability of extracting more heat from the CO_2, which ease the achievement of the critical point. In this region, the heat capacity of the working fluid increases dramatically, with a positive impact on the overall heat transfer coefficient achieved in the heat exchanger.
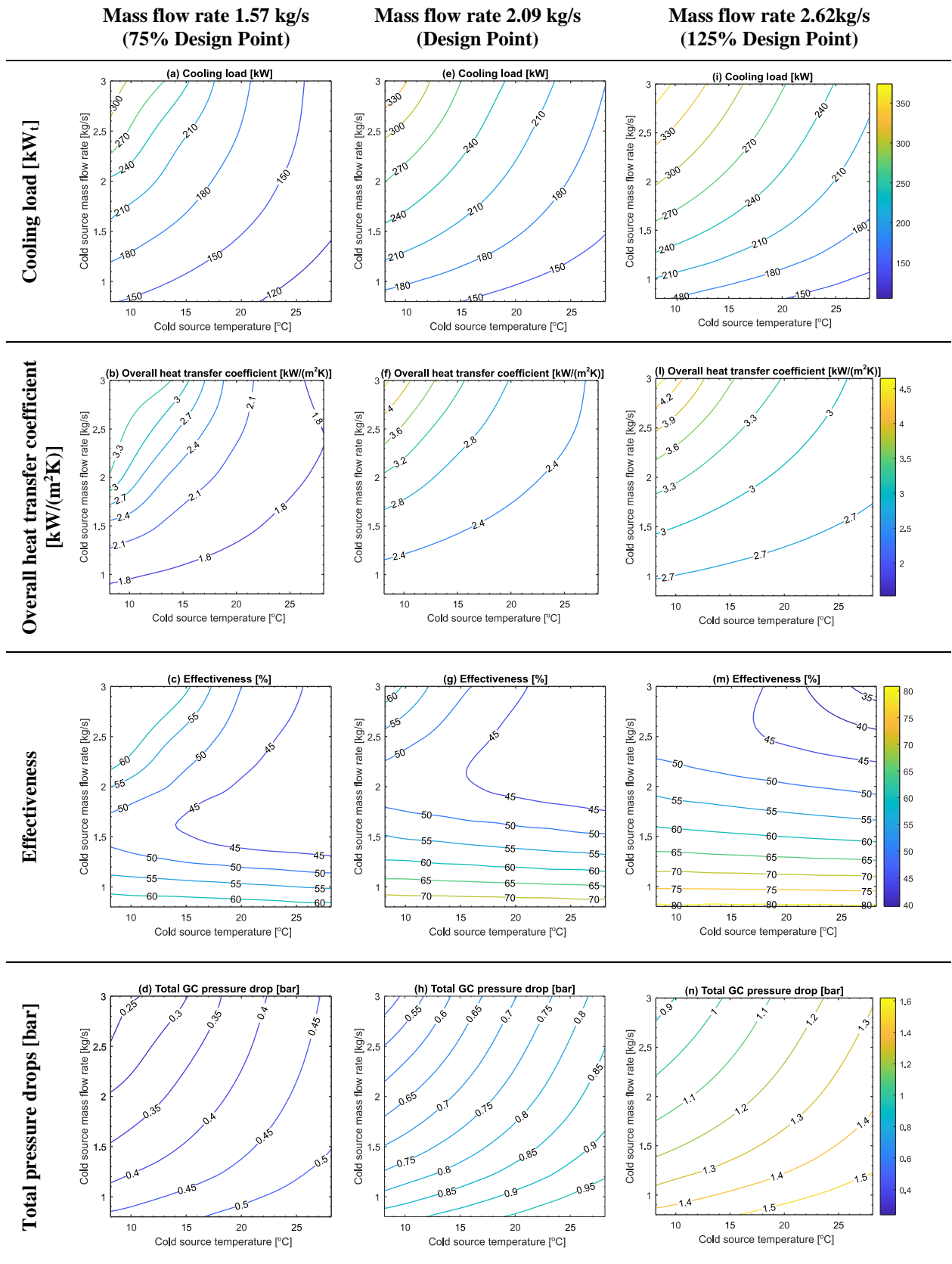
Figure 57 – Off-design performance maps of the PHE gas cooler (GC) obtained varying the cold source mass flow rate and inlet temperature for different values of sCO$_2$ mass flow rates: 1.57 kg/s (a-d), 2.09 kg/s (e-h) and 2.62 kg/s (i-n)

Furthermore, the higher mass flow rate of the cold source allows also to increase the water-glycol flow velocity in the heat exchanger, with a consequent additional benefit in terms of heat transfer enhancement.

Regarding the gas cooler effectiveness, the analysis shows a similar trend to the heater case, with the effectiveness increasing following a decrease of the cooling fluid mass flow rate. Different is instead for the pressure drops, which show an increasing trend following a decrease of the cooling load (increasing inlet temperature and decreasing mass flow rate of the cooling fluid, as showed in Figure 57.d, Figure 57.h and Figure 57.n). The explanation still relies in the variation of the flow velocity. A decreasing cooling load leads to CO_2 thermodynamic conditions far from the critical point, with consequent lower average densities. Such decrease in density has to be balanced, for an assumed constant value of the CO_2 mass flow rate, from an increase of the flow velocity, which leads to increasing pressure drops across the device.

From a more general point of view, the higher heat transfer coefficients achievable in the heat exchanger (Figure 57.b, Figure 57.f and Figure 57.l) thanks to the enhanced heat transfer between water and sCO_2 closer to the critical point allow to substantial downsize the heat exchanger. A further positive aspect showed by the analysis are the similar trend of the heat transfer coefficient and pressure drops to respect of the inlet conditions of the cold source. Lowering in fact its inlet temperature and increasing the mass flow rate can lead at the same time to an increase of the overall heat transfer coefficient and a decrease of the pressure drops across the heat exchanger.

System Off-design Analysis

Figure 58.a shows how the power output of the sCO_2 unit changes following the variations of the heat load, namely the inlet temperature and mass flow rate. The quantities consider pure mechanical quantities, since the effect of electric generator has been discarded. In this set of simulations, the inlet conditions of the heat sink have been maintained constant and equal to the design values. The cycle pressure ratio slightly changes depending on the heat load supplied at the heater. In particular, it can be seen that the map gives an indication of the limit conditions of the waste heat source for which the sCO_2 system is not able to generate power.

It can be observed that for flue gas mass flow rates lower than 0.8 kg/s, the inlet temperature of the heat exchanger must be higher than 500°C in order to have a not null net power output. For lower temperatures, the compressor requires more power than the one generated by the turbine and consequently the net power output of the system is negative, around -15 kW (Figure 58.a). This is mainly due to the low design pressure ratio of the cycle, which together

with the low divergence of the CO_2 isobaric lines, requires the achievement of high turbine inlet temperatures to reach a positive power output.

For this reason, high exhaust temperatures are needed to achieve high system power outputs. For instance, for a unitary exhaust mass flow rate, considering a flue gas temperature increase from 600°C to 850°C, the unit power output rises from 45 kW to 90 kW. If the same percentage change in the hot source mass flow rate occurs, for example at 650°C, the net outcome varies only from 50 kW to 62 kW.

The increase of the hot source mass flow rate only leads to a slightly higher working fluid mass flow rate in the circuit to balance the higher thermal load available at the primary heater. Consequently, the thermal efficiency of the system remains almost constant and the power output gain is achieved thanks to the greater mass flow rate of CO_2 processed. On the contrary, a rise of the hot source temperature leads to a higher working fluid temperature at the turbine inlet, with a positive effect on the cycle thermal efficiency.

(a)   (b)
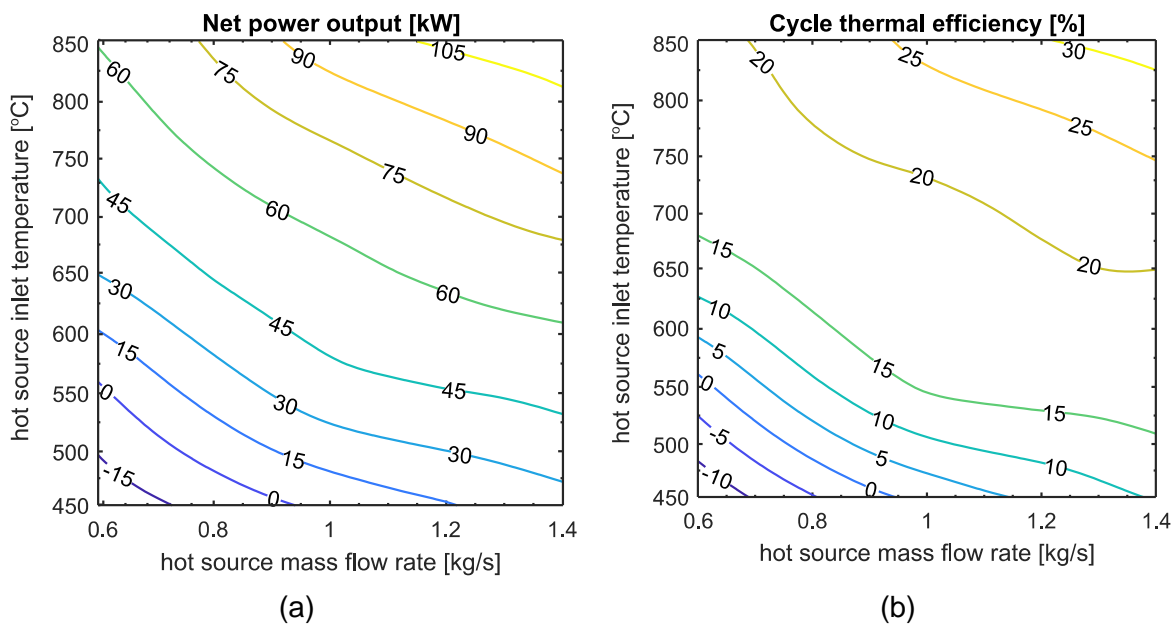
Figure 58 – sCO$_2$ unit net power output (a) and thermal efficiency as a function of the hot source inlet temperature and mass flow rate.

Figure 58.b confirms the abovementioned statement, showing a higher sensitivity of the cycle thermal efficiency to the hot source inlet temperature rather than its mass flow rate. In fact, a variation of the latter quantity from 0.8 kg/s to 1.2 kg/s at 650°C, leads to an efficiency rise of almost 12% (from 16% to 18%), against a 52% increase (from 10% to 22%) for the same percentage change of flue gas temperature (considering a 1.0 kg/s mass flow rate). An even higher efficiency (around 30%) can be achieved for an exhaust temperature of 850°C and a mass flow rate of 1.4 kg/s. A further increased efficiency can be obtained by increasing the design cycle pressure ratio, which would lead however to increased investment and

operational costs due to higher-end materials and more expensive components, which is not desirable for WHR applications.

The efficiency of the cycle is also strongly influenced by the sCO_2 temperature at the turbine inlet. For the design adopted, the highest system power output and efficiency occur when a temperature at the turbine inlet of 650°C is reached (Figure 9). and are equal to 105 kW (Figure 58.a) and 30% (Figure 58.b) respectively. For turbine inlet temperature lower than 275°C, occurring for a hot source mass flow rate and inlet temperature lower than 0.9 kg/s and 550°C respectively (Figure 59.a), the system is not able to generate net power output (Figure 58.a).

In particular, the results shown in Figure 59.a suggest that it is possible to reduce the relevant temperature difference between the inlet temperature of the flue gases and the CO_2 at the turbine inlet by increasing the flue gas mass flow rate. For instance, if a hot source inlet temperature of 650°C is considered, increasing the hot source mass flow rate from 1 kg/s up to 1.4 kg/s can lead to a rise in the turbine inlet temperature from 400°C to 450°C, with a consequent increase in the power output from 50 kW to 63 kW (Figure 58.a) and of the thermal efficiency from 17% to almost 20% (Figure 58.b).
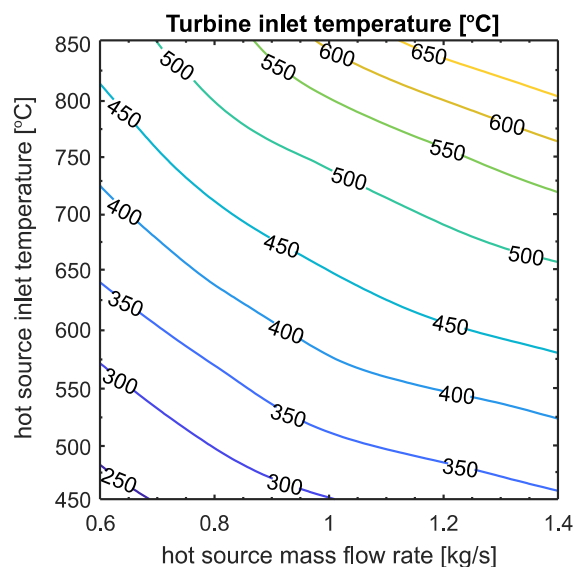
Figure 59 – Variation of CO_2 temperature at the turbine inlet as a function of the hot source inlet temperature and mass flow rate.

This increase in performance is due to the lower exergy loss occurring in the primary heater. Increasing the mass flow rate of the hot source counterbalances the higher thermal capacity of the CO_2. Then, a better matching of the temperature profiles of the two fluids in the heat exchanger can be achieved, leading to a higher exergy efficiency. A further solution would be the adoption of different cycle layouts designed to achieve better temperature profile matching. However, the higher investment cost due to the additional components required (i.e. heat exchangers, compressors and turbines), may increase the payback period of the heat to power conversion unit disproportionally.

A further positive effect on the system performance can also be achieved by reducing the inlet temperature of the cold source, as showed in Figure 60.a. Given a cooling fluid mass flow rate of 1.6 kg/s, a reduction of 20% in its inlet temperature can actually lead to a power output increase from 48 kW to 64 kW. Similarly, the same percentage variation of cold source mass flow rate, at an inlet temperature of 18°C, allows an increase in the system power output from 54 kW to 64 kW.

In particular, an increase of the cooling load allows to decrease the compressor inlet temperature of the CO_2, which gets closer to the critical point. At critical conditions, the CO_2 isothermal compressibility increases steeply, allowing a more efficient compression. The decreased compression power then leads to an increased system net power output and thermal efficiency.

The thermal efficiency gain achievable is shown in Figure 60.b. Considering a cold source mass flow rate of 1.6 kg/s, a decrease of its inlet temperature from 26°C down to 16°C leads to an increase in the cycle thermal efficiency from 9% to 21%. A higher efficiency value of 24% can be reached by increasing the cooling flow rate to 2.4 kg/s, and keeping its inlet temperature lower than 18°C. For higher cooling fluid temperatures the maximum efficiency is limited to 20%.

(a)   (b)
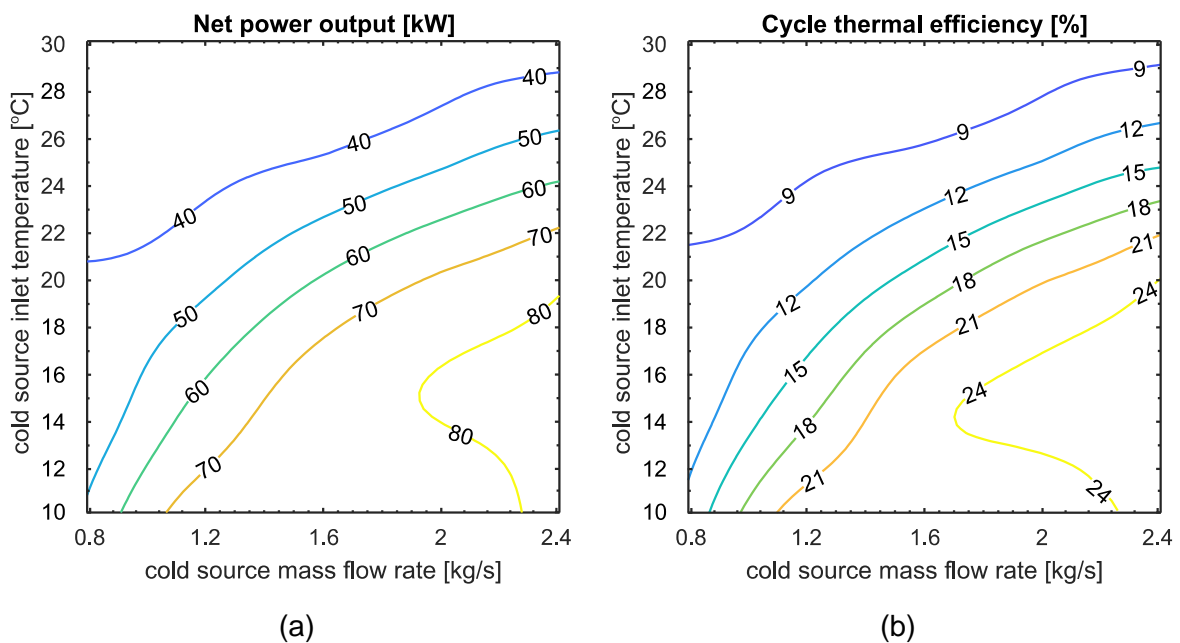
Figure 60 – Variation of sCO_2 unit net power output (a) and thermal efficiency (b) with cold source inlet temperature and mass flow rate.

It can also be seen from Figure 60.a and Figure 60.b, that for mass flow rates higher than 1.6 kg/s and inlet temperatures lower than 20°C, less steep performance improvements can be observed. Considering for instance a cold source inlet temperature of 14°C and a variation of

mass flow rate from 1.6 kg/s to 2.4 kg/s (Figure 60.a), the system power output increases only from 75 kW to 80 kW and the thermal efficiency from 23% to 24% (Figure 60.b).
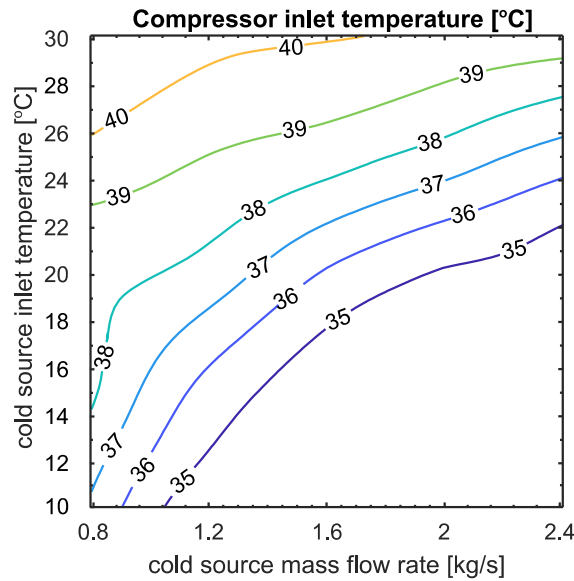
Figure 61 – Variation of sCO$_2$ temperature at the compressor inlet as a function of the cold source inlet temperature and mass flow rate.

The reason for this can be explained by referring to Figure 61, which shows the variation in the CO$_2$ temperature at the compressors inlet as a function of the cooling load available at the gas cooler. In the range of cold source inlet conditions considered, the compressor inlet temperature is constant and equal to 35°C. No further temperature reductions could be achieved even for increased cooling flow rate, due to the higher thermal capacity that the CO$_2$ assumes close to the critical point. This ensures a CO$_2$ temperature at the compressor inlet always higher than the critical temperature which avoids condensation and dry conditions at the start of compression.

Independent drives

The model so far investigated resembles the facility commissioned at Brunel University London, and considers the compressor and turbine rotating at the same speed since mounted on the same rotating shaft. Therefore, to assess the advantages of having independent drived machines, a new turbine has been modelled and integrated in the sCO$_2$ unit model previously presented. The new device has been considered as disconnected from the compressor, therefore for this model, two revolution speeds have to be inserted as boundary condition.

The new turbine has been designed following the methodology developed in [161]. The approach considers a three-step technique to design and optimise the turbine performance in part load/off-design conditions. A mean line procedure considers the design of the rotor, the stator and the volute of the turbine, assumed for simplicity as a circular cross section, in order to accurately estimate the fluid dynamic losses. To start the procedure, first, a set of

geometrical and thermodynamics parameters are required [161], chosen respectively by manufacturability considerations and according to the design operating point of the sCO_2 system object of this work.

Given these input data, an isentropic efficiency value at the design point of the turbine is estimated, which is used to compute the enthalpy drops in the rotor, stator and in the volute.

Consequently, a new isentropic efficiency value is calculated and compared with the previous estimated one. The procedure is repeated iteratively until a convergence is achieved. The MATLAB optimisation toolbox has been used to optimise the inlet parameters, using as objective function the isentropic efficiency of the machine.

After this preliminary design stage, RITAL, a commercial 0D/1D software tool, has been used to calculate the turbine performance at off-design conditions, and thus obtain the operating and isentropic efficiency map of the machine. To do so, RITAL has been firstly calibrated to predict the turbine design conditions and then to calculate the off-design performance of the expander. The maps resulted from this design and optimization process have been implemented in GT-SUITE^{TM} are displayed in Figure 62. The discontinuity in the turbine maps noticeable is due to the extrapolation of the turbine operating curves and isentropic efficiency lines made by the software for pressure ratios lower than 1.4.

Compared to the speed constrained turbine design (Figure 53 in chapter 5), the independent one can provide a higher range of CO_2 mass flow rates even at lower pressure ratios. For instance, with reference to a pressure ratio of 1.2, the new turbine design can process for its entire revolution speed range a mass flow rate of working fluid going from 1.59 kg/s to 2.51 kg/s. For the same pressure ratio, the old turbine design could a CO_2 mass flow rate only from 0.11 kg/s to 1.48 kg/s respectively. As concerns the isentropic efficiency, the old design presents an optimal operating value in a wider range of mass flow rates and pressure ratios compared to the new one.

To investigate the benefits deriving from the adoption of independently driven turbomachinery the methodology presented in the previous section has been followed. A series of simulations at different operating conditions of the sCO_2 heat to power conversion system have been carried out varying the thermal load supplied by the waste heat source (inlet temperature and mass flow rate). On the other hand, the cooling water mass flow rate and inlet temperature have been kept equal to 1.6 kg/s and 25°C respectively.
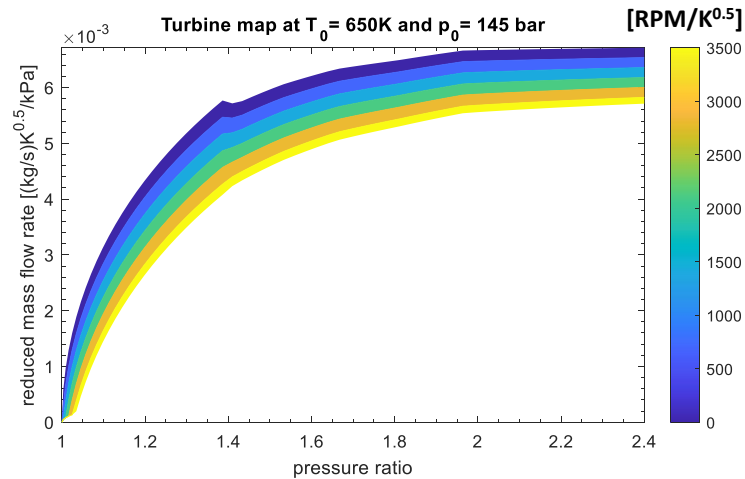
(a)
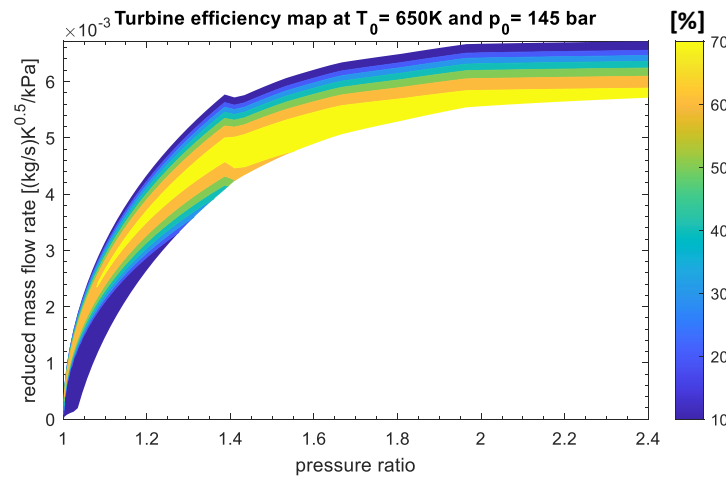
(b)

Figure 62 – Turbine operating (a) and efficiency (b) maps for Independent Drive (ID) case

In each case, the net power output has been maximised acting on the compressor and turbine revolution speeds as independent variables. The optimisation algorithm employed is the Nelder Mead SIMPLEX one, which is suitable for finding a local minimum and at a low computational cost since no calculations of derivative terms are involved. For the independent drive configuration, two independent variables must be optimised, the compressor and turbine revolution speeds, and thus the method is a pattern search that compares function values at the three vertices of a triangle. The worst vertex is rejected and replaced with a new vertex. A new triangle is formed, and the search is continued. The process generates a sequence of triangles for which the values of the optimization function at the vertices get smaller and smaller. The size of the triangles is reduced, and the coordinates of the minimum point are found. When the sCO_2 system configuration with coupled turbomachines is considered, the optimisation method is similar but considers a segment line instead of a triangle, since only one independent variable must be optimised. Even if the algorithm adopted also allows to

perform constrained optimisation by penalizing the regions which violate the constraints imposed [24, 34], in this study, no constraints have been imposed.

The results of the optimisation for the Coupled Drive (CD) case (baseline case as in the facility) have been reported in Figure 63.a. The results resemble the ones presented in Figure 58, since the optimization of the revolution speed of the turbomachines led to speed similar to the design one (as showed in Figure 66.b). Even in this case for reduced thermal loads, i.e. waste heat mass flow rate and inlet temperature below 0.7 kg/s and 500°C respectively, the system is not able to generate any power output since the power required by the compressor is equal or greater than the one generated by the fluid expansion in the turbine. At higher thermal loads, i.e. for waste heat source mass flow rates and inlet temperatures above 1.3 kg/s and 800°C respectively, the sCO$_2$ unit is able to generate a maximum power output of 105kW, thanks to an increased turbine inlet temperature and cycle pressure ratio which consequently lead to a higher cycle thermal efficiency and enthalpy drop across the turbine.

(a)   (b)
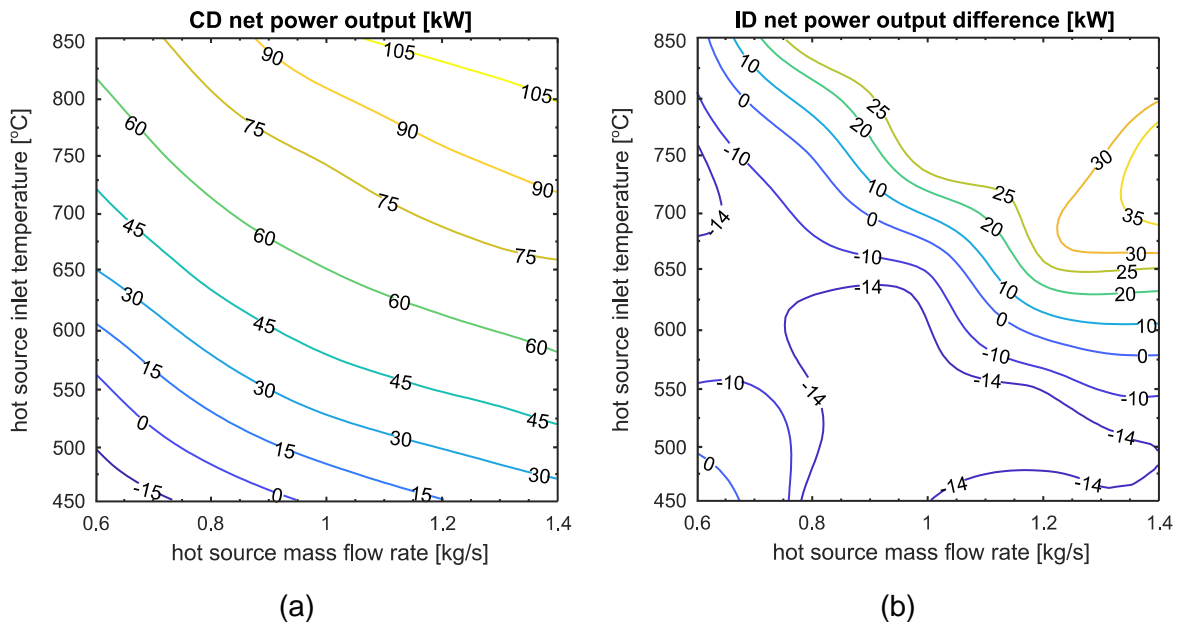
Figure 63 – Net thermal power output at different heat inputs to the sCO$_2$ unit: Coupled turbomachinery Drive (CD) (a) and differential net power output between Independent and Coupled turbomachinery Drive solutions (ID- CD) (b)

Figure 63.b shows the net power difference between independent and coupled turbomachinery drive simulations (ID-CD). At the same operating conditions, the adoption of independent drives for the turbine and compressor can lead to an improvement of the system performance. Indeed, for a heat source inlet temperature of 700°C and mass flow rates higher than 1.0 kg/s, 1.1 kg/s and 1.2 kg/s, decoupling the turbomachines leads to a net power output increase of 10 kW, 20 kW and 30 kW respectively. Close to the design point (1 kg/s, 650°C), the independent speed regulation does not lead to any performance benefits. When the heat source mass flow rate and inlet temperature are below 1 kg/s and 650°C, there is actually a

131

slight decrease of the system net power output up to -10 kW. Hence, the independent drive solution is only beneficial for part-load operating conditions exceeding the design point. In particular, the additional power output is more affected by the heat source temperature than the mass flow rate.

A more in-depth insight on the power output trends is provided by the optimised performance of the compressor and the turbine in both the configurations investigated. In particular, Figure 64 displays the power required by the compressor (Figure 64.a) and the one generated by the turbine (Figure 64.b) when the machines are coupled. The compressor presents a low sensitivity to the thermal load supplied by the waste source, showing a power consumption increase of the 6.7% for a decrease of the thermal load of 30% (Figure 64.a). This worse performance mainly occurs since a reduction of the heat source inlet temperature or mass flow rate do not allow supercritical conditions of the working fluid at the compressor inlet. For the same thermal load variation, the turbine shows a performance decrease of the 36.4% (Figure 64.b). Therefore, the optimisation of the turbine operating conditions based on the heat source availability is the most effective contribution to improve the system performance.

This is further evidenced in Figure 65, which shows the difference between the optimised compressor power consumption (Figure 65.a) and the power generated by the turbine (Figure 65.b) considering an ID configuration and the ones obtained in CD configuration. In fact, the improvement of sCO_2 system performance achieved in the ID case showed in Figure 63.b is driven by an improvement of the turbine performance rather than the compressor ones. For instance, for a waste heat source mass flow rate and inlet temperature of 1 kg/s and 750°C respectively, the 20 kW increase in the system net power output (Figure 63.b) results from the optimisation of the turbine operating conditions (30 kW increase in the power generated, Figure 65.b). The performance increase is obtained thanks to a higher mass flow rate of CO_2 flowing across the machine which leads however to a small decrease in the compressor performance (10 kW increase in the power consumption, Figure 65.a) since the cycle pressure ratio remains almost constant.

Figure 66 shows the optimal speeds for the independent and coupled turbine designs. With reference to Figure 66.a, the turbine performance optimisation in the ID configuration is achieved by increasing the machine revolution speed accordingly to the thermal load provided by the heat source. In fact, assuming a unitary mass flow rate of the waste heat source, when the inlet temperature of the flue gas increase from 650°C up to 850°C, the optimised turbine revolution speed is increased from 86000 RPM to almost 100000 RPM.
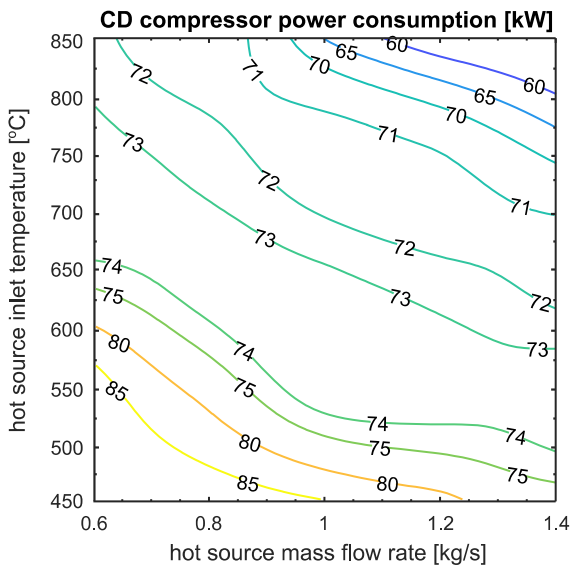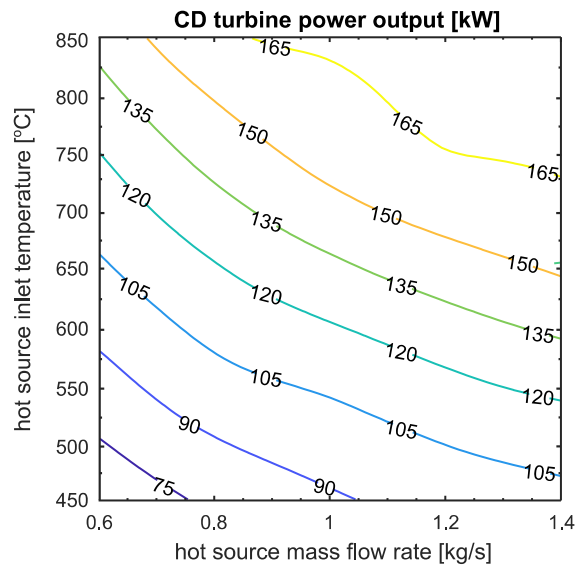
(a)   (b)

Figure 64 – Compression power consumption of the sCO$_2$ unit for different heat inputs: Coupled turbomachinery Drive (CD) (a) and differential compression power consumption between Independent and Coupled turbomachinery Drive solutions (ID- CD) (b)
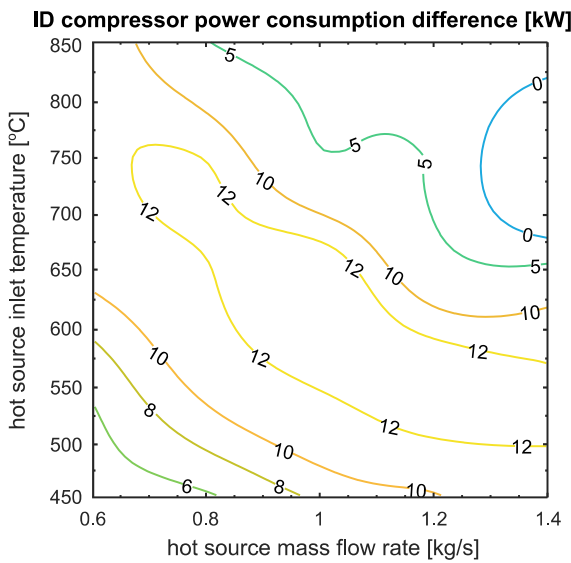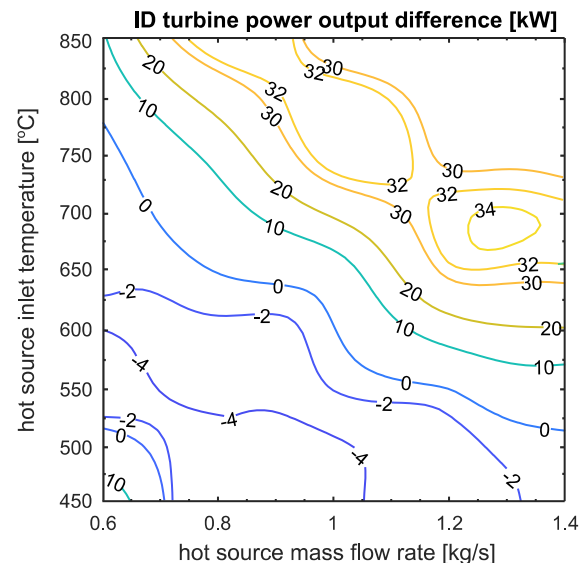
(a)   (b)

Figure 65 – Expansion power output of the sCO$_2$ unit at different heat inputs: Coupled turbomachinery Drive (CD) (a) and differential net power output between Independent and Coupled turbomachinery Drive solutions (ID- CD) (b)

For the CD configuration the revolution speed range of the turbine is constrained by the compressor design and cannot thus assume values higher than 90000 RPM, as showed in Figure 66.b, which displays the optimal revolution speed assumed by the compressor and the turbine for the different thermodynamic conditions of the waste heat source. Furthermore, it can be noticed in Figure 66 that when the thermal load supplied by the waste heat source

133

decreases (mass flow rate and inlet temperature lower than 1 kg/s and 650°C respectively) the maximisation of the system power output is achieved in both cases by lowering the revolution speed of the turbomachines, which are decreased down to the minimum value of 80000 RPM and 82000 RPM for the ID and CD configuration respectively. Indeed, the maximum and minimum value of the pressure in the cycle are fixed by the thermal loads in the primary heater and gas cooler respectively. For this given cycle pressure ratio, a decrease of the machine revolution speed leads to a slight increase of the CO_2 mass flow rate flowing in the sCO2 loop, which consequently positively impacts the system net power output.
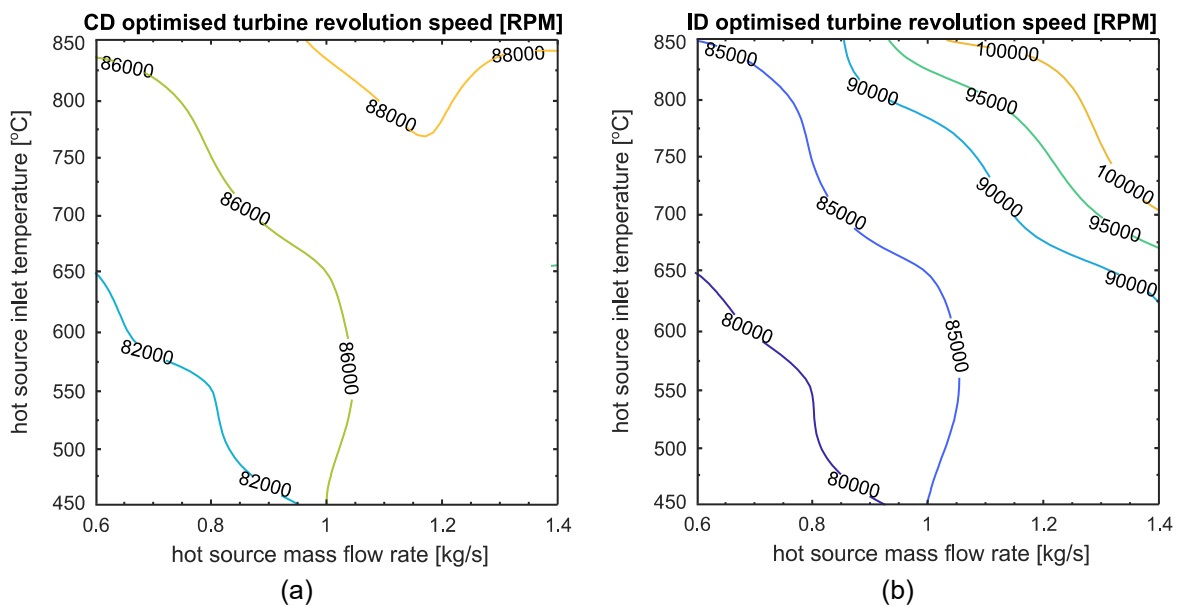
Figure 66 – Optimised speeds for the Independent (a) and Coupled (b) turbine design configurations

6.2 Transient Heat Load Variations

Besides the steady-state analysis of the sCO2 unit, a further important aspect is the investigation of the unit dynamic response to time varying heat loads as well as in extra-ordinary operations such as startup and shutdown. Indeed, even for small power outputs, heat to power conversion technologies such as Steam or Organic Rankine cycles have relatively large components, with high thermal mass and working fluid inventories.

These lead to a high thermal inertia which influences the system dynamics [109] and has an impact on the operation of the single components. To investigate these aspects, two transient heat load profiles have been simulated. In particular, the first profile has been obtained by varying the flue gas mass flow rate and maintaining the flue gas inlet temperature equal to the design condition. For the second one, the mass flow rate of the flue gas has been kept constant while the inlet temperature has been varied.

The results of the simulation showed that, for the particular sCO_2 system under consideration, the inertial effects are less prominent, and a higher operational flexibility can be obtained due to the high density of the working fluid and the small size of components.

Figure 67.a demonstrates this concept, showing the response of the CO_2 temperature at the inlet of the turbine (continuous line) and the compressor (dashed line) to a variation of the heat load at the primary heat exchanger resulting from a change in the flue gases mass flow rate. In particular, the time varying mass flow rate profile consists of a number of ramps and plateaus. The time length of the plateaus is of 400s while the ramp lasts 200s. During the plateaus, the mass flow rate of the flue gases assumes the same minimum and maximum values of 0.75 kg/s and 1.25 kg/s respectively.

No delays are noticeable in Figure 67.a with regards to the dynamic response of the turbine inlet temperature. Hence, for this specific system, the thermal inertia effects are negligible. In particular, the turbine inlet temperature (red line) promptly varies from the value of 470°C to 525°C, when the gas flow rate goes from 1.00 kg/s to 1.25 kg/s and drops to 410°C when the gas flow rate decreases to 0.75 kg/s. The same trend holds for the pressure, which goes from a minimum of 135 bar at 0.75 kg/s of flue gas up to a maximum of 140 bar when the flue gas mass flow rate increases to 1.25 kg/s.

The changes of the working fluid thermodynamic conditions at the compressor inlet change less notably following the heat source mass flow rate variations, with the compressor inlet pressure remaining almost constant and equal to 72.5 bar. This effect is mainly due to the receiver placed downstream the gas cooler, whose large capacity contributes to decouple the hot and the cold sides of the sCO_2 loop.

The inverse response of the compressor inlet temperature, which goes from 39°C to 40°C (Figure 67.a) when the mass flow rate of the flue gases decreases from 1.25 kg/s to 0.75 kg/s, can be explained by the increase of the CO_2 mass flow rate circulating in the system. A higher heat load leads to a decrease of the working fluid density, due to the increase of its temperature, and consequently to a reduced CO_2 mass flow rate (Figure 67.a). However, the cooling load supplied by the heat sink remains fixed, and therefore a lower temperature at the compressor inlet is achieved. The opposite occurs for a decrease of the hot source mass flow rate (Figure 67.a).

Figure 67.b shows the response of the system to a variation of the flue gas inlet temperature (black line) from 450°C to 850°C with same time duration of ramps and plateaus imposed for Figure 67.a. The trends of the thermodynamic conditions (pressure and temperature) of the working fluid at the inlet of the compressor and the turbine resemble the ones shown in Figure 67.a, but more accentuated given the deeper effect of the hot source inlet temperature on the

cycle parameters. In particular, the turbine inlet temperature goes from 350°C for the minimum temperature value of the flue gases (450°C), up to 650°C for its maximum one (850°C), while the compressor one goes from 39°C to 41°C for the same temperature variation of the flue gases (Figure 67.b).
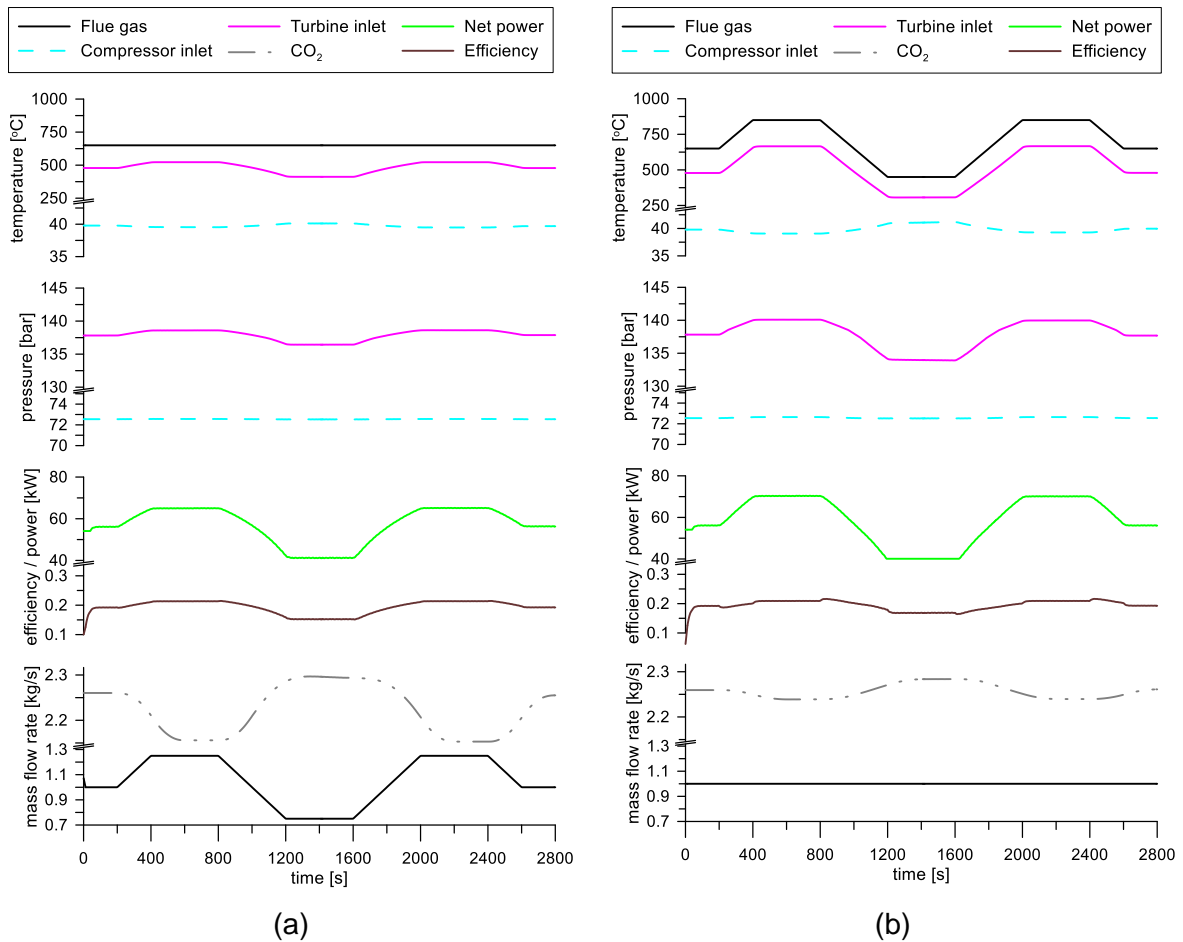
Figure 67 – Dynamic response of the sCO$_2$ system to a transient waste heat load profile: constant waste heat inlet temperature and variable mass flow rate (a) and variable waste heat inlet temperature and constant mass flow rate (b).

6.3 Startup and Shutdown

The system behaviour during the startup and shutdown stage has been assessed with particular reference to the turbomachinery operations. After a pre-heating phase in which the working fluid is brought above the supercritical state to prevent any liquid pocket in the loop, the turbomachines are span to their nominal revolution speed. To investigate the system dynamics during these conditions, a rotational speed profile has been imposed to the single-shaft turbomachinery unit as boundary condition as shown in Figure 68.

In particular, the turbine and compressor speed increases from 0 to 86000 RPM in 900s during the startup phase, it is then held to the nominal value of 86000 RPM for 1200s and then is

decreased from 86000 RPM to 0 RPM in 700s. The ramp rates have been set according to the maximum acceleration allowed for the generator rotor, which is equal to an increase of 100 RPM every second for the startup stage and to a 130 RPM decrease every second for the shutdown (black dashed-line in Figure 68). During the whole transient simulation, the heat source mass flow rate and inlet temperature have been kept constant and equal to their nominal values of 1 kg/s and 650°C respectively.
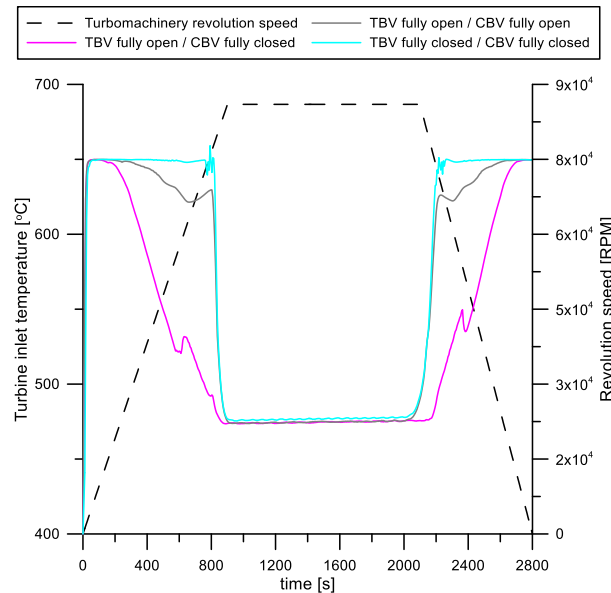
Figure 68 – Dynamic response of the turbine inlet temperature during the startup and shutdown for different operating strategies of the turbine (TBV) and the compressor by-pass (CBV) valves: fully opened and/or fully closed.

When the turbine and compressor bypass valves (Figure 47) are both closed, for low values of the turbomachinery speed, the temperature at the turbine inlet would be equal to 650°C due to the low mass flow rate in the system and the low pressures achieved in the circuit (cyan line, Figure 68). To overcome this issue, two different strategies for the turbine by-pass globe valve (TBV) and the compressor by-pass globe valve (CBV) have been simulated. In the first case, both the TBV and the CBV are fully open during the acceleration and deceleration decrease ramps and closed when the nominal value of 86000 RPM is achieved.

In the second strategy, the CBV is kept fully closed and only the TBV is operated. Similarly to the first strategy, the TBV is opened during the startup and shutdown stages (when the revolution speed of the turbomachines is increased and decreased respectively) and closed when the nominal value of 86000 RPM is achieved. In both strategies, the valve opening profiles are the same: the second strategy differs from the first one only because the CBV is not operated.

The standalone opening of the TBV (magenta line, Figure 68) achieves better results in terms of turbine inlet temperature reduction, since it allows the temperature to decrease after a

137

limited time period of 225s, bringing it down from 650°C to 480°C when the speed increases from 25000 RPM to 86000 RPM. A much less pronounced effect is produced by the simultaneous opening of both valves (grey line, Figure 68). In this case, the turbine inlet temperature is reduced only from 650°C to 630°C when the turbomachinery speed exceeds 55000 RPM. Therefore, the beneficial effect due to the opening of the turbine by-pass valve is counter-balanced by the opening of the compressor bypass, which decreases the mass flow rate going through the primary heater and therefore leads to a temperature increase at the turbine inlet.

To better understand how the turbine by-pass valve opening affects the dynamics of the working fluid temperature at the turbine inlet, reference can be made to Figure 69. This chart displays the startup and shutdown turbine mass flow rate and pressure ratio evolution for the three strategies presented in Figure 68 superimposed to the turbine operating map. When TBV and CBV are both closed (cyan circles) the working fluid flows entirely through the turbine and this prevents the achievement of the suitable pressure ratio across the machine during the revolution speed increasing and decreasing ramps (as shown in the low part of the left-hand side of Figure 69, where the pressure ratio starts to increase only for revolution speeds higher than 50000 RPM during the unit startup and shutdown).

As a consequence, a lower CO_2 mass flow rate circulates in the loop and higher temperatures are achieved at the heater outlet despite the same heat load. When TBV and CBV are fully opened (grey circles), the mass flow rate flowing into the turbine decreases. During the startup and shutdown, this leads to higher pressure ratios than the former case (lower left-hand side part of Figure 69). However, since the compressor by-pass valve is also open, the compressor is not able to fully pressurise the fluid due to the lower mass flow rate.

On the contrary, the sole opening of the turbine by-pass valve (magenta circles), allows to achieve a more gradual build-up of the pressure ratio across the machine, which leads to higher mass flow rates circulating throughout the loop and a faster achievement of the nominal working fluid temperature at the turbine inlet (Figure 69). From this analysis it can be concluded that during the startup and shutdown phase of the unit, acceleration and deceleration ramps of the turbomachinery revolution speed, by-passing the turbine (thus reducing the mass flow rate throughout the machine) and normally operating the compressor, leads to a faster and more gradual increase of the working fluid mass flow rate circulating in the loop and thus the achievement of the nominal operating conditions of the system limiting the exposure of the components to extreme temperatures.

Figure 69 further allows to explain the small fluctuations of the turbine inlet temperature depending on the strategy considered in Figure 68. This is mainly due to the different build-up

of pressure in the machine for each different case. Indeed, it is possible to observe that, during the startup and the shutdown of the turbomachinery, the pressure ratio across the turbine changes with time following a different path for each of the considered strategies. These pressure ratio variations lead to small fluctuations of the working fluid mass flow rate processed by the turbine and, in turn, in the whole circuit. Since the heat load is assumed as constant in these simulations and the energy balance must hold at the primary heater, these variations of working fluid mass flow rate result in temperature fluctuations at the turbine inlet.
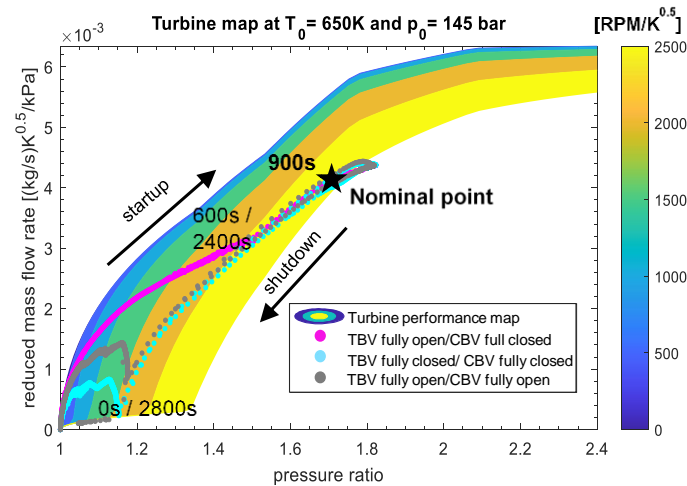
Figure 69 – Turbine operating map with superimposed transient trends during the startup and shutdown profiles considered in Figure 68. Revolution speed expressed in reduced revolutions per minute [RPM/$K^{0.5}$].

6.4 Summary

In this chapter the off-design performance of the supercritical CO_2 (sCO_2) system designed and constructed at Brunel University London have been assessed through steady state simulations at different mass flow rates and temperatures of the exhaust gases acting as heat source and of the cooling water-glycol mixture acting as heat sink. For a 20% increase in the exhaust gas temperature the system showed a 50% increase in the power output whereas for a 20% increase in the exhaust mass flow rate the system showed a 20% in the power output.

A decrease in the cooling fluid inlet temperature from 26°C to 16°C leads to an increase in the system power output and efficiency from 40 kW to 72 kW and from 9% up to 21% respectively, Moreover, the analysis showed that no condensation at the compressor inlet occurs since the minimum temperature achieved is 35°C, which ensures safe operating conditions for the compressor over the whole range of cooling fluid inlet temperatures investigated.

Other key features of transient variations of the flue gas flow rate and temperature in time intervals of 1200s and 2800s always led to changes in the turbine inlet temperature. The

turbine inlet pressure was slightly affected (max 3% of design point), especially at variable flow conditions but constant temperature of the heat source. More importantly, unlike in the case of ORC systems of similar power output [46], the turbine inlet temperature variation did not experience any delay with respect to the topping process. This demonstrates the flexible nature of sCO_2 systems. The simulation of the unit startup and shutdown stages showed that such operations can be substantially helped using by-pass compressor and turbine valves, which can lead to a much safer build-up of temperatures and pressures along the loop.

7. Control System Design

As it has been shown in Chapter 6 the performance of the sCO_2 unit strongly depend on the heating and cooling loads available. In WHR applications, the waste heat source presents a strong variability due to sudden change in the topping industrial processes. These fluctuations may result in a decrease of the unit performance as well as in the overheating of the working fluid with the risk of overexposing the system components to excessive thermal loads and stresses, with the consequent risk of damages or failures.

Variations in the system performance could also be caused by a change in the cooling load, which with the use of a dry cooler as heat sink depends on the environmental conditions. In particular, too high environmental temperatures could lead to CO_2 temperatures at the compressor inlet higher than 35°C, with a consequent detrimental effect on the net power output generated by the unit (since the compressor power consumption increases when the CO_2 is compressed far from its critical point).Therefore, it is important to assess the most suitable control variables for the regulation of the main cycle parameters, as for instance the working fluid temperature at the turbine and compressor inlet. Such regulation has a two-fold objective, the optimisation of the system performance and the safe operation of the power block under such variations of the heat source and sink.

To do so, a sensitivity analysis has been carried out on different system control variables. Among the several options available, the revolution speed of the turbomachines as well as the mass charge of the system, namely the inventory, have been selected. Therefore, a control strategy has been designed and numerically tested during transient loads of the waste heat source adopting as controlled variable the Turbine Inlet Temperature (TIT). Benefits and disadvantages have been also outlined. Finally, a further control strategy aiming to ensure safer operating conditions for the turbine in case of excessive heat loads has been proposed.

7.1 Sensitivity Analysis

The sensitivity analysis considered the mass charge (or inventory) in the sCO_2 loop and the revolution speed of the turbomachines varying in a range from 20 kg to 60 kg and from 50000 RPM to 90000 RPM respectively. During these simulations, the inlet conditions of the heat sink and the heat source (e.g. mass flow rates and temperature) have been kept constant and equal to their nominal values. These quantities are reported in Table 35.

It is worth to start by clarifying that the results presented strongly depend on the nature of the turbomachine maps. As such, the same sCO_2 system equipped with different turbomachines might exhibit a different behaviour. Figure 70.a shows the effects of the variations of the

turbomachinery revolution speed and the system inventory on the Turbine Inlet Temperature (TIT). For a CO_2 nominal charge of 40 kg, varying the revolution speed from 90000 RPM to 50000 RPM, leads to change of the turbine inlet temperature from 500°C to 450°C. On the contrary, a lower percentage variation of the system charge (from 30 kg to 55 kg) is able to change the TIT from 500°C to 350°C, considering the nominal revolution speed of 86000 RPM (Figure 70.a). Hence, the TIT is more sensitive to variations of the system inventory rather than the turbomachinery revolution speed. This difference can be explained by referring to Figure 70.b. Increasing the system mass charge at higher revolution speeds leads to higher CO_2 mass flow rates circulating in the system, which allow to lower the temperature of the working fluid at the inlet of the turbine. Operating the system at these conditions is particularly important in order to reduce the turbine inlet temperature in case of high peaks of the waste heat source temperatures. Using the revolution speed as control variable would in fact not allow to keep the TIT in the safe temperature margin.
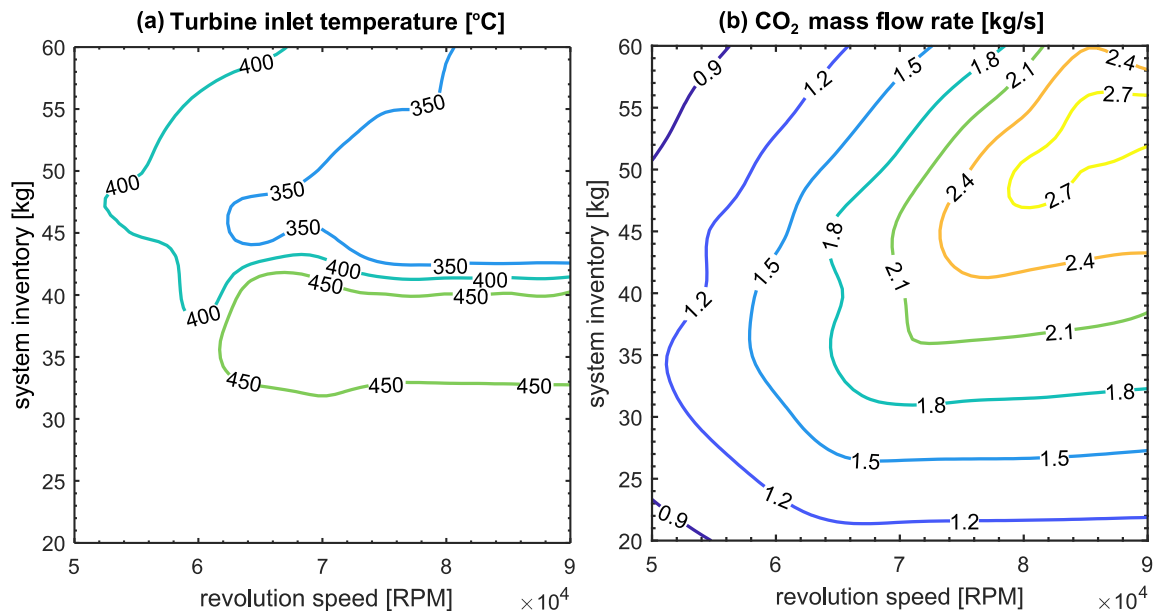
Figure 70 – Contour maps of turbine inlet temperature (a) and CO_2 mass flow rate (b) as a function of the turbomachinery revolution speed and the system inventory.

With regards to the CO_2 pressures at the turbine inlet, the variation of both the turbomachinery revolution speed and the CO_2 inventory in their whole respective range does not lead to excessive pressures. For an inventory of 60 kg/s and a revolution speed of 90000 RPM, the maximum pressure achieved at the turbine inlet is equal to 150 bar (Figure 71.a), which can be considered in the safe operating margin of the system. Figure 71 also shows the effect of the CO_2 injection in the system on the compressor inlet pressure, which goes from 50 bar to more than 80 bar when the mass charge varies from 20 kg to 60 kg (Figure 71.b).
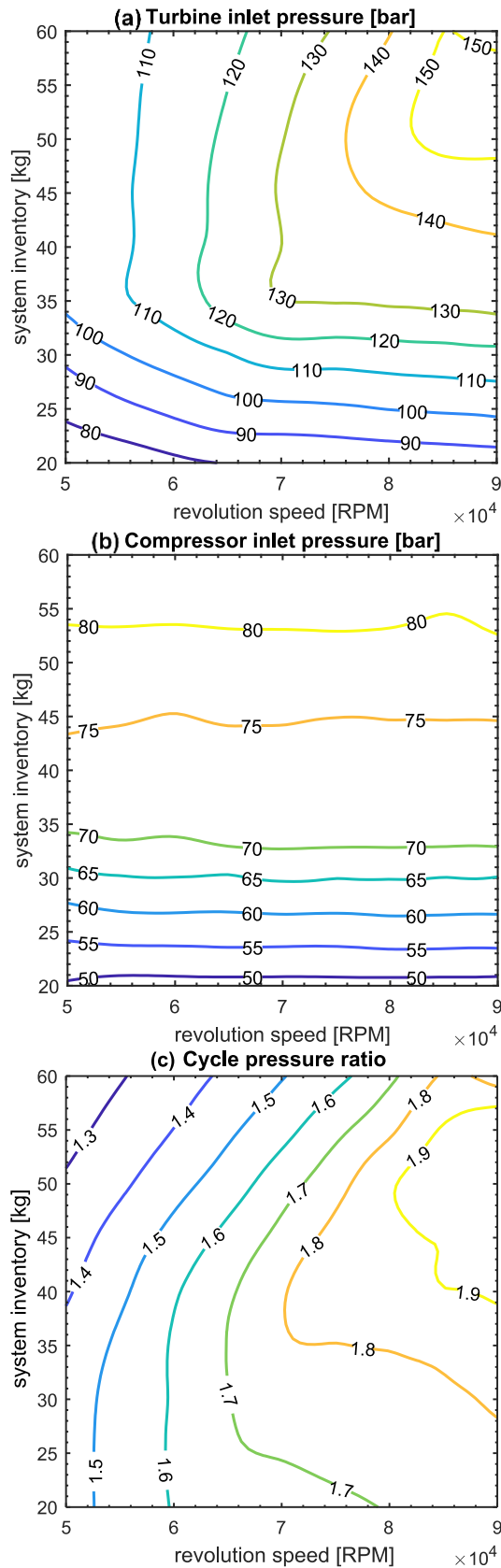
Figure 71 – Contour maps of the turbine (a) and compressor (b) inlet pressure, and the cycle pressure ratio (c) as a function of the turbomachinery revolution speed and the system inventory.

It is possible to notice that the compressor inlet pressure is only affected by the supercharging of the circuit. On the contrary, the turbine inlet pressure depends on both control variables since the pressure at the inlet of the machine is affected by the lowest cycle pressure (set at the compressor inlet) and also from the cycle pressure ratio, which depends mainly on the turbomachinery revolution speed (Figure 71.c). For this reason, the turbine inlet pressure increases following the rise of both the system inventory and the turbomachinery revolution speed (upper part of Figure 71.a).

The cycle pressure ratio also affects the turbine inlet temperature as can be noticed from comparison of Figure 70.a and Figure 71.c. Increased expansion ratios across the turbine (top right-hand side of Figure 71.c) lead to lower temperatures at the turbine outlet and, in turn, to reduced residual heat available at the hot side of the recuperator. This lower amount of residual thermal energy available, leads to lower temperatures at the outlet of the recuperator cold side and, assuming a constant heat supply from the flue gases, and lower temperatures at the turbine inlet.
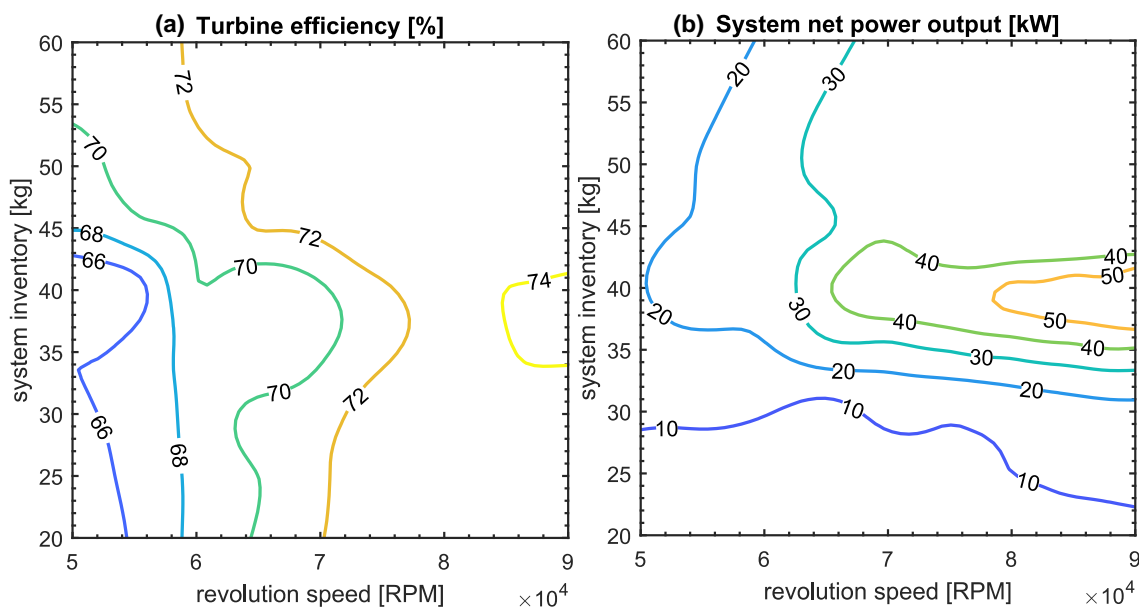
Figure 72 – Contour maps of turbine total-to-static efficiency (a) and sCO$_2$ system net thermal power output (b) as a function of the turbomachinery revolution speed and the system inventory.

A further interesting aspect is the effect of turbomachinery revolution speed and the system inventory on the turbine performance and on the system net power output. Figure 72.a shows the inventory change, for a given fixed revolution speed of 80000 RPM and the CO$_2$ inventory range, does not affect substantially the turbine isentropic efficiency of 73%. On the contrary, the change in the revolution speed has a more pronounced effect on the turbine isentropic efficiency, which drops from the optimal value of 74% at 86000 RPM to 65% when the speed

is decreased to 50000 RPM (for a system mass charge of 40 kg as shown in Figure 72.a). This trend can be explained by looking at the turbine maps shown in Figure 53. The map shows that, for a wide operating range of the machine, the isentropic efficiency remains almost constant, while it drops consistently for small cycle pressure ratio and lower CO_2 mass flow rates. These operating conditions are mainly achieved at lower revolution speeds of the compressor-turbine-generator unit.

The losses in the turbine performance directly affect the system net power output, which decreases for the same variation of the revolution speed from 50 kW to 20 kW (Figure 72.b). At the nominal revolution speed of the turbomachines, the net power output of the system strongly depends also by the system inventory, going from 10 kW when the system is filled with 20 kg of CO_2 to 50 kW for a CO_2 mass in the circuit of 40 kg (Figure 72.b). When the system is in fact undercharged, the pressure at the compressor inlet is lower than 74 bar and thus the supercritical conditions of the CO_2 are not achieved, compromising the performance of the unit.

7.2 Inventory Control Design

The results from the steady-state analysis showed that, for the system considered, the regulation of the inventory represents a more suitable option to control the turbomachinery inlet conditions without excessively compromising the system performance and operational stability. In particular, the control strategy here proposed acts on the CO_2 mass in the circuit to regulate the turbine inlet temperature, which is an important parameter both from a cycle performance perspective as well as to prevent unsafe operating conditions due to unforeseen peaks in the waste heat load.

The inventory control envisaged works as follows: for a given change of the heat load, if the turbine inlet temperature becomes higher than the set point value, the system is charged with additional mass of working fluid, which flows from the high pressure inventory control tank to the circuit. The increased CO_2 mass in the system (or system inventory) leads to a rise of the minimum cycle pressure at the compressor inlet and the CO_2 mass flow rate processed until the control error is eliminated. On the other hand, if the temperature at the turbine inlet drops, the working fluid is withdrawn from the main loop and flows into the low-pressure inventory control tank, lowering the minimum cycle pressure and mass flow rate.

The addition and the withdrawal of the CO_2 is thus possible thanks to two inventory control tanks, one at higher and one at lower pressure compared to the circuit charging point. The tank used to inject the CO_2 in the system is at higher pressure than the circuit charging location, while the tank used to store the extracted CO_2 from the system is at a lower one. By

modulating these pressure differentials between the high/low pressure tanks and the circuit charging point (which can be done by using two pressure regulators located downstream the tanks), the control system is able to set the right amount of CO_2 to be injected/withdrawn into/from the circuit.

The hardware implementation of this control approach would require, in addition to the two tanks at high and low pressure connected to the same charging point, a three-way valve to exclude the addition or withdrawal line depending on the desired control action. Two pressure regulators should be placed upstream the tanks to be able to change the pressure level between the two extreme values of the high- and low-pressure tanks. From a modelling perspective, this hardware architecture can be simplified by considering just one inventory tank able to assume a certain level of pressure between the maximum and minimum values of 110 bar and 55 bar, as shown in Figure 73.

The two inventory tanks are connected to a circuit feeding point between the gas cooler and the receiver, as shown in Figure 73. This design choice allows to avoid detrimental effects on the compressor operation due to a possible fast charge or discharge of the system. In fact, the large volume of the receiver smooths the sudden pressure variations following the increase or decrease of the working fluid mass charge in the system. The working fluid temperature injected in the main loop is assumed to be at 35°C.

Firstly, the inventory tank is assumed as an infinite capacity and the dynamics of the pressure regulators and of the three-way valve has been neglected. Afterwards, to investigate the effective dynamics of such control action, the capacity of the tank has been considered.

The modulation of the inventory control tank pressure is commanded by a Proportional-Integral (PI) controller to reduce the error between the actual turbine inlet temperature and the set point. The derivative term has been set to zero because of the possible high control actions resulting from noisy signals. To prevent the saturation of the control action caused by the integral term, an anti-wind-up scheme has also been adopted. The proportional and integral coefficients have been calculated via a lambda tuning procedure [162]. In particular, a first order relationship has been considered between the mass flow rate of the fluid injected in the system and the controlled process variable (turbine inlet temperature).

Therefore, the control output has been modified in the entire admissible range and the process variable response analysed [148]. From the calculated time constant (τ) and process gain (K), the resulting proportional and integral coefficients of the PI controller are 0.177 and 0.011 respectively. Firstly, the inventory tank is assumed as an infinite capacity The tank is also assumed to have an infinite capacity while the dynamics of the pressure regulators and of the three-way valve have been neglected in the current study.
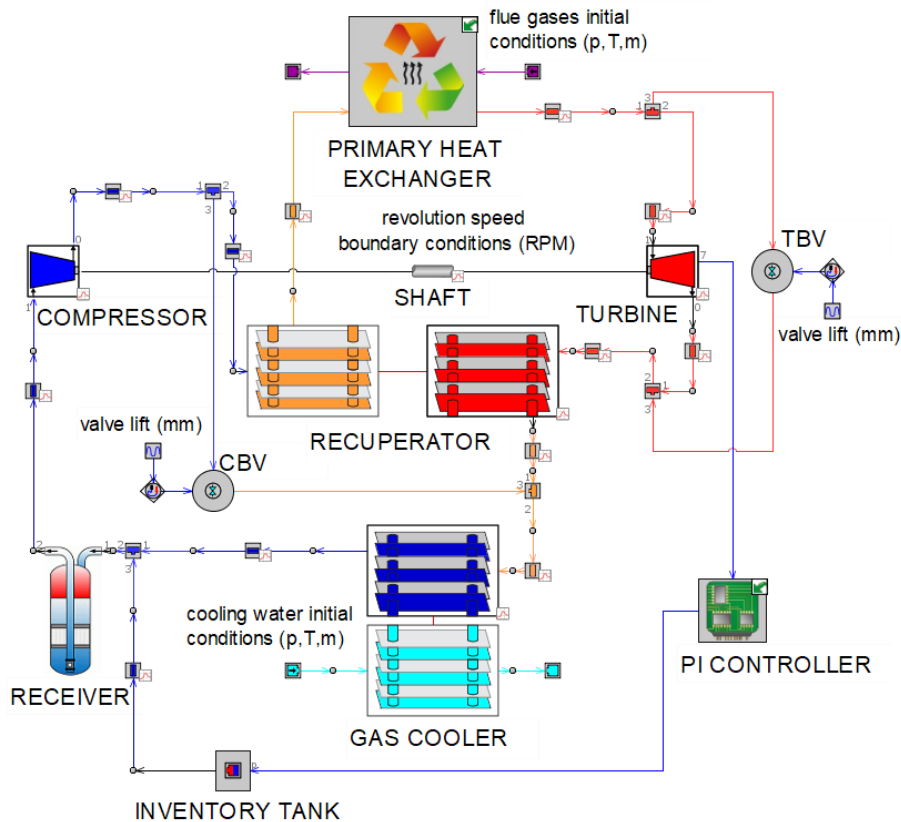
Figure 73 – Model block diagram of the full sCO$_2$ heat to power block including the PI controller.

7.3 Inventory Control Performance

To firstly assess its performance, the turbine inlet temperature is regulated assuming the transient heat load profile reported in Figure 67.b, where the turbine inlet temperature of the waste heat source is varied between the two plateaus of 450°C and 850°C while the mass flow rate has been kept constant and equal to the nominal value of 1 kg/s. Both the uncontrolled and controlled response of the turbine inlet temperature system have been reported in Figure 74. The temperature set point has been assumed equal to 500°C and it is displayed as a dashed grey line. It is possible to notice that the controller is able to regulate the turbine inlet temperature despite the large variations of the heat source temperature. The effects of the saturation of the control action are not fully compensated by the anti-wind-up scheme as it can be observed at 400s, 1200s, 1800s and 2400s, where the controlled inlet temperature assumes peak values of 520°C, 220°C, 550°C and 491°C respectively. The only case when the controller is not able to achieve the set point is when the waste heat source temperature assumes a value of 450°C. In this case, the controller sets the temperature value at the closest feasible temperature possible, which is 330°C (Figure 74).

From a performance perspective, it is possible to notice that the control of the CO_2 inventory leads to an improvement of the system thermal efficiency (which is calculated with respect to thermal energy recovered by the waste stream) and power output when the temperature of the flue gas increases. In particular, for the controlled case an increase of the 25% and of the 101% in the system thermal efficiency and net power output respectively can be observed, compared to the uncontrolled case, when the flue gas temperature achieves the maximum value of 850°C. On the contrary, when the flue gas temperature decreases to 450°C, the action of the inventory controller is detrimental, leading to a system operating condition where no electric power can be extracted by the heat recovered (net power output of -10 kW and system thermal efficiency equal to -0.05).
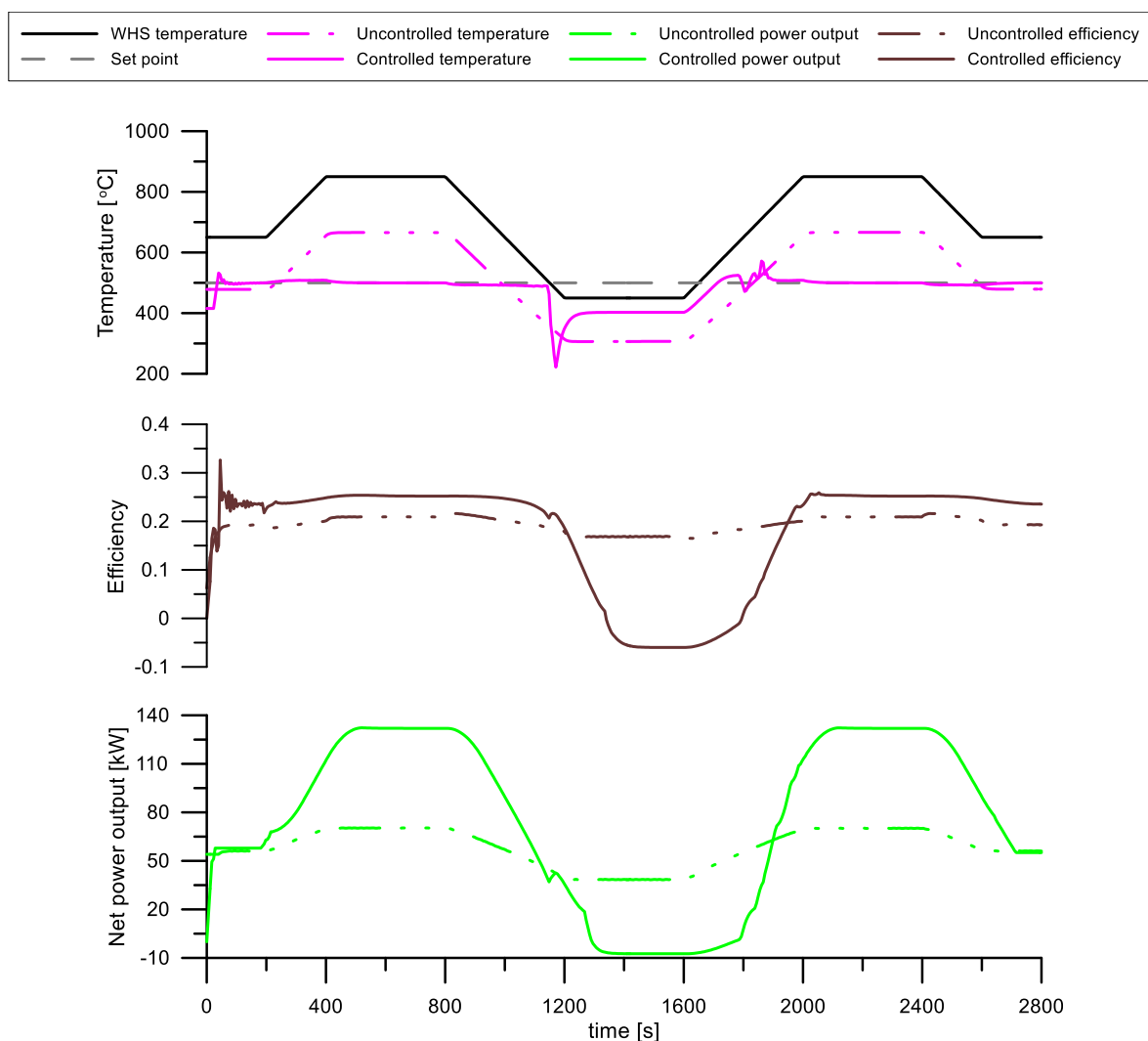
Figure 74 – Uncontrolled and controlled responses of the turbine inlet temperature for a 2800s transient waste heat load profile.

These effects are due to working fluid mass flow rate injection and extraction imposed by the controller. Indeed, following an increase of the flue gas temperature, the loop is charged with additional mass of working fluid, while the system is discharged in the opposite case.

148

Therefore, when the temperature of the flue gases is too low, to achieve the desired temperature set point, the inventory control system imposes an excessive extraction of CO_2 mass from the loop, leading to an operating condition where the turbine cannot supply the required mechanical power required from the compression to pressurise the working fluid. Indeed, for a lower mass flow rate circulating in the circuit, the isentropic efficiency of the turbine and especially the one of the compressor decrease, causing the detrimental effect on the system performance. Table 36 shows the different coordinates of the turbine and compressor efficiency maps when the waste heat source assumes the minimum temperature value of 450°C for both the uncontrolled and controlled system response.

Table 36 – Coordinates of the turbine and compressor maps for a waste heat source temperature of 450°C in case of a system uncontrolled and controlled response

	Variables	Units	Uncontrolled case	Controlled case
Turbine	Temperature	°C	307	402
	Pressure	bar	134	92
	Revolution speed	RPM	86000	86000
	Reduced mass flow rate	$(kg/s)K^{0.5}/kPa$	0.005	0.004
	Pressure ratio	-	1.8	1.7
	Isentropic efficiency	-	0.74	0.72
Compressor	Temperature	°C	41	57
	Pressure	bar	72	55
	Revolution speed	RPM	86000	86000
	Reduced mass flow rate	$(kg/s)K^{0.5}/kPa$	0.006	0.008
	Pressure ratio	-	1.8	1.7
	Isentropic efficiency	-	0.67	0.55

Despite then the inventory control has been considered as one of the most suitable control strategies for sCO_2 systems in the power generation sector [163], where the system thermal efficiency is optimised depending on the electric load set by the grid, this does not apply when waste heat recovery applications are considered. When indeed the objective is to maximise the power recovery depending on the dynamics of heat load supplied by the topping process, namely a heat load following strategy, the use of an inventory control system presents some criticalities since introduces a strong detrimental effect on the system performance for reduced thermal levels of the waste heat source. This limitation could be overcome by the adoption of

multi-level control system combining multiple control actions depending on the heat load available.

To test the performance of the controller on a real industrial case, a second transient heat load profile has been simulated. The profile refers to a typical process in an energy intensive industry. Figure 75 shows the transient heat load trend, composed by five different temperature plateaus of 650°C, 600°C, 700°C, 650°C and 725°C, with durations of 25s, 150s, 525s, 300s and 175s respectively (black continuous line, Figure 75).

The controlled response shows that the designed controller not only eliminates the error between the actual turbine inlet temperature and the set point, but also shows good dynamic performance. The slight overshoots at 300s, 860s and 1240s due to the control action saturation are indeed limited.
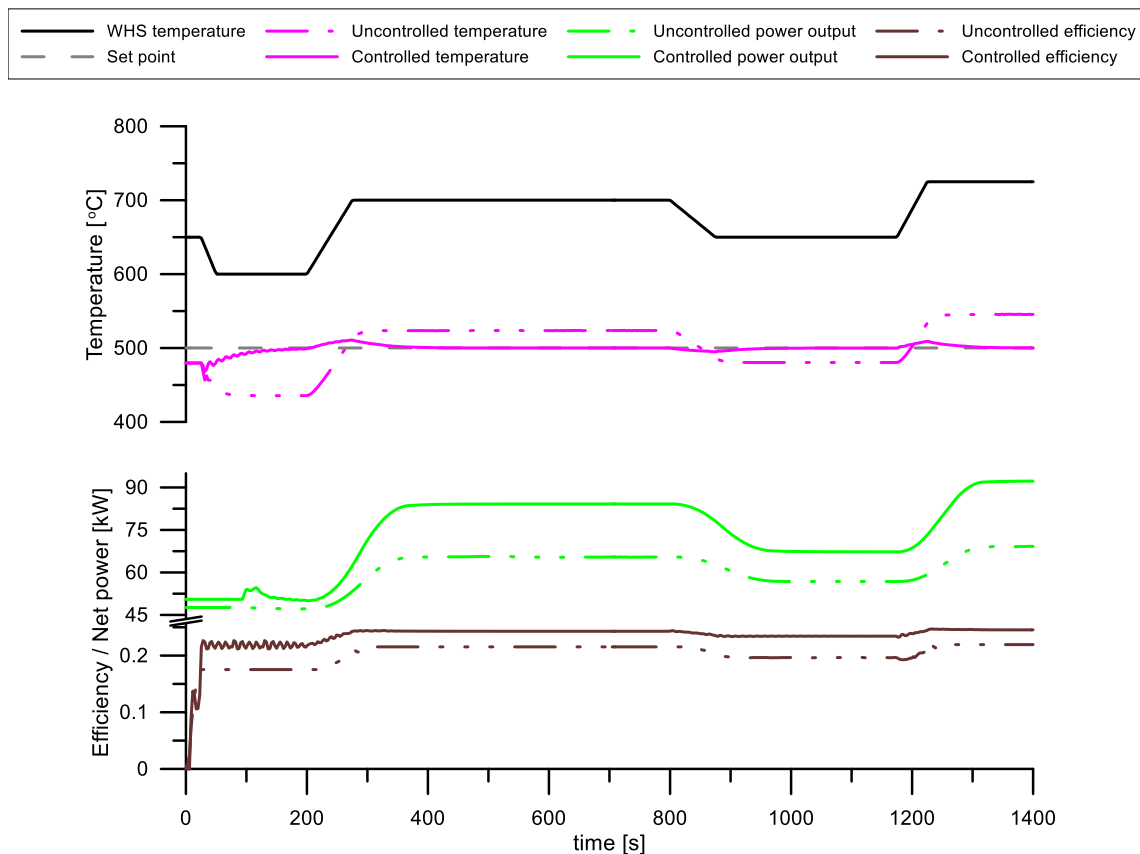
Figure 75 – Uncontrolled and controlled responses of the turbine inlet temperature for an industrial 1400s transient waste heat load profile.

It is possible also to notice that the turbine inlet temperature in the uncontrolled system is not able to achieve the set point value of 500°C. Values of 420°C, 520°C, 480°C and 545°C are indeed achieved for waste heat source temperatures of 600°C, 700°C, 650°C and 725°C respectively (Figure 75). From a performance perspective, for a such waste heat load profile, the inventory control leads to a net improvement of the system power output and thermal efficiency since the no substantial decreases of the waste heat source inlet temperature occur.

150

7.4 Heater By-pass Control

Besides the CO_2 system performance strongly depend on the turbine inlet temperatures achieved in the cycle as showed by the steady-state analysis, constraints exist on the maximum temperature achievable at the inlet of the machine. The turbine is the most stressed component in the system and for this reason its operating temperature should be kept in the design range.

This issue is particularly relevant in WHR applications because the waste heat source temperature can present a fluctuating trend (which follows the overlying topping industrial process). Therefore, a control strategy may be required to prevent temperature peaks of the working fluid and ensure safe operating conditions. In this sense, an inventory control strategy could present a too low dynamics to be effective in such situations [163].

Among the various options, the compressor and turbine by-pass globe valve are not suitable. The operation of the compressor globe valve could lead to a reduced mass flow rate of CO_2 flowing in the primary heater and consequently to higher temperatures at the turbine inlet. Similarly, the use of the turbine by-pass globe valve could lead to an excessive detrimental effect on the system performance.

A further method to regulate the turbine inlet temperature could be the by-passing of the heater, which could be realized by including in the system a needle by-pass valve between the cold side recuperator outlet and the turbine inlet as showed Figure 76. The valve has not been installed in the sCO_2 test facility at Brunel, it has been considered only from a numerical perspective to assess the eventual benefits and limitations.

When the valve is open, a part of the CO_2 mass flow rate (1.4 kg/s when the valve is fully opened) flows from the recuperator outlet directly to the inlet of the turbine, where it is mixed with the remaining flow at the outlet of the primary heater. The valve maximum flow area has been designed to ensure the safe operating conditions of the primary heater. In particular, when the valve is fully open, a CO_2 stream still flows in the heat exchanger to keep its wall temperature within design limits (<700°C).

The valve lift position is regulated by a PI controller, whose objective is to minimize the error between the target turbine inlet temperature and the measured one. The controller coefficients for the design strategy are -0.038 for the proportional term and -0.063 for the integral one.
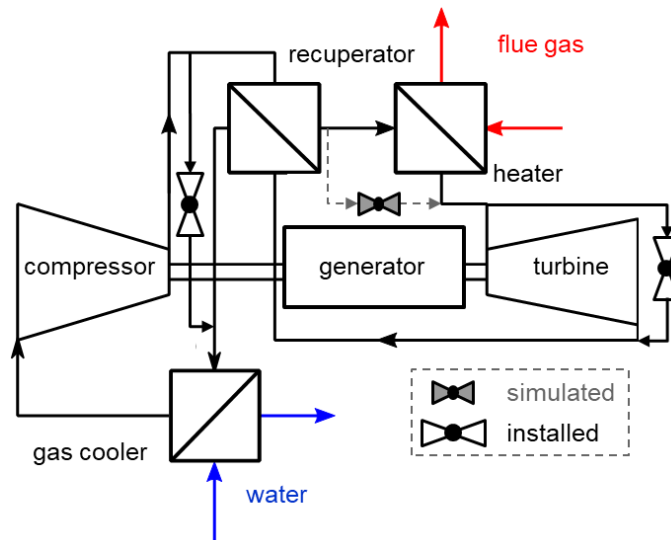
Figure 76 – Schematic representation of the sCO$_2$ system including the heater by-pass valve (not installed in the test facility developed at Brunel)

To test the performance of the controller, the same transient waste heat load profile showed in Figure 75 has been simulated. Figure 77 shows the results of the analysis. The black line represents the inlet temperature of the flue gases (FG), which varies between the values of 650°C, 600°C, 700°C, 650°C and 725°C (1st, 2nd, 3rd, 4th and 5th plateau respectively). While the mass flow rate of the flue gases has been kept equal to 1 kg/s.

For flue gases temperatures higher than 650°C, the uncontrolled turbine inlet temperature increases up to 560°C, which may impact the operating lifetime of the machine. It is possible to notice that the action of the controller is capable to prevent this detrimental effect (Figure 77).

For higher temperatures of the flue gases (500s and 200s plateaus at 700°C and 725°C respectively), the valve assumes the fully open position but the mixing of the high and low temperature flows (from the primary heater and the valve outlet respectively) is not sufficient to achieve the desired temperature at the turbine inlet. However, the controller is able to keep the TIT at 480°C (Figure 77), which can be considered within the temperature safe margin of the machine.

In general, the controller shows a good promptness and its action allows a safe operating temperature range for the turbine without compromising the system performance.
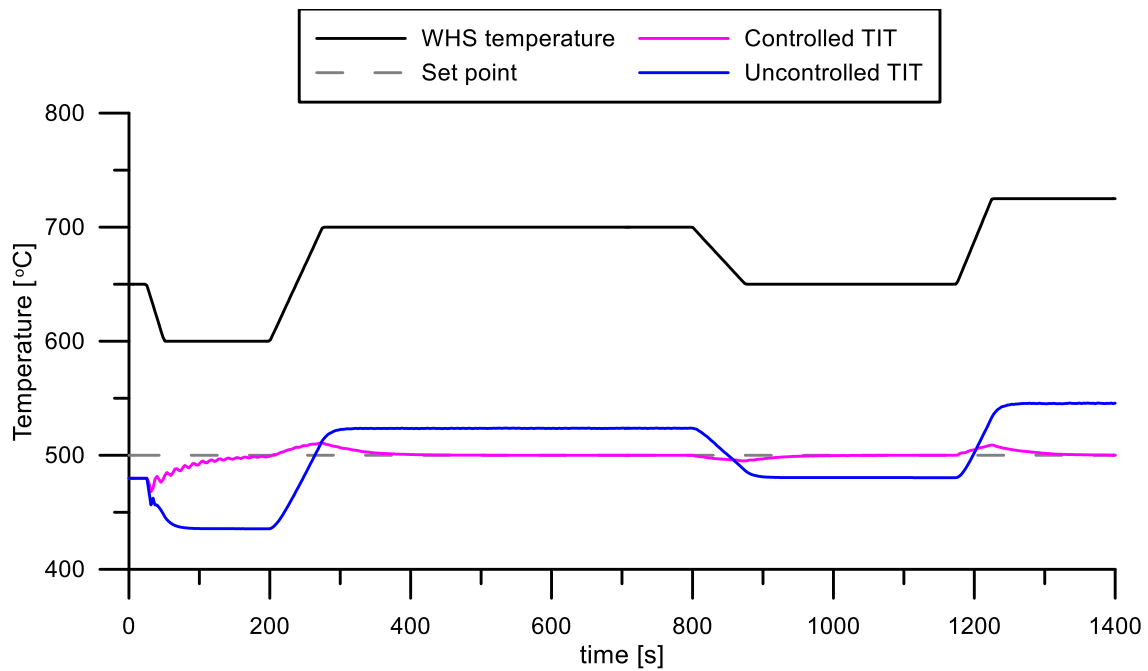
Figure 77 – Dynamic response of the sCO$_2$ unit to a transient waste heat load profile with and without the operation of the heater by-pass valve.

7.5 Summary

A steady-state analysis was performed to assess the most suitable control variables for the regulation of the inlet conditions at the turbine. The system inventory was shown to be a good parameter for the control of the turbine inlet temperature having only a small impact on turbine performance. A reduction in CO$_2$ from 60 to 20 kg would indeed result to only 1.0% reduction in the turbine isentropic efficiency.

Based on these outcomes, an inventory control strategy was designed to regulate the turbine inlet temperature during transient heat load profiles. The PI controller showed good accuracy and dynamic performance, being able to reduce the error. Considering a single location for additions/withdrawals of CO$_2$ downstream the gas cooler allowed to prevent instability in the compressor operation for sharp decreases of the waste heat source temperature.

The analysis further highlighted the possible detrimental effect on the system performance introduced by the inventory control action when a heat load following control strategy is considered. Indeed, when the waste heat source is supplied at a low temperature, an excessive extraction of the working fluid mass flow rate from the circuit can lead to a negative balance between the mechanical power supplied by the turbine and the compressor.

Conclusions

The research presented an in-depth investigation of the potential and capabilities of the sCO_2 power cycle technology for high temperature industrial waste heat recovery applications. After an overview on the state-of-the-art and recent advancements in the technology, the main conclusions from the research program are:

1. The identification of the main operating range of sCO_2 power cycles in Waste Heat Recovery (WHR) applications. In particular, for waste heat source temperatures higher than 700°C, sCO_2 power cycles are the only option available. For industrial WHR, mean capacities of the waste heat sources lower than 1 MW, sCO_2 systems still remain a strong technically feasible candidate down to 400°C. Lower operational limits in terms of waste heat source temperature and capacity have been found to be around 350°C and 300 kW thermal respectively, which, considering a thermal efficiency of 20% leads to an electric net power output of the unit of 50 kW_e. These limits are set by the technoeconomic challenges arising from operating conditions such as low cycle pressure ratio and maximum temperature achievable (due to the need of reducing costs) and reduced size of the turbomachines, which lead to issues in terms of leakage and high vibration levels due to the elevated speeds. On the other hand, limitations in the scale up of these systems arise from the high cost of heat exchangers and the need of compactness and high strength materials rather than the turbomachinery.

2. The technoeconomic analysis revealed that the turbine inlet temperature is the most influencing parameter on cycle performance. The second most important one has been identified to be the compressor inlet temperature, which must closely approach the critical point of the CO_2 working fluid. Among the eight different sCO_2 power cycle layouts investigated, the more complex configurations originally designed for concentrated solar power and nuclear applications, namely the Simple Regenerated (SR), Reheating (RH), Recompression (RC) and Recompression Reheating (RCRH), present higher thermal efficiencies but lower net power outputs. Architectures more oriented to waste heat recovery applications, such as the Split-Heating Split-Expansion (SHSE), Pre-heating (PH), Pre-Heating Split-Expansion (PHSE) and Pre-Heating Pre-Compression (PHPC), are able to achieve higher net power outputs, which is the main objective in WHR applications, but lower efficiency. The best trade-off between performance and cost-effectiveness for heat recovery applications has been found to be offered by the SR layout due to the reduced number of components required, simplicity in design and control and lower costs. In WHR applications where the waste

heat is freely available, the primary consideration is low cost to make the case for investment more attractive rather than the energy conversion efficiency.

3. The 50 kW_e supercritical CO_2 experimental facility is based on a simple recuperated Joule-Brayton cycle layout. The demonstrator embeds a 830 kW_t gas fired process air heater to provide the exhaust heat and a 500 kW_t dry cooler to act as the heat sink. The dry cooler utilises a water-glycol mixture as intermediate heat transfer loop to reject residual heat from the gas cooler to the environment. A key component in the facility is a micro-tube CO_2 heater which is able to provide high performance and compactness. The core of the sCO_2 unit is a compressor-generator-turbine unit (CGT) composed of a single shaft turbomachinery. The power loop is packaged in a 20ft container which is CE marked according to the Pressure Equipment Directive (PED) (2014/68/EU). High accuracy instrumentation based on RTD temperature sensors, Coriolis flow meter and piezoresistive pressure transducers can provide reliable and accurate measures of the main thermodynamic process variables. This instrumentation allowed for instance to reduce the maximum uncertainty on the compressor isentropic efficiency of 2.3%, as showed by a preliminary uncertainty analysis. A remote control and monitoring system based on the IEC 61499 standard enables data retrieval from the sensors and interfacing of several PLCs from the controls of the facility. An innovative feature of the developed control system allows to transmit real time data about the unit performance on an online platform which will enable the operation and control of the system based on power demand, waste heat availability, electricity prices as well as environmental conditions.

4. The geometrical and performance figures for the several components of the sCO_2 demonstrator supplied by manufacturers enabled the development of numerical one-dimensional computational fluid dynamics (1D CFD) model of the sCO_2 unit. When performance data provided by manufacturers were not available, more complex three-dimensional computational fluid dynamics (3D CFD) models were used to obtain the required performance figures. The model considers the heat exchangers, pipes and the receiver as one-dimensional equivalent objects and the turbomachinery as lumped objects given their faster dynamics. This approach allows to reduce the complexity and computational effort required by the development and solving of 3D CFD models but still ensuring a good prediction accuracy of the underlying fluid dynamic phenomena occurring in the heat to power conversion process.

5. The results of the steady-state analysis allowed to obtain an operating map of the unit which can be adopted as baseline for the setting up of control strategies. In particular,

it showed that the system can generate up to 105 kW (intended as mechanical power), a 100% increase with respect to the nominal power, for an increase of the heat source temperature and mass flow rate by 31% and 20% respectively. The performance can be further improved if an independent drive configuration for the turbine is adopted. For the same operating conditions a net power output increase of almost 25% can be better matching compressor and turbine speeds to waste heat flow and temperature characteristics. Ambient temperature affects the system performance given the significant influence the temperature of the cold sink can have on the unit net power output and efficiency. For a fixed heat load and assuming a coolant mass flow rate of 1.6 kg/s, a decrease in the cooling fluid inlet temperature from 26°C to 16°C leads to an increase in the system power output and efficiency from 40 kW to 72 kW and from 9% to 21% respectively. A positive aspect is that the analysis showed that no condensation at the compressor inlet occurs since the minimum temperature achieved is 35°C, which is above the critical temperature of the CO_2.

6. Time varying profiles of the flue gas operating parameters, mass flow rate and inlet temperature, lead to variations in the CO_2 temperature at the turbine inlet. Unlike ORC systems and other more conventional heat to power conversion technologies of similar power output, the turbine inlet temperature variation has been shown to experience very little lag with respect to the time varying waste heat load profile. This demonstrates the flexible nature of the sCO_2 system investigated. Furthermore, the results showed that during the start-up and shutdown of the unit, the opening of the turbine by-pass globe valve can guarantee a safer operation of the turbine and a quicker build-up of the pressures and temperatures in the sCO_2 loop.

7. Different control strategies for the sCO_2 heat to power system have been proposed and discussed. Such control approaches refer to typical operating conditions of sCO_2 power blocks, such as transient heat load profiles from the topping industrial process. Firstly, the steady-state analysis revealed that the regulation of the system inventory represents the most suitable alternative for the control of the inlet conditions at the turbine. Based on this, a Proportional Integral (PI) inventory controller has been designed and tested within the system simulation and showed to provide good control of the dynamic performance of the system in terms of stability during changes in thermal load. The most appropriate location for additions/withdrawals of CO_2 was identified to be downstream of the gas cooler.

Recommendations for Future Work

Future work should focus primarily on the validation of the numerical analyses presented. This would be primarily assessed thanks to the sCO_2 test facility constructed at Brunel University London. The effective heater capability of directly recovering the heat supplied by the stream of flue gases must be assessed. So far, the only existing test facilities developed considered only electric heaters as primary heat source for sCO_2 systems. The ability to use gas flows for the study is of paramount importance since a low pinch point in the heat exchanger must be achieved in order to enhance the performance of the unit in terms of heat recovery and power generation, as showed in this research.

The dynamic behaviour of the turbomachines must also be investigated since no experimental data is available. The data is important also for the development of suitable regulation strategies for the machines, as for instance the surge control for the compressor. The ability to operate the compressor close to the CO_2 critical point may also represent an issue, given the high variability of the fluid thermophysical properties close to the critical region, and therefore this is an aspect that needs further research.

From a control perspective, the operation of the facility and the integration of additional CO_2 vessels at high pressure will allow to test the effectiveness of the inventory control strategies with real operating conditions. Critical phenomena observed in the numerical analysis could therefore being verified and confirmed.

From a numerical point of view, other control schemes could be investigated, and the implementation of a simpler model for control purposes could lead to a better assessment and understanding of the complex relationship between controlled and uncontrolled variables in the system.

Further important aspects for the advancement of the technology readiness level of sCO_2 power cycles are the assessment of the effective corrosion resistance of the main components to real operating environments and the design of more cost effective heat exchangers (recuperators and heaters), which actually are responsible for almost 80% of the overall capital expenditure for sCO_2 systems.

To do so, at Brunel University a smaller scale CO_2 heat exchanger test facility is being constructed that will enable the investigation of such aspects in much more detail. Different heat exchangers could be tested, and corrosion experiments could be carried out with different materials and at harsher operating conditions (higher temperatures and pressures) compared to the sCO_2 test facility detailed in this thesis.

References

[1]   IEA (2019). IEA, World Energy Outlook 2019. Paris: 2019.

[2]   Trends and projections in Europe 2017 — European Environment Agency https://www.eea.europa.eu/publications/trends-and-projections-in-europe-2017.

[3]   IEA (2018). IEA, World Energy Outlook 2018. Paris: 2018.

[4]   European Commission. EU energy in figures. 2016. doi:10.2833/15026.

[5]   Stark C, Thompson M, Change COC. Reducing UK emissions – 2019 Progress Report to Parliament. Hydrogen Knowledge Centre.

[6]   Cullen JM, Allwood JM. Theoretical efficiency limits for energy conversion devices. Energy 2010; 35:2059–69. doi:10.1016/J.ENERGY.2010.01.024.

[7]   Forman C, Muritala IK, Pardemann R, Meyer B. Estimating the global waste heat potential. Renewable and Sustainable Energy Reviews 2016; 57:1568–79. doi:10.1016/J.RSER.2015.12.192.

[8]   IEA (2016). Energy Efficiency Market Report 2016 - IEA . Paris: 2016.

[9]   MarketsandMarkets Research (2016). Waste Heat Recovery System Market by Application (Preheating and Steam & Electricity Generation), End-Use Industry (Petroleum Refining, Metal Production, Cement, Chemical, Paper & Pulp, and Textile) - Global Trends & Forecasts to 2021.

[10]   Siddique ARM, Mahmud S, Heyst B Van. A review of the state of the science on wearable thermoelectric power generators (TEGs) and their existing challenges. Renewable and Sustainable Energy Reviews 2017; 73:730–44. doi:10.1016/j.rser.2017.01.177.

[11]   Khalid KAA, Leong TJ, Mohamed K. Review on Thermionic Energy Converters. IEEE Transactions on Electron Devices 2016; 63:2231–41. doi:10.1109/TED.2016.2556751.

[12]   Timmer MAG, de Blok K, van der Meer TH. Review on the conversion of thermoacoustic power into electricity. The Journal of the Acoustical Society of America 2018; 143:841–57. doi:10.1121/1.5023395.

[13]   Jouhara H, Khordehgah N, Almahmoud S, Delpech B, Chauhan A, Tassou SA. Waste heat recovery technologies and applications. Thermal Science and Engineering Progress 2018; 6:268–89. doi:10.1016/j.tsep.2018.04.017.

[14]   Hung TC. Waste heat recovery of organic Rankine cycle using dry fluids. Energy Conversion and Management 2001; 42:539–53. doi:10.1016/S0196-8904(00)00081-9.

[15]   Angelino G, Gaia M, Macchi E. Review of Italian Activity in the Field of Organic Rankine Cycle. VDI Berichte, 1984, p. 465–82.

[16]   Marchionni M, Bianchi G, Zaher O, Miller J, Tassou SA. Numerical investigations of a Trilateral Flash Cycle under system off-design operating conditions. Energy Procedia 2019; 161:464–71. doi:10.1016/J.EGYPRO.2019.02.070.

[17]   Freund P, Bachu S, Simbeck D, Thambimuthu K. Annex I: Properties of CO_2 and carbon-based fuels. IPCC Special Report 2005.

[18]   White M, Sayma AI. A preliminary comparison of different turbine architectures for a 100 kW supercritical CO_2 Rankine cycle turbine. The 6th International Supercritical CO_2 Power Cycles Symposium, 2018.

[19]   Brun K, Friedman P, Dennis R. Fundamentals and applications of supercritical carbon dioxide (sCO_2) based power cycles. Woodhead Publishing an imprint of Elsevier; 2017.

[20]   Sulzer G. Verfahren zur Erzeugung von Arbeit aus Warme. Swiss Patent 1950.

[21]   Feher E. Investigation of supercritical (Feher) cycle. Astropower Laboratory, Missile & Space Systems 1968.

[22]   Angelino G. Perspectives for the liquid phase compression gas turbine. ASME Journal for Engineering for Gas Turbines and Power 1967; 89:229-36. doi:10.1115/1.3616657.

[23]   Angelino G. Carbon Dioxide Condensation Cycles for Power Production. ASME Journal of Engineering for Gas Turbines and Power 1968; 90:287–96. doi:10.1115/1.3609190.

[24]   Angelino G. Real Gas Effects in Carbon Dioxide Cycles. ASME International Gas Turbine Conference and Products Show 1969. doi:10.1115/69-GT-102

[25]   Van Dievoet JP, Dewandeleer JG, Odon R. Nuclear Fuel Subassemblies and Combinations Thereof. US patent No. 3567582. U.S. Patent and Trademark Office 1971.

[26]   Strub R, Frieder A. High Pressure Indirect CO_2 Closed-cycle Gas Turbines. Nuclear Gas Turbines 1970, 5:51-61.

[27]   Corman J. Energy Conversion Alternatives Study-ECAS-: General Electric Phase II Final Report 1976.

[28]   Dostal V, Driscoll M, Hejzlar P. A supercritical carbon dioxide cycle for next generation nuclear reactors. PhD thesis, Massachusetts Institute of Technology, 2004.

[29]   Imre AR, Ramboz C, Deiters UK, Kraska T. Anomalous fluid properties of carbon dioxide in the supercritical region: application to geological CO_2 storage and related hazards. Environmental Earth Sciences 2015; 73:4373–84. doi:10.1007/s12665-014-3716-5.

[30]   Span, R; Wagner W. A new EOS for CO_2 covering the fluid region from the triple point temperature to 1100K at pressures up to 800MPa.pdf. Journal of Physical and Chemical Reference Data 1996; 25:1509–96. doi:10.1063/1.555991.

[31]   Carlès P. A brief review of the thermophysical properties of supercritical fluids. The Journal of Supercritical Fluids 2010; 53:2-11. doi.org/10.1016/j.supflu.2010.02.017.

[32]   Onuki A, Hao H, Ferrell R. Fast adiabatic equilibration in a single-component fluid near the liquid-vapor critical point. Physical Review A 1990; 41, 2256. doi.org/10.1103/PhysRevA.41.2256.

[33]   Boukari H, Shaumeyer J, Briggs M, Gammon R. Critical speeding up in pure fluids. Physical Review A 1990; 41, 2260. doi.org/10.1103/PhysRevA.41.2260.

[34]   Zappoli B, Carles P, Amiroudine S, Ouazzani J. Inversion of acoustic waves reflection rules in near critical pure fluids. Physics of Fluids 1995; 7, 2283. doi.org/10.1063/1.868476.

[35]   Miura Y, Yoshihara S, Ohnishi M, Honda K. High-speed observation of the piston effect near the gas-liquid critical point. Physical Review E 2006; 74, 010101. doi.org/10.1103/PhysRevE.74.010101.

[36]   Carlès P. Thermoacoustic waves near the liquid-vapor critical point. Physics of Fluids 2006; 18, 126102. doi.org/10.1063/1.2397577.

[37]   Huck P, Freund S, Lehar M, Peter M. Performance comparison of supercritical CO_2 versus steam bottoming cycles for gas turbine combined cycle applications.   The 5th International Symposium - Supercritical CO_2 Power Cycles, 2016.

[38]   Wright S a, Radel RF, Vernon ME, Rochau GE, Pickard PS. Operation and Analysis of a Supercritical CO_2 Brayton Cycle. Sandia National Laboratories (SNL). Technical Report, 2010. doi:10.2172/984129.

[39]   Yin H, Sabau AS, Conklin JC, McFarlane J, Qualls A Lou. Mixtures of SF6-CO_2 as working fluids for geothermal power plants. Applied Energy 2013; 106:243–53. doi:10.1016/j.apenergy.2013.01.060.

[40]   Jeong WS, Jeong YH. Performance of supercritical Brayton cycle using CO_2-based binary mixture at varying critical points for SFR applications. Nuclear Engineering and Design 2013; 262:12–20. doi:10.1016/j.nucengdes.2013.04.006.

[41]   Crespi F, Sánchez D, Martínez GS, Sánchez-Lencero T, Jiménez-Espadafor F. Potential of Supercritical Carbon Dioxide Power Cycles to Reduce the Levelised Cost of Electricity of Contemporary Concentrated Solar Power Plants. Applied Sciences 2020; 10:5049. doi:10.3390/app10155049.

[42]   Clifford T. Fundamentals of supercritical fluids. Oxford University Press, 1999.

[43]   Conboy TM, Wright SA, Ames DE, Lewis TG. CO_2 -Based Mixtures as Working Fluids for Geothermal Turbines. Sandia National Laboratories (SNL). Technical Report, 2012. doi:10.2172/1049477.

[44]   Ayub A, Invernizzi CM, Di Marcoberardino G, Iora P, Manzolini G. Carbon Dioxide Mixtures as Working Fluid for High-Temperature Heat Recovery: A Thermodynamic Comparison with Transcritical Organic Rankine Cycles. Energies 2020; 13:4014. doi:10.3390/en13154014.

[45]   Dunlevy M. An Exploration of the Effect of Temperature on Different Alloys in a Supercritical Carbon Dioxide Environment. PhD thesis, Massachusetts Institute of Technology, 2009.

[46]   Gibbs J. Corrosion of various engineering alloys in supercritical carbon dioxide. PhD thesis, Massachusetts Institute of Technology, 2010.

[47]   Saari H, Petrusenko R, Zanganeh K, Parks C, Maybee B. Corrosion testing of high temperature materials in supercritical carbon dioxide. The 4th International Symposium - Supercritical CO_2 Power Cycles, 2014.

[48]   Anderson M. Materials, Turbomachinery and Heat Exchangers for Supercritical CO_2 Systems. University of Wisconsin. Technical Report, 2012. doi.org/10.2172/1053848

 [49]   Parks C. Corrosion of candidate high temperature alloys in supercritical carbon dioxide. Master's Thesis, Carleton University, 2013.

[50]   Fleming D, Pasch J, Carlson M, Conboy T. Corrosion and Erosion Behavior in Supercritical CO_2 Power Cycles. Volume 3B: Oil and Gas Applications; Organic Rankine Cycle Power Systems; Supercritical CO_2 Power Cycles; Wind Energy. ASME Turbo Expo 2014. doi:10.1115/GT2014-25136.

[51]   Sridharan K, Anderson M. Corrosion in Supercritical Carbon Dioxide : Materials, Environmental Purity, Surface Treatments, and Flow Issues. University of Wisconsin. Technical Report, 2013. doi:10.2172/1111547.

[52]   Mehos M, Turchi CS, Jorgenson J, Denholm P, Ho C, Armijo K. On the Path to SunShot - Advancing Concentrating Solar Power Technology, Performance, and Dispatchability. National Renewable Energy Laboratory (NREL) and Sandia National Laboratories (SNL). Technical Report, 2016. doi:10.2172/1344199.

[53]   Moore R, Conboy T. Metal corrosion in a supercritical carbon dioxide-liquid sodium power cycle. Sandia National Laboratories (SNL). Technical Report, 2012. doi.org/10.2172/1039408.

[54]   Kung SC, Shingledecker JP, Thimsen D, Wright IG, Tossey BM, Sabau AS. Oxidation/Corrosion in Materials for Supercritical CO_2 Power Cycles. The 5th International Symposium - Supercritical CO_2 Power Cycles, 2016.

[55]   Mahaffey J, Anderson M, Adam D, Sridharan K, Brittan A, Arik M. Effect of Oxygen Impurity on Corrosion in Supercritical CO_2 Environments. The 5th International Symposium - Supercritical CO_2 Power Cycles, 2016.

[56]   Sabau AS, Shingledecker JP, Kung SC, Wright IG, Nash J. Exfoliation Propensity of Oxide Scale in Heat Exchangers Used for Supercritical CO_2 Power Cycles. The 5th International Symposium - Supercritical CO_2 Power Cycles, 2016.

[57]   Rouillard F, Charton F, Moine G. Corrosion behavior of different metallic materials in supercritical carbon dioxide at 550 C and 250 bars. Corrosion, The Journal of Science & Engineering 2011; 67: 095001–7. doi:10.5006/1.3628683.

[58]   Poláčková J, Janák M, Berka J, Krausová A. Materials for use in calcium looping technology for CCS – Corrosion Processes in High-temperature CO_2. Koroze a Ochrana Materialu 2017. doi:10.1515/kom-2017-0017.

[59]   Lim JY, McKrell TJ, Eastwick G, Ballinger RG. Corrosion Of Materials In Supercritical Carbon Dioxide Environments. Corrosion, NACE International Corrosion Conference and Expo, 63, NACE International; 2008.

[60]   Balje O. Turbomachines-A guide to design, selection, and theory. John Wiley & Sons Inc, 1981.

[61]   De Miol M, Bianchi G, Henry G, Holaind N, Tassou SA, Leroux A. Design of a single-shaft compressor, generator, turbine for small-scale supercritical CO_2 systems for waste heat to power conversion applications. The 2nd European SCO_2 Conference 2018. doi:10.17185/DUEPUBLICO/46086.

[62]   Fuller R, Preuss J, Noall J. Turbomachinery for supercritical CO_2 power cycles. Volume 5: Manufacturing Materials and Metallurgy; Marine; Microturbines and Small Turbomachinery; Supercritical CO_2 Power Cycles. ASME Turbo Expo 2012. doi:10.1115/GT2012-68735.

[63]   Sienicki J, Moisseytsev A, Fuller R, Wright S. Scale dependencies of supercritical carbon dioxide Brayton cycle technologies and the optimal size for a next-step supercritical CO_2 cycle. Supercritical CO_2 Power Cycle Symposium, 2011.

[64]   Beckman K, Patel V. Review of API Versus AGMA Gear Standards/Rating, Data Sheet Completion, and Gear Selection Guidelines. The 29th Turbomachinery Simposium, 2000. doi.org/10.21423/R1TH31

[65]   Wilkes J, Allison T, Schmitt J, Bennett J. Application of an Integrally Geared Compander to an SCO_2 Recompression Brayton Cycle. The 5th International Symposium - Supercritical CO_2 Power Cycles, 2016.

[66]   Ertas B. Compliant hybrid journal bearings using integral wire mesh dampers. Turbo Expo: Power for Land, Sea, and Air, 2009. doi:doi.org/10.1115/GT2008-50984.

[67]   Delgado A. Experimental identification of dynamic force coefficients for a 110 mm compliantly damped hybrid gas bearing. Journal of Engineering for Gas Turbines and Power, 2015; 137:072502-10. doi:10.1115/1.4029203.

[68]   Thatte A, Loghin A, Shin Y, Ananthasayanam B. Performance and Life Characteristics of Hybrid Gas Bearing in a 10 MW Supercritical CO_2 Turbine. Volume 9: Oil and Gas Applications; Supercritical CO_2 Power Cycles; Wind Energy. ASME Turbo Expo 2016. doi:10.1115/GT2016-57695.

[69]   Chapman PA. Advanced Gas Foil Bearing Design for Supercritical CO_2 Power Cycles. The 5th International Symposium - Supercritical CO_2 Power Cycles, 2016.

[70]   Bidkar RA, Sevincer E, Wang J, Thatte AM, Mann A, Peter M, Musgrove G, Allison T, Moore J. Low-Leakage Shaft-End Seals for Utility-Scale Supercritical CO_2 Turboexpanders. Journal of Engineering for Gas Turbines and Power, 2017; 139:1–8. doi:10.1115/1.4034258.

[71]   Thatte A, Dheeradhada V. Coupled Physics Performance Predictions and Risk Assessment for Dry Gas Seal Operating in MW-Scale Supercritical CO_2 Turbine. Volume 9: Oil and Gas Applications; Supercritical CO_2 Power Cycles; Wind Energy. ASME Turbo Expo 2016. doi:10.1115/GT2016-57670.

[72]   Kalra C, Sevincer E, Brun K, Hofer D. Development of high efficiency hot gas turbo-expander for optimized CSP supercritical CO_2 power block operation. The 4th International Symposium - Supercritical CO_2 Power Cycles, 2014.

[73]   Jin H. Surface Patterning and Rotordynamic Response of Annular Pressure Seals Used in Turbomachinery. PhD Thesis, Virginia Polytechnic Institute and State University, 2019.

[74]   Jin, H, Untaroiu, A, Fu, G. Effect of Surface Patterning on the Dynamic Response of Annular Hole-Pattern Seals. Volume 7A: Structures and Dynamics. ASME Turbo Expo 2017. doi:10.1115/GT2017-64875.

[75]   Du Q, Zhang D. Numerical Investigation on Flow Characteristics and Aerodynamic Performance of a 1.5-Stage SCO 2 Axial-Inflow Turbine with Labyrinth Seals. Applied Sciences. 2020; 10:373-90. doi:10.3390/app10010373.

[76]   Baltadjiev, N.D. An Investigation of Real Gas Effects in Supercritical CO_2 Compressors. Master's Thesis, Massachusetts Institute of Technology, 2012.

[77]   Lettieri C, Yang D, Spakovszky Z. An investigation of condensation effects in supercritical carbon dioxide compressors. Journal of Engineering for Gas Turbines and Power, 2015. 137:082602-10. doi:10.1115/1.4029577

[78]   Lettieri C, Baltadjiev N, Casey M, Spakovszky Z. Low-Flow-Coefficient Centrifugal Compressor Design for Supercritical CO_2. Journal of Turbomachinery 2014;136:081008-17. doi:10.1115/1.4026322.

[79]   Baltadjiev ND, Lettieri C, Spakovszky ZS. An Investigation of Real Gas Effects in Supercritical CO_2 Centrifugal Compressors. Journal of Turbomachinery 2015;137:091003-16. doi:10.1115/1.4029616.

[80]   Clementoni EM, Cox TL, King MA, Rahner KD. Transient Power Operation of a Supercritical Carbon Dioxide Brayton Cycle. Volume 9: Oil and Gas Applications; Supercritical CO_2 Power Cycles; Wind Energy, ASME Turbo Expo 2017. doi:10.1115/GT2017-63056.

[81]   Hacks AJ, Vojacek A, Dohmen HJ, Brillert D. Experimental investigation of the sCO_2-HeRo compressor. The 2nd European sCO_2 Conference 2018. doi:10.17185/duepublico/46088.

[82]   Wang Y, Dostal V, Hejzlar P. Turbine design for supercritical CO_2 Brayton cycle. Proceedings of Global'03, 2003.

[83]   Jeong WS, Kim TW, Suh KY. Computational fluid dynamics of supercritical carbon dioxide turbine for brayton thermodynamic cycle. Volume 2: Fuel Cycle and High Level Waste Management; Computational Fluid Dynamics, Neutronics Methods and Coupled Codes. ASME 16th International Conference on Nuclear Engineering 2008. doi:10.1115/ICONE16-48240.

[84]   Zhang H, Zhao H, Deng Q, Feng Z. Aerothermodynamic design and numerical investigation of supercritical carbon dioxide turbine. Volume 9: Oil and Gas Applications; Supercritical CO_2 Power Cycles; Wind Energy. ASME Turbo Expo 2015. doi:10.1115/GT2015-42619.

[85]   Valdés M, Abbas R, Rovira A, Martín-Aragón J. Thermal efficiency of direct, inverse and sCO_2 gas turbine cycles intended for small power plants. Energy 2016; 100:66–72. doi:10.1016/j.energy.2016.01.072.

[86]   Shanechi MM, Veidt M, Hooman K. Forced response analysis of supercritical CO_2 radial inflow turbine designed for concentrating solar power. Volume 9: Oil and Gas Applications; Supercritical CO_2 Power Cycles; Wind Energy. ASME Turbo Expo 2016. doi:10.1115/GT2016-58144.

[87]   Qi J, Reddell T, Qin K, Hooman K, Jahn IHJ. Supercritical CO_2 radial turbine design performance as a function of turbine size parameters. Volume 9: Oil and Gas Applications; Supercritical CO_2 Power Cycles; Wind Energy. ASME Turbo Expo 2016. doi:10.1115/GT2016-58137.

[88]   Qi J, Reddell T, Qin K, Hooman K, Jahn IHJ. Supercritical CO_2 Radial Turbine Design Performance as a Function of Turbine Size Parameters. Journal of Turbomachinery 2017;139:081008-19. doi:10.1115/1.4035920.

[89]   Clementoni EM, Cox TL. Practical Aspects of Supercritical Carbon Dioxide Brayton System Testing. The 4th International Symposium - Supercritical CO_2 Power Cycles, 2014.

[90]   Clementoni EM, Cox TL, Sprague CP. Startup and Operation of a Supercritical Carbon Dioxide Brayton Cycle. Volume 8: Supercritical CO_2 Power Cycles; Wind Energy; ASME Turbo Expo 2013. doi:10.1115/GT2013-94275.

[91]   Moore J, Evans N, Kalra C, Brun K. Development of 1 MWe Supercritical CO_2 Test Loop. Volume 9: Oil and Gas Applications; Supercritical CO_2 Power Cycles; Wind Energy. ASME Turbo Expo 2015. doi:10.1115/GT2015-43771.

[92]   Held TJ. Initial Test Results of a Megawatt-Class Supercritical CO 2 Heat Engine. The 4th International Symposium - Supercritical CO 2 Power Cycles, 2014.

[93]   Cho J, Shin H, Cho J, Baik YJ, Choi B, Roh C. Design, flow simulation, and performance test for a partial admission axial turbine under supercritical CO_2 condition. Volume 9: Oil and Gas Applications; Supercritical CO_2 Power Cycles; Wind Energy. ASME Turbo Expo, 2018. doi:10.1115/GT2018-76508.

[94]   Cha JE, Bae SW, Lee J, Cho SK, Lee JI, Park JH. Operation Results of a Closed Supercritical CO 2 Simple Brayton Cycle. The 5th International Symposium - Supercritical CO_2 Power Cycles, 2016.

[95]   Cho J, Shin H, Ra HS, Lee G, Roh C, Lee B. Development of the Supercritical Carbon Dioxide Power Cycle Experimental Loop in KIER. Volume 9: Oil and Gas Applications;

Supercritical CO$_2$ Power Cycles; Wind Energy. ASME Turbo Expo, 2016. doi:10.1115/GT2016-57460.

[96]   De Miol M, Bianchi G, Henry G, Holaind N, Tassou SA, Leroux A. Design of a single-shaft compressor, generator, turbine for small-scale supercritical CO$_2$ systems for waste heat to power conversion applications. The 2nd European sCO$_2$ Conference 2018. doi:10.17185/duepublico/46086.

[97]   Hacks A, Schuster S, Dohmen HJ, Benra FK, Brillert D. Turbomachine Design for Supercritical Carbon Dioxide Within the sCO$_2$-HeRo.eu Project. Journal of Engineering for Gas Turbines and Power 2018; 140: 121017-25. doi:10.1115/1.4040861.

[98]   Utamura M, Hasuike H, Ogawa K, Yamamoto T, Fukushima T, Watanabe T. Demonstration of supercritical CO$_2$ closed regenerative Brayton cycle in a bench scale experiment. Volume 3: Cycle Innovations; Education; Electric Power; Fans and Blowers; Industrial and Cogeneration. ASME Turbo Expo 2012. doi:10.1115/GT2012-68697.

[99]   Moisseytsev A, Sienicki JJ. Investigation of alternative layouts for the supercritical carbon dioxide Brayton cycle for a sodium-cooled fast reactor. Nuclear Engineering and Design 2009; 239:1362–71. doi:10.1016/j.nucengdes.2009.03.017.

[100]   Marchionni M, Chai L, Bianchi G, Tassou SA. Numerical modelling and transient analysis of a printed circuit heat exchanger used as recuperator for supercritical CO$_2$ heat to power conversion systems. Applied Thermal Engineering 2019; 161:114190. doi:10.1016/j.applthermaleng.2019.114190.

[101]   Sienicki JJ, Moisseytsev A, Lv Q. Dry air cooling and the sCO$_2$ brayton cycle. Volume 9: Oil and Gas Applications; Supercritical CO$_2$ Power Cycles; Wind Energy. ASME Turbo Expo 2017. doi:10.1115/GT2017-64042.

[102]   Musgrove GO, Pierres R Le, Nash J. Heat Exchangers for Supercritical CO$_2$ Power Cycle Applications. The 4th International Symposium - Supercritical CO$_2$ Power Cycles 2014.

[103]   Musgrove GO, Sullivan S, Shiferaw D, Pittaway C, Carrero J, Le Pierres R. Heat Exchangers for Supercritical CO$_2$ Power Cycle Applications Tutorial. The 4th International Symposium - Supercritical CO$_2$ Power Cycles, 2014.

[104]   Carlson M, Kruizenga AM, Schalansky C, Fleming DF. Sandia progress on advanced heat exchangers for sCO$_2$ Brayton cycles. The 4th International Symposium - Supercritical CO$_2$ Power Cycles, 2014.

[105]   Bianchi G, Saravi SS, Loeb R, Tsamos KM, Marchionni M, Leroux A. Design of a high-temperature heat to power conversion facility for testing supercritical CO$_2$ equipment and

packaged power units. Energy Procedia 2019; 161:421–8. doi:10.1016/J.EGYPRO.2019.02.109.

[106]   Clementoni EM, Cox TL. Steady-state Power Operation of a Supercritical Carbon Dioxide Brayton Cycle. Volume 3B: Oil and Gas Applications; Organic Rankine Cycle Power Systems; Supercritical CO_2 Power Cycles; Wind Energy. ASME Turbo Expo 2014. doi:10.1115/GT2014-25336.

[107]   Cho J, Shin H, Cho J, Choi B, Roh C, Lee B. Development and Power Generating Operation of the Supercritical Carbon Dioxide Power Cycle Experimental Test Loop in KIER. The 3rd European sCO2 Conference 2019. doi:10.17185/duepublico/48905.

[108]   Vojacek A;, Hacks A, Johannes ;, Melichar T;, Frybort O;, Hájek P. Challenges in supercritical CO_2 power cycle technology and first operational experience at CVR. The 2nd European sCO2 Conference 2018. doi:10.17185/duepublico/46075.

[109]   Marchionni M, Bianchi G, Karvountzis-Kontakiotis A, Pesyridis A, Tassou SA. An appraisal of proportional integral control strategies for small scale waste heat to power conversion units based on Organic Rankine Cycles. Energy 2018; 163:1062–76. doi:10.1016/J.ENERGY.2018.08.156.

[110]   Fourspring PM, Nehrbauer JP, Sullivan S, Nash J. Testing of Compact Recuperators for a Supercritical CO_2 Brayton Power Cycle. The 4th International Symposium - Supercritical CO_2 Power Cycles, 2014.

[111]   Generation IV Nuclear Reactors: WNA - World Nuclear Association. http://www.world-nuclear.org/information-library/nuclear-fuel-cycle/nuclear-power-reactors/generation-iv-nuclear-reactors.aspx.

[112]   Alpy N, Cachon L, Haubensack D, Floyd J, Simon N. Gas Cycle testing opportunity with ASTRID, the French SFR prototype. Supercritical CO_2 Power Cycle Symposium, 2011.

[113]   Moullec Y Le. Conceptual study of a high efficiency coal-fired power plant with CO 2 capture using a supercritical CO_2 Brayton cycle. Energy 2013; 49:32-46. doi:10.1016/j.energy.2012.10.022.

[114]   Allam R, Martin S, Forrest B, Fetvedt J, Lu X, Freed D, et al. Demonstration of the Allam Cycle: An Update on the Development Status of a High Efficiency Supercritical Carbon Dioxide Power Process Employing Full Carbon Capture. Energy Procedia 2017; 114:5948–66. doi:10.1016/j.egypro.2017.03.1731.

[115]   Johnson G, McDowell M. Supercritical CO_2 Cycle Development at Pratt and Whitney Rocketdyne. Volume 5: Manufacturing Materials and Metallurgy; Marine; Microturbines and

Small Turbomachinery; Supercritical CO_2 Power Cycles. ASME Turbo Expo 2012. doi:10.1115/GT2012-70105.

[116]   Iverson BD, Conboy TM, Pasch JJ, Kruizenga AM. Supercritical CO_2 Brayton cycles for solar-thermal energy. Applied Energy 2013; 111: 957–70. doi:10.1016/j.apenergy.2013.06.020.

[117]   Singh R, Miller SA, Rowlands AS, Jacobs PA. Dynamic characteristics of a direct-heated supercritical carbon-dioxide Brayton cycle in a solar thermal power plant. Energy 2013; 50:194–204. doi:10.1016/j.energy.2012.11.029.

[118]   Singh R, Rowlands AS, Miller SA. Effects of relative volume-ratios on dynamic performance of a direct-heated supercritical carbon-dioxide closed Brayton cycle in a solar-thermal power plant. Energy 2013; 55:1025–32. doi:10.1016/j.energy.2013.03.049.

[119]   L'Estrange T, Truong E, Rymal C, Rasouli E, Narayanan V, Apte S, et al. High flux microscale solar thermal receiver for supercritical carbon dioxide cycles. 13th International Conference on Nanochannels, Microchannels, and Minichannels; ASME 2015. doi:10.1115/ICNMM2015-48233.

[120]   Sabau A, Yin H, Qualls A, McFarlane J. Investigations of supercritical CO_2 Rankine cycles for geothermal power plants. Supercritical CO_2 Power Cycle Symposium, 2011.

[121]   Higgins BS, Oldenburg CM, Muir MP, Pan L, Eastman AD. Process Modeling of a Closed Loop SCO_2 Geothermal Power Cycle. The 5th International Symposium - Supercritical CO_2 Power Cycles, 2016.

[122]   Waste heat recovery: technologically and economically viable solutions for industrial businesses A white book on industrial waste heat recovery. Fives 2016.

[123]   Dai X, Shi L, Qian W. Review of the Working Fluid Thermal Stability for Organic Rankine Cycles. Journal of Thermal Science 2019 ;28:597–607. doi:10.1007/s11630-019-1119-3.

[124]   Zywica G, Kaczmarczyk TZ, Ihnatowicz E. A review of expanders for power generation in small-scale organic Rankine cycle systems: Performance and operational aspects. Proceedings of the Institution of Mechanical Engineers, Part A: Journal of Power and Energy 2016; 230:669–84. doi:10.1177/0957650916661465.

[125]   Tanuma T. Advances in steam turbines for modern power plants. Woodhead Publishing, 2016.

[126]   Li C, Wang H. Power cycles for waste heat recovery from medium to high temperature flue gas sources – from a view of thermodynamic optimization. Applied Energy 2016; 180:707–21. doi:10.1016/j.apenergy.2016.08.007.

[127]   Bianchi G, McGinty R, Oliver D, Brightman D, Zaher O, Tassou SA, et al. Development and analysis of a packaged Trilateral Flash Cycle system for low grade heat to power conversion applications. Thermal Science and Engineering Progress 2017; 4:113–21. doi:10.1016/J.TSEP.2017.09.009.

[128]   Marchionni M, Bianchi G, Tassou SA. Techno-economic assessment of Joule-Brayton cycle architectures for heat to power conversion from high-grade heat sources using CO_2 in the supercritical state. Energy 2018; 148:1140–52. doi:10.1016/J.ENERGY.2018.02.005.

[129]   Yuansheng L, Jun W, Can M, Chunhui D, Zhenxing Z, Mo T. Design and analysis of key instruments of supercritical carbon dioxide Brayton cycle in future nuclear power field. Volume 2: Plant Systems, Structures, Components and Materials. 25th International Conference on Nuclear Engineering. ASME 2017. doi:10.1115/ICONE25-67155.

[130]   Turchi CS, Ma Z, Dyreby J. Supercritical carbon dioxide power cycle configurations for use in concentrating solar power systems. Volume 5: Manufacturing Materials and Metallurgy; Marine; Microturbines and Small Turbomachinery; Supercritical CO_2 Power Cycles. ASME Turbo Expo 2012. doi:10.1115/GT2012-68932.

[131]   McClung A, Brun K, Delimont J. Comparison of supercritical carbon dioxide cycles for oxy-combustion. Volume 9: Oil and Gas Applications; Supercritical CO_2 Power Cycles; Wind Energy. ASME Turbo Expo 2015. doi:10.1115/GT2015-42523.

[132]   Halimi B, Suh KY. Computational analysis of supercritical CO_2 Brayton cycle power conversion system for fusion reactor. Energy Conversion and Management 2012; 63:38–43. doi:10.1016/J.ENCONMAN.2012.01.028.

[133]   Padilla RV, Benito RG, Stein W. An Exergy Analysis of Recompression Supercritical CO_2 Cycles with and without Reheating. Energy Procedia 2015; 69:1181–91. doi:10.1016/J.EGYPRO.2015.03.201.

[134]   Mondal S. Transcritical CO_2 power cycle – effects of regenerative heating using turbine bleed gas at intermediate pressure. Energy 2015; 87:95-103. doi:10.1016/j.energy.2015.06.060.

[135] Song J, Simpson MC, Wang K, Markides CN. Thermodynamic assessment of combined supercritical CO_2 (SCO2) and organic Rankine cycle (ORC) systems for concentrated solar power. International Conference on Applied Energy 2019.

[136] Mahmoudi SM, D. Akbari A, Rosen MA. Thermoeconomic Analysis and Optimization of a New Combined Supercritical Carbon Dioxide Recompression Brayton/Kalina Cycle. Sustainability 2016; 8:1079-98. doi:10.3390/su8101079.

[137] Wright SA, Davidson CS, Scammell WO. Thermo-Economic Analysis of Four sCO$_2$ Waste Heat Recovery Power Systems. The 5th International Symposium - Supercritical CO$_2$ Power Cycles, 2016.

[138] Kulhánek M, Dostál V. Supercritical Carbon Dioxide Cycles Thermodynamic Analysis and Comparison. Supercritical CO$_2$ Power Cycle Symposium, 2011.

[139] Kimzey G. Development of a Brayton Bottoming Cycle using Supercritical Carbon Dioxide as the Working Fluid. EPRI Report 2012.

[140] Ahn Y, Bae SJ, Kim M, Cho SK, Baik S, Lee JI, Cha JE. Cycle layout studies of S-CO 2 cycle for the next generation nuclear system application. Transactions of the Korean Society Autumn Meeting, 2014.

[141] TU Delft - 2011. Cycle-Tempo^{TM}.

[142] Lemmon EW, Huber ML, Mclinden MO. NIST Reference Fluid Thermodynamic and Transport Properties— REFPROP User's Guide 2013.

[143] Wang X, Yang Y, Zheng Y, Dai Y. Exergy and exergoeconomic analyses of a supercritical CO$_2$ cycle for a cogeneration application. Energy 2017; 119:971–82. doi:10.1016/J.ENERGY.2016.11.044.

[144] I-ThERM – Industrial Thermal Energy Recovery Conversion and Management. http://www.itherm-project.eu/.

[145] Holaind N, De Miol M, Saravi SS, Tassou SA, Leroux A, Jouhara H. Design of radial turbomachinery for supercritical CO$_2$ systems using theoretical and numerical CFD methodologies. Energy Procedia 2017; 123:313–20. doi:10.1016/J.EGYPRO.2017.07.256.

[146] Holaind N, Bianchi G, De Miol M, Saravi S, Savvas SA, Leroux A, Jouhara H. Design of radial turbomachinery for supercritical CO$_2$ systems using theoretical and numerical CFD methodologies. Energy Procedia 2017; 123:313-20. doi:10.1016/j.egypro.2017.07.256

[147] Vyatkin V. The IEC 61499 standard and its semantics. IEEE Industrial Electronics Magazine 2009; 3:40–8. doi:10.1109/MIE.2009.934796.

[148] T Gamma - Gamma Technologies Inc 2020. GT-SUITE-Flow Theory Manual 2020.

[149] Brkić D. Review of explicit approximations to the Colebrook relation for flow friction. Journal of Petroleum Science and Engineering 2011; 77:34–48. doi:10.1016/J.PETROL.2011.02.006.

[150]   Gnielinski V. New equation for heat and mass transfer in turbulent pipe and channel flow. International Chemical Engineering 1976; 16:359–68.

[151]   Dittus FW, Boelter LMK. Heat transfer in automobile radiators of the tubular type. International Communications in Heat and Mass Transfer 1985; 12:3–22. doi:10.1016/0735-1933(85)90003-X.

[152] Jang DS, Jetli R, Acharya S. Comparison of the PISO, SIMPLER and SIMPLEC Algorithms for the Treatment of the Pressure-Velocity Coupling in Steady Flow Problems. Numerical Heat Transfer 1986; 10:209-228. doi:10.1080/10407788608913517.

[153]   Chai L, Tassou SA. Effect of cross-section geometry on the thermohydraulic characteristics of supercritical CO_2 in minichannels. Energy Procedia 2019; 161:446–53. doi:10.1016/J.EGYPRO.2019.02.077.

[154]   Cheng L, Ribatski G, Thome JR. Analysis of supercritical CO_2 cooling in macro- and micro-channels. International Journal of Refrigeration 2008; 31:1301–16. doi:10.1016/j.ijrefrig.2008.01.010.

[155]   Cipollone R, Bianchi G, Di Battista D, Fatigati F. Experimental and numerical analyses on a plate heat exchanger with phase change for waste heat recovery at off-design conditions. Journal of Physics: Conference Series 2015; 655:012038. doi:10.1088/1742-6596/655/1/012038.

[156]   Yan Y, Lio H, Lin T. Condensation heat transfer and pressure drop of refrigerant R-134a, R1234ze(E), R245fa and R1233zd(E) in a plate heat exchanger. International Journal of Heat and Mass Transfer 2019; 128:136-49. doi:10.1016/j.ijheatmasstransfer.2018.08.124.

[157]   SSP G7 - SWEP http://swep.net/support/ssp-calculation-software/ssp-g7.

[158]   Prosperetti A. A generalization of the Rayleigh–Plesset equation of bubble dynamics. Physics of Fluids 1982; 25:409. doi:10.1063/1.863775.

[159]   Saravi SS. An investigation into sCO_2 compressor performance prediction in the supercritical region for power systems. Energy Procedia 2019; 161:403–11. doi:10.1016/J.EGYPRO.2019.02.098.

[160]   Son S, Jeong Y, Cho SK, Lee JI. Development of supercritical CO_2 turbomachinery off-design model using 1D mean-line method and Deep Neural Network. Appl Energy 2020; 263:114645. doi:10.1016/j.apenergy.2020.114645.

[161]   Alshammari F, Karvountzis-Kontakiotis A, and Pesiridis A. Radial Expander Design for an Engine Organic Rankine Cycle Waste Heat Recovery System. Energy Procedia 2017; 129:285-92. doi:10.1016/j.egypro.2017.09.155.

[162]   Lennartson B, Kristiansson B. Evaluation and tuning of robust PID controllers. IET Control Theory and Applications 2009; 3:294–302. doi:10.1049/iet-cta:20060450.

[163]   Moisseytsev A, Sienicki JJ. Supercritical Carbon Dioxide Cycle Control Analysis. Argonne National Laboratory (ANL). Technical Report, 2011. doi.org/10.2172/1011299.

[164]   Dhalla A, Jones GL. ASME code classification of pipe stresses: a simplified elastic procedure. International Journal of Pressure Vessels and Piping 1986; 26:145-66. doi: 10.1016/0308-0161(86)90038-4.

[165]   Hechmer J, Hollinger G. The ASME code and 3D stress evaluation. ASME Journal of Pressure Vessel Technology 1991; 113:481-7. doi.org/10.1115/1.2928784.

Appendix A

Pipe flexibility assessment and insulation details

As stated in Chapter 4, the 10-meters long pipes connecting the packaged, plug & play sCO_2 system to the heat recovery exchanger run from the container to the heat source (Figures 2 and 3) and are labelled as PP-19 ("inlet") and PP-20 ("outlet") in Figure 5. Despite the absence of pulsating flow, the combination of high pressure and temperature load required an assessment of the piping flexibility during operation. As such, a finite element analysis study was outsourced (Pickering Engineering Design Ltd) and reviewed by the notified body (Lloyd's Register UK) in charge of the design appraisal for the compliance with the Pressure Equipment Directive (PED) 2014/68/EU. An excerpt of the FEA report is presented in Figure A1.

The results of the analysis have been summarized in Table A1 and Table A2. In particular Table A1 reports the maximum stress of Von Mises during the pipe operation and the highest utilization factors (~ ratio between current and maximum allowable stresses) under four different load case scenario [164,165]. Table A2 reports on the contrary the several loads on the nozzles of the heater (inlet and outlet) and on the pipe connected to the sCO_2 loop (PP-19, Figure 38).

Table A1 - Von Mises stress and utilisation factor under several load conditions according to the ASME B31.1 code (cit)

		Inlet pipe	Outlet pipe
Stresses			
Operation SIG-V	N/mm^2	58.5	60.3
Utilisation Factors			
Internal pressure	%	84.7	92.3
01 SL (Sustained Loads)	%	53.6	93.5
02 SE (Secondary Loads)	%	49.1	69.7
03 SE (Sustained + Secondary Loads)	%	40.2	54.1

Table A2 - Nozzle loads in the worst case scenario and analysis result

Nozzle	Fx [N]	Fy [N]	Fz [N]	Mx [Nm]	My [Nm]	Mz [Nm]	Result
Heater inlet	68.81	196.80	319.55	86.53	67.71	21.75	PASS
Heater outlet	50.90	307.85	425.28	118.98	249.25	28.29	PASS
sCO_2 loop	397.41	322.54	28.78	144.5	320.91	34.41	PASS

RESULTS SUMMARY

STRESSES		Inlet Pipe	Outlet Pipe
Operation SIG-V	:	58.5 N/mm²	60.3 N/mm²

STRESS RATIOS (UTILISATION FACTORS)

Internal Pressure	:	84.7 %	92.3%
01 SL Sustained Loads	:	53.6 %	93.5%
02 SE Secondary Loads	:	49.1 %	69.7%
03 SE Sustained + Secondary Loads	:	40.2 %	54.1%

DISPLACEMENTS

Dead Load	:	6.54 mm	Resultant at Node 49
Operation	:	28.91 mm	Resultant at Node 31
Shutdown	:	2.18 mm	Resultant at Node 15

NOZZLE LOADS

Heater

Inlet Nozzle	$Fx = 68.81$ N	$Fy = 196.80$ N	$Fz = 319.55$ N	PASS
	$Mx = 86.53$ Nm	$My = 67.71$ Nm	$Mz = 21.75$ Nm	PASS
Outlet Nozzle	$Fx = 50.90$ N	$Fy = 307.85$ N	$Fz = 425.28$ N	PASS
	$Mx = 118.98$ Nm	$My = 249.25$ Nm	$Mz = 28.29$ Nm	PASS

CO_2 Loop Heater

Nozzle	$Fx = 397.41$ N	$Fy = 322.54$ N	$Fz = 28.78$ N
	$Mx = 144.5$ Nm	$My = 320.91$ Nm	$Mz = 34.41$ Nm

EXPANSION BELLOWS

Required	:	NO

SPRING SUPPORTS

Required	:	YES
Specification	:	Refer to Appendix 2 and Note (i) above

CONCLUSION	:	**SOLUTION** (See Note !! below)
		Stresses Pass
		Local Loads Pass and/or are Low

NOTE !! The 'Initial Configuration' of Pipework and Supports submitted for Pipe Stress Analysis FAILED SUBSTANTIALLY !! That Pipework System must NOT be used. The 'Solutions' presented herein are based on Revised Support Arrangements and an up-grading of the Inlet Pipes from Sch 80 to Sch 160.

Figure A1: Summary of pipe flexibility analysis

Based on the recommendations of the pipe flexibility study, despite the completion of the assembly, the pipes connecting the recuperator outlet to the heater inlet (labelled as PP-02, PP-19A and PP-20 in the complete P&ID) had to be replaced with a higher schedule ones (160 instead of 80).

Furthermore, the pipe supports had to be replaced with some bespoke fixings which will allow a correct deformation of the pipes during operation. The layout of the pipe fixings is reported in Figures A2 and A3.
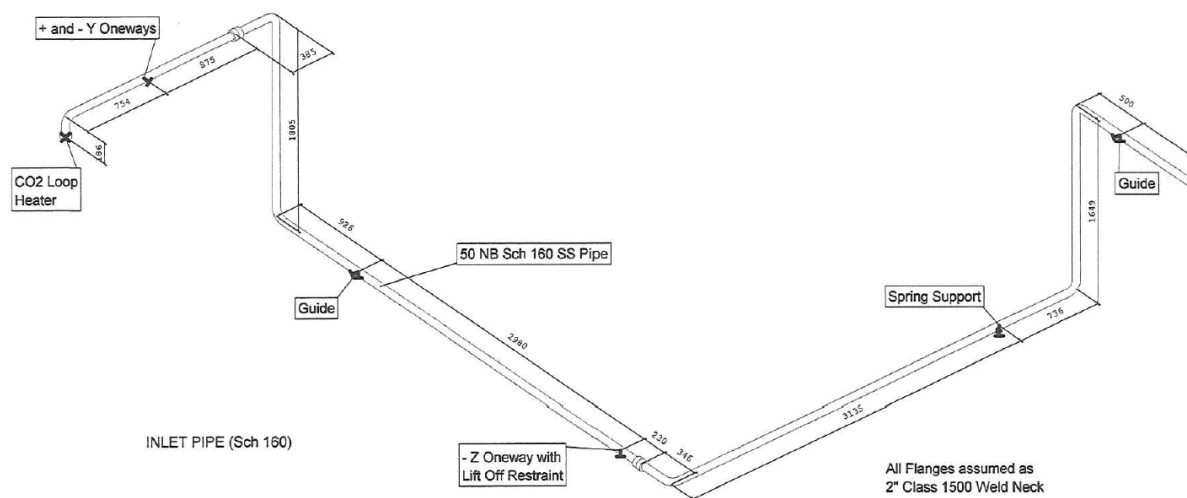

Figure A2: Layout of fixings for the pipes connecting the recuperator outlet to the heater inlet
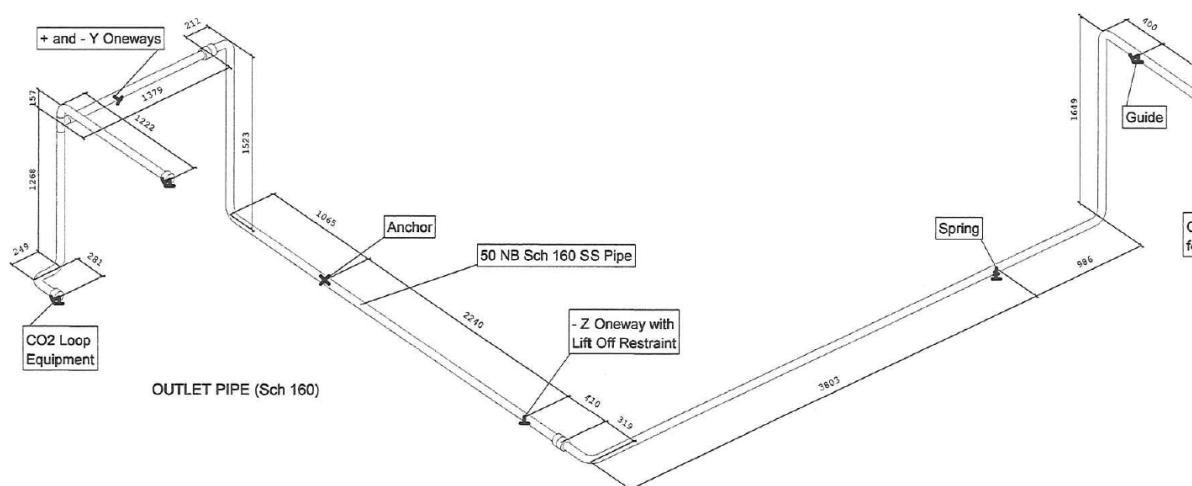

Figure A3: Layout of fixings for the pipes connecting the heater outlet to the turbine inlet

Additional results of the pipe flexibility assessment are reported in the Figures below. In particular:

- Figure A4 shows the utilisation factor, intended as the ratio between current and maximum allowable stresses, in the worst case scenario for the inlet pipe;
- Figure A5 reports the flange equivalent pressure results in the worst case load scenario;
- Figure A6 displays the utilisation factor in the worst case scenario for the outlet pipe;
- Figure A7 shows the maximum displacements in the worst case load scenario for both the inlet and outlet pipes;
- Figure A8 reports the load on the supports for both pipes in the worst case scenario.
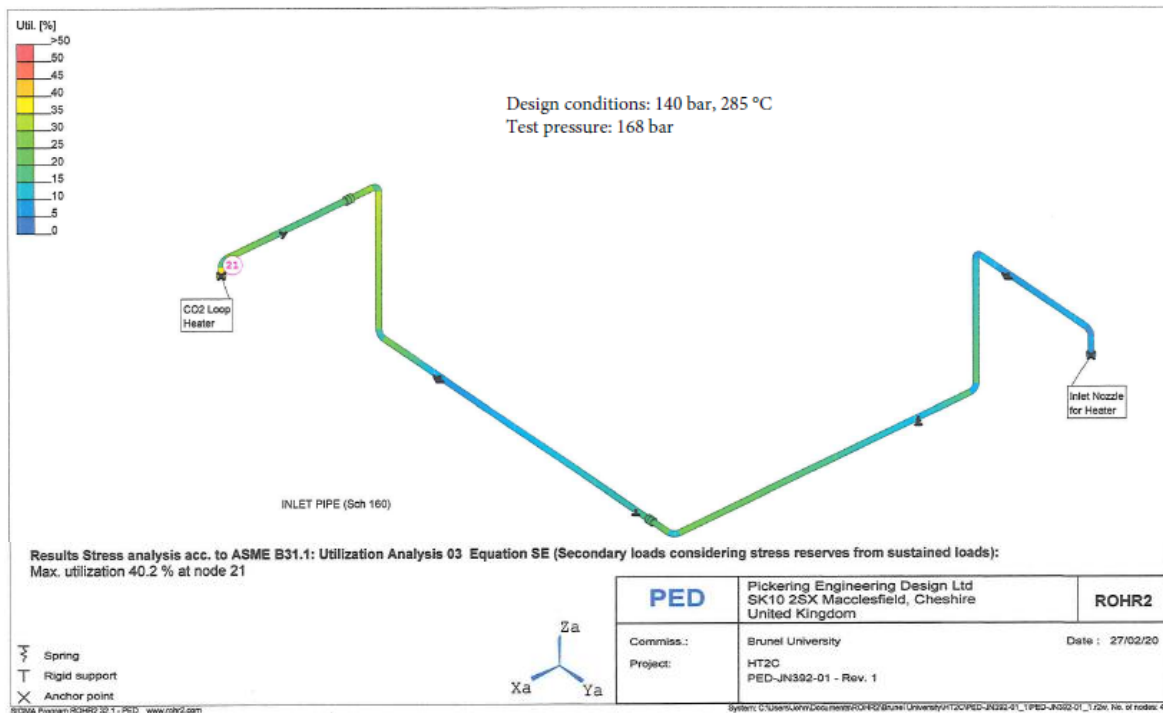

Figure A4: Utilisation factor "inlet pipe" in the worst case load scenario

Flange loads Lc Operation

Node	Standard	Nom. diameter	DA [mm]	S [mm]	PN [bar(g)]	d3e [mm]	PB [bar(g)]	TB [°C]	N [N]	MB [Nm]	Q [N]	MT [Nm]	Nres [N]	SigV [N/mm²]	Peq. [bar(g)]	Peq/PN
33	ASME B16.5 2500	NPS2.0	60.33	8.74	425.41	166.04	140.00	400.0	-202.24	454.29	852.27	-122.07	10741.53	49.7	214.49	0.50
23	ASME B16.5 2500	NPS2.0	60.33	8.74	425.41	166.04	140.00	400.0	-425.28	276.19	312.03	-28.29	6228.17	49.0	183.19	0.43
39	ASME B16.5 2500	NPS2.0	60.33	8.74	425.41	166.04	140.00	400.0	-336.94	269.23	255.12	-112.62	6148.93	49.4	182.64	0.43
51	ASME B16.5 2500	NPS2.0	60.33	8.74	425.41	166.04	140.00	400.0	-12.78	0.00	1078.99	0.00	-12.78	49.0	139.91	0.33
45	ASME B16.5 2500	NPS2.0	60.33	8.74	425.41	166.04	140.00	400.0	-31.33	0.00	75.58	-0.00	-31.33	48.9	139.78	0.33
21	ASME B16.5 1500	DN50	60.33	8.74	255.45	159.94	140.00	285.0	-28.78	351.76	511.82	-34.41	8768.52	49.0	200.80	0.79
11	ASME B16.5 1500	DN50	60.33	8.74	255.45	159.94	140.00	285.0	-162.18	331.22	399.73	-4.80	8121.47	49.0	196.32	0.77
17	ASME B16.5 1500	DN50	60.33	8.74	255.45	159.94	140.00	285.0	-229.64	200.01	614.09	84.06	4772.57	49.3	173.10	0.68
1	ASME B16.5 1500	DN50	60.33	8.74	255.45	159.94	140.00	285.0	-319.55	109.82	207.83	-21.75	2426.85	49.0	156.83	0.61

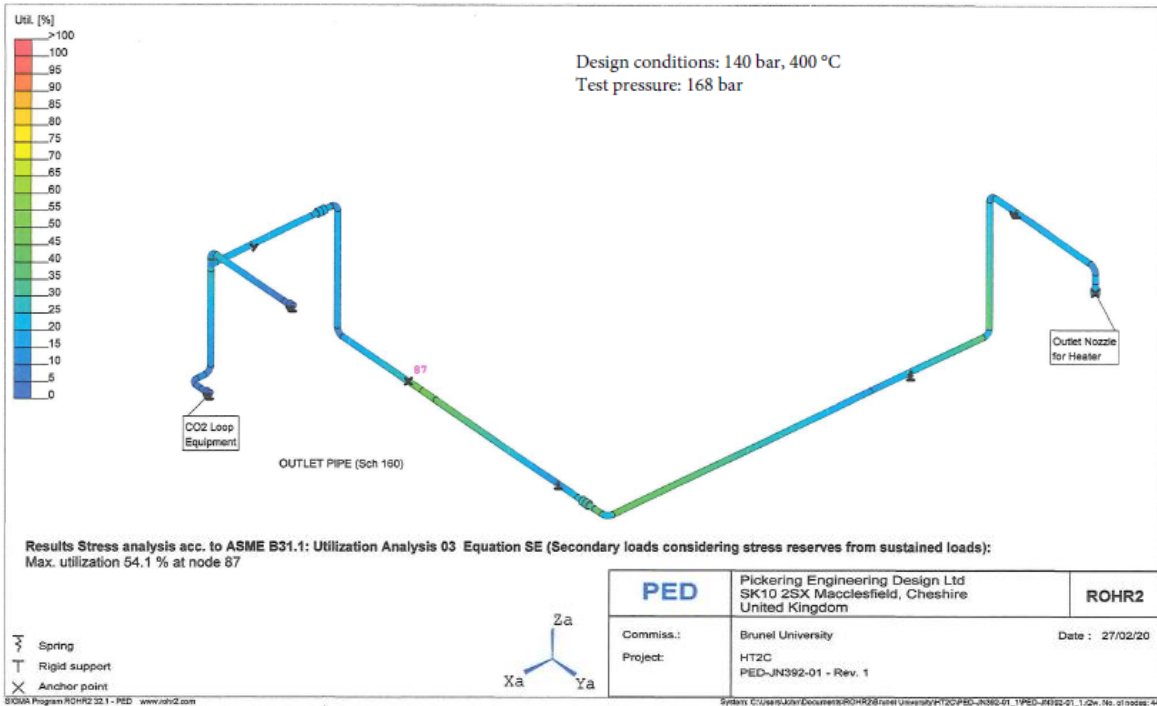Figure A5: Flange equivalent pressure results in the worst case load scenario

Figure A6: Utilisation factor "outlet pipe" in the worst case load scenario
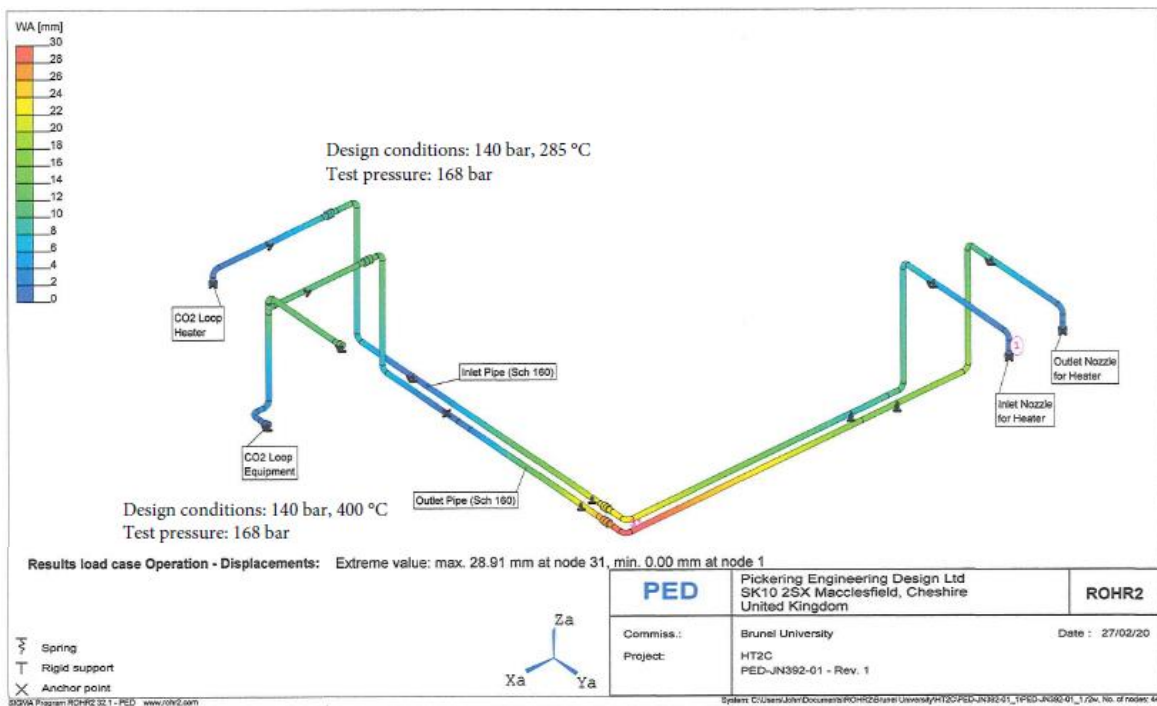

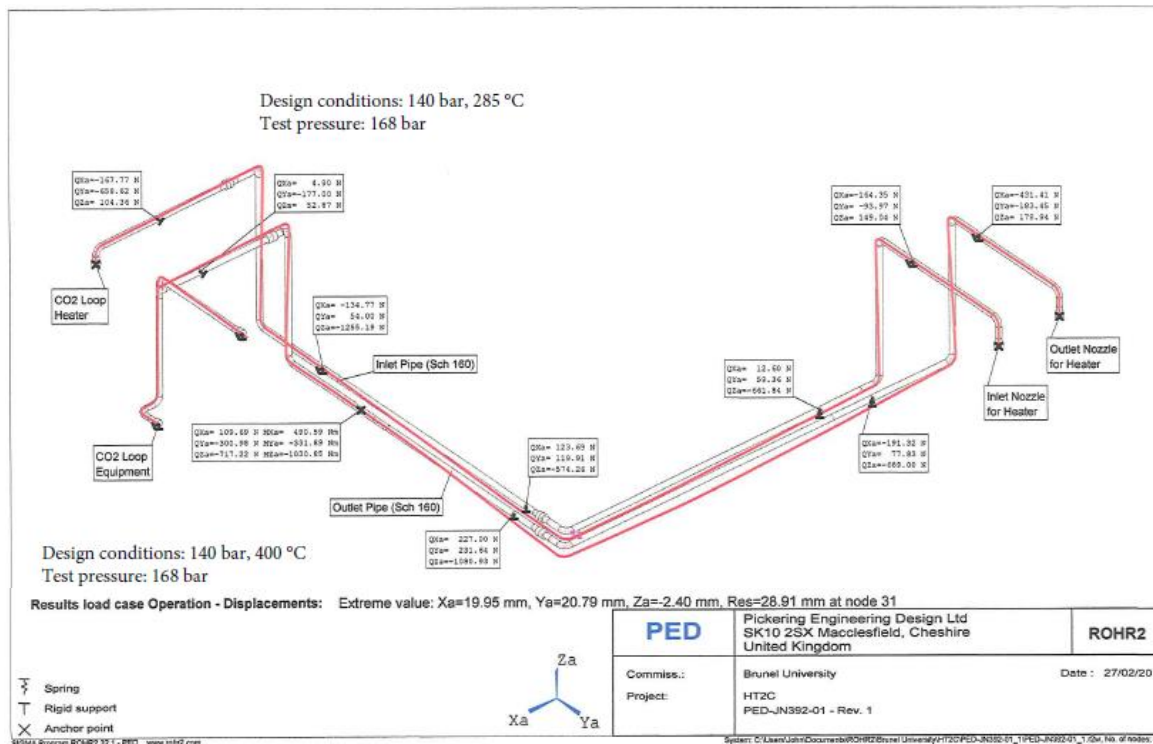Figure A7: Maximum displacements in the worst case load scenario

Figure A8: Support loads in the worst case load scenario

In the analysis, the insulation jackets have been taken into account. The materials and thicknesses selected vary accordingly to the maximum operating temperature of the part of the system considered. Table A3 summarizes the different insulation types provided.

Table A3 - Summary of insulation types

Location	Operating Temperature	Inner layer	Insulation	Outer layer
Indoor	<100°C	L1	I1	L1
Indoor	<350°C	L2	I2	L1
Indoor	>350°C	L3	I3	L1
Outdoor	<350°C	L2	I2	L4
Outdoor	>350°C	L3	I3	L4

I1 Mineral Wool [Icerock_Ductwrap_datasheet]
I2 Needlemat, Insulation [THS-Needlemat (997, 998, 999, Issue 07)]
I3 Ceramic Wool Insulation [SIG-Insulfrax S Blanket-R12.11.15]
L1 Grey Silicone Coasted Glass Cloth [Double sided grey silicone THS -TDS 8590SR120]
L2 Plain Weavelocked Glass Cloth (Weavelocked E-Glass Cloth (THS TDS 8590WL701 Issue 6))
L3 Silica Wash Treated Glass Cloth [Silica Wash Treated Glass Cloth]
L4 Grey PTFE Coated Glass Cloth [TDS QSG16]

Manufacturing and testing considerations

The pipes welding has been made by outsourced specialists (Orbital fabrications Ltd) with approved qualifications in terms of welding procedures and qualifications of the operators.

This was reviewed through an audit that the notified body (Lloyd's register UK) carried out at the fabricator's premises. An excerpt of the inspection report is shown in Figure A9.

Visit Report

Visit report number VR01	Date of issue 04 November 2019	Office Birmingham	Control number PRJ11100229696
Report of visit to Orbital Fabrications Ltd, Unit 1, Stephenson Road, St Ives, Cambridgeshire PE27 3WJ			Date of visit 08 October 2019
Client Brunel University London		Project sCO2 heat to energy system.	
Client reference 601476		Co-ordinated contract reference	
Supplier Orbital Fabrications Ltd		Main order number Job No: 25300	
Sub-supplier		Sub-order number	
Period covered by this visit report 08 October 2019		Order status Incomplete	
Item number		Tag number	

Description of item
sCO2 Loop
High Pressure Circuit Design Pressure (PS) = 127.5 Bar
Low Pressure Circuit Design Pressure (PS) = 75.0 Bar
Operating Fluid Carbon Dioxide (R744)

Primary documents
Pressure Equipment Directive 2014/68/EU
Brunel University I-Therm Schematic Diagram dated 05/07/2019
Orbital Fabrications Ltd General arrangement Drawing 8635 Rev 1.

Scope of Inspection: Supplementary assurance visit PED Compliance

1. Verified correct PED classification of piping for group 2 gasses. Ref PED Chart 7 Pipe work <DN100 = Category I conformity assessment Module A applied.
2. Review of Orbital fabrications Welding Procedure Approval Certificate PQR 320036 to ASME IX (GTAW P. No 8 Groove Weld) Zurich certificate ZE/WP/JT/000806.
3. Review of Zurich ASME IX Welder Performance Qualification for Richard Stanton. Zurich ZE/WPQ/BDW/00163.
4. Verified traceability and identification of materials on a sample basis from manufacturer's mill markings and stampings.
   - 2" NB Sch 10 ASTM A312 Grade 316L tube ref Sandvic 3.1 material certificate A/19-800175. Heat No.553271
   - 1.1/2" NB Sch 80 ASTM A312 Grade 316L tube ref Sandvic 3.1 material certificate A/19-781256 Heat No 558034
5. Confirmed CE marking of 'Free issue' equipment.
   - Recuperator Heat Exchanger manufactured by Heatric CE 0038 Serial no. H2786
   - Brazed Plate Heat Exchanger manufactured by SWEP CE 1155 Serial no.619027942000032
   - Liquid Receiver Vessel manufactured by ESK Shultze CE 0035 Serial no. 0318/180191/002.
6. Undertook visual inspection of welded joints, so far as permitted by construction, examined assembly for correct integration of components and supports.
7. Verified calibration status of Pressure Gauge used for Strength testing of assembled piping.
8. 0 to 3500PSI (+/- 0.25% FSD) gauge serial No. 67969002 calibrated by Chamois Metrology Ltd (UKAS 0822) on 19/12/2018 due 19/12/2019 reference certificate No. 57213.
9. Witnessed strength testing of Low-Pressure Pipe Work assembly with OFN2 at 107.25 Bar (1.43x PS). Pressure Held for 10 mins. No evidence of pressure decay.
10. Visual inspection of assembly after strength testing. No deformation observed.

Figure A9: Inspection report with regards to materials and welding qualifications

Orbital Ltd also has been responsible of strength-testing the sCO$_2$ loop assembly (Figure A10). Oxygen free nitrogen has been used with a pressure up to 107 bar for the low-pressure side of the system and up to 170 bar for the high-pressure side of the loop. The test at 107bar has been witnessed by Lloyd's register as reported at point 9 of the inspection report (Figure A9). The testing certificate has been instead been reported in Figure A10.

Orbital Fabrications Ltd

ORBITAL FABRICATIONS

CERTIFICATE OF TESTING & COMPLIANCE

Customer: Brunel University .... Certificate no: PT 16576

Project: SCO2 Loop .... P.O. no: 601476

Site of Test: Orbital Fabrications, St Ives .... Our job no: 25300

Procedure for Pressure / Helium Leak Testing: HLT1/PTP1/HPTP1/HSP1 ....

Line no: N/A .... Location: N/A .... Line Gas: N/A ....

Pressure Test:

Test Gas: Nitrogen

Duration of Test: 30 minutes

Exemptions: ....

Test Date: 10/10/19

Pressure: 170 Bar and 107 Bar

Pressure Gauge serial no: 67969002

Test Results / Description: No drop detected

Snoop Test:

Test Gas: ....

Pressure: ....

Exemptions: ....

Test Date: ....

Pressure Gauge serial no: ....

Test Results: ....

Helium Leak Test:

Test Gas: Helium ....

Vacuum Test: 1×10^{-10} mbar l/sec ....

Leybold UL200/ UL1000 Leak Checker serial no: 90001225737/90001103321/20600077245

Calibrated Leak serial no: built in

Exemptions: ....

Test Date: ....

Pressure: N/A ....

Pressure Gauge serial no: N/A ....

Test Results / Description: No. Assemblies - No leaks found

Additional Comments / Special Instructions:

We certify that the work carried out has been checked to the above specification. Any alterations, modifications or design changes to the system should be notified to the company. Without such notification this certificate is invalidated.

Witnessed:

R. Stanton on behalf of Orbital Fabrications Ltd Signed: ....

Figure A10 - Pneumatic strength testing certificate of the sCO₂ loop

After the strength test, to obtain the conformity of the full sCO_2 system to the PED, the following steps have been done:

- CE marking of the sub-systems (provided by manufacturers);
- strength testing of the 10-meter pipes detailed in the first section of the appendix;
- Leak testing of the whole facility.

CE marking and leak test

To ensure the maximum safety for the demonstration of the sCO_2 system, the demonstrator underwent through a rigorous assessment based on the Pressure Equipment Directive (PED) 2014/68/EU. More specifically, since the sCO_2 system falls in the Category IV of PED, the assessment was carried out according to module G, which implied a thorough design appraisal, as indicated in Figure A11. The documentation for the Global Conformity Assessment under the PED has been submitted for review to the notified body (Lloyd's register UK).
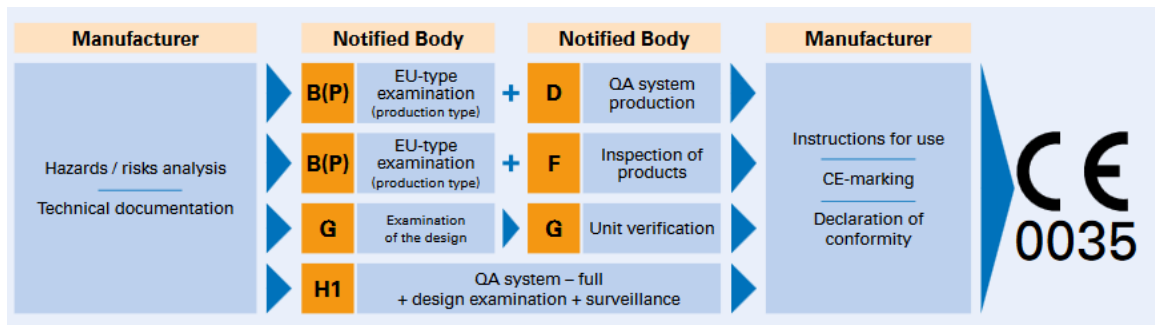

Figure A11 - CE marking workflow (source: TUV)

Turbomachinery 3D CFD model development approach

For the modelling of the turbomachines, performance maps have been used, generated by using three-dimensional Computational Fluid Dynamic (CFD) models. The compressor and turbine impeller geometries selected during the design stage are similar to the ones tested at the Sandia sCO_2 compression loop facility [143]. The number of vanes are equal (6+6, as shown in Figure A12) but the blade shape has been modified and the wheels dimensions scaled to achieve a higher efficiency. A wheel diameter of 57.12 mm has been selected for the turbine and 44.03 mm for the compressor. For the design and model of the turbomachines, different packages in ANSYS have been used (i.e. CCD, RTD and BladeGen).

To perform validation of the model, simulations have been carried out assuming the initial thermodynamic conditions of the CO_2 to be in the supercritical region. The inlet temperature has been set equal to 32.5°C, the inlet pressure 78.7 bar, and the design shaft speed has

been set at 55,000 RPM. Compressor inlet operating conditions were determined to avoid the formation of liquid where the flow is accelerated locally.

ANSYS CFX 17.1 was employed to perform single-passage steady state calculations. The wheel's mesh has been generated in ANSYS-TurboGrid, shown in Figure A12, together with the flow path of the compressor. An Automatic Topology and Meshing feature (ATM optimized) has been employed inside the impeller, with a mesh of approximately 10+6 nodes (Figure 2). The k-ε and total energy models have been used to take into account the flow turbulence and its compressibility, with total pressure and total temperature defined as inlet boundary conditions and the flow direction considered normal to the boundary. Outlet average static pressure has been chosen as outlet boundary condition.

To simulate the real gas effect, the Span-Wagner Equation of State model has been used to accurately generate the flow properties [30]. For this purpose, a Real Gas Property (RGP) format table has been created to implement the variable properties in the CFX code. The user-defined table includes CO_2 features such as specific heat ratio and density near the critical point, which fluctuates due to the phase change effect. These features have been created using the NIST Refrop 8.0 fluid property database. The generated property files have been combined with a MATLAB code to create a lookup table as an input of TASCflow RGP in ANSYS CFX 17.1.
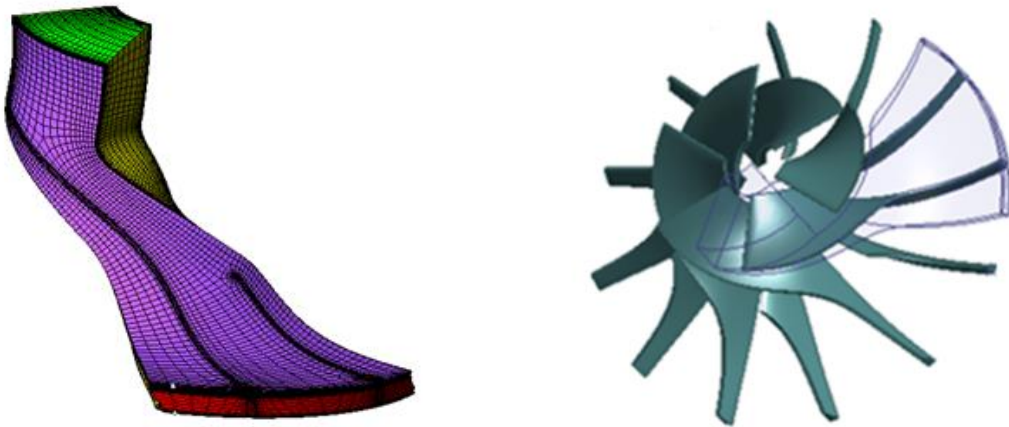

Figure A12 - ANSYS-TurboGrid Mesh and flow path for Supercritical CO_2 compressor.